Chemically Modified Hafnium Diboride for Hypersonic Applications: Synthesis and Characterisation

---

by

Pengxiang Zheng

A doctoral thesis submitted in partial fulfilment of the requirements for the reward of
Doctor of Philosophy of Loughborough University

May 2016

Supervisors: Prof. Bala Vaidhyanathan

Prof. Jon Binner

Loughborough University

To:

My Family

Acknowledgements

I would like to express my special appreciation and thanks to my supervisors and mentors, Prof. Jon Binner and Prof. Bala Vaidhyanathan for giving me the opportunity to conduct my Ph.D. on the most interesting and niche area of ultra-high-temperature ceramics. I would like to thank them for encouraging my research and guiding me with their valuable ideas. Their advice on both research as well as on my life has been priceless. I appreciate their patience and support which allows me to grow as a researcher. I would also like to thank Loughborough University for financial support, without it all this wouldn't have been possible.

I would like to give my sincere thanks to Mr. Andrew Lau, Mr. Ray Owens, Dr. Keith Yendall, Dr. Zhaoxia Zhou, Dr. Scott Doak and Mr. David Grandy their continual support with day-to-day lab requirements and characterization techniques. I would also like to express my gratitude to Dr. Doni Jayaseelan and Dr. Luc Vandeperre from ICL, London, Dr. Salvatore Grasso from QMU, London, Dr. Carmen Carney from AFRL, US and Dr. Ji Zou from UoB, Birmingham for their help and valuable discussions.

I shall acknowledge all my colleagues and ex-colleagues in the Advanced Ceramic Research Group, Loughborough University, who consistently supported me throughout my Ph.D. In particular, I would like to thank Dr. Saranya Venugopal, Dr. Anish Paul, Dr. Sina Saremi, Dr. Siyuan Qi, Dr. Yifei Zhang, Dr. Prabhu Ramanujam, Miss Ying Zhu, and Mr. Aashu Anshuman for all their scientific and emotional advice.

I thank my parents, sister and all my friends residing in Uk and China who supported me in writing and inspired me to strive towards my goal. At the end, I would like to express my appreciation to my lovely girlfriend, Miss Yumeng Chen, who always backed me up when there was no one to answer my queries.

Abstract

Hypersonic flight at a speed greater than Mach 5 (1715 ms^{-1}) requires materials that can withstand temperatures up to 3000^{o}C, high heat flux, rapid heating and disassociated reactive oxygen in the extreme environment of space and during re-entry. A number of advanced ceramic materials have melting points over 3000^{o}C, of which the refractory metal carbides and borides are of main interest due to their excellent thermal conductivity from room temperature to over 2500^{o}C, good chemical stability and ablation resistance at high temperatures. These materials are classified as ultra-high-temperature ceramics (UHTCs). Among the family of UHTCs, ZrB_2 and HfB_2 are reported as the most promising candidates to be used as thermal protection systems (TPS) for the nose tip and sharp leading edges. However, the issue of using monolithic ZrB_2 and HfB_2 is the phase transformation of ZrO_2 and HfO_2 oxide by-products at elevated temperature, leading to a volume change that results in cracking of the formed oxide scale. Hence, it is necessary to use dopants to stabilize the oxidation products of ZrB_2 and HfB_2 *in-situ* and to minimise the transformation induced cracking and thus improving the oxidation resistance. This research is focused on introducing dopants, such as Y and Ta into HfB_2 and to understand its effect on the oxidation behaviour of HfB_2 based UHT ceramics. The primary objectives were to: (a) Synthesize sub-micron pure and doped HfB_2 powders; (b) Sinter the HfB_2 based ceramics to achieve relative density >95% (i.e. with close porosity); (c) Assess the effect of dopants on the oxidation resistance of HfB_2 ceramics at high temperatures.

Sub-micron pure HfB_2 powder of ~200 nm was synthesized by a modified sol-gel approach combined with subsequent carbothermal reduction process using hafnium tetrachloride, boric acid, and phenolic resin as the starting materials. HfC and residual carbon were found to be the main impurity phase, owing to the lack of removal of carbon-containing species in the argon atmosphere during the heat treatment. Therefore, a precipitation approach was developed to transfer hafnium tetrachloride into hafnium hydroxide during the mixing stage to

get rid of the Cl^- and carbon-containing functional groups. Based on the detailed study of the formation mechanism of HfB_2, it was found that the particle size of the HfB_2 powders was decided by the particle size of the starting Hf source. Although the powders were slightly coarser (~400-800 nm) from the precipitation approach, importantly phase-pure HfB_2 was formed at the same furnace heating conditions (1600°C/2 hrs). The precipitation method was also used to prepare doped HfB_2 powders as the homogeneity of the dopants (TaB_2, Y_2O_3) could be improved by controlling the pH values at ~8.5 to achieve the simultaneous precipitation of the dopants and HfB_2 precursors. As a result, $(Hf,Ta)B_2$ solid solution was prepared successfully at the temperature of 1600°C.

Spark plasma sintering (SPS) was used to densify the pure and doped HfB_2 powders. The optimized density achieved was around 97% at 2150°C without the use of any sintering aids and the addition of TaB_2 slightly improved the sinterability of the HfB_2 based powders due to the formation of the $(Hf,Ta)B_2$ solid solution. The sintered density of commercial micron HfB_2 powders (Treibacher) was only 94% in the same condition, and the resultant grain size (5-10 μm) is also significantly larger than that from synthesized HfB_2-based ceramics (2-6 μm). The oxide impurities, such as HfO_2 and B_2O_3, on the surface of the fine HfB_2 based powders were attributed as the main reason for inhibiting further densification.

The oxidation behaviours of the HfB_2 based ceramics were investigated via both static oven oxidation and oxyacetylene torch testing. In low and intermediate temperature regime (<1600°C), it was indicated that the addition of dopants didn't significantly improve the oxidation resistance as the glassy B_2O_3 was the critical factor controlling the oxygen permeation rate. However, in the high-temperature regime (>1600°C), it was found the oxidation product was mainly tetragonal HfO_2, which was stabilized by the Ta-dopants at temperatures well below the HfO_2 phase transformation temperature. Therefore, the cracking and volume change due to phase transformation can be avoided and in return, oxidation resistance was improved at high temperature, which should be beneficial for the application of these materials in hypersonic aviation.

Table of Contents

1. Introduction 1
1.1 Hypersonic aviation and the need for Ultra High Temperature Ceramics (UHTCs) 1
1.2 Challenges of developing UHTCs 4
1.3 Description of chapters 5
2. Literature Review 7
2.1 Definition of Ultra High Temperature Ceramics (UHTCs) 7
2.2 Historical development of ultra-high temperature materials 8
2.3 Useful attributes for the design of UHTC components in hypersonic applications 12
2.3.1 Melting point 12
2.3.2 Oxidation/ablation resistance 14
2.3.3 Physical properties 14
2.3.4 Thermal properties 16
2.3.5 Mechanical properties 17
2.3.6 Surface properties 18
2.4 Refractory borides and other monolithic UHTCs 19
2.4.1 Refractory borides 19
2.4.2 Refractory carbides 29
2.4.3 Refractory oxides 32
2.4.4 Refractory nitrides 33
2.4.5 The most promising materials for hypersonic applications – ZrB_2 and HfB_2-based ceramics 34
2.5 Synthesis of refractory metal boride powders 35
2.5.1 Reactive routes 35
2.5.2 Chemical routes 37
2.5.3 Reduction processes 38
2.6 UHTC composites 43
2.6.1 Various refractory metal boride based composites 43
2.6.2 Densification of UHTCs 50
2.6.3 Oxidation behaviours of UHTCs and UHTC based ceramics 59

2.6.4 Physical properties of UHTC composites 72
3. Experimental 76
3.1 Raw materials 76
3.2 Characterisation of raw materials 77
3.3 Preparations of HfB_2-based ceramic powders 77
3.3.1 Borothermal reduction reaction-precursors 77
3.3.2 Carbothermal reduction reaction precursors 82
3.4 Heat treatments of the precursors 88
3.5 Densification of HfB_2-based ceramics 90
3.5.1 Pressureless sintering of HfB_2-based ceramics 90
3.5.2 Pressure assisted densification: spark plasma sintering 93
3.6 Oxidation testing of HfB_2-based ceramics 94
3.6.1 Static furnace oxidation 94
3.6.2 Oxyacetylene torch testing 96
3.7 Sample preparation and characterization techniques used 97
3.7.1 Fourier transform infra-red (FTIR) spectroscopy 97
3.7.2 BET surface area measurements 97
3.7.3 Mastersizer 98
3.7.4 X-ray diffraction (XRD) 98
3.7.5 X-ray photoelectron spectroscopy (XPS) 99
3.7.6 Thermal gravimetric analysis (TGA) 100
3.7.7 Sample mounting and polishing 100
3.7.8 Cutting of the sintered ceramics 101
3.7.9 Density measurements 102
3.7.10 X-ray fluorescence analysis (XRF) 102
3.7.11 Thermal and electrical conductivity measurements 103
3.7.12 Field emission gun scanning electron microscopy 104
3.7.13 Focused ion beam (FIB) 104
3.7.14 Transmission electron microscopy (TEM) 105
4. Results and discussion 106
4.1 Synthesis of pure and doped HfB_2 powders by carbothermal reduction reaction method 106
4.1.1 Characterization of the starting materials 106

4.1.2 Synthesis of HfB_2 powders by carbothermal reduction reaction from sol-gel derived precursors 111

4.1.3 Synthesis of doped HfB_2 powders by carbothermal reduction reaction…. 134

4.2 Synthesis of pure and Ta-doped HfB_2 powder by borothermal reduction reaction 148

4.2.1 Synthesis of HfB_2 powder by borothermal reduction reaction 149

4.2.2 Synthesis of Ta-doped HfB_2 powders by borothermal reduction reaction using co-precipitation-derived precursors 153

4.3 Densification of the HfB_2-based ceramics 158

4.3.1 Pressureless sintering 158

4.3.2 Pressure assisted densification of HfB_2–based ceramics..... 163

4.4 Characterization of pure and Ta-doped HfB_2 sintered ceramics..... 173

4.4.1 Thermal and electrical conductivity measurements..... 173

4.4.2 Static oxidation testing 176

4.4.3 Oxyacetylene torch testing 182

5. Conclusions 186

6. Future work..... 190

7. References 192

List of Tables

Table 2.1 List of recent research efforts in UHTCs [63] 10
Table 2.2 Comparison of some physical and thermodynamic properties of UHTCs (HfB_2, HfC and ZrB_2) with that of other materials that can be used in different components of hypersonic vehicles [23], [42], [50], [52], [53], [72], [73] 15
Table 2.3 Some structural, physical and thermodynamic properties of the transition metal borides [85]–[92] 20
Table 2.4 Properties of HfC_x at room temperature [21] 30
Table 2.5 Brief summary of the oxidation products and behaviours of some UHTCs 34
Table 2.6 Various reduction reactions to synthesize HfB_2. The reactions are also applicable to ZrB_2 [135] 38
Table 2.7 Hot pressing conditions and densities of hot-pressed commercial ZrB_2 and HfB_2 with various additives 53
Table 2.8 SPS conditions and densities of SPS-ed commercial ZrB_2 and HfB_2 with various additives 56
Table 2.9 Summary of oxidation behaviour of SiC containing ZrB_2 and HfB_2 over a wide temperature range [154], [219]–[223] 60
Table 2.10 Gas-condensed phase equilibria during the oxidation of ZrB_2-SiC. The gaseous Si containing products forms under the oxide scale where the oxygen partial pressure is low and then condenses at the surface to form an outer silica layer and leave a silicon depleted zone in the oxide scale near the boride [220], [224] 61
Table 2.11 Comparison of the oxidation behaviours of some refractory borides based ceramics 66
Table 2.12 Comparison of the ground based testing facilities for UHTCs 72
Table 3.1 The chemicals used in this project and their suppliers 76
Table 3.2 Composition of the precursors used for borothermal reduction 80
Table 3.3 Composition of the precursors used for carbothermal reduction 83
Table 3.4 Various calcination temperatures and time for Cl- removal in HfB_2 86
Table 3.5 Various heat treatment profiles for HfB_2 powder synthesis 89
Table 3.6 HfB_2-based samples for furnace oxidation testing at various temperatures with 10 min dwelling time 94
Table 3.7 Grinding and polishing cycle for sintered HfB_2-based ceramics ... 101
Table 4.1 Thermal degradation temperature and products of $HfOCl_2{\cdot}8H_2O$, H_3BO_3 and novolac phenolic resin, summarized from Figure 4.3, 4.4 and 4.5 114
Table 4.2 XPS composition analysis of the HfB_2 precursor powders before and after calcined at 400°C for 3 h in air 114
Table 4.3 Comparison of the mean particle size and surface area between the HfB_2 powder prepared by sol-gel derived precursors and commercial HfB_2 123

Table 4.4 Composition analysis of the contamination deposited on the end caps of the tube furnace after HfB_2 synthesis 127
Table 4.5 Elemental analysis of the calcined $Hf(OH)_4$ by XPS..... 129
Table 4.6 Properties of several group V and VI refractory metal borides..... 135
Table 4.7 Literature and measured values of the lattice parameter for pure HfB_2 and TaB_2 140
Table 4.8 Measured values of the lattice parameter for HfB_2 and Ta-doped HfB_2..... 146
Table 4.9 Hf/Ta atomic ratio measurement by XRF for the pure and Ta-doped HfB_2..... 156
Table 4.10 Density and grain size of the sintered pure and Ta-doped HfB_2 ceramics, prepared by different synthesis methods 167
Table 4.11 Weight gain of the pure and Ta-doped HfB_2 after oven oxidation at 1000, 1300, 1600, 1700, 1800 and 1900^{o}C for 10 min..... 180

List of Figures

Figure 1.1 (a) Space Shuttle Orbiter Endeavour by NASA; (b) X-43-A, a design of reusable space vehicle by NASA [5], [6] 2
Figure 1.2 Comparison of heat flux distribution on blunt and sharp leading edge [10] 3
Figure 2.1 Schematics of heat flow in (a) blunt leading edge and (b) sharp leading edge, (the effects that lead to heating are in red, including by q_{conv}: convective flow, q_{rad}: radiation, q_{chem}: chemical reactions and q_{catal}: surface catalysis, while the effects that lead to heat dissipation are in blue including by q_{cond}: conduction, and q_{rerad}: reradiation) [66]. 12
Figure 2.2 A comparison of melting temperatures between the most refractory members of different classes of materials [50]. 13
Figure 2.3 Energy balance of the leading-edge of hypersonic flight [71] 17
Figure 2.4 The MB_2-type structure of HfB_2 or ZrB_2 [42] 21
Figure 2.5 The thermal conductivities of HfB_2, HfN, $HfC_{0.67}$ and $HfC_{0.98}$ [21]. 22
Figure 2.6 Monolithic ZrB_2 oxidized at (a) 900°C for 8 h and (b) 1500°C for 2 h, the thicknesses of oxide layers are 10 μm and 400 μm respectively [66]. . 24
Figure 2.7 Schematic sketch of the different oxidation products of ZrB_2 at different oxidation regimes [99]. 25
Figure 2.8 Comparison of parabolic rate constants for oxidation of HfB_2 and ZrB_2 as a function of temperature [105] 27
Figure 2.9 (a) Model predictions of the boride recession in air as a function of temperature is compared with Fenter's data [109]. (b) The model predictions for mass change are shown compared to experimental data obtained in Ar/O_2 gas in 2 h [21]. (c) The scale thickness obtained after 5 h in air by Opeka et. al [21] is shown compared to the predictions [108]. 28
Figure 2.10 The phase equilibrium diagram for HfC_x [116]. 30
Figure 2.11 Multi-layer structures in hafnium carbide, oxidized at 1865°C for 600s in an atmosphere of 93% argon and 7% oxygen [97] 31
Figure 2.12 Post-test photographs showing evidence of porous, adherent scale on HfN and dense oxide that formed on $HfN_{0.75}$ [48] 33
Figure 2.13 SEM micrographs of ZrB_2 formed via (a) SHS, after NaCl removal, 10 wt% NaCl was added; (b) reactive hot pressing, at 600°C for 360 min [126], [127]. 36
Figure 2.14 SEM images of the ZrB_2 powders synthesized by (a) carbothermal reduction at 1600°C for 1h, and (b) borothermal reduction at 1650°C for 1h [78], [138]. 39
Figure 2.15 TEM image of the nano HfB_2 synthesized via a sol-gel approach [141]. 39
Figure 2.16 SEM image of HfB_2 synthesized at 1600°C for 1h, via carbo/borothermal reduction, using $HfCl_4$, B_4C and C powders [147]. 41

Figure 2.17 Chemical reactivity of hafnium and its derived boride, carbide and nitride compounds. Reactions with reagents marked in bold letters proceed (at least partially) at 1500°C or blow. The rest require higher temperatures, e.g. borothermal, carbothermal, and carbo/borothermal reduction reactions. Additional reaction products within each of the reactions (if present) are omitted. [135] 42
Figure 2.18 Schematic of the combined sol–gel and microwave boro/carbothermal reduction process used to prepare ultrafine ZrB_2–SiC composite powders [159] 44
Figure 2.19 X-ray diffraction patterns for heat treated ZrB_2-TaB_2 powders. The samples placed in a graphite tube furnace in flowing argon [153]..... 46
Figure 2.20 Failure stress of FC2 fibre and PANEX 33 fibre as a function of temperature [178]..... 48
Figure 2.21 An illustration of typical UHTC/carbon preform composite [75] .. 48
Figure 2.22 Stress/displacement curves from bending tests of: (A) uncoated composites and (B) HfB_2/SiC-coated composites [109] 49
Figure 2.23 A flowchart of impregnation-infiltration process for Cf/UHTC composites and its products [75]..... 50
Figure 2.24 Schematic of the sintering processes of ceramics [182] 51
Figure 2.25 Schematic of SPS setup [200]..... 55
Figure 2.26 Relative density as a function of sintering temperature for phase pure ZrB_2 and ZrB_2+4 vol% B_4C [152]..... 58
Figure 2.27 (a) Schematic oxide structure of ZrB_2-SiC ceramics and (b) cross-section of the ZrB_2-SiC after oxidation at 1500°C [98], [220]..... 62
Figure 2.28 Studies of oxidation resistance of pure and additive containing ZrB_2-SiC ceramics – comparison of mass gain versus time at 1500°C [84]... 63
Figure 2.29 Cross-section (a) of ZrB_2-6 mol% WC oxidized at 1600°C for 3 h along with EDS element maps for O (b), Zr (c), and W (d). The SEM image showed a two-layer oxide scale. The EDS maps showed that the outer scale had lower W (d) and O (b) contents than the inner layer, indicating depletion of WO_3 and probably B_2O_3 from the outer layer [173] 65
Figure 2.30 Simulation of hypersonic flow conditions in arc-jet testing [236]. 67
Figure 2.31 Oxidized layer thicknesses versus temperature of ZrB_2-SiC after arc-jet and oven oxidation testing [239]..... 68
Figure 2.32 Heat flux evaluation: (a) real test and (b) simulated temperature field [241] 69
Figure 2.33 Various UHTC/carbon fibre composites after 60 s oxyacetylene testing. Diameter of the composites was 30 millimetres [14]..... 70
Figure 2.34 SEM images of cross section of three samples laser tested at 44 MW m^{-2} for 1 second using a defocused ytterbium laser [243]. 71
Figure 2.35 Thermal conductivity as a function of temperature for ZrB_2 and ZrB2-30 vol% SiC [254]..... 73

Figure 2.36 Flexure strength as a function of test temperature for hafnium diboride (HfB_2) containing 20-30 vol% SiC. The HfB_2-based samples were densified by various sintering techniques [219] 74
Figure 3.1 Flowchart of preparing HfB_2 precursor powders 81
Figure 3.2 Flow chart of mixing different starting powders in sol-gel approach 84
Figure 3.3 Schematic of the experimental system used for the sol-gel approach 85
Figure 3.4 Flow chart of mixing different starting powders for precipitation approach. 87
Figure 3.5 High temperature tube furnace and alumina tube used for the synthesis of HfB_2-based powders 88
Figure 3.6 Schematic of the experimental arrangement used for the synthesis of HfB_2-based powders 89
Figure 3.7 Schematic of the microwave furnace for the densification of HfB_2-based ceramics 91
Figure 3.8 Schematic of the sample holder for flash sintering of HfB_2-based specimen 92
Figure 3.9 The graphite die used for SPS, Queen Mary University, London . 93
Figure 3.10 Schematic of HfB_2-based specimens tested in the zirconia element furnace 95
Figure 3.11 Oxyacetylene torch test set up [14], [263] 96
Figure 4.1 XRD patterns of $HfCl_4$ powder after exposing to air for 24 hours indicating mainly $HfOCl_2 \cdot 8H_2O$ 107
Figure 4.2 Octahedral chain structure of $HfCl_4$ and the composition of a partially hydrated $HfCl_4$ particle [261] 108
Figure 4.3 Thermal decomposition of $HfOCl_2 \cdot 8H_2O$ from ambient temperature to 1000°C 109
Figure 4.4 Molecular structure of novolac phenolic resin 109
Figure 4.5 TGA of novolac phenolic resin from ambient temperature to 1000°C in different atmosphere 110
Figure 4.6 TGA of boric acid from ambient temperature to 1000°C in argon 111
Figure 4.7 FTIR spectra of $HfCl_4$, H_3BO_3 and novolac phenolic resin solution and dried precursor powders 112
Figure 4.8 SEM-EDX images of the precursor powders obtained from $HfOCl_2$, H_3BO_3 and novolac phenolic resin solution 113
Figure 4.9 Thermal degradation of $HfOCl_2 \cdot 8H_2O$ in air, at 400°C for 3 h 115
Figure 4.10 TGA-DTA curve of the sol-gel derived precursor, the elemental ratio of Hf:B:C=1:3:5 116
Figure 4.11 XRD patterns of the HfB_2 precursor powders, elemental ratio of Hf:B:C=1:3:5, heated from 600°C to 1500°C with 0.1 h dwell in argon 117
Figure 4.12 X-ray diffraction patterns of the precursors (elemental ratio of Hf:B:C=1:4:5) heat treated at 1600°C with various dwell time 118

Figure 4.13 XRD patterns of the powders synthesized with various Hf:B:C ratio, 1:2:5, 1:3:5 and 1:4:5, at 1600°C for 2 h 119
Figure 4.14 HfB_2 mass fractions vs. the intensity ratio of the strongest peaks of HfC/HfB_2 120
Figure 4.15 XRD patterns of the precursor powders (Hf:B:C=1:3:5) heat treated at 1600°C for 2 h, with argon flow rates of 60 and 100 cm^3min^{-1} 121
Figure 4.16 Comparison of the particle size and morphology of the (a)-(c) HfB_2 powders synthesized by carbothermal reduction reaction from sol-gel derived precursors with different Hf:B:C ratios and (d) commercial HfB_2 powders ... 123
Figure 4.17 Schematic of the synthesis of HfB_2 powder via carbothermal reduction reaction, from sol-gel derived precursor to sub-micro sized HfB_2 powder 124
Figure 4.18 Particle size distributions of (a) the HfB_2 powder prepared by the sol-gel derived precursor with Hf:B:C ratio of 1:4:5 and (b) commercial HfB_2 powder 125
Figure 4.19 FEGSEM images of (a) the bulk $HfOCl_2$, boric acid and phenolic resin precursors with Hf:B:C ratio of 1:4:5 and (b) the hard agglomerates in the resultant HfB_2 powder 126
Figure 4.20 The methods of arranging the precursor powders (Hf:B:C ratio of 1:4:5) in alumina crucibles and their effect on the homogeneity of the HfB_2 powders yielded from the carbothermal reduction reaction..... 127
Figure 4.21 XPS elemental survey for the HfB_2 powders obtained from carbothermal reduction. The precursors were placed in alumina crucible using the method shown in Figure 4.20(a) and the HfB_2 powder at the top analysed by XPS 128
Figure 4.22 Surface area and particle size of the calcined $Hf(OH)_4$ vs. pH value 130
Figure 4.23 TEM image of the $Hf(OH)_4$ precipitates formed at pH of 8.5, followed by drying at 400°C and grinding using a pestle and mortar..... 131
Figure 4.24 TEM images of HfO_2 nuclei formed by calcination of (a) $HfOCl_2$, H_3BO_3 and phenolic resin precursor and (b) $Hf(OH)_4$, H_3BO_3 and phenolic resin precursor at 1100°C for 1 h in air..... 131
Figure 4.25 XRD of the HfB_2 powder synthesized by precipitation approach, the precursors with an Hf:B:C ratio of 1:3:5 was held at 1600°C for 2 h 132
Figure 4.26 Comparison of the morphology and particle size of the HfB_2 powders yielded from (a) sol-gel derived precursors, (b) precipitation derived precursor with stoichiometric Hf:B:C ratio and (c) precipitation derived precursor with excess boron 133
Figure 4.27 Schematic of the chelation process in the synthesis of Y_2O_3 doped HfO_2 136
Figure 4.28 EDX mapping for hafnium and yttrium in the mixed precursors yielded from 8 wt% $Y(NO_3)_3 \cdot 6H_2O$ and $HfOCl_2 \cdot 8H_2O$ 137

Figure 4.29 XRD patterns for pure and Y-doped HfB_2 powders obtained from carbothermal reduction synthesis. LaB_6 was used as a reference for the investigation of diffraction peak shifting..... 137
Figure 4.30 EDX mapping for hafnium and yttrium in the Y-doped HfB_2 obtained from carbothermal reduction..... 138
Figure 4.31 XRD patterns of the pure and Y-doped HfB_2 powders oxidized at 1600°C for 0.1 h in air 139
Figure 4.32 XRD patterns of the TaB_2 and HfB_2 powder synthesised by carbothermal reduction using precipitation-derived precursors. The Ta:B:C and Hf:B:C molar ratio of the corresponding precursors to yield pure TaB_2 and HfB_2 powder were 1:3:5.5 and 1:3:5, respectively..... 140
Figure 4.33 SEM image and EDX mapping of the co-precipitation derived precursors which was for the synthesis of 10 wt% Ta-doped HfB_2..... 141
Figure 4.34 XRD patterns for the 10 wt% Ta-doped HfB_2 precursor heat treated at various temperatures. The heating rate was 5°C min^{-1} and the sample was soaked for 2 hrs at each targeted temperature. 142
Figure 4.35 (a) SEM image and EDX mapping of the fracture surface of the powder compacts of TaB_2 and HfB_2 heat treated at 1600°C for 2 h; (b) EDX line scan was performed along the solid line shown in Figure 4.35(a) 144
Figure 4.36 XRD patterns for pure and 5, 10 and 15 wt% Ta-doped HfB_2 powders heat treated at 1600°C for 2 hours 145
Figure 4.37 High-resolution XRD patterns for the diffraction peak associated with (101) plane in pure and Ta-doped HfB_2. 146
Figure 4.38 SEM image and EDX mapping of the 10 wt% Ta-doped HfB_2 powder 147
Figure 4.39 SEM images of the (a) 0, (b) 5, (c) 10 and (d) 15 wt% Ta-doped HfB_2 powders synthesized by carbothermal reduction reaction 148
Figure 4.40 The weight and heat flow changes for the mixture of $Hf(OH)_4$ and boron (molar ratio of Hf:B=1:4) as a function of temperature 150
Figure 4.41 XRD patterns of the $Hf(OH)_4$ and boron precursors with different Hf:B ratios, 1:3.3, 1:4 and 1:5. The precursors were heat treated at 1600°C for 2 h in argon 150
Figure 4.42 High-resolution XPS scan of the boron species for B_2O_3 and B powder mixture after heat treatment at 1000°C for 1 h 152
Figure 4.43 The morphology and particle size of the HfB_2 powders with different Hf:B ratios (a) 1:3.3, (b) 1:4 and (c) 1:5, synthesized by borothermal reduction reaction at 1600°C for 2 h..... 153
Figure 4.44 XPS analysis of the 10 wt% Ta-doped HfB_2 powders synthesized by borothermal and carbothermal reduction reaction, both at 1600°C for 2 h 154
Figure 4.45 XRD patterns of the 10 wt% Ta-doped HfB_2 powders synthesized by borothermal reduction reaction at 1600°C for 2 h..... 155

Figure 4.46 (a) SEM image of the 10 wt% Ta-doped HfB_2 powders synthesized by borothermal reduction reaction at 1600°C for 2 h and the distribution of (b) Hf, (c) Ta and (d) B in the powders 155
Figure 4.47 Area analysis of the composition of 10 wt% Ta-doped HfB_2 powders synthesized by borothermal reduction reaction at 1600°C for 2 h . 156
Figure 4.48 Particle size distributions of the 10 wt% Ta-doped HfB_2 powders synthesized by borothermal reduction reaction at 1600°C for 2 h 157
Figure 4.49 (a) Dielectric constant vs. temperature and (b) dielectric loss vs. temperature for pure and Ta-doped HfB_2, measured at 2470MHz. 159
Figure 4.50 Sample temperatures vs. powder output of the microwave furnace for 10 wt% Ta-doped HfB_2. Argon was continuously passing through the tube furnace with a flow rate of 200 cm^3 min^{-1} 160
Figure 4.51 IR camera images for the 10 wt% Ta-doped HfB_2 with furnace temperature of 1450°C during flash sintering 161
Figure 4.52 The relationship between power density and furnace temperature for the flash sintering of 10 wt% Ta-doped HfB_2 162
Figure 4.53 Force- and temperature-time profiles used for SPS of the HfB_2-based powders at 2150°C 164
Figure 4.54 Temperature-, shrinkage- and displacement-time profiles measured during the SPS run of 15 wt% Ta-doped HfB_2 powders at (a) 2000°C, (b) 2100°C, (c) 2150°C and (d) pure HfB_2 powder at 2150°C..... 165
Figure 4.55 Polished surfaces of the 15 wt% Ta-doped HfB_2 samples sintered at (a) 2000, (b) 2100 and (c) 2150°C 166
Figure 4.56 Fracture surfaces of (a) 0 wt%, (b) 5 wt%, (c) 10 wt% and (d) 15 wt% Ta-doped HfB_2 ceramics, sintered at 2150°C. The powders used for SPS were synthesized by carbothermal reduction reaction 168
Figure 4.57 (a) Fracture surface and (b) polished surface of 15 wt% Ta-doped HfB_2 sintered at 2150°C at higher magnification. The powders used for SPS were synthesized by carbothermal reduction reaction 168
Figure 4.58 Polished surfaces of (a) 0, (b) 5, (c) 10 and (d) 15 wt% Ta-doped HfB_2 ceramics, sintered at 2150°C. The powders used were synthesized by borothermal reduction reaction 169
Figure 4.59 BSD images of the polished surface of 15 wt% Ta-doped HfB_2. (a) and (c) were prepared by the carbothermal reduction powders. (b) and (d) were prepared by the borothermal reduction powders. The colour difference of the HfB_2 grains in the BSD images is due to the orientation of the particles 170
Figure 4.60 EDX elemental scan for 15 wt% Ta-doped HfB_2 grains preapared by FIB. The scan was performed along the solid yellow line across the pore 171
Figure 4.61 XRD pattern of the post-SPS pure and Ta-doped HfB_2 samples 172
Figure 4.62 High resolution scan of (a) (001) and (b) (101) lattice plan of the post SPS pure and Ta-doped HfB_2 173

Figure 4.63 (a) Thermal diffusivity, (b) specific heat capacity and (c) thermal conductivity for pure and 15 wt% Ta-doped HfB_2, measured from room temperature to 1500°C. 174
Figure 4.64 Electrical conductivity vs. temperature for pure and 15 wt% Ta-doped HfB_2 176
Figure 4.65 XRD patterns of the (a) pure HfB_2 and (b) 15 wt% Ta-doped HfB_2 powders oxidized in air at various temperatures 177
Figure 4.66 XRD patterns of the pure and Ta-doped HfB_2 powders left in oven at 1600°C for 30 min 178
Figure 4.67 Mass change of the pure and Ta-doped HfB_2 powders at temperatures from room temperature to 1500°C with a heating rate of 5° min^{-1} 178
Figure 4.68 Cross-section of the pure and 15 wt% Ta-doped HfB_2 after exposing to air at 1600°C for 10 min 179
Figure 4.69 HfB_2-based ceramics after oxidation testing at 1700, 1800 and 1900°C in a zirconia oven 181
Figure 4.70 Cross section of the pure and 15 wt% Ta-doped HfB_2 after exposure to air at 1800°C for 10 min 181
Figure 4.71 Sample photos of (a) HfB_2 and (b) 15 wt% Ta-doped HfB_2 tested at 2300°C for 240 s and (c) 15 wt% Ta-doped HfB_2 tested at 2800°C for 240s 182
Figure 4.72 (a) Top surface and (c) fracture surface of 15 wt% Ta-doped HfB_2 tested at 2300°C and (b) top surface and (d) fracture surface of pure HfB_2 tested at 2300°C 183
Figure 4.73 Top surface of 15 wt% Ta-doped HfB_2 tested at 2800°C 184

Journal papers and conferences

1. *Synthesis and Static Oxidation Testing of Doped HfB_2 Powders*, P Zheng, J Binner, and B Vaidhyanathan, Engineering Conferences International ECI Digital Archives, Page 1, 2015

2. *Synthesis of sub-micron sized doped HfB_2 powders*, P Zheng, J Binner, and B Vaidhyanathan, International Conference and Exposition on Advanced Ceramics and Composites (38^{th} ICACC), The American Ceramic Society, Florida, USA, January 26-31, 2014.

3. *A comparative study of the synthesis of sub-micron sized HfB_2-base powder via sol-gel and co-precipitation approach*, P Zheng, J Binner, and B Vaidhyanathan, under revision, to be submitted to Journal of American Ceramic Society

4. *Investigation of tantalum doped hafnium diboride: powder synthesis, sintering and oxidation tests,* P Zheng, J. Zou, S. Grasso, J Binner, and B Vaidhyanathan, under revision, to be submitted to Acta Materialia

Abbreviations

ε'	Dielectric constant
ε''	Dielectric loss factor
σ	Electric conductivity
ρ	Density
μm	micrometer σ
AFRL	Air Force Research Laboratory
B	Boron
BET	Brunauer-Emmett-Teller
B_2O_3	Boron trioxide
C	Carbon
Cf	Carbon fibre
C_p	Specific heat capacity
DC	Direct current
DSC	Differential scanning calorimetry
DSTL	Defence Science and Technology Laboratory
EDX	Energy dispersive x-ray analysis
FEGSEM	Field emission gun scanning electron microscope
FIB	Focused ion beam
FTIR	Fourier transform infrared spectroscopy
GPa	Giga Pascal
Hf	Hafnium
HfB_2	Hafnium diboride
HfC	Hafnium carbide
$HfCl_4$	Hafnium tetrachloride
$HfOCl_2$	Hafnium oxychloride
$Hf(OH)_4$	Hafnium hydroxide
ICL	Imperial College London
K	Thermal conductivity
MPa	Mega Pascal
pH	Potential of hydrogen
PPR	Powder phenolic resin
PSD	Particle size distribution
SPS	Spark plasma sintering
Ta	Tantalum
TaB_2	Tantalum diboride
$TaCl_5$	Tantalum pentachloride
Ta_2O_5	Tantalum pentaoxide
$Ta(OH)_5$	Tantalum hydroxide
TEM	Transmission electron microscope
TGA	Thermo-gravimetric analysis
UHTC	Ultra high temperature ceramics
UoB	University of Birmingham
XPS	X-ray photoelectron spectrometer
XRD	X-ray diffraction
XRF	X-ray fluorescence

1. Introduction

1.1 Hypersonic aviation and the need for Ultra High Temperature Ceramics (UHTCs)

Hypersonic air- and spacecrafts can travel through the atmosphere at speeds above Mach 5, a speed where dissociation of air becomes significant and existence of high heat loads begin. The V-2 rocket, first used in World War II by Nazi Germany and later used by the United States in its early rocketry work, was the first manufactured object to achieve hypersonic flight, i.e. reaching the speed Mach 5 [1]. Although the first rocket was destroyed due to high temperature during its atmospheric re-entry, the steps of developing faster and safer hypersonic vehicles never stopped. Significant research efforts were contributed to realise the dream of on-demand access to space and rapid access to distant points on Earth. In April 1961, Russian Yuri Gagarin became the first human to travel at hypersonic speed, during the world's first piloted orbital flight. Soon after, in May 1961, American Alan Shepard also achieved hypersonic flight when his capsule re-entered the atmosphere at a speed of Mach 5 at the end of his suborbital flight over the Atlantic Ocean. In June 1961, United States Air Force and NASA launched the X-15 research flight, which reached the speed Mach 6.7 and is still holding the official world record for the highest speed ever reached by a manned, powered aircraft [2].

Since then, numerous flights have flown at hypersonic speeds, including aircraft Space Ship One and Space Ship Two, and especially the US Space Shuttle Orbiters, as shown in Figure 1.1a, which have been the only reusable atmospheric re-entry vehicles for the past 30 years. Recently the development of hypersonic vehicles has drawn much more attention as they are also suited for military applications because of the great difficulty of defending against them [3]. A few hypersonic aircraft and cruise missiles are under development in

various countries, including X-43 (unmanned experimental hypersonic aircraft by NASA, USA), shown in Figure 1.1b, X-51 (unmanned experimental hypersonic aircraft by Boeing, USA), Falcon HTV-2 (experimental rocket glider by DARPA, USA), Kholod (hypersonic rocket, Russia), IXV (experimental suborbital re-entry vehicle by European Space Agency), SHEFEX (Sharp Edge Flight Experiment conducted by the German Aerospace Centre), Skylon (experimental re-usable spaceplane by Reaction Engine Limited, UK) and WU-14 (hypersonic glide vehicle, China). The Mach number of the hypersonic vehicles ranges from 5 to 12. In these modern hypersonic vehicles design, no matter whether they are jet-propelled or only driven by gravity in their atmospheric re-entry, a slender body with sharp leading edges is employed to produce laminar flow across the control surfaces, thus reducing the vehicle's drag and enhancing manoeuvrability [4].

(a) (b)

Figure 1.1 (a) Space Shuttle Orbiter Endeavour by NASA; (b) X-43-A, a design of reusable space vehicle by NASA [5], [6]

In order to make next-generation hypersonic vehicles fly in the sky, it requires not only a slender body and stronger propelling force, but also advanced materials that can withstand higher temperatures and survive extreme environments. As mentioned, the speed of the Space Shuttle is about Mach 5 during the atmospheric re-entry. As a result of the aerodynamic heating of the

surface due to friction and shock wave heating, the surface temperature of the Shuttles increases rapidly. The maximum surface temperature on the shuttle reaches ~1650^{o}C since a blunt edge design is employed to transfer the intense heat associated with atmospheric re-entry [7]. The blunt surfaces produce a shock wave ahead of the vehicle that deflects some of the heat away from the surface by transferring most of the kinetic energy to the air behind the vehicle [8]. The issue with the sharp leading edge design is the convective heat to the surface. The leading edge of the Space Shuttle has a radius of approximately 10 cm at the tip while the design concepts for some hypersonic manoeuvring vehicles, such as Falcon HTV-2, which is under development by DARPA, have leading-edge radii on the level of millimetres. The increase in surface temperature is inversely proportional to the radius of the curvature of the edge tip as the heat flux impinges directly on the sharp tip as shown in Figure 1.2. Hence, the temperature developed on the sharp leading edges can rapidly exceed 2000^{o}C [9].

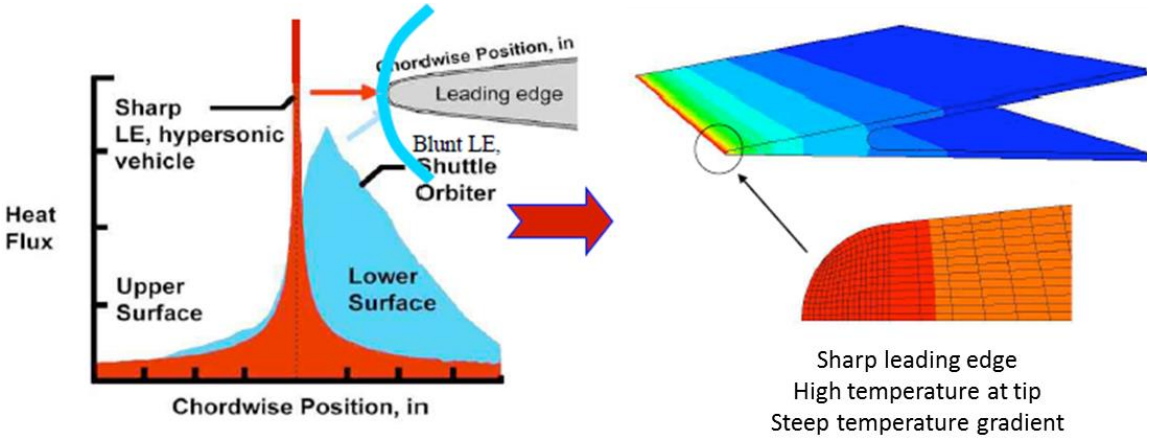

Figure 1.2 Comparison of heat flux distribution on blunt and sharp leading edge [10]

Silicon-based ceramics are widely used as thermal protection coatings on the Space Shuttles for aerospace applications [11]. Dense and stable SiO_2 formed on the surface acts as a protective barrier. However, at temperatures >1600^{o}C,

the silica evaporates, thus restricting its use for higher temperatures. Although other refractory oxides like zirconia and hafnia are very stable and possess high melting points (>2700^{o}C), their use is limited by poor thermal shock resistance and high creep rates at elevated temperatures [12], [13]. In hypersonic applications, the combination of extreme temperature and rapid heating/cooling encountered is beyond the capabilities of the current engineering materials, thus, explaining the interest in the development of UHTCs.

1.2 Challenges of developing UHTCs

For hypersonic vehicles, designers prefer to use metals or complex systems rather than using advanced ceramics due to the advantages of ductility and superior mechanical properties. It is generally believed that UHTCs will be mainly used as the thermal protection system (TPS) for the nose tip and sharp leading edges of the hypersonic vehicles. However, there is still a long way to go for current UHTCs to become practical materials for TPS application since the development of UHTCs is faced with processing and mechanical challenges as well as oxidation limitations.

The mechanical challenges include high density, low thermal shock resistance, low fracture toughness and the occurrence of phase transformations. Low thermal shock resistance and low fracture toughness can be overcome by fibre reinforcing the UHTCs, i.e. fabricating a composite [14], [15]. The stability of the oxide scale of the UHTCs can also be improved by adding various dopants into UHTCs [16]–[20], which is one of the primary goals of this work.

The oxidation limits the SiC-based UHTCs, the most widely studied UHTC system, to ~1600^{o}C temperature range for extended use [10], [21]–[28]. Above this temperature range, active oxidation and non-protective oxide scales result in the continual degradation of UHTCs. The SiC, which is added to improve the

oxidation resistance of UHTCs below ~1600^{o}C, is one of the primary contributors to the active oxidation and rapid degradation above ~1600^{o}C. Hence, UHTCs, either as monolithic ceramics or as UHTC/UHTC composites, have the potential for very higher temperature use.

Processing of UHTCs is also a big challenge for their advancement. Since UHTCs are usually boride, carbides and nitrides, which are difficult to densify, pressure-assisted sintering techniques, such as hot pressing and spark plasma sintering, are necessary to produce dense UHTCs or UHTC composites [16], [29]–[32]. The last and most critical challenge is to test UHTCs. However, it is nearly impossible to perform the testing in real extreme environments during the material development stages. Therefore, researchers have to simulate the extreme environments by creating testing methods such as arc jet testing [33]–[35] and oxyacetylene torch testing [14], [36]–[38], and then combine the results with static oven testing results to analyse and assess the possibility of using UHTCs for hypersonic applications.

1.3 Description of chapters

The sequence of the chapters in this report is following a standard scientific study order: introduction – literature review – experimental – results and discussion – conclusions – future work. After the introductory chapter, the next chapter provides a literature survey associated with the historical studies and achievements of UHTCs. Chapter 3 describes the experimental work performed, including all the details about the synthesis approaches, sintering procedures, testing methods and characterization techniques. The aim of this chapter is to make sure that the experimental work is repeatable for other researchers. Chapter 4 exhibits the results of the Ph.D. research, including the synthesis of HfB_2-based powders, the densification of the HfB_2-based ceramics and the study of the oxidation behaviours and thermal properties of the sintered HfB_2-

based ceramics. The conclusions are drawn in chapter 5 and possible future experimentation is outlined in chapter 6.

2. Literature Review

2.1 Definition of Ultra High Temperature Ceramics (UHTCs)

Ceramics are defined as inorganic, non-metallic solids comprising metal, non-metal or metalloid atoms primarily held by ionic and covalent bonds. Differently, the definition of a UHTC is extended to include some of the material characteristics: the common definition for a UHTC is a material with its melting point not lower than 3000^{o}C. There are very few materials that meet this criterion, including some metals: W (3400^{o}C), Re (3200^{o}C) and Ta (3000^{o}C). ThO_2 (3250^{o}C) is the only simple oxide that has a melting temperature beyond 3000^{o}C. Most of the materials that can be classified as UHTCs using this criterion are borides, carbides and nitrides of early transition metals Ta, Hf, Zr, Ti and Nb. Among these, ZrB_2, HfB_2, TaB_2, ZrC, HfC and TaC are the most studied for applications in extreme environments [39]–[42]. However, the melting point criterion itself is with significant uncertainty because of the difficulty of measuring temperature precisely at such high temperatures and the common occurrence of dissociation before the materials' melting. For example, although ZrB_2 belongs to the UHTC family, the reported melting point for ZrB_2 ranges from 3040^{o}C to 3517^{o}C from different publications [43]–[45]. Hence, the selection of a melting point above 3000^{o}C is arbitrary and only reflects one key property of UHTCs.

Another method to define UHTCs is associated with the material's long-term stability in extreme environments, i.e. the highest use temperature in air. The practical definition fits well with the name 'engineering materials'. As introduced before, materials like SiC, Si_3N_4 and composites of these materials which are currently used as protective coatings on the Space Shuttle Orbiters are able to be used in air at temperatures up to 1600^{o}C [46], [47]. Since the modern

hypersonic applications involve higher use temperatures, a lot of papers take the use temperature of 2000^{o}C as the threshold for UHTCs [23], [48]–[51]. Again, borides, carbides and nitrides of refractory metals (e.g. hafnium, zirconium and tantalum) meet this criterion since their oxidation products protect them during continuous use in extreme environments.

The definition of UHTCs based on the highest use temperature are still arbitrary as well as the one based on the melting temperature. UHTCs usually also need to fulfil other criteria, such as good thermal conductivity and high ablation resistance [42], [52]. In fact, the most widely used definition for UHTCs, which is used in this work as well, is not quantitative but the most summarised: most UHTC compounds are borides, carbides or nitrides of early transition metals. Hence, any compound containing a transition metal such as Zr, Hf, Ta, W or Nb along with B, C or N has the potential to be a UHTC.

There has been significant interest in these materials in recent decades and a lot of UHTC composites have also been developed to overcome some shortcomings of monolithic UHTCs. These UHTC composites can be a combination of two UHTCs (borides, carbides or nitrides of early transition metals, for example, TaB_2-HfB_2) or one UHTC and one non-UHTC. A typical composition for the latter is ZrB_2-SiC, which is very arguably in the terms of the definition of UHTCs because one of the constituents SiC cannot be used in air at temperatures above 1600^{o}C and it reduces the melting point of the composition to below 3000^{o}C [53].

2.2 Historical development of ultra-high temperature materials

The research of ultra-high temperature materials started with refractory metal coatings in the early 1950s [54]. The lack of oxidation resistance at elevated

temperature of these materials motivated the investigation of oxidation- resistant intermetallic compounds, especially compositions containing silicon, aluminium and chromium, which were found suitable for gas turbine applications [55]. Another branch of high-temperature materials, refractory metal oxides, were developed in parallel with the refractory metal coatings in 1950s. However, they have not been pursued due to their poor thermal shock resistance.

In the early 1960s, demand for high-temperature materials by the nascent aerospace industry prompted the Air Force Materials Laboratory (AFML) to begin funding the development of a new class of materials that could withstand the environment of proposed hypersonic vehicles, e.g. the Space Shuttle Orbiter by Manlabs Incorporated. Extensive work done by Manlabs and AFML showed that diborides of group IV, especially ZrB_2 and HfB_2, were promising candidates for use as nose-cones and leading edge materials [56]–[59].

UHTC research was largely abandoned after the pioneering work by Manlabs due to the completion of the Space Shuttle missions and the elimination of US Air Force spaceplane development. Three decades later, however, research interest was rekindled by a string of 1990s era NASA programmes aimed at developing new generation hypersonic flights such as the National Aerospace Plane, Hyper-X series hypersonic vehicles, and the Air Force's Blackstar programme [60]. New research in UHTCs was led by NASA Ames, which revived interest in HfB_2/SiC and ZrB_2/SiC for sharp leading edges [61], [62]. NASA Ames, teamed with Air Force Research Laboratory (AFRL), also tested these UHTCs in their hypersonic flight SHARP-B1 (1997) and SHARP-B2 (2000), showing the capability of UHTCs for extreme environment applications. Since this test, NASA Ames has continued refining production techniques for UHTC synthesis and performing basic research on UHTCs [62].

Table 2.1 List of recent research efforts in UHTCs [63]

Zr-B_2-Based Ceramics
Missouri University of Science & Technology, USA
AFRL, USA
NASA Glenn Research Center, USA
University of Illinois at Urbana-Champaign, USA
Harbin Institute of Technology, China
Naval Surface Warfare Center (NSWC)
NIMS, Tsukuba, Japan
Imperial College, London, UK
NASA Ames Research Center, USA
CNR-ISTEC, Italy
Leuven University, Belgium
Loughborough University, UK
HfB_2-Based Ceramics
NASA Ames Research Center, USA
Loughborough University, UK
University of Birmingham, UK
CNR-ISTEC, Italy
Imaging and Analysis (Modeling)
Imperial College, London, UK
AFRL, USA
NASA Ames Research Center, USA
Oxidation of UHTCs
AFRL, USA
NASA Glenn Research Center, USA
Georgia Institute of Technology, USA
Loughborough University, UK
Texas A & M University, USA
CNR-ISTEC, Italy
NSWC-Carderock Division, USA
Harbin Institute of Technology, China
Missouri University of Science & Technology, USA
University of Birmingham, UK

Field Assisted Sintering of UHTCs
Queen Mary University, London, UK
Shanghai Institute of Ceramics, China
AFRL, USA
CNR-ISTEC, Italy
Stockholm University, Sweden
Kennametal, UK
Loughborough University
Reactive Hot-Pressing
Shanghai Institute of Ceramics, China
NASA Ames Research Center,USA
National Aerospace Laboratories, Bangalore, India
Sandia National Laboratories, New Mexico, USA
McGill University, Montreal, Canada
UHTC Powder Production of Power Processing
Shanghai Institute of Ceramics, China
Loughborough University, UK
NIMS, Tsukuba, Japan
UHTC Polymeric Precursors
SRI international, California, USA
University of Pennsylvania, USA
Missouri University of Science & Technology, USA
MATECH/GSM Inc., California, USA
Fiber Reinforced UHTCs
Chinese Academy of Sciences, Shenyang, China
The University of Arizona, USA
MATECH/GSM Inc., California, USA
Catalytic Properties of UHTCs
PROMES-CNRS Laboratory, France
CIRA Capua, Italy
CNR-ISTEC, Italy

Further research efforts have been drawn to the field of UHTCs when various aerospace-related programmes were started in Europe and China. Though the development of these materials is a time-consuming process, but the improvements in UHTCs may enable many advanced applications in the future. Hence, substantial current ongoing projects on the fundamental aspects of UHTCs are carried out in universities, government agencies and international laboratories across the world as shown in Table 2.1. The fundamental research of UHTCs includes the synthesis of UHTC powders, use of various additives such as SiC, $MoSi_2$, ZrSi and WSi_2 to increase the oxidation resistance of UHTC compounds, investigating the kinetics of oxidation mechanism of the diboride-based materials and understanding the mechanical and thermal behaviours of UHTCs at high use temperatures [19], [30], [64], [65] .

The research of UHTCs in the UK started about a decade ago since Defence Science and Technology Laboratory (DSTL) funded 3 phases for the UHTC work (2008-11, 2011-13 and 2014-16), which were carried out simultaneously at Loughborough University and Imperial College, London. In 2013, another project, Material Systems for Extreme Environments (XMat), which was funded by EPSRC (Engineering and Physical Sciences Research Council), was initiated to establish the UK's capability to discover and understand UHTCs that can operate under increasingly demanding conditions. The aims of these projects are to develop the essential understanding of how the processing, microstructures and properties of materials systems operating in extreme environments interact to the point where materials with the required performance can be designed and manufactured.

2.3 Useful attributes for the design of UHTC components in hypersonic applications

2.3.1 Melting point

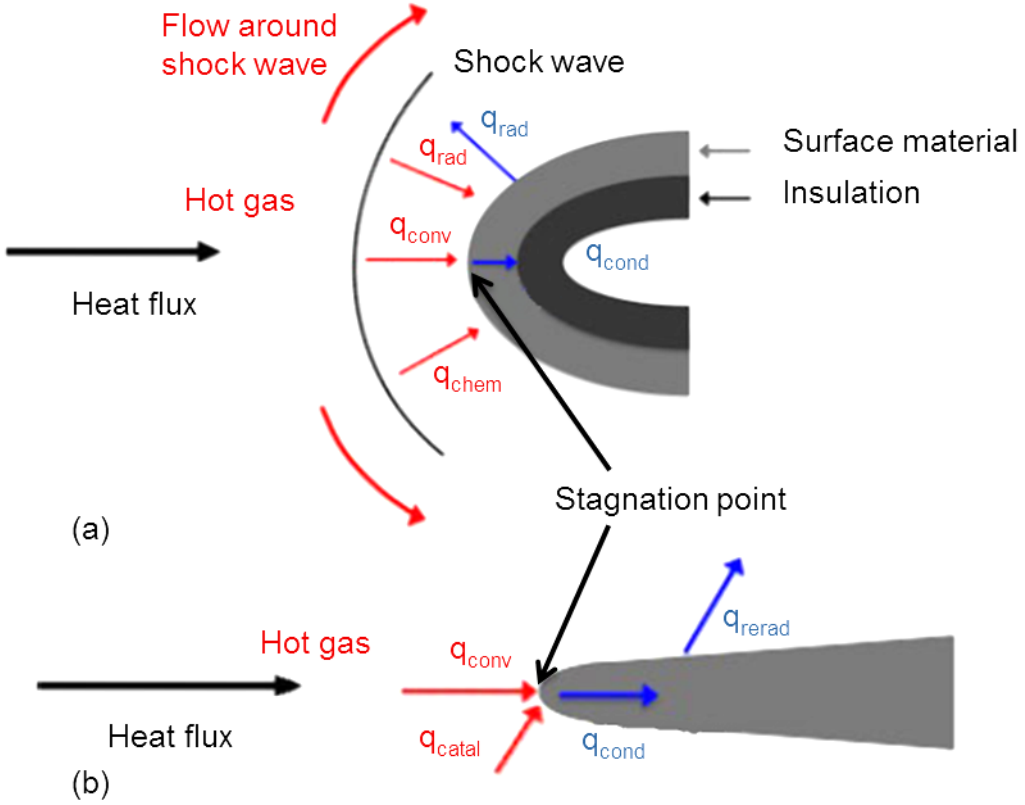

Figure 2.1 Schematics of heat flow in (a) blunt leading edge and (b) sharp leading edge, (the effects that lead to heating are in red, including by q_{conv}: convective flow, q_{rad}: radiation, q_{chem}: chemical reactions and q_{catal}: surface catalysis, while the effects that lead to heat dissipation are in blue including by q_{cond}: conduction, and q_{rerad}: reradiation) [66].

At hypersonic speed (above Mach 5), a bow shock forms in front of the blunt leading edges, as shown in Figure 2.1a, deflecting some of the heat away from the surface. To obviate excessive drag and improve manoeuvrability, hypersonic vehicles require sharp leading edges. The adverse consequence is an extreme local heat flux at the stagnation point (tip of the leading edges, Figure 2.1b).

Without rapid spatial redistribution of the heat, the temperature would be generated that exceed the usage temperature of most materials.

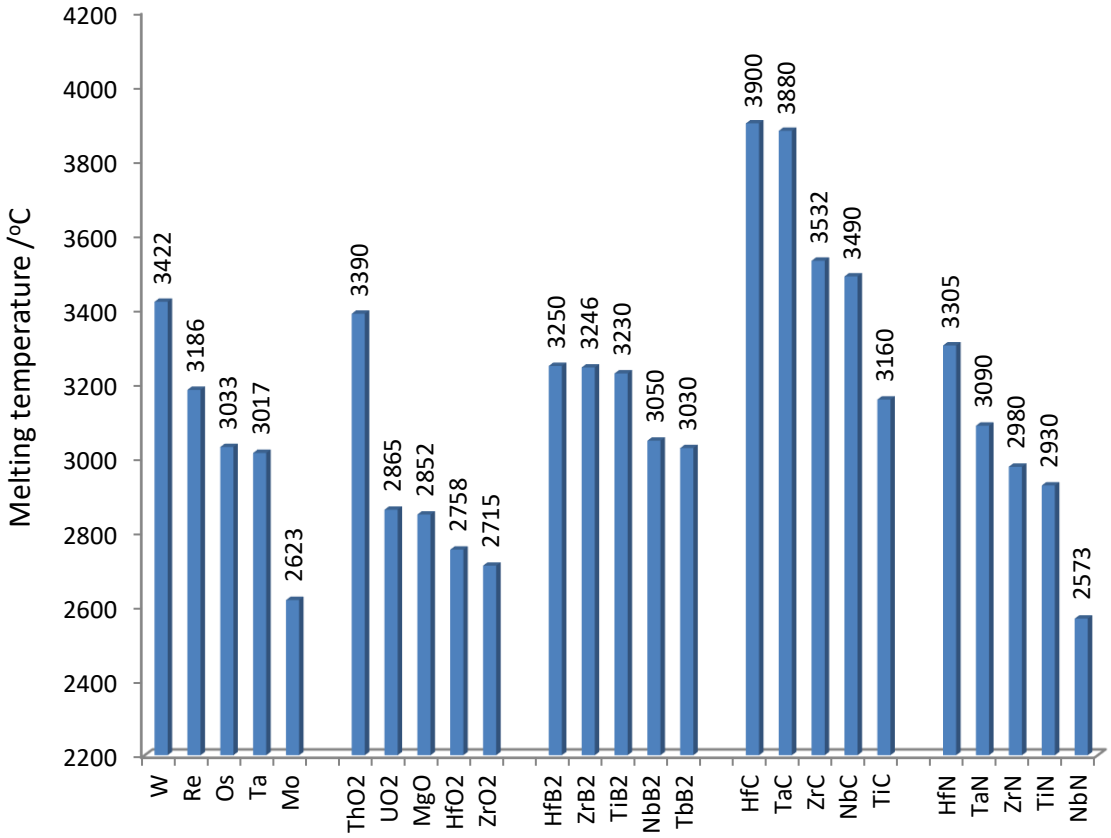

Figure 2.2 A comparison of melting temperatures between the most refractory members of different classes of materials [50].

Only a few materials, as shown in Figure 2.2, have a melting temperature approaching or more than 3000°C, of which, the UHTCs of interest including several borides, carbides and nitrides of the transition metals Hf, Zr and Ta, meet the melting point requirements of hypersonic applications. Moreover, the melting points of the oxides of the transition metals, HfO_2 and ZrO_2, which are the oxidation products of the borides and the carbides, are 2758°C and 2715°C, which are also significantly higher than the 2000°C working temperature of the sharp leading edges [67], [68].

2.3.2 Oxidation/ablation resistance

Other than heat flux, the oxidation/ablation resistance is another critical property of UHTCs needed for hypersonic applications. At hypersonic speed, gases passing through the bow shock are compressed and increase in density, pressure, static enthalpy and temperature. At sufficiently high enthalpies, the gas may become disassociated and ionised, which means that the N_2 and O_2 molecules break apart to become highly reactive N and O atoms. Because of their lower bond energy (5.1eV vs. 9.8eV), O_2 molecules dissociate at lower enthalpy levels than N_2 molecules [69]. The dissociated oxygen formed in the bow shock impinges on the leading edge, causing the TPS materials of the leading edges to oxidise. If active oxidation takes place, the component will lose its function of ability far below its melting temperature.

Although the UHTCs often start oxidation at <1000^{o}C in air, some borides and carbides, especially ZrB_2 and HfB_2, have been proved to have good oxidation/ablation resistance at elevated temperature [23], [48], [66], because the borides and carbides can form a protective oxide layer to prevent further oxidation of the substrate. The nature of the oxides formed also play a key role in controlling the oxidation rate of the UHTCs [66], thus, a lot of research effort has been devoted to understanding the oxidation mechanisms of the UHTCs and the use of design engineering methods to enhance oxidation resistance of some specific UHTCs, such as exploring composites with silicon carbide and the addition of a second UHTC phase [19], [30], [37], [64], [65], [70].

2.3.3 Physical properties

The most important physical properties of UHTCs are the density and the coefficient of thermal expansion (CTE). In hypersonic vehicle design, UHTCs

are considered as a candidate for TPS, so comparing to other functional materials used in different components of a hypersonic vehicle, such as aluminium alloys and SiC-based materials, only a small amount of UHTCs would be used at the wing leading edges and nose cap. Since UHTCs are much denser than aluminium alloy and SiC based materials as shown in Table 2.2, the small amount of UHTCs will play an important role in determining the mass distribution of an aerospace vehicle. For example, the high-density UHTCs at the nose cap of a vehicle move the centre of gravity of the vehicle further forward, usually resulting in better flight stability [71].

Table 2.2 Comparison of some physical and thermodynamic properties of UHTCs (HfB_2, HfC and ZrB_2) with that of other materials that can be used in different components of hypersonic vehicles [23], [42], [50], [52], [53], [72], [73]

	Density /gcm^{-3}	**Young's modulus /GPa**	**Flexural strength /MPa**	**CTE /x10^{-6} K^{-1}**	**Thermal conductivity /Wm^{-1}K^{-1}**
ZrB_2	6.12	489	568	5.9	60
HfB_2	11.21	480	--	6.3	104
HfC	12.2	450	340	6	22
SiC	3.1	406	482	4.3	106
Si_3N_4	3.29	310	689	3.3	30
HfO_2	9.68	--	--	5.9	23
Carbon fibres*	1.74	>420	600-680	0-8	--
Aluminium alloys*	2.6-2.8	70-79	--	24.4-25	190

**Only general values are shown here. These values vary a lot for different kinds of carbon fibre or aluminium alloy.*

Most materials exhibit changes in density as a function of temperatures associated with thermal expansion. The coefficient of thermal expansion (CTE) is another critical property when UHTCs are designed to adhere to other materials in hypersonic vehicles. The thermal expansion within UHTC components produces inevitable and undesirable internal strains and stresses,

particularly when temperature changes rapidly [74]. Different thermal expansion between UHTC components and the substrate material can cause undesirable contact stresses, leading to thermal shock failure and loss of adherence. Hence, the CTE mismatch is a big concern for UHTC components, especially when UHTCs are incorporated with other materials, such as SiC and carbon fibres [15], [75]. It can be seen from Table 2.2, UHTCs and some carbon fibres have similar CTE, meaning UHTC/carbon fibre composites have the potential to be used in extreme environments. Another possible method to solve the CTE mismatch issue is developing UHTC fibres.

2.3.4 Thermal properties

The primary thermal properties required for UHTC materials are specific heat capacity, thermal shock resistance and, particularly, thermal conductivity. Specific heat capacity has a great effect on the transient heating or cooling of a UHTC component because more heat is required to raise the temperature of the materials with higher specific heat capacity. For UHTCs, specific heat is a strong function of temperature. For instance, the specific heat of HfB_2 increases by a factor of two when temperature increases from room temperature to 1000^{o}C [52]. The increasing specific heat, to some extent, leads to better thermal shock resistance (CTE is another factor deciding the thermal shock resistance as thermal shock resistance varies inversely with CTE). The thermal shock resistance can be evaluated by the maximum allowable temperature change in transient heating or cooling without failure (ΔT_m) [42]. The experimental value ΔT_m of HfB_2 can be as high as 395^{o}C, which is much higher than that of refractory metal oxides [42].

The wall temperature on the leading edges is determined by an energy balance, as shown in Figure 2.3, which accounts for all the heat transfer processes

transporting energy not only into, but also out of the surface. High thermal conductivity is highly required for sharp-leading-edge applications because it allows more energy to be conducted from the tip of sharp leading edge, lowering the temperature, spreading the heat to an internal cooling system or cooler component surface areas, thus enhancing vehicle performance under high heat flux. It also improves a material's thermal shock resistance by reducing temperature gradients.

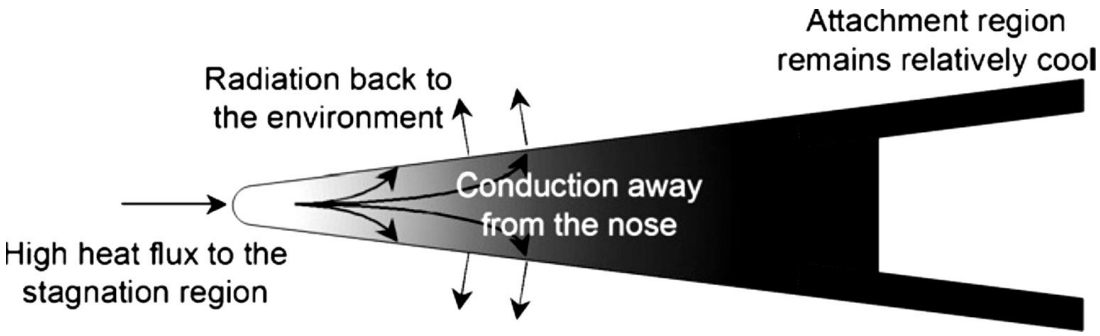

Figure 2.3 Energy balance of the leading-edge of hypersonic flight [71]

The thermal conductivity of UHTCs is largely dependent on the manufacturing, and depends on various factors, including microstructure, composition, defect and impurity levels, contact resistance between grains, and porosity [52].The general values of thermal conductivity of some common UHTCs are also shown in Table 2.2. Compared to metal oxides, UHTCs (e.g. HfB_2) show elevated thermal conductivity, the value of which is even more than half of that of aluminium alloys.

2.3.5 Mechanical properties

In the case of using UHTCs as TPS for the leading edges of hypersonic vehicles, although oxidation resistance and thermal properties are the priorities to be considered, the mechanical properties, such as hardness, Young's modulus and

flexural modulus, are also important for the design of UHTC components [71]. As introduced in Table 2.2, UHTCs, e.g. HfB_2, ZrB_2 and HfC, have high Young's modulus and moderate flexural modulus, which is due to their limited ductility. With the further incorporation of SiC or carbon fibres, the mechanical properties can be significantly improved (i.e. Young's modulus up to 466 GPa and flexural modulus up to 1003 MPa) [76], [77]. Consequently, UHTC-SiC and UHTC-carbon composites have become one of the major research subjects for UHTCs.

However, the Young's modulus and flexural modulus measured at room temperature are meaningless for the use of UHTCs in extreme environments. As mechanical properties are highly-temperature-related, it is more accurate to use high temperature measurements for mechanical analyses. Non-linear, elastic deformation behaviours are observed for some UHTC materials at elevated temperatures [21], [47], [78], [79]. Among these UHTCs, ZrB_2 and HfB_2 based material[1] showed good strength retention at elevated temperature as the Young's modulus and bending strength measured at 1400^{o}C in air are 362 GPa and 439 MPa respectively, remaining approximately 70% of that at ambient temperature [79].

2.3.6 Surface properties

In terms of use as TPS for leading edges, the surface properties of the UHTC components play an important role in controlling surface temperature because the surface properties such as emissivity and catalytic efficiency have a large effect on the ability of the surface to reject heat and, thus, on the steady state surface temperature reached by a component. High emissivity and low surface catalycity towards the exothermal recombination of oxygen atoms will improve

[1] Defects caused by diamond blade cutting or electrical discharge machining (EDM) can lower measured strengths significantly.

the material performance in extreme environments by reducing temperature gradients and thermal stresses. Scatteia et.al [80], [81] measured hemispherical emissivity for ZrB_2-15SiC-2$MoSi_2$ and ZrB_2-15SiC composites and the emissivity values ranged from 0.49-0.81, depending on temperature, machining method and oxygen ambient environment. Alfano et.al [82], [83] measured the emissivity and catalycity for similar ZrB_2-15SiC based composites which used Si_3N_4 and $ZrSi_2$ as sintering aids, finding that these materials presented a low catalytic activity with an almost constant recombination coefficient of 0.1 at temperatures up to 2000^{o}C, while ZrB_2-15SiC-5Si_3N_4 showed the higher emissivity, reaching 0.9 at 1500^{o}C.

2.4 Refractory borides and other monolithic UHTCs

2.4.1 Refractory borides

The refractory diborides, especially ZrB_2 and HfB_2, are important members from the family of UHTCs, as they exhibit an unusual combination of high melting point, good oxidation resistance, metal-like thermal conductivity and good strength retention at elevated temperature. They and their composites are considered as promising candidates for thermal barrier coatings on future hypersonic vehicles. Some other refractory diborides, e.g. TiB_2, are also attractive for the applications such as wear components and cutting tools, due to their low specific weight, high hardness and elastic moduli [84].

2.4.1.1 Structure and structure-property relations

Zr and Hf are chemically very similar elements and the borides of these elements are also very similar. As shown in Figure 2.4 and Table 2.3, the group IV transition metal diborides exist with a hexagonal crystal structure of the MB_2

prototype. The structure is composed of layers of B atoms in 2D graphite-like rings, which alternate with metal layers in a hexagonally close-packed array. Each B atom is surrounded by 3 B neighbours and 6 metal atoms, whilst each metal atom is surrounded by 12 B atoms and 6 metal neighbours. The B-B distance is influenced by the radius of neighbouring metal atoms. It is equal to $a/\sqrt{3}$, as shown in Table 2.3, and is 0.183 nm for ZrB_2 and 0.181 nm for HfB_2. The M-B distance is equal to $(a^2/3+c^2/4)^{1/2}$, as shown in Table 2.3. It increases linearly with the M:B radius ratio, which is 0.254 nm for ZrB_2 and 0.251 nm for HfB_2 [42].

Table 2.3 Some structural, physical and thermodynamic properties of the transition metal borides [85]–[92]

Property	**ZrB_2**	**HfB_2**	**TiB_2**	**TaB_2**
Crystal system space group prototype structure	Hexagonal P6/mmm AlB_2	Hexagonal P6/mmm AlB_2	Hexagonal P6/mmm AlB_2	Hexagonal P6/mmm AlB_2
a / nm	0.317	0.314	0.302	0.306
c / nm	0.353	0.347	0.322	0.330
Density / g cm^{-3}	6.12	10.50 (11.21 theoretical)	4.52	11.15 (12.54 theoretical)
Melting temperature / °C	3245	3380	3230	~3000
Young's modulus / GPa	489	480	565	587
Hardness / GPa	23	28	25	36
Coefficient of thermal expansion / K^{-1}	5.9×10^{-6}	6.3×10^{-6}	6.4×10^{-6}	8.2×10^{-6}
Electrical conductivity / S m^{-1}	1.0×10^{7}	9.1×10^{6}	1.4×10^{7}	3.3×10^{7}
Thermal conductivity / $Wm^{-1}K^{-1}$	60	104	96	16-36

The order of the radius of the group IV transition metals is hafnium > zirconium > titanium, which affects the B-B, B-M and M-M bond strength in the refractory metal borides, and thus decides the mechanical, thermal and physical

properties of the refractory metal borides. In addition, the group V transition metal diboride, TaB_2, has a similar crystal structure and metal atom radius as HfB_2 and ZrB_2, so TaB_2 is likely to merge with HfB_2 or ZrB_2 to form solid solution. As a result of similar M-B, B-B and M-M bond strength, TaB_2 also show very similar physical and thermal properties as HfB_2 or ZrB_2.

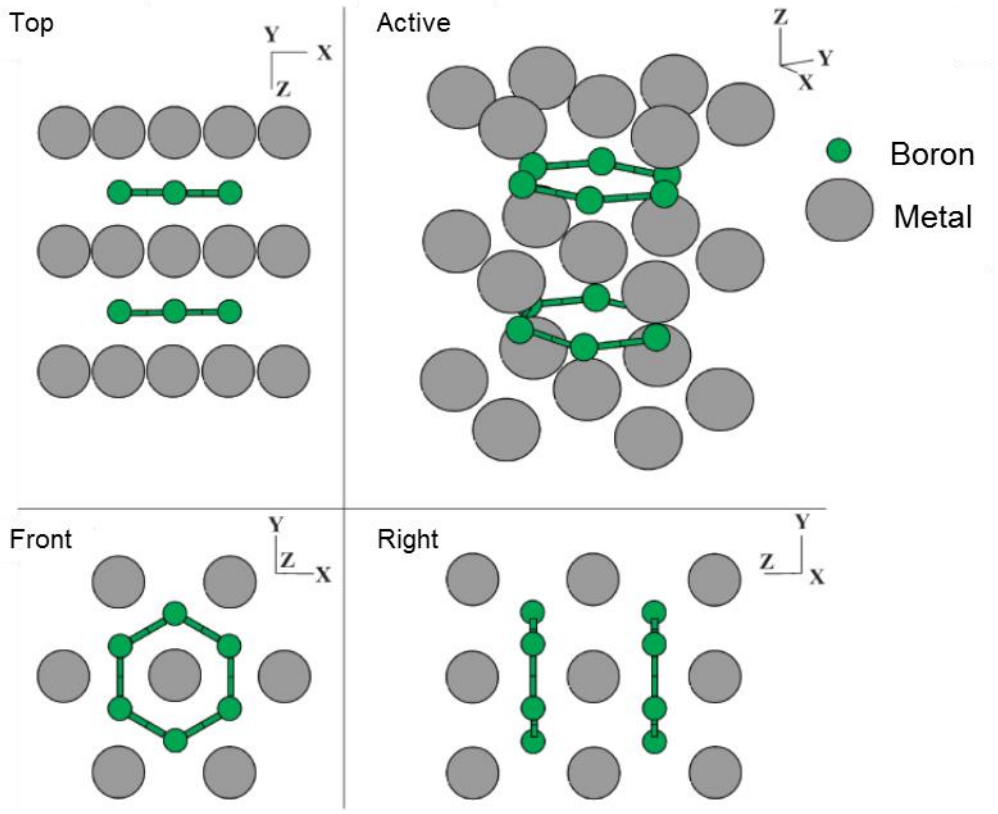

Figure 2.4 The MB_2-type structure of HfB_2 or ZrB_2 [42]

Some properties of the pure refractory diborides are affected by the combination of the bonds (B-B, M-B and M-M):

(a) Melting temperature: It was reported that the M-B bond strength rather than B-B decided the melting temperature of the refractory diborides [93]. So in theory, the larger the metal atoms the diborides have in their structure, the higher the melting temperature they exhibit. For example, the melting points

of HfB_2, ZrB_2 and TiB_2 are 3250°C, 3246°C and 3230°C, respectively.

(b) CTE: Although CTE anisotropy is prevalent among the refractory diborides. ZrB_2 and HfB_2 show lower CTE anisotropy than that of the diborides of Ti, Nb and Ta [94]. It is due to the fact that larger metal atoms lead to stronger bond strength, resulting in a lower CTE. For this reason, ZrB_2 and HfB_2 would develop lower stress during fast cooling than other diborides. The values of CTE of HfB_2 and ZrB_2 are 5.9×10^{-6} K^{-1} and 6.3×10^{-6} K^{-1}, respectively, which are similar as that of HfC and HfN [47].

(c) Young's modulus: The refractory diborides have very high Young's modulus due to the strong M-B and B-B bonds.

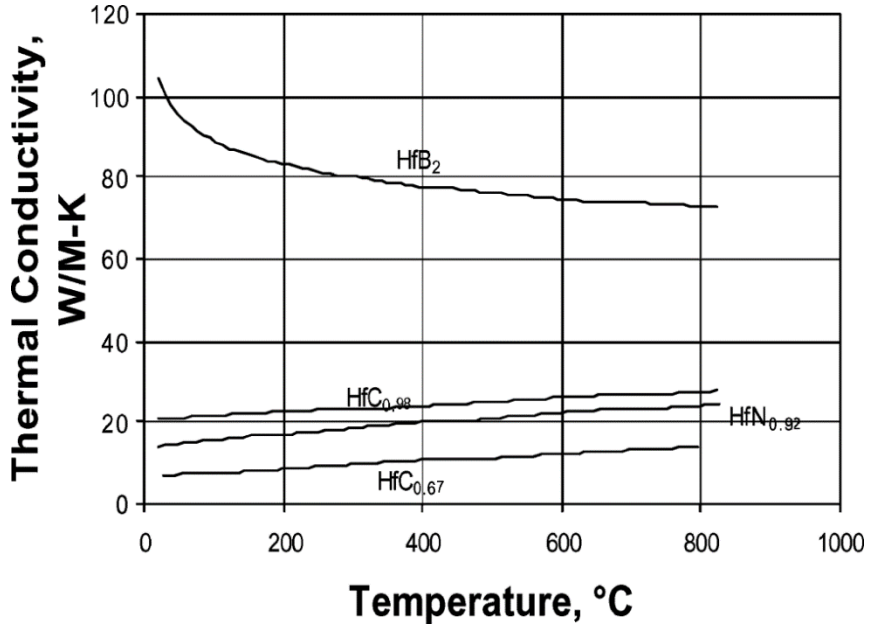

Figure 2.5 The thermal conductivities of HfB_2, HfN, $HfC_{0.67}$ and $HfC_{0.98}$ [21]

(d) Thermal conductivity: Group IV metal diborides (TiB_2, ZrB_2 and HfB_2) are high thermal conductivity ceramics due to the contributions from both electronic and photonic thermal carriers to the total thermal conductivity [63]. They possess higher thermal conductivity than Group V metal diborides (VB_2,

NbB_2 and TaB_2) and HfB_2 tops the list with the highest thermal conductivity, compared to HfC or HfN, over a wide temperature range, as shown in Figure 2.5 [47].

The physical properties of pure transition metal boride can be modified by adding various materials. The effect of additives on the physical properties of HfB_2 and ZrB_2 will be discussed in Chapter 2.6.4.

2.4.1.2 Oxidation mechanism

The oxidation resistance of the monolithic refractory diborides is studied by plotting the oxidation rate as a function of temperature. Significant research efforts were focused on understanding the oxidation mechanism of ZrB_2 and HfB_2 and it was found that the oxide scale, rather than the borides themselves is the key role in controlling oxygen permeation, thus it decides the oxidation rate [95]–[99].

As shown in Equation 2.1 and 2.2, the diborides undergo stoichiometric oxidation when exposed to air at elevated temperature [100].

$$\mathrm{ZrB_{2(c)}} + \frac{5}{2}\mathrm{O_{2(g)}} \rightarrow \mathrm{ZrO_{2(c)}} + \mathrm{B_2O_{3(l)}}, \mathrm{T} > 873\ \mathrm{K} \quad (2\text{-}1)$$

$$\mathrm{HfB_{2(c)}} + \frac{5}{2}\mathrm{O_{2(g)}} \rightarrow \mathrm{HfO_{2(c)}} + \mathrm{B_2O_{3(l)}}, \mathrm{T} > 873\ \mathrm{K} \quad (2\text{-}2)$$

Fahrenholtz's work [101], [102] focused on thermodynamic study and investigated the forming mechanism of the condensed and gaseous oxidation products in the oxidation of diborides. Three oxidation regimes were reported: 'low' temperature, 'intermediate' temperature and 'high' temperature, based on different oxidized structures.

In the low temperature regime, i.e. 600°C-1000°C, a porous zirconia is filled with liquid boron oxide according to Equation 2.1. The reaction products, boron oxide and zirconia, show limited mutual solubility and hence exist as distinct phases as shown in Figure 2.6(a) [66]. In this regime, the vapour pressure of boron oxide being low, a protective layer of boron oxide is formed on the outer surface which acts as an effective diffusion barrier thickness limiting the permeation of oxygen through these oxide layers to reach the substrate. Hence, both ZrB_2 and HfB_2 show mass gain kinetics consistent with diffusion limited processes in this regime [103].

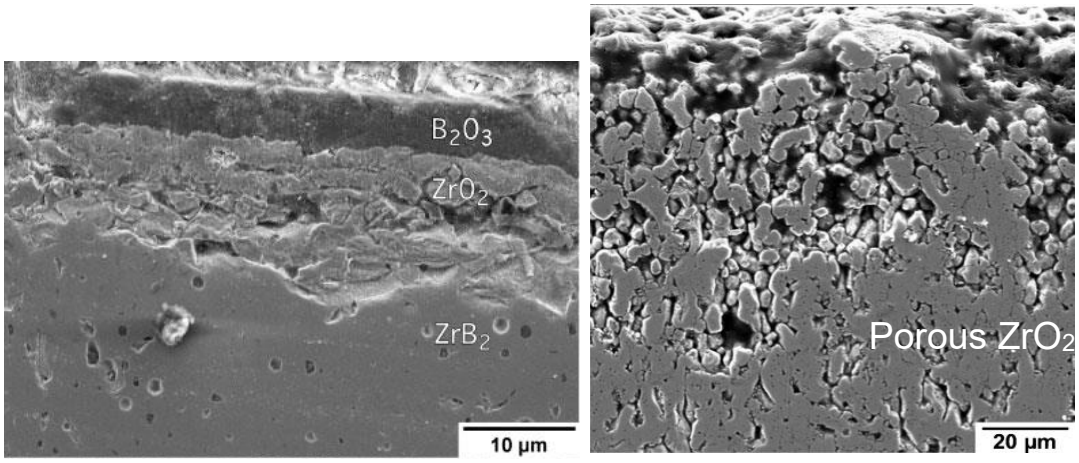

(a) (b)

Figure 2.6 Monolithic ZrB_2 oxidized at (a) 900°C for 8 h and (b) 1500°C for 2 h, the thicknesses of oxide layers are 10 μm and 400 μm respectively [66].

$$B_2O_{3(l)} \rightarrow B_2O_{3(g)},\ T > 1273\ K \tag{2-3}$$

The lower limit of 'intermediate' regime is usually believed to be ~1000°C. According to Equation 2.3, at temperature above 1000°C, volatilization as B_2O_3(g) occurs, resulting in a loss of the outer boron oxide layer and from the pores of zirconia layer. The depth of the boron oxide filling in the pores of zirconia layer is decided by both the formation and evaporation rate of the boron

oxide. When the temperature reaches 1500°C, only a porous zirconia layer is left as shown in Figure 2.6(b). In this regime, oxygen first diffuses through the outer zirconia channels, and then permeates the boron oxide to the base of the pore channels. The oxygen permeation through zirconia is however negligible.

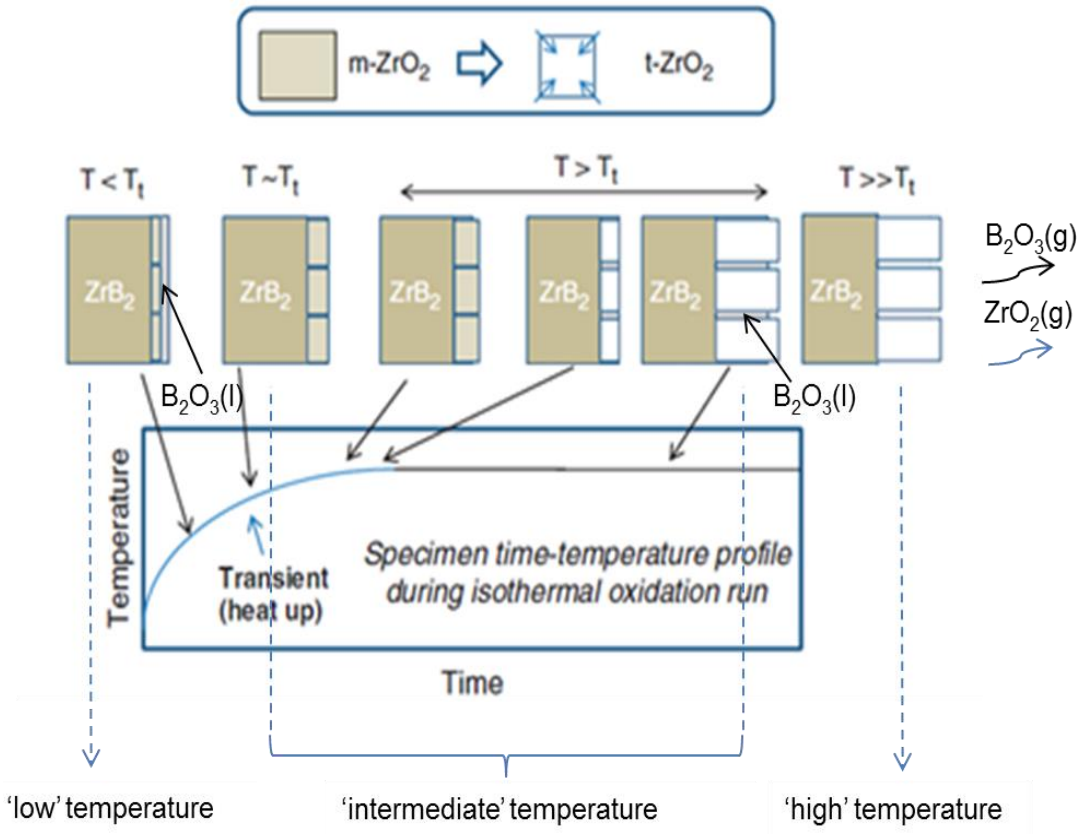

Figure 2.7 Schematic sketch of the different oxidation products of ZrB_2 at different oxidation regimes [99].

In the intermediate temperature regime, the phase transformation of metal oxide affects the oxidation rate of the corresponding diborides. It is well known that ZrO_2 and HfO_2 undergo phase transformation from monoclinic to tetragonal at higher temperatures. The phase transformation temperature range is 1000°C – 1200°C for ZrO_2 and is 1500°C – 1600°C for HfO_2 [104]. The phase transformation results in volumetric shrinkage, increasing the porosity of the zirconia layer as illustrated in Figure 2.7 [99]. Even small changes in the porosity

of the zirconia can change the oxidation rate significantly. Therefore, in the intermediate temperature regime, at temperatures above the transformation temperature, the shrinkage of zirconia opens up the pathway for oxygen to diffuse through, together with the loss of boron oxide protective layer, enhancing oxidation [99]

The high temperature regime starts from the temperature of 1800°C, above which, based on Equation 2.4, boron oxide evaporates as fast as it forms. Simultaneously, the evaporation of ZrO_2 reduces the thickness of the oxide layer, enhancing oxidation.

$$\mathrm{ZrB_{2(c)}} + \frac{5}{2}\mathrm{O_{2(g)}} \rightarrow \mathrm{ZrO_{2(c)}} + \mathrm{B_2O_{3(g)}}, \mathrm{T} > 2073\mathrm{K} \quad (2\text{-}4)$$

A parabolic trend of the oxidation rate of ZrB_2 against temperature from 800°C to 1500°C was reported by Tripp et.al [57] and Berkowitz-Mattuck et.al [103] by TGA analysis and measuring oxygen consumed, respectively. McClaine et.al [105] compared the oxidation behaviour of HfB_2 and ZrB_2 as shown in Figure 2.8 and concluded that at temperature below 1700°C, the parabolic rate constants for oxidation of HfB_2 were almost an order of magnitude less than the corresponding constants for ZrB_2. He also reported that the oxidation rate of HfB_2 increased sharply around 1700°C whilst for ZrB_2, it increased at 1100°C, which could be due to the phase transformation of their oxides.

Several thermodynamic models employing volatility diagrams or kinetic models have been created with the evaporation of B_2O_3 being considered as the cause of the transition of the different oxidation regimes [106], [107]. Parthasarathy et. al established a model to predict the oxide scale thickness, boride recession and weight gain of ZrB_2 and HfB_2 as a function of temperature, time and partial pressure of oxygen [108]. As shown in Figure 2.9, the model was proved to

match very well with experimental data of the laboratory oxidation of ZrB_2, showing a parabolic change of oxidation rate, when the porosity fraction and pore radius were assumed to be 0.05 and 0.5 μm [21], [108], [109]. The model can be extended to HfB_2 and other refractory metal diborides by simply changing the parameters such as molecular mass and density.

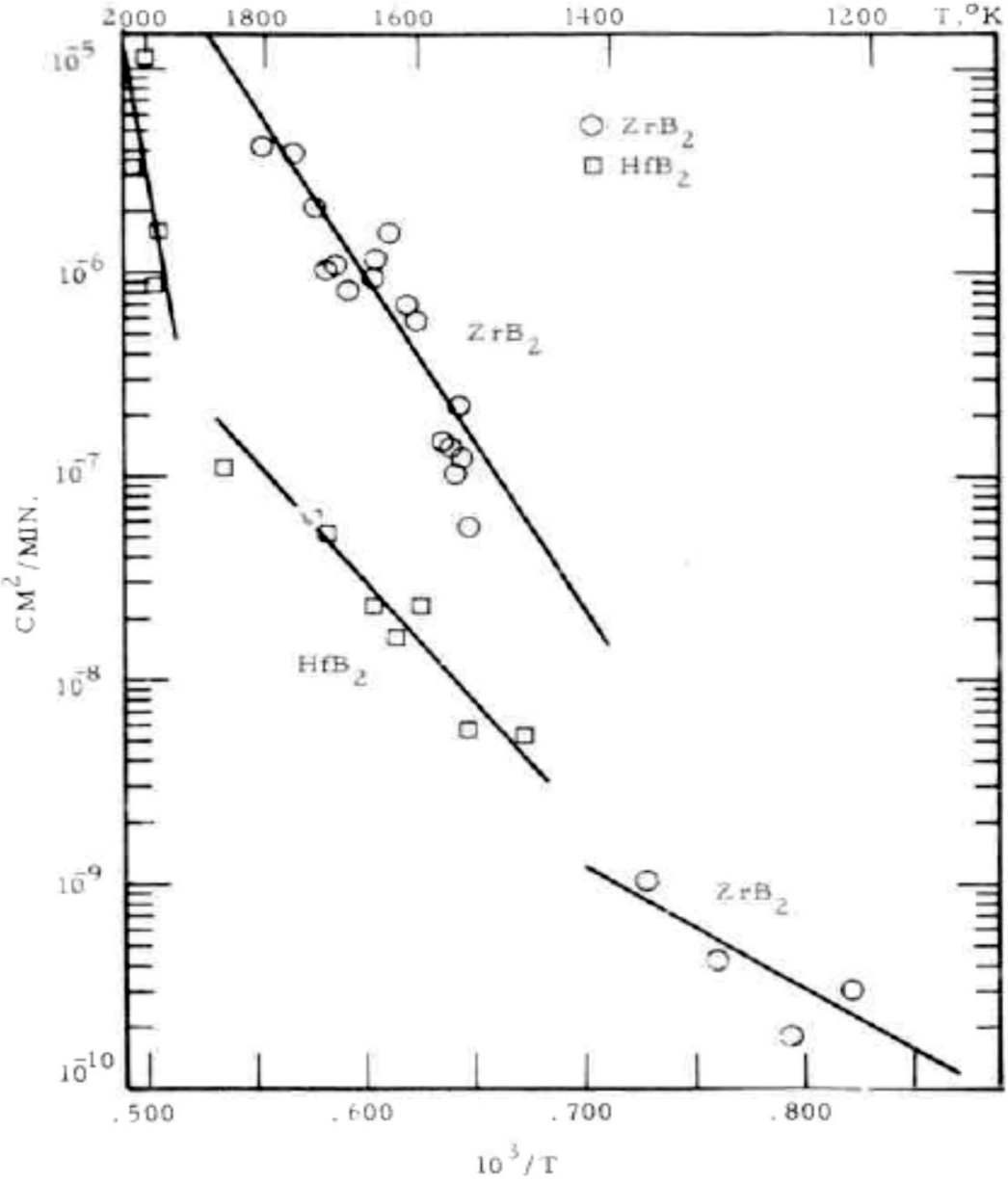

Figure 2.8 Comparison of parabolic rate constants for oxidation of HfB_2 and ZrB_2 as a function of temperature [105]

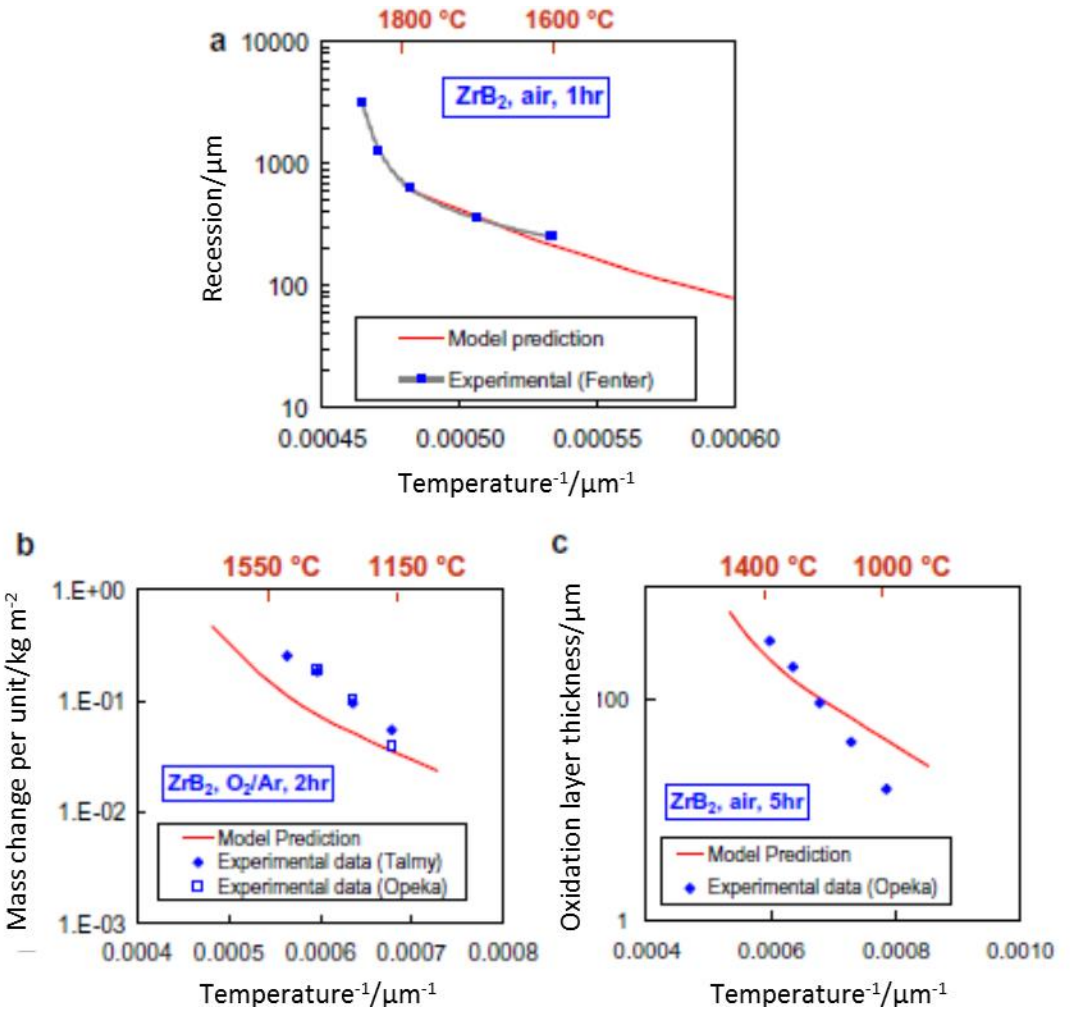

Figure 2.9 (a) Model predictions of the boride recession in air as a function of temperature is compared with Fenter's data [109]. (b) The model predictions for mass change are shown compared to experimental data obtained in Ar/O_2 gas in 2 h [21]. (c) The scale thickness obtained after 5 h in air by Opeka et. al [21] is shown compared to the predictions [108].

Parthasarathy et. al also modified the model for the high temperature regime (>1800°C), taking the phase transformation of the metal oxides (ZrO_2 and HfO_2) into consideration and, again, the model compared very well with experimental data [57], [103], [110]–[112]. Based on this analysis, it was also concluded that the significant advantage of HfB_2 over ZrB_2 was credited to the higher transformation temperature and lower oxygen permeability of HfO_2 compared with ZrO_2. The latter may be because that at temperatures > 1600°C, the oxide

layer of HfB_2 that remains after B_2O_3 evaporation has a more equiaxed microstructure than that of ZrB_2, resulting in greater resistance to oxygen transport [56].

All the analysis described above are based on furnace oxidation tests, which are appropriate to understand the oxidation mechanisms of the borides and select candidate materials for hypersonic applications, but cannot reproduce the harsh conditions of extreme environments during hypersonic flight. The arc-jet testing of ZrB_2 at 2500°C for 30 min resulted in an oxide scale that was 250 μm thick, which is only 1/10 of the same materials after oven oxidation at 2000°C for 30 min [46]. The big difference in the two tests is attributed to the existence of a large temperature gradient and the ablation of the sample surface during arc-jet testing. Further, it could be concluded that the more severe conditions encountered during arc-jet testing may promote the formation of an oxide scale (ZrO_2 or HfO_2) having a higher density that is more protective than the scale formed in static laboratory furnace tests [66]. However, the very limited number of comparative experimental studies do not allow for strong conclusions to be drawn about the oxidation behaviour differences of these materials.

2.4.2 Refractory carbides

The refractory carbides are also considered as UHTCs due to their extremely high melting points, which are even higher than these of the refractory borides. The common monocarbides (HfC, ZrC and TaC) exist with the NaCl-type face-centred cubic crystal structure. The strong interatomic bonds in the structure, especially the strongest covalent bonds, leading to the monocarbides possessing high melting points (HfC: 3928°C, ZrC: 3445°C and TaC: 3980°C), as well as excellent hardness and elastic modulus [113], [114]. Generally, the chemical formula of HfC and TaC are more appropriately written as HfC_x and

TaC_x, where x ranges from 0.50 to 0.98 and is temperature dependent, as shown in Figure 2.10. This wide phase stability field allows a large number of vacancies to exist in the crystal lattice, which reduces thermal conductivity and mechanical properties, as shown in Table 2.4 [21], [115]. The vacancies can be occupied by large quantities of oxygen as well, thus influencing the oxidation behaviour of the carbides.

Table 2.4 Properties of HfC_x at room temperature [21]

	Young's modulus /GPa	**Flexural strength /MPa**	**CTE at 2000°C /°C^{-1}**	**Thermal conductivity /W m^{-1}K^{-1}**
$HfC_{0.98}$	450	340	13	22
$HfC_{0.67}$	320	260	13	7

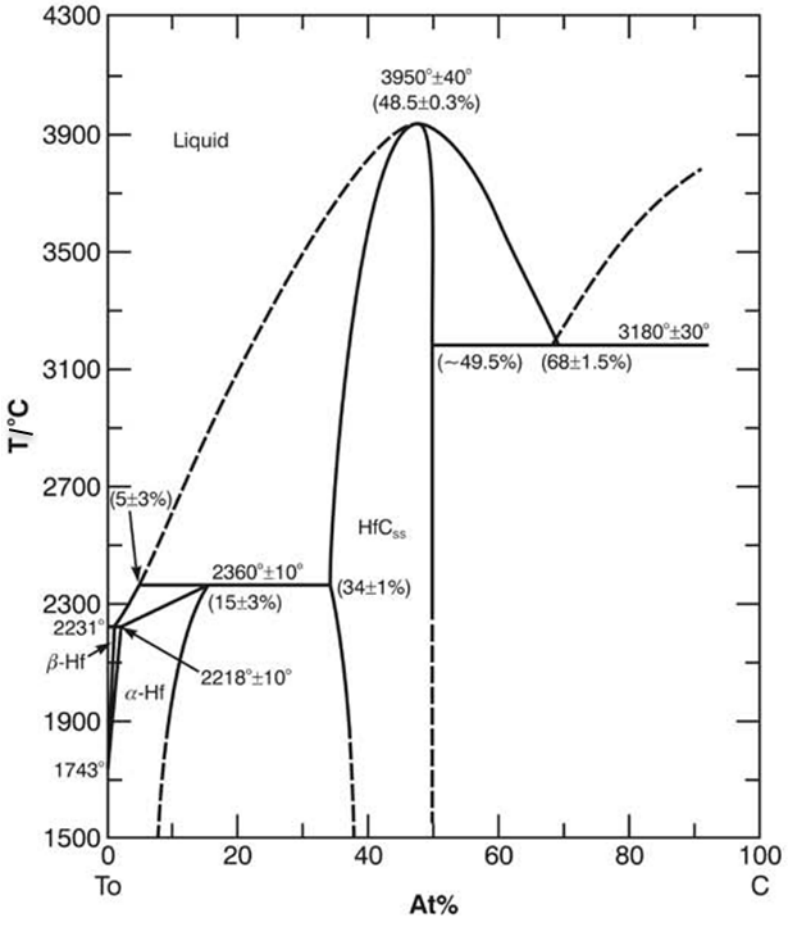

Figure 2.10 The phase equilibrium diagram for HfC_x [116].

The oxidation behaviour of HfC has been studied over a wide temperature range [112], [117]–[119]. At low temperatures, the HfO_2 forms a porous scale due to the evolution of CO_2 during the oxidation, as shown in Equation 2.5, the oxidation kinetics are linear and the oxidation rates depend on the permeation of oxygen through the oxide scale [112].

$$HfC(s) + O_2(g) \rightarrow HfO_2(s) + CO_2(g) \quad (2\text{-}5)$$

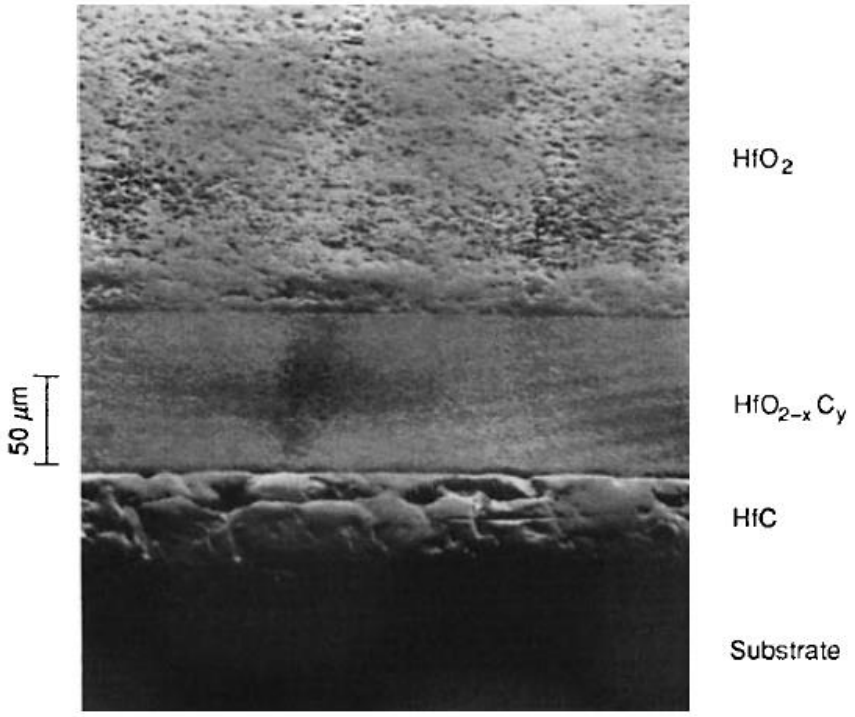

Figure 2.11 Multi-layer structures in hafnium carbide, oxidized at 1865°C for 600s in an atmosphere of 93% argon and 7% oxygen [97]

At higher temperatures, the oxidized scale of HfC consists of three distinct layers, illustrated in Figure 2.11: an outer porous HfO_2 layer, the residual hafnium carbide layer with a measurable oxygen gradient and an interlayer described as $HfO_{2-x}C_y$. Bargeron et.al [97], [120] reported that the dense oxycarbide layer acted as an oxygen diffusion barrier limiting the oxidation rate

and the oxidation kinetics followed a parabolic trend, similar to the oxidation behaviours of refractory borides.

However, the carbides are vulnerable to form a porous and non-adherent oxide scale. During the oxidation of HfC, the formation of gaseous CO_2 and the phase transformation of HfO_2 are the main reasons leading to the porous oxide layer. The presence of free carbon at the interlayer was also reported after oven oxidation at lower temperatures (800-1500^oC) [119]. The carbon oxidizes at high oxygen pressures, leading to a loss of both oxidation resistance and adhesion at the interface. Compared with HfC, TaC shows worse adhesion, as the oxides formed can easily slough off the parent carbides [121].

2.4.3 Refractory oxides

Although refractory oxides such as ZrO_2 and HfO_2 are intrinsically oxidation resistant, they are classified as high temperature ceramics rather than ultra-high temperature ceramics. It is mainly because their melting points, as shown in Figure 2.3, are below 3000^oC. It has been reported that hafnium oxide is used as a refractory material in the insulation of such devices as thermocouples, where it can be operated at temperatures up to 2500^oC. However, its low thermal shock resistance, fracture toughness and thermal conductivity limit its development for aerospace applications. When UHTCs are used as protective coating for leading edges, low thermal shock resistance can cause the coating to crack, leading to component failure. Another issue associated with the refractory oxides is the phase transformations. ZrO_2 and HfO_2 experience solid phase transformations, from monoclinic to tetragonal at 1150^oC and 1650^oC respectively, and from tetragonal to cubic at 2370^oC and 2700^oC respectively [47], [122]. These phase transformations result in volume changes and cracking.

2.4.4 Refractory nitrides

With a melting temperature of 3300°C, HfN certainly qualifies as a UHTC material. This material offers a wide range of thermal and mechanical properties, so it is widely used as an interlayer/diffusion barrier in magnetic recording devices, as well as in the world of structural ceramics [123]. But the UHTC nitrides (ZrN and HfN) are less well known than the diborides or monocarbides.

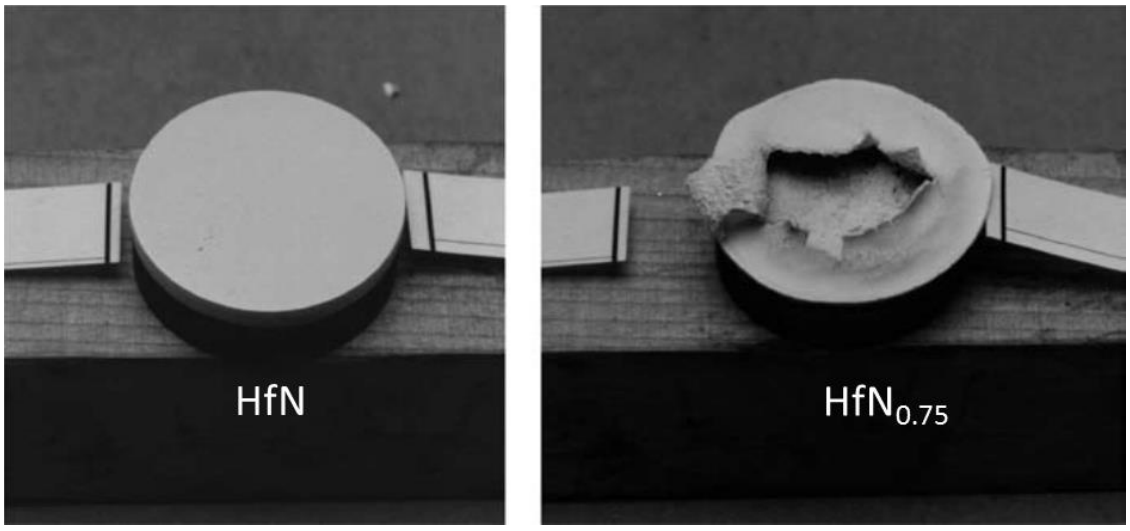

Figure 2.12 Post-test photographs showing evidence of porous, adherent scale on HfN and dense oxide that formed on $HfN_{0.75}$ [48]

Like the monocarbides, HfN can exist over a range of stoichiometry [124]. The melting temperature increases with increase in the nitrogen percentage in HfN_x, and reaches a maximum of 3387°C at HfN_1. Thus, for long exposure at high temperatures, the loss of N from the lattice is thought to be a considerable problem to overcome. For the HfN phase, the thermal expansion, strength and modulus are all very close to that measured for HfC, while the thermal conductivity is slightly higher. However, oxidation tests indicate that the HfN materials are not as good as HfC when used as thermal proactive coatings [21]. In arc-jet testing, HfN showed evidence of porosity and cracking [48]. Another significant issue is observed for $HfN_{0.75}$, i.e. a 'blowout' after oxidation, as shown

in Figure 2.12. It is mainly due to that $HfN_{0.75}$ has a different oxidation mechanism to HfN_1. The gas pressures at the interface must be significantly lower, leading to the formation of an extremely dense and adherent oxide scale, which trapped the gaseous products below it until the pressure reached a critical value [48].

2.4.5 The most promising materials for hypersonic applications – ZrB_2 and HfB_2-based ceramics

Table 2.5 Brief summary of the oxidation products and behaviours of some UHTCs

	Melting temperature /°C	**Density /g cm^{-3}**	**Oxidation products in air**	**Thermal conductivity at RT /W m^{-1}K^{-1}**	**Oxidation behaviors**
HfB_2	3250	10.50	HfO_2+B_2O_3	80	Protective glassy phase inhibit oxidation
ZrB_2	3200	6.08	ZrO_2+B_2O_3	99	Protective glassy phase inhibit oxidation
HfC	3890	12.22	HfO_2+CO_2	22	Porous oxide layer with poor adherency
ZrC	3530	6.73	ZrO_2+CO_2	34	Porous oxide layer with poor adherency
HfN	3305	13.80	HfO_2+NO_2	11	Porous oxide layer with cracking and poor adherency

Refractory borides and carbides, rather than oxides and nitrides, are considered as the UHTC materials of the most interest as they possess not only high melting

temperatures, but also good thermal conductivity and thermal shock resistance. Within these carbides and borides, the oxidation behaviour of Hf and Zr compounds are reported to be superior to Ta, Ti and Nb compounds [57], [99], [105]. Furthermore, by comparing the oxidation behaviours and rate of the carbides and the borides of Hf and Zr, Table 2.5, it can be seen that the carbides are faced with the issue of the formation of a porous oxide layer with poor adherency, which reduces the oxidation resistance of the carbides. Hence, ZrB_2 and HfB_2 are regarded as the most promising materials for hypersonic applications and attract most research effort in the UHTC field [42], [47], [66]. Although ZrB_2 and HfB_2 exhibit low oxidation rates, UHTC-carbon composites and addition of dopants are investigated to overcome the issues associated with poor fracture toughness and phase transformation that lead to high porosity.

2.5 Synthesis of refractory metal boride powders

HfB_2 and ZrB_2 can be synthesized by a variety of routes, which can be classified into reactive routes, chemical routes and reduction processes, based on the reaction involved. Each route has its own advantages and disadvantages. The reduction processes are widely studied and are the basis of the current commercial method to synthesize HfB_2 and ZrB_2 powders due to their relative lower cost and simplicity of the process involved compared to reactive and chemical routes [125]. However, as coarser particles of the borides result in poorer sinterability, some lab-based routes are aiming to yield high-purity nano-sized HfB_2 and ZrB_2 powders.

2.5.1 Reactive routes

Reactive routes are based on the simple reactions between elemental precursor powders, Equation 2.6 and 2.7:

$$Zr + 2B \rightarrow ZrB_2, \quad \Delta H^o_{rxn} = -323\ \text{kJ, at } 25°C \tag{2-6}$$

$$Hf + 2B \rightarrow HfB_2, \quad \Delta H^o_{rxn} = -328\ \text{kJ, at } 25°C \tag{2-7}$$

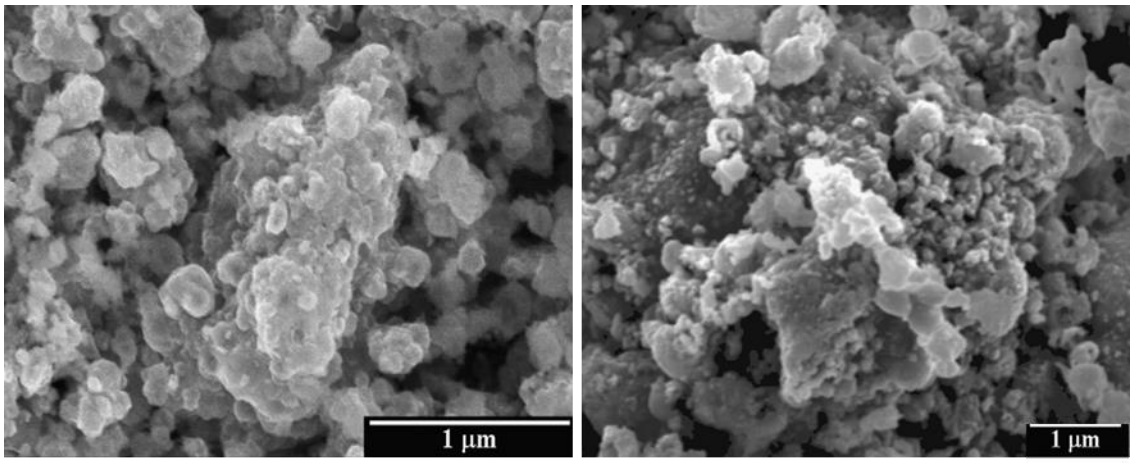

Figure 2.13 SEM micrographs of ZrB_2 formed via (a) SHS, after NaCl removal, 10 wt% NaCl was added; (b) reactive hot pressing, at 600°C for 360 min [126], [127].

These two reactions are both strongly exothermic and result in extremely high adiabatic temperatures that can ignite a self-propagating reaction. Thus these reactions are used to synthesize ZrB_2 and HfB_2 with the presence of external ignition sources, i.e. by self-propagation high-temperature synthesis (SHS) [128], [129]. Camurlu et.al [126] showed that the grain size of the resultant ZrB_2 powders increased with increasing the adiabatic temperature, and he obtained nano-size ZrB_2 by using NaCl as a diluent to reduce the adiabatic temperature. The consequent particle size ranged from 200 nm to a few microns as shown in Figure 2.13(a). The advantage of SHS is that the high heating and cooling rates involved result in high defect concentration in the powders obtained and thus improve their sinterability by providing a driving force for rearrangement of atoms [130]. HfB_2 has also been prepared by using a hafnium and boron powder mixture in a non-self-propagating high-temperature synthesis process at

1500°C [131], but large Hf particles were detected, in another words, the extent of reaction was low because the diffusivity of boron in HfB_2 was small.

In contrast to SHS, Chamberlain et. al [127] synthesized nano-size ZrB_2 using fine powders of Zr and B via reactive hot pressing at temperature of 600°C without an ignition, as shown in Figure 2.13(b). The synthesized powders were the same size as the Zr precursor particles, i.e. ~10 nm, after attrition milling for 240 min. Hence, the particle size of ZrB_2 can be controlled by reducing the particle size of the Zr precursor powders.

2.5.2 Chemical routes

Chemical routes involve the reaction between Zr- or Hf-containing and boron-containing precursors. Nano-crystalline ZrB_2 and HfB_2 have been synthesized following Equation 2.8 and 2.9 at temperatures of 500°C and 600°C, respectively, using a hydrothermal reaction method [132], [133]. These are the lowest temperatures reported for the synthesis of HfB_2 and ZrB_2 in the literature. The particle sizes of the resulting powder were reported to be as small as 10-25 nm.

$$HfCl_4(g) + NaBH_4(g) \rightarrow HfB_2(c) + 2NaCl(c) + 2HCl(g) + 3H_2(g) \quad (2\text{-}8)$$

$$ZrCl_4(g) + NaBH_4(g) \rightarrow ZrB_2(c) + 2NaCl(c) + 2HCl(g) + 3H_2(g) \quad (2\text{-}9)$$

$$2Ti(BH_4)_3(c) \rightarrow 2TiB_2(c) + B_2H_6(g) + 9H_2(g) \quad (2\text{-}10)$$

Titanium diboride has also been prepared by thermal decomposition of titanium borohydride via reaction 2.10. Powders prepared by this method were also nano-sized with diameters of 100-200 nm [134]. Whilst a variety of chemical routes have been investigated, the processing of these powders into coatings or ceramics has not been fully explored [134].

2.5.3 Reduction processes

Several reduction processes are used to synthesize the diborides of Hf and Zr, including carbothermal, borothermal and carbo/borothermal reduction reactions, as listed in Table 2.6. According to the thermodynamic calculations, these reactions are all extremely endothermic, thus a high temperature, which is usually above 1500°C, is required to complete the reduction reactions [135], [136]. Besides the common reducing agents, boron, carbon and boron carbide, aluminium and magnesium can also be used as well as the combinations of reducing agents [78], [137], [138].

Table 2.6 Various reduction reactions to synthesize HfB_2. The reactions are also applicable to ZrB_2 [135]

Equation	Category	Example	ΔG_{1500^oC} /KJ mol^{-1}
(2-11)	Carbothermal	$HfO_2(c) + B_2O_3(l) + 5C(g) \rightarrow HfB_2(c) + 5CO(g)$	14
(2-12)	Borothermal	$3HfO_2(c) + 10B(c) \rightarrow 3HfB_2(c) + 2B_2O_3(l)$	-9
(2-13)	Carbo/borothermal	$2HfO_2(c) + B_4C(c) + 3C(g) \rightarrow 2HfB_2(c) + 4CO(g)$	25

2.5.3.1 Carbothermal reduction

Carbothermal reduction is used to produce HfB_2 and ZrB_2 commercially due to the low cost of the starting materials and simplicity of the process [139]. As mentioned earlier, this reaction is strongly endothermic and becomes thermodynamic favourable above ~1500°C. In order to yield high-purity powders and shorten the reaction time, a higher temperature was usually employed to synthesize HfB_2 or ZrB_2 powders [78]. The reaction also produces significant volumes of various gases, which must be removed for the reactions to proceed

to completion. Hence, the reaction is usually carried out in vacuum or with flowing inert gas.

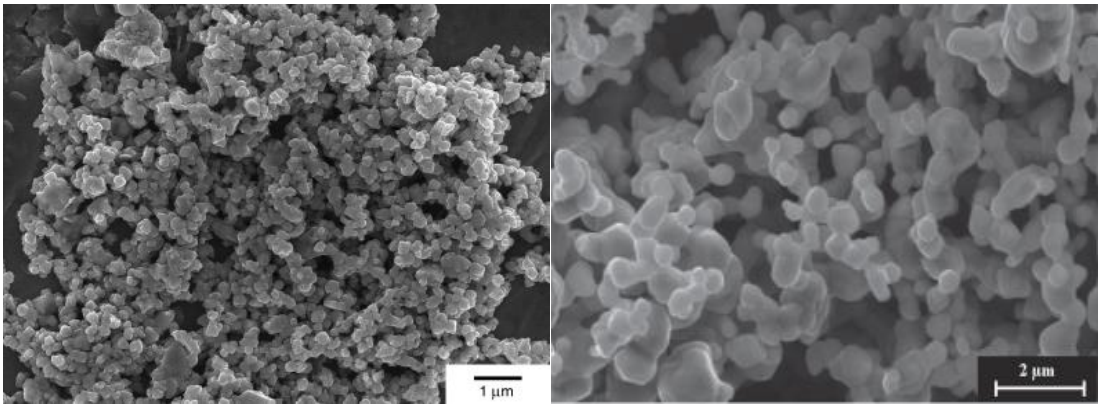

(a) (b)

Figure 2.14 SEM images of the ZrB_2 powders synthesized by (a) carbothermal reduction at 1600°C for 1h, and (b) borothermal reduction at 1650°C for 1h [78], [138].

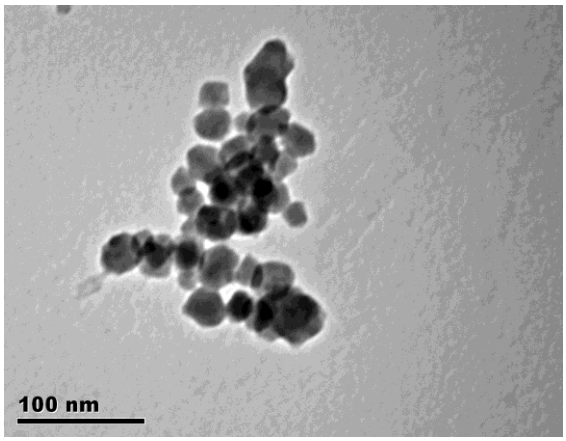

Figure 2.15 TEM image of the nano HfB_2 synthesized via a sol-gel approach [141].

In terms of the drawbacks of the carbothermal reduction, B_4C, HfC/ZrC and HfO_2/ZrO_2 are found as common impurities, so that excess B_2O_3 is often added to improve purity by promoting the formation of diborides over carbides [136], [142]. Much research effort is also focused on the sol-gel route synthesis of HfB_2

and ZrB_2, which is based on carbothermal reduction. This is because the sol-gel approach improves the mixing of the reactants to a molecular, or even atomic, level, which is beneficial for the completion of the carbothermal reduction reaction. Yan et. al [143], [144] prepared high-purity ZrB_2 and TiB_2 powders with particle sizes from 100-200 nm, as shown in Figure 14(a), via a sol-gel approach at a temperature of 1500^oC.

Venugopal et. al [141] succeeded in synthesizing high-purity HfB_2 via a sol-gel approach and showed that the carbothermal reduction can be completed at 1300^oC for 25 h. The average crystallite size of HfB_2 was only 25 nm, shown in Figure 2.15. Compared to the other HfB_2 and ZrB_2 powder syntheses reported in literature, the Loughborough prepared HfB_2 powders had homogeneous and finer particles. According to the oxidation testing of the HfB_2/carbon preform composites prepared by these HfB_2 powders, the oxidation resistance of the nano HfB_2 powders was not as good as that of the commercial submicron-size powders as nano powders were more reactive with oxygen due to larger surface area.

2.5.3.2 Borothermal reduction

Although borothermal reduction reaction involves monolithic boron, which is more expensive than carbon, the main advantage of the lab-based borothermal reduction reaction is the purity of the powders obtained, as boron is the only possible impurity [140], [145]. A recent report showed that the correct amount of B can remove the oxygen impurities and improve the densification process of ZrB_2 ceramics [146]. Moreover, as B_2O_3 is the intermediate product of Equation 2.12, the contamination of the graphite from heating elements and insulations can be reduced via the reaction of Equation 2.11 [138].

High-purity nano-scale zirconium diboride powder was synthesized by borothermal reduction of nano-sized ZrO_2 powder in vacuum at temperature of ~1650^oC [145]. It was reported that ZrO_2 started to convert to ZrB_2 at temperature as low as 1000^oC, but in order to improve the purity of the final powder and to remove all boron-related species a temperature above 1600^oC was required. The high-purity ZrB_2 powder had a particle size of 0.4-1.5 μm as shown in Figure 2.14(b).

2.5.3.3 Carbo/borothermal reduction

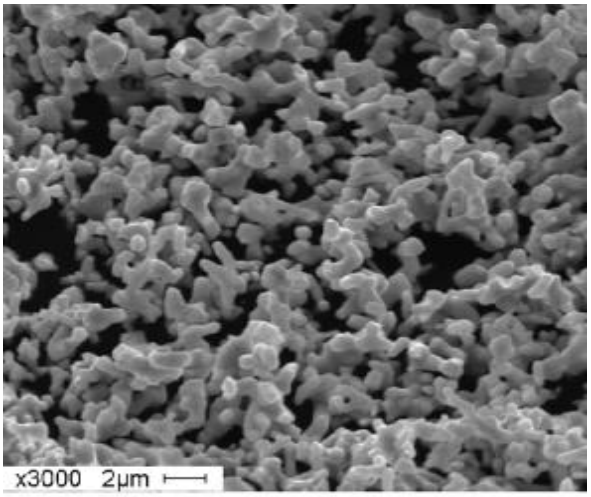

Figure 2.16 SEM image of HfB_2 synthesized at 1600^oC for 1h, via carbo/borothermal reduction, using $HfCl_4$, B_4C and C powders [147].

Carbo/borothermal reduction is actually a modified carbothermal reduction, using the combination of B_4C and C instead of only C as a reducing agent, as shown in Equation 2.13. The reaction is also endothermic and becomes favourable at a temperature around 1200^oC. The starting temperatures of carbo/borothermal reduction for forming HfB_2 [148] and ZrB_2 [149] were reported as 1300^oC and 1200^oC respectively, but to yield high-purity powders, a higher heat treatment temperature of 1600^oC was preferred. Zhang et. al [147] investigated the effect of stoichiometry on the purity of the formed HfB_2. The

high-purity powders he synthesized had an average crystallite size of ~1 μm as shown in Figure 2.16. The carbo/borothermal reduction reaction has also been exploited to promote densification of ZrB_2 due to the ability of excess B_4C to react with oxides and thereby reduce the amount of oxide impurities in the non-oxide ceramics [150]–[152].

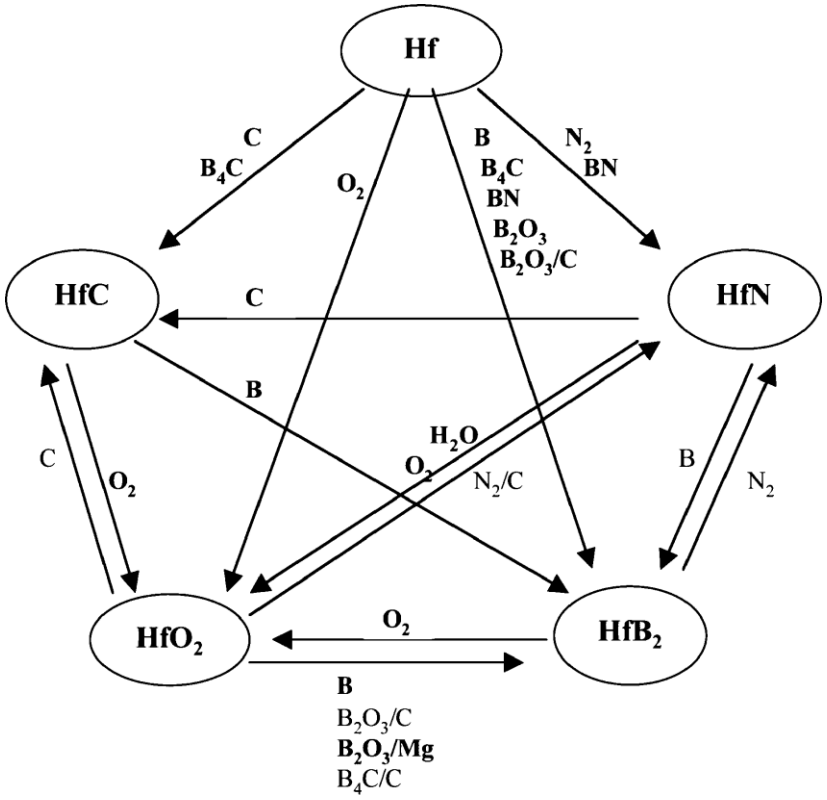

Figure 2.17 Chemical reactivity of hafnium and its derived boride, carbide and nitride compounds. Reactions with reagents marked in bold letters proceed (at least partially) at 1500ºC or blow. The rest require higher temperatures, e.g. borothermal, carbothermal, and carbo/borothermal reduction reactions. Additional reaction products within each of the reactions (if present) are omitted. [135]

Figure 2.17 summarizes the broad range of reactions that were found to occur at 1500ºC and below. Various reactions other than borothermal and carbothermal reduction reactions, using elemental Hf or its carbide and nitride derives, lead to the formation of HfB_2. These reactions provide much more

flexibility in using combinations of polymeric precursors and reactive powders to synthesize the group IV metal borides. All of them should be considered during the design and development of any practical precursor processing as the intermediate reactions and their products may play a key role obtaining the desired phases and microstructures.

2.6 UHTC composites

The borides of Hf and Zr are recognized as the most promising candidates for hypersonic applications, hence significant research effort has been focused on developing UHTC composites to improve the former's high temperature performance, as in extreme environments, these monolithic materials are faced with not only ultra-high temperatures, but also very high heat fluxes, rapid heating/cooling and activated oxygen. The high temperature performance of the monolithic materials can be significantly reduced due to the evaporation of the protective B_2O_3 scale (boiling point of 1860^{o}C, but evaporates quickly above 1600^{o}C) and the increased porosity caused by the phase transformation of the hafnia or zirconia scale. Various additives, such as SiC, $MoSi_2$, LaB_6, TaC, TaB_2 and their combination have been used to form ternary diboride compositions to improve the high-temperature performance of the borides [19], [27], [66], [153].

2.6.1 Various refractory metal boride based composites

2.6.1.1 Various dopants for ZrB_2 and HfB_2 based composite

The most widely studied UHTC composites are ZrB_2-SiC and HfB_2-SiC based ceramics. The dopant SiC is selected because it reduces the oxidation rate of both HfB_2 and ZrB_2 by forming a stable borosilicate glass layer on the surface of the oxidized ceramics [66], [154]. The silica layer is stable at temperatures

below 1600°C, but the protective layer forms volatile SiO(g) above 1600°C, which leads to a porous ZrO_2 scale being formed [154]. Thus at temperatures above 1600°C, because of active oxidation and evaporation of SiO_2, SiC additives actually reduce the oxidation resistance of borides rather than improving it. Although other dopants, e.g. WC and $TaSi_2$, have been added into HfB_2- or ZrB_2-SiC ceramics to improve the stability of the protective glassy phase, no significant improvement has been reported [155]–[157]. Some researchers also reported using Si_3N_4 instead of SiC to prepare ZrB_2-based composites. Although the sinterability, mechanical properties and low temperature (<1500°C) oxidation resistance of ZrB_2 can be significantly improved by adding Si_3N_4, the system is faced with the same issue as SiC due to the evaporation of silica at temperature above 1600°C [158]. The details of the oxidation behaviours of the UHTC-SiC based ceramics will be discussed later.

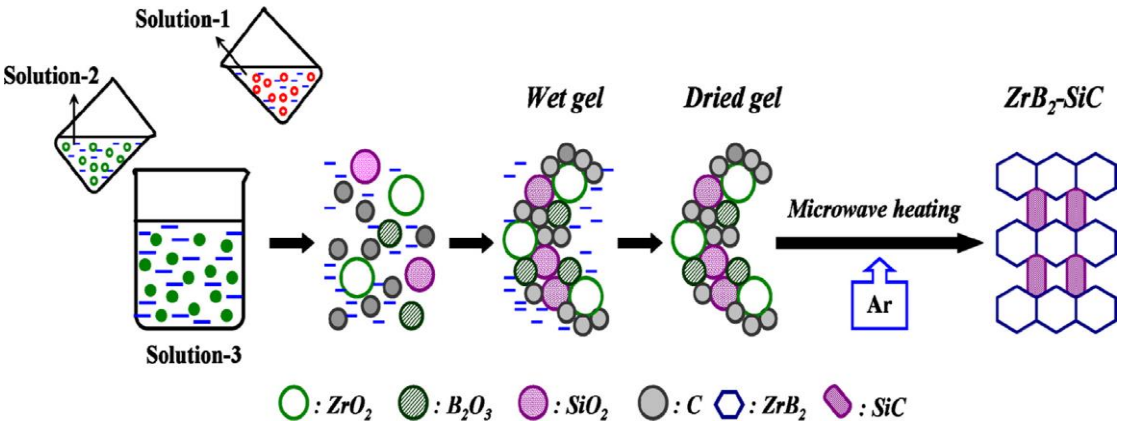

Figure 2.18 Schematic of the combined sol–gel and microwave boro/carbothermal reduction process used to prepare ultrafine ZrB_2–SiC composite powders [159]

The preparation of the UHTC-SiC green body is usually based on solid state mixing, e.g. via ball milling or attrition milling, using commercially available micron-scale ZrB_2, HfB_2 and SiC powders [37], [160]–[163]. It should be noted that homogeneously mixed SiC and UHTC powders were needed to improve

their sinterability. The ball milling of UHTC-SiC composites commonly involves high-purity SiC or WC balls to avoid contamination and ethanol as the milling media to avoid oxidation [22], [26]. It was reported the milling time should be no less than 10 h in normal ball milling, however the time could be shortened to 2 h if using planetary mono-milling [22]. Recently, submicron ZrB_2-SiC powders were synthesized via sol-gel methods, which involved using tetraethoxysilane (TEOS)/ethanol (Solution 1) mixed with $ZrOCl_2$ (Solution 2) and boric acid/phenolic resin (Solution 3) solutions as shown in Figure 2-18 [159], [164].

In order to improve the oxidation resistance and mechanical properties of ZrB_2 and HfB_2 at temperatures above 1600^oC, other group IV and V metal borides dopants such as TiB_2, NbB_2, TaB_2, W_2B_5, LaB_6 etc., have been added to modify the morphology of the crystalline phase in the oxide scale without forming glassy oxides to reduce the oxygen permeation rate [153], [165]–[167]. Among these dopants, some Group IV and Group V transition metal diborides can form continuous solid solutions due to similar crystal structures and atomic radii. For example, HfB_2 and ZrB_2 form continuous solid solution with TiB_2, NbB_2 and TaB_2 because their radii differ by only <10%, but a larger radius difference leads to limited solubility between these diborides and CrB_2 [168], [169].

Solid solution formation appears to depend on diffusion of the metal atoms, not the strongly bonded B atoms as the solid solution of these diborides still show hexagonal structure. The activation energy for metal atom diffusion can be used to compare the difficulties of forming solid solution among different Group IV and V atoms. The values for ZrB_2-TiB_2, TiB_2-NbB_2 and NbB_2-CrB_2 systems are 112, 175 and 400 kJ/mol, respectively, which correspond to the atomic radii differences between Ti and Nb (1%), Zr and Ti (9%) and Nb and Cr (13%) [169]. Since the metal atom diffusion in these systems is time and temperature dependent, good mixing between the metal boride dopants and matrix is desired.

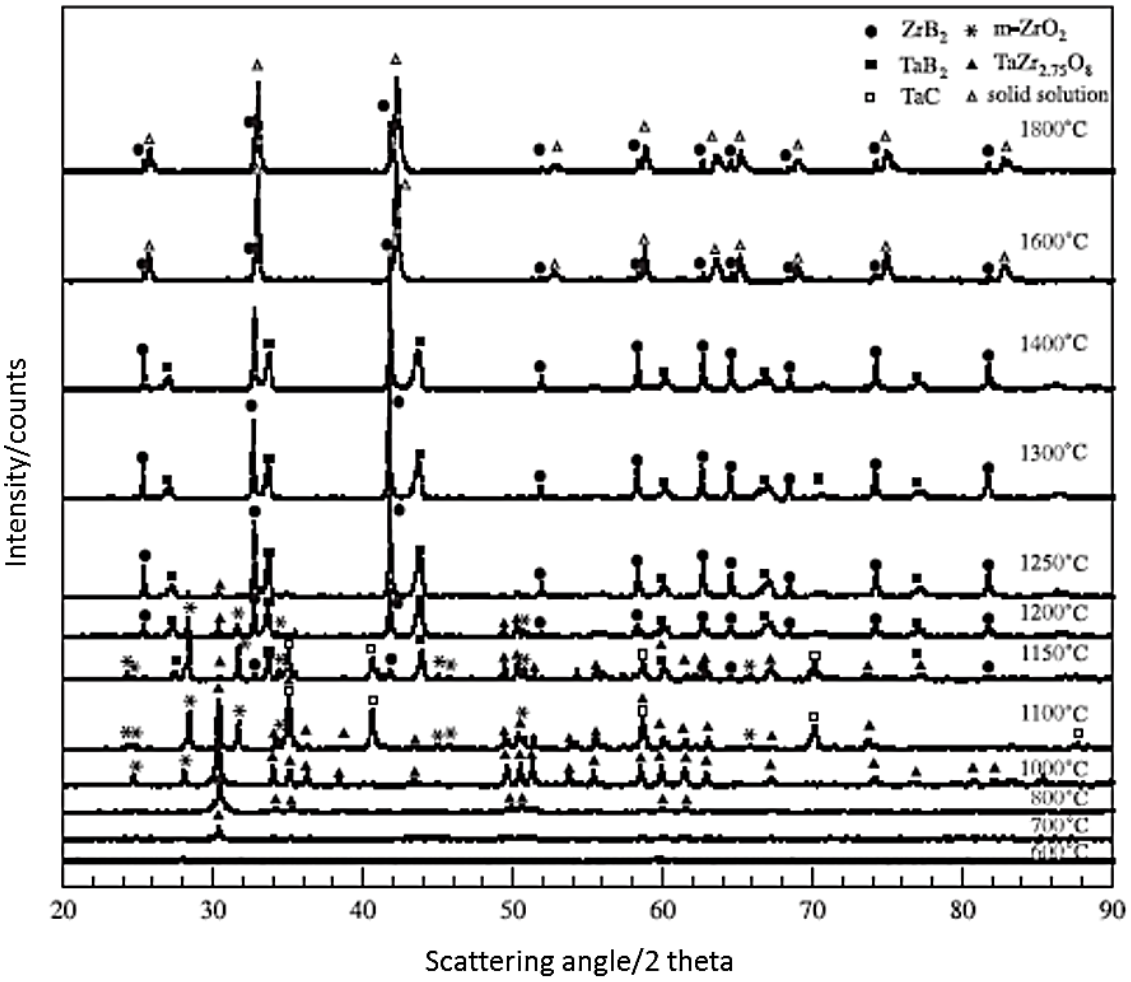

Figure 2.19 X-ray diffraction patterns for heat treated ZrB_2-TaB_2 powders. The samples placed in a graphite tube furnace in flowing argon [153]

Solid state mixing techniques, e.g. ball mill, attrition mill and planetary mill, have been reported to be succeeded in mixing commercially available ZrB_2 and TaB_2 powders, but the subsequent solid solution forming temperature was ~2000°C with hot pressing [157]. In contrast, when a solution based route involving tantalum ethoxide solution and zirconium n-propoxide/acacH was used to prepare ZrB_2-TaB_2 composite powders, it was reported that a solid solution formed at around 1600°C due to the homogeneous distribution of the dopants, as shown in Figure 2.19 [153]. The sol-gel method, which was developed to synthesize submicron HfB_2 powders using $HfCl_4$, boric acid and phenolic resin

[170], could also be extended to prepare HfB_2 based composite by adding ethanol-soluble Ti or Ta sources. Another approach to promote the distribution of dopants is via the co-precipitation method, which needs precise control of the pH values to force the dopant and matrix to precipitate at the same time. Jiang used a co-precipitation method to synthesize ZrO_2-WO_3 precursors which were subsequently reacted with amorphous boron at 1550°C to produce W-doped ZrB_2 powders with a particle size of around 400 nm [171].

Besides the borides, other derivatives of the Group IV and V refractory metals, such as $TaSi_2$, TaC, WC were also used to dope HfB_2 and ZrB_2 [158], [172]–[175]. These carbide and silicide dopants, when they absorb sufficient thermal energy, can be partially reduced by boron and become mutually soluble with HfB_2 and ZrB_2, hence modifying the crystalline phase in the oxide scale, which is similar to how the Group IV and V boride dopants work.

2.6.1.2 UHTC/carbon fibre composite

Although the Hf and Zr diborides have excellent oxidation resistance at elevated temperature, their poor thermal shock resistance and fracture toughness limit their high temperature performance. Even with the addition of a second or third phase such as SiC or other Group IV and V borides, the thermal shock resistance or fracture toughness were not improved at temperatures over 1600°C due to the volatilization of the oxides formed [176]. In recent years, UHTC/carbon fibre composites have attracted much research interest as these composites are able to overcome the shortages of monolithic UHTCs owing to the ready availability of the carbon fibres and the ability to form them into complex shapes [177]. Moreover, carbon fibre has reasonable strength retention at temperatures up to 2000°C [178], as show in Figure 2.20. However, these excellent properties are limited to non-oxidizing environments. Carbon fibre can

oxidize at 500°C in air and lose their function. Therefore, UHTCs are chosen to protect the carbon material from oxidation to help retain the desired mechanical performance, as shown in Figure 2.21 [75].

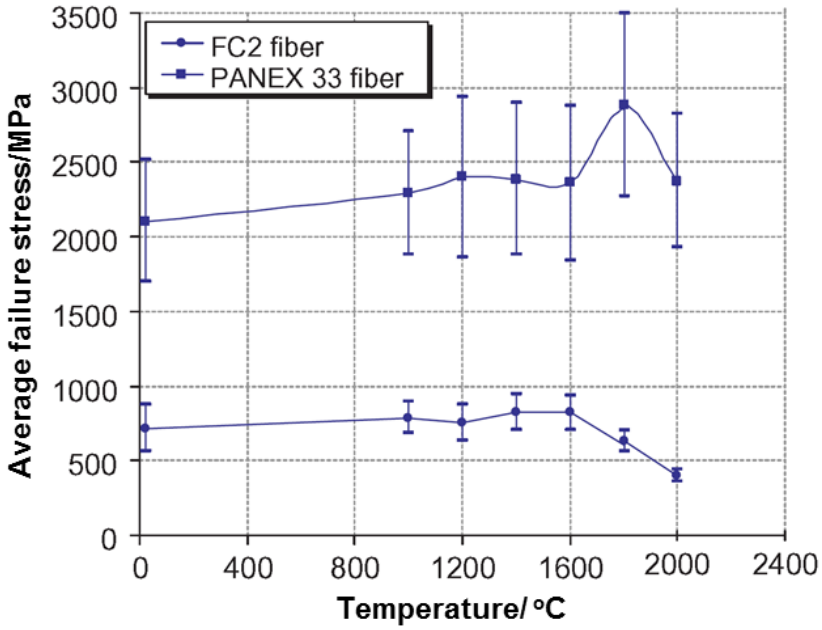

Figure 2.20 Failure stress of FC2 fibre and PANEX 33 fibre as a function of temperature [178]

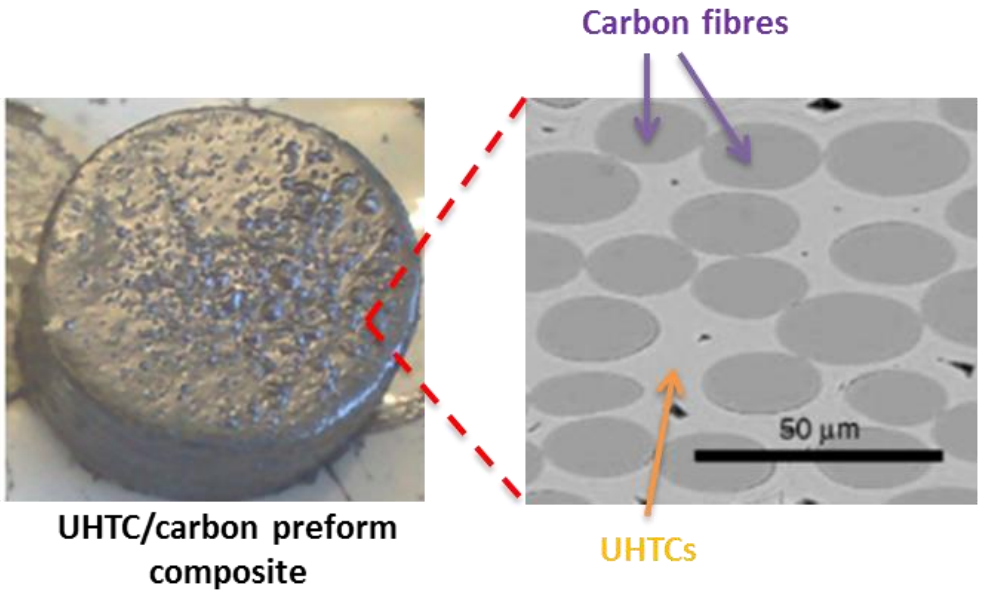

Figure 2.21 An illustration of typical UHTC/carbon preform composite [75]

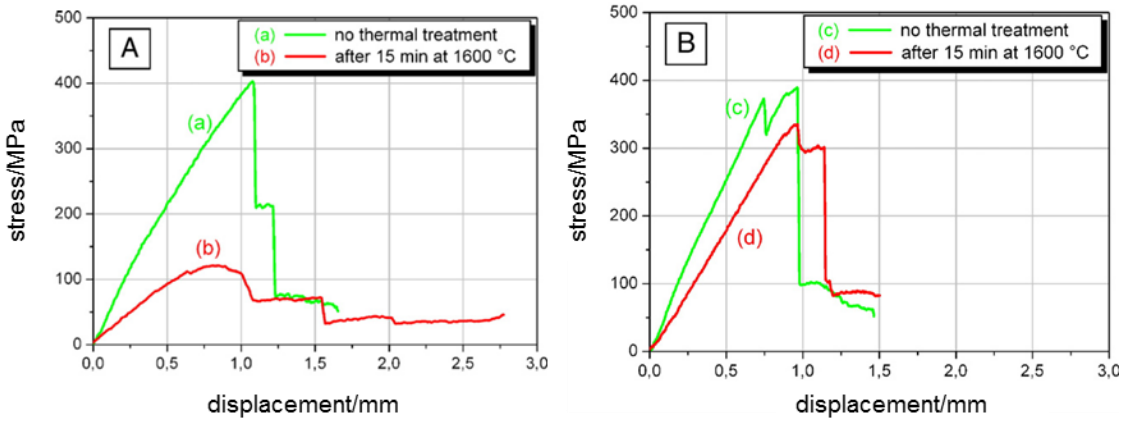

Figure 2.22 Stress/displacement curves from bending tests of: (A) uncoated composites and (B) HfB_2/SiC-coated composites [109]

Several reports have described the fabrication and the high temperature performance of UHTC/carbon composites to date. Levine et.al [179] prepared SiC fibre reinforced ZrB_2-20 vol% SiC via slurry infiltration and hot pressing, but all the samples were severely damaged at 1927°C. Tang et.al [180] used pressure assisted suspension infiltration to fabricate Cf/ZrB_2 and Cf/ZrB_2-SiC composites. The results of subsequent oxyacetylene torch tests revealed that the composites containing SiC demonstrated a lower erosion depth at 1600°C, whilst the composite based on Cf/ZrB_2 showed the least damage at 2700°C. This result is consistence with the previous discussion on the effect of SiC additions on the oxidation resistance of ZrB_2. Pavese et.al [181] produced Cf/HfB_2-SiC composites using polymeric Hf-containing precursors to infiltrate carbon preforms, followed by pyrolysis to obtain HfB_2 with a subsequent hot pressing for densification. The mechanical properties of the composites after oven oxidation testing at 1600°C were measured and it was found that the carbon fibre survived owing to the protection provided by HfB_2 and the strength was largely retained as shown in Figure 2.22.

Recently, Venugopal et.al [141] prepared carbon fibre/HfB_2 composites via dip coating from a HfB_2 precursor gel and the HfB_2 coatings showed good adhesion

without any cracking. However, these coatings are too thin to protect the carbon fibres. Paul et.al [75] fabricated several composites including Cf-HfC, Cf-ZrB_2, Cf-HfB_2, Cf-ZrB_2-SiC and Cf-ZrB_2-SiC-LaB_6, via pressure assisted slurry infiltration, as shown in Figure 2.23. As the porosity was as high as 35% after impregnation, chemical vapour infiltration (CVI) was used to fill the porosity inside the composites with carbon. It should be noted that the ZrB_2 and HfB_2 were not sintered in these composites. Their oxidation behaviour will be discussed in Section 2.6.3.

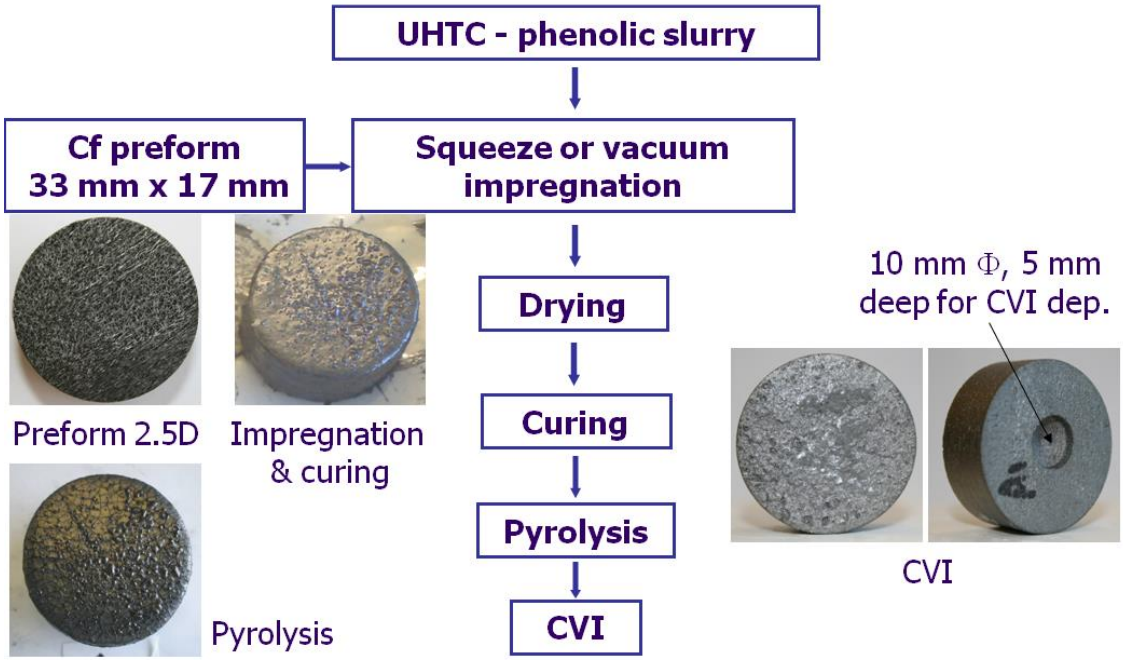

Figure 2.23 A flowchart of impregnation-infiltration process for Cf/UHTC composites and its products [75]

2.6.2 Densification of UHTCs

In typical ceramics processing, sintering involves the densification of a particulate ceramic compact by utilizing thermal energy to remove the pores between the starting particles, as well as minimizing the surface free energy by achieving particle bonding [182]. Figure 2.24 shows these three ceramic

sintering stages, i.e. initial particle rearrangement due to the driving force and followed by inter-particle necking, neck growth and grain growth which results in high shrinkage and continuous pore phase. In the final stage, discontinuous pore phase and grain boundary pores are eliminated with grain growth.

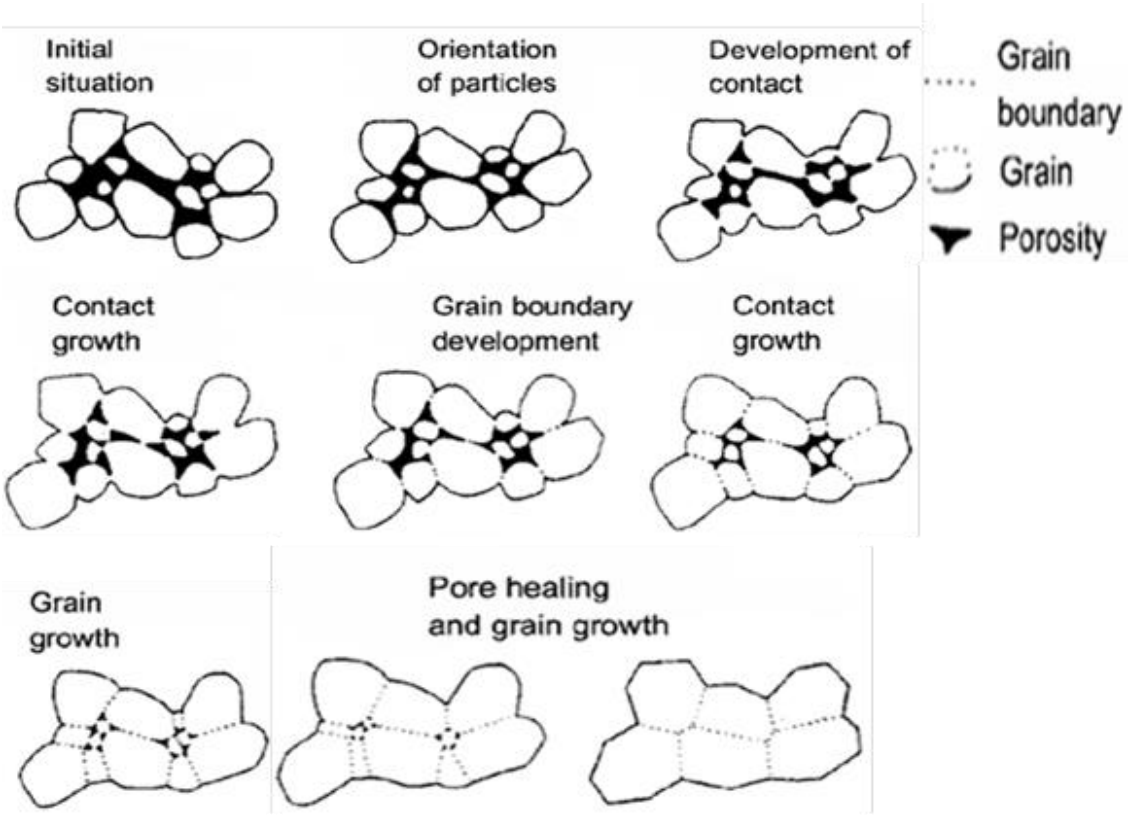

Figure 2.24 Schematic of the sintering processes of ceramics [182]

The need for dense UHTCs is driven by hypersonic applications which require continuous use of the UHTCs in the extreme environment. The full densification of ZrB_2 and HfB_2 usually requires high temperatures and high pressures due to the strong bonding and low self-diffusion of the borides [183]. Fully density for the ZrB_2 and HfB_2 was first achieved by reactive hot pressing (RHP) back in 1953 [54]. However, hot pressing is limited by the size and geometry of the samples to be sintered. In order to sinter UHTCs with larger size and more complex shape, recent research has been focused on developing novel

sintering methods, e.g. spark plasma sintering (SPS), microwave sintering (MS), flashing sintering (FS), and using various sintering additives such as Ni, Si_3N_4, $MoSi_2$, SiC, $TaSi_2$, to improve the sinterability of the refractory diborides.

2.6.2.1 Hot pressing

In historic studies, monolithic ZrB_2 and HfB_2, without any additives, have only been densified by hot pressing (HP) at 2000°C or higher with pressures of 20-30 MPa, or at reduced temperatures (~1800°C) with extremely high pressures (>800 MPa) [184], [185]. Recent studies revealed that the particle size and defects can significantly affect the sinterability of the ZrB_2 and HfB_2 powders [21], [127]. HP of the HfB_2 powders with a nominal starting particle size of 10 μm at 2160°C and 27.3 MPa for 180 min resulted in a relative density of <95% [21], while the ZrB_2 powders with a starting particle size of ~20 μm was only ~73% dense after HP at 2000°C and 20 MPa [186]. Chamberlain et.al reported that commercial ZrB_2 powders with a starting particle size of 2 μm could be further comminuted by attrition milling to submicron sized (d<0.5 μm) and the resulting powders were densified to >95% by HP at 1900°C and 32 MPa for 45 min [127]. It was found that the reduced particle size and the defects introduced by attrition milling can improve the sinterability of ZrB_2 [127]. However, WC impurities were incorporated during attrition milling due to the wear of the WC-based milling media. It is important to avoid using oxides milling media, such as Al_2O_3 and ZrO_2, which will inhibit the densification of the borides.

Research on various ceramic additions (e.g. WC, SiC, Si_3N_4, $TaSi_2$) to ZrB_2 and HfB_2 showed improved densification and, more importantly, enhanced oxidation resistance within certain temperature ranges [158], [172], [174], [187]. Among these additives, SiC and Si_3N_4 are non-reactive additives. Their primary effect is the depletion of the diboride particles from oxygen, which severely limits the

maximum attainable density [160], [188]. The formation of a silicon-based melt is believed to be another reason to improve the densification of the diborides via liquid phase forming, despite the fact that the exact composition of the amorphous melt is not yet fully understood [161].

Table 2.7 Hot pressing conditions and densities of hot-pressed commercial ZrB_2 and HfB_2 with various additives

		Hot pressing condition			
Materials	**Particle size/μm**	**Temperature /°C**	**Pressure /MPa**	**Time /min**	**Final density**
ZrB_2 [79]	6	1900	30	30	87%
HfB_2 [21]	10	2160	27	180	90-95%
ZrB_2+2.5wt% Si_3N_4 [189]	2	1700	15	30	>98%
ZrB_2+4wt% Ni [190]	-	1850	30	30	98%
HfB_2+15wt% $MoSi_2$ [30]	~2	1900	30	10	98.7%
HfB_2+20vol% SiC [176]	4	2200	25	60	~100%
ZrB_2+8vol% Ta_5Si_3 [191]	-	1900	30	30	97%
ZrB_2+20vol%SiC+ 4vol% TaB_2 [191]	2	1800	200	30	100%

Other additives, such as Ni, WC, $MoSi_2$, $TaSi_2$ and TaB_2, can produce a liquid phase or result in solid solution formation to improve densification of ZrB_2 and HfB_2 [148], [192], [193]. Hence the high HP temperature and pressures of historic studies are not necessary with the finer starting powders and additives. The conditions required in the literature to hot press ZrB_2 and HfB_2 to near full density by adding Ni, Si_3N_4, $MoSi_2$, SiC, $TaSi_2$ or combination of additives, are summarized in Table 2.7.

2.6.2.2 Reactive hot pressing

Reactive hot pressing (RHP) has been used to sinter ZrB_2–SiC and HfB_2–SiC based ceramics at lower temperature and pressure than that required for HP [127], [187],
[194], [195]. In RHP processes, the in-situ reaction and densification are combined into a single step. These processes used the precursors Zr, Si and B_4C to synthesize ZrB_2-SiC. It was reported that a relative density of ~95% was achieved by RHP at 1650^oC and 50 MPa and the density was increased to ~98% with RHP at 1900^oC, which is lower than the 2100^oC required by conventional HP for ZrB_2-SiC [187], [195]. The significant improvement of densification by RHP was attributed to the formation of nano-sized ZrB_2 and HfB_2 particles during the reactive process resulting in large surface areas and surface reactivity which provide more driving force for sintering. The presence of SiC also had a dramatic effect on reducing the RHP densification temperature and controlled the grain size of the ZrB_2 to about 0.5 μm since SiC can reduce the surface area of ZrB_2 and deplete the oxide impurities such as B_2O_3 and ZrO_2.

2.6.2.3 Spark plasma sintering

Since the sintering temperature for UHTCs is high and this creates complex requirements on furnace design, several new approaches, e.g. spark plasma sintering (SPS) have been considered for sintering ZrB_2- and HfB_2-based ceramics with a significant reduction in furnace temperature. SPS has been used to densify UHTCs recently [30], [148], [196], [197] and in this process, a uniaxial load and a direct or pulsed electric current are simultaneously applied to a powder compact. As shown in Figure 2.25, the applied electric field is applied through an electrically conducting graphite die and can heat both the die and the powder compact if the powders are also electrically conductive. Thus

the SPS process is suitable for the densification of ZrB_2 and HfB_2, which show excellent electrical conductivity [87]. Hubert et. al investigated different experimental methods such as in-situ atomic emission spectroscopy, AES, to monitor the sintering process during SPS. They found it was interesting that neither a spark nor a plasma were generated throughout the sintering process [198]. Compared to HP, SPS involves a rapid heating rate up to hundreds of ^oC/min, leading to rapid densification, which in turn, minimizes grain growth [199]. However, the down side of SPS is carbon contamination from the graphite foils that are used as a sacrificial layer to avoid direct interaction of the graphite punches with the sample.

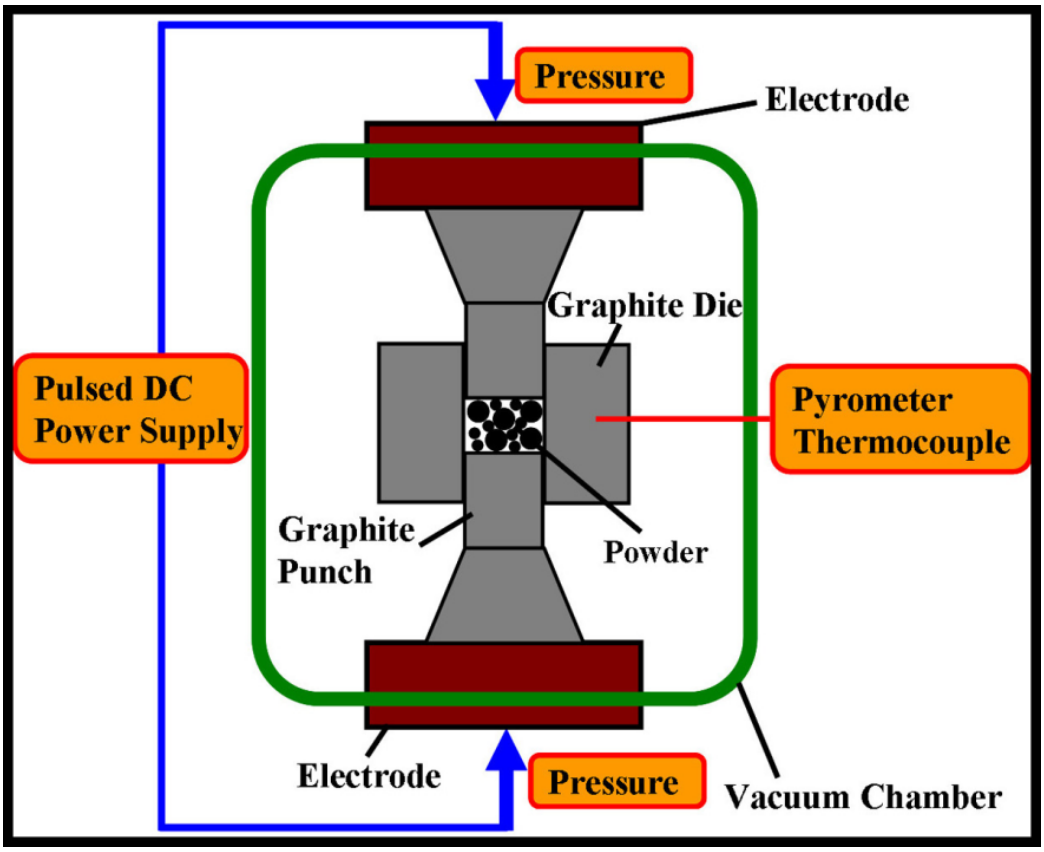

Figure 2.25 Schematic of SPS setup [200]

SPS facilities can be equipped with a liquid nitrogen cooling system, which allow the entire SPS cycle to be finished even within 1 h. Monteverde et. al [32]

synthesized HfB_2-SiC with near full density by using SPS at 30 MPa and 2100°C, with a heating rate of 100°C/min, which resulted in a mean grain size of around 2 μm. Medri et. al [29] also achieved full density for ZrB_2+30 vol% ZrC+10 vol% SiC using SPS at 2100°C for 60 min. The densification rate was 2×10^{-4} s^{-1} over a broad temperature range (1750-2050°C), whilst the densification rate of the same materials prepared by HP was only 1.3×10^{-5} s^{-1} at 1870°C. The SPS conditions required to densify ZrB_2- and HfB_2-based ceramics to near full density are summarized in Table 2.8 for comparison and it can be seen that the temperature and pressure required are similar to that of HP. The idea of high pressure and low temperature SPS could also be used for the densification of ZrB_2 and HfB_2 to limit grain growth. Grasso et. al reported low temperature SPS of WC powders that 99% relative density was achieved by using 500 MPa pressure at 1400°C [201].

Table 2.8 SPS conditions and densities of SPS-ed commercial ZrB_2 and HfB_2 with various additives

		SPS conditions			
Materials	**Particle size (μm)**	**Temperature (°C)**	**Pressure (MPa)**	**Time (min)**	**Final density (%)**
HfB_2-+30 vol% SiC [32][70]	1.7	2100	30	10	>99
HfB_2+30 vol% HfC+10 vol% SiC [202]	2.5-7	1800	20	10	98.5
ZrB_2+30 vol% ZrC+10 vol% SiC [29]	-	2100	30	60	100
ZrB_2+15 vol% $MoSi_2$ [196]	1.7	1750	30	24	97.7
HfB_2+15 vol% $MoSi_2$ [30]	2.08	1750	30	10	95
ZrB_2+5wt% ZrC [203]	-	1900	40	15	97.5

2.6.2.4 Field assisted sintering/flash sintering

Flash sintering, introduced and defined by Cologna et. al, is a new and novel sintering method to densify ceramic materials [204]. Both electric field and thermal energy are involved to achieve the rapid densification. Cologna et. al [204] described that flash sintering could densify ceramics under lower furnace temperature in few seconds. The flash sintering phenomenon are believed to be attributed predominantly to the local Joule heating at grain boundary [205], [206]. In flash sintering process, the specimen first needs to be heated up to a specific temperature, which leads to a reduction in resistance and the promotion of diffusion at grain boundaries [207]. Then, controlled current is passing through the specimen to induce Joule heating. Due to the assistance of joule heating, the actual specimen temperature is found to be significantly higher than the furnace temperature.

Very limited work has been done to investigate the possibility of flash sintering UHTCs, currently being persuaded at Lougborough University, UK. Matthaw et. al prepared HfB_2-based ceramics by HP and field-assisted sintering (FAS) with 10–20 vol% SiC, 5 vol% $TaSi_2$ and 5 vol% iridium [208]. Typical HP conditions required for densification (above 95% density) were 1900–2200^{o}C for 1 h at 25 MPa, whist similar density was achieved by FAS at 1800–1900^{o}C for only 5–10 min. The grain size of the samples prepared by FAS was half of that from HP. Recently, Grasso et. al [209] reported that pure ZrB_2 powder was Flash sintered in an SPS furnace (FSPS) using a very rapid heating rate (4000°C/min) and a constant uniaxial force of 5 kN. The samples were pre-sintered to 63% density at 1600^{o}C and then discharged under a peak power of 25 kW for 35 s to achieve 95% density without cracking.

2.6.2.5 Pressureless sintering

Pressureless sintering (PS) of refractory metal borides would enable the fabrication of near net shape components using standard powder processing methods. Compared to HP, PS reduces costs and can potentially open the door for other applications. As mentioned before, however, ZrB_2 and HfB_2 require very high temperatures and pressures to densify, hence, there aren't any researchers currently reporting achieving near full density for undoped ZrB_2 and HfB_2 prepared by PS. This is because the hexagonal crystal structure of the borides allows anisotropic grain growth and entraps porosity (i.e. coarsening is more favourable than densification).

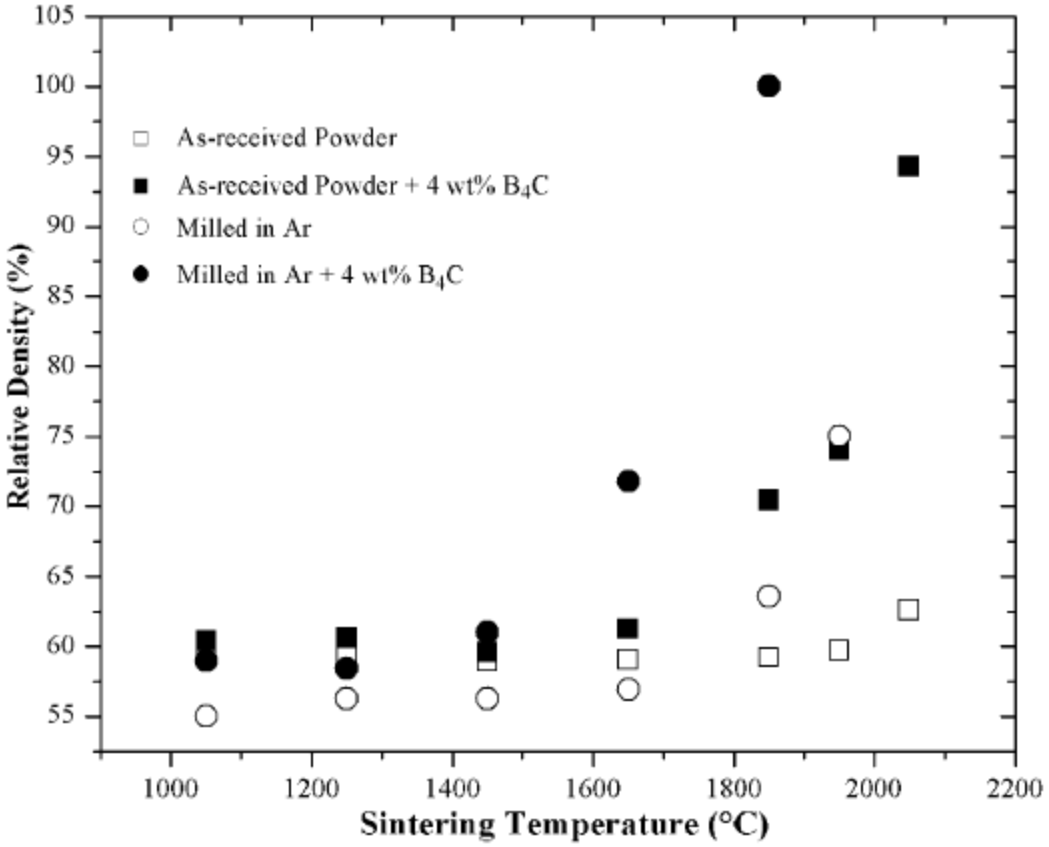

Figure 2.26 Relative density as a function of sintering temperature for phase pure ZrB_2 and ZrB_2+4 vol% B_4C [152]

The approaches to improve the densification are to use finer starting powders and sintering aids, which are similar to the methods used in HP and SPS. Intensive mechanical milling, such as attrition milling and vibratory milling have also been reported to enhance the sinterability of ZrB_2 as the milling was believed to not only increase the surface area, but also to increase the number of defects near the surface of the particles, enhancing the driving force for densification by grain boundary diffusion [210]. Mishra et.al studied metal Cr and Fe additions to ZrB_2 and the density of the ZrB_2+10 vol% Fe prepared by PS at 1800^{o}C reached ~93% [211]. The relative density of ~99% for ZrB_2 was achieved by PS at 1850^{o}C with significant amounts of $MoSi_2$ (20 vol%), which led to liquid phase formation [212], [213]. However, the addition of metals or the additives leading to liquid phase densification not only reduces the densification temperature, but also reduce the melt temperature, hardness and high-temperature-strength of ZrB_2 [190], [211]. In order to avoid liquid phase formation, small amounts of WC (~2 vol%) and B_4C (4 vol%), which could remove oxide impurities (B_2O_3 and ZrO_2) from the ZrB_2 system, have also been added to promote densification and minimize particle coarsening [152], [214]–[218]. ZrB_2+2 vol% WC was sintered to >98% density at 2150^{o}C for 540 min and ZrB_2+4 vol% B_4C was sintered to ~95% density at 2050^{o}C for 60 min, which was a significant improvement compared to the densification of pure-phase ZrB_2 by PS (~62%) under the same conditions, as shown in Figure 2.26 [152], [214].

2.6.3 Oxidation behaviours of UHTCs and UHTC based ceramics

2.6.3.1 Static furnace oxidation and thermogravimetric analysis

Although the hypersonic applications for ZrB_2 and HfB_2 involve not only oxidation conditions and elevated temperatures, but also reactive environments, rapid heating and erosive conditions, static furnace oxidation is still the most

common method to investigate the oxidation behaviour of ZrB_2-and HfB_2- based ceramics due to the techniques' low cost and availability. The oxidation behaviour discussed in this chapter is focused on ZrB_2- and HfB_2- based composites.

Table 2.9 Summary of oxidation behaviour of SiC containing ZrB_2 and HfB_2 over a wide temperature range [154], [219]–[223]

Temperature range	Scale	Oxidation behavior
<600°C	ZrO_2 or HfO_2	Mass gain due to the oxidation of the diborides
600-1100 °C	ZrO_2 or HfO_2 + B_2O_3 SiC not oxidized	Parabolic kinetics due to presence of a dense glassy oxide layer (B_2O_3)
1100-1300 °C	Borosilicate glass outer layer ZrO_2 or HfO_2 + SiO_2 layer	B_2O_3 evaporation and SiC oxidation Paralinear kinetics due to evaporation of B_2O_3 Protection from borosilicate glass
1300-1600 °C	Borosilicate glass outer layer (lower B content) ZrO_2 or HfO_2 + SiO_2 layer	B_2O_3 evaporation, ZrO_2 transport, and SiC oxidation Parabolic kinetics due to dense borosilicate glass layer
1600-1900 °C	ZrO_2 or HfO_2 + SiO_2 layer	Evaporation of silica from scale
>1900 °C	ZrO_2 or HfO_2	Less protection from more ZrO_2 or HfO_2 porous scale

As indicated before, ZrB_2-SiC and HfB_2-SiC are the most widely studied systems. The addition of SiC as a second phase can reduce the thickness of the oxide scale of ZrB_2 and HfB_2 across a wide temperature range (1100-1600°C) when compared to phase-pure diboride [220]–[222]. As shown in Table 2.9, at temperatures <600°C, the oxidation of ZrB_2 and HfB_2 are negligible as the borides showed limited mass gain when exposed to air [98]. In the temperature range 600-1100°C, the addition of SiC shows no influence on the oxidation of

ZrB_2 and HfB_2 because in this stage ZrB_2 and HfB_2 rather than SiC are preferably oxidized [220]. As temperature is increased to 1100°C and above, the SiC is oxidized and B_2O_3 starts to evaporate. The improved oxidation resistance in this regime was attributed to the formation of a stable borosilicate glass layer, which can significantly reduce oxygen permeation and remain on the surface of the oxidised ceramics at temperature up to 1600°C, as shown in Table 2.9 [221]–[223].

Table 2.10 Gas-condensed phase equilibria during the oxidation of ZrB_2-SiC. The gaseous Si containing products forms under the oxide scale where the oxygen partial pressure is low and then condenses at the surface to form an outer silica layer and leave a silicon depleted zone in the oxide scale near the boride [220], [224]

Species	Species in equilibrium with ZrB_2–SiC	Species in equilibrium with the stable oxides
$B_2O_3(g)$	$ZrB_2 + 2.5O_2(g) = ZrO_2 + B_2O_3(g)$	$B_2O_3(l) = B_2O_3(g)$
$B_2O_2(g)$	$ZrB_2 + 2O_2(g) = ZrO_2 + B_2O_2(g)$	$B_2O_3(l) = B_2O_2(g) + 0.5O_2(g)$
$BO_2(g)$	$ZrB_2 + 3O_2(g) = ZrO_2 + 2BO_2(g)$	$B_2O_3(l) + 0.5O_2(g) = BO_2(g)$
BO(g)	$ZrB_2 + 2O_2(g) = ZrO_2 + BO(g)$	$B_2O_3(l) = 2BO(g) + 0.5O_2(g)$
$B_2O(g)$	$ZrB_2 + 1.5O_2(g) = ZrO_2 + B_2O(g)$	$B_2O_3(l) = B_2O(g) + O_2(g)$
$B_2(g)$	$ZrB_2 + O_2(g) = ZrO_2 + B_2(g)$	$B_2O_3(l) = B_2(g) + 1.5O_2(g)$
B(g)	$ZrB_2 + O_2(g) = ZrO_2 + 2B(g)$	$B_2O_3(l) = 2B(g) + 1.5O_2(g)$
$SiO_2(g)$	$SiC + 1.5O_2(g) = SiO_2(g) + CO(g)$	$SiO_2(l) = SiO_2(g)$
SiO(g)	$SiC + O_2(g) = SiO(g) + CO(g)$	$SiO_2(l) = 0.5O_2(g) + SiO(g)$
Si(g)	$SiC + 0.5O_2(g) = Si(g) + CO(g)$	$SiO_2(l) = O_2(g) + Si(g)$

After furnace oxidation at temperatures between 1100 and 1600°C, the formation of a SiC depleted region has been observed by some researchers [220]–[222]. The depletion of SiC from the partially oxidised layer has been attributed to active oxidation of SiC due to the oxygen activity gradient through the outer layer of the dense glassy oxide [225], as shown in Table 2.10 and Figure 2-27. Very few researchers have examined the SiC-containing borides at temperature above 1600°C [226]–[228]. Since the evaporation of SiO_2 results in bubbles/voids in the oxide scale [107], which was confirmed by in-situ

observations of oxidizing ZrB_2-SiC composite [229]. In this temperature regime, the oxidation resistance of the entire system is dependent on the microstructure and density of the oxides [37].

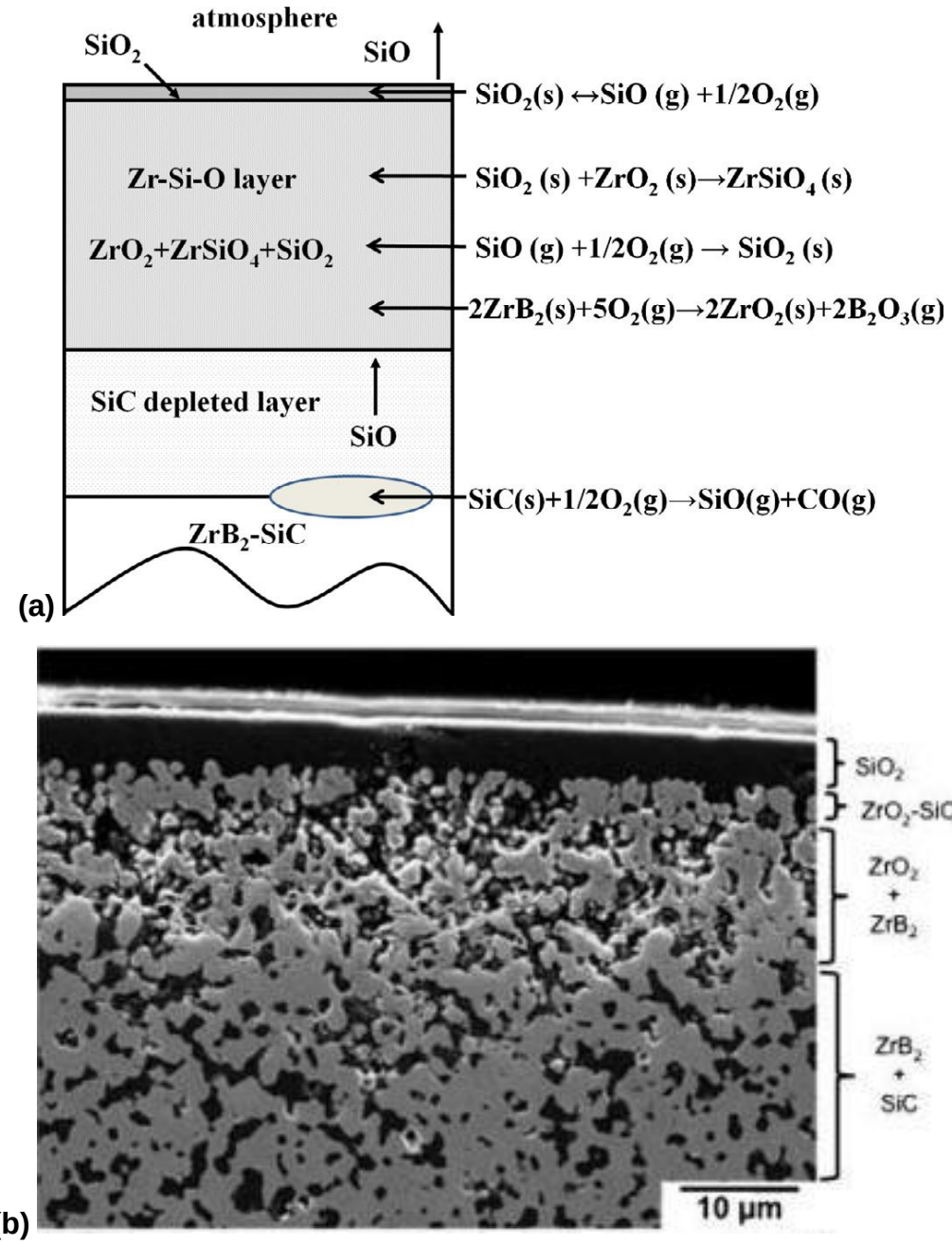

Figure 2.27 (a) Schematic oxide structure of ZrB_2-SiC ceramics and (b) cross-section of the ZrB_2-SiC after oxidation at 1500°C [98], [220]

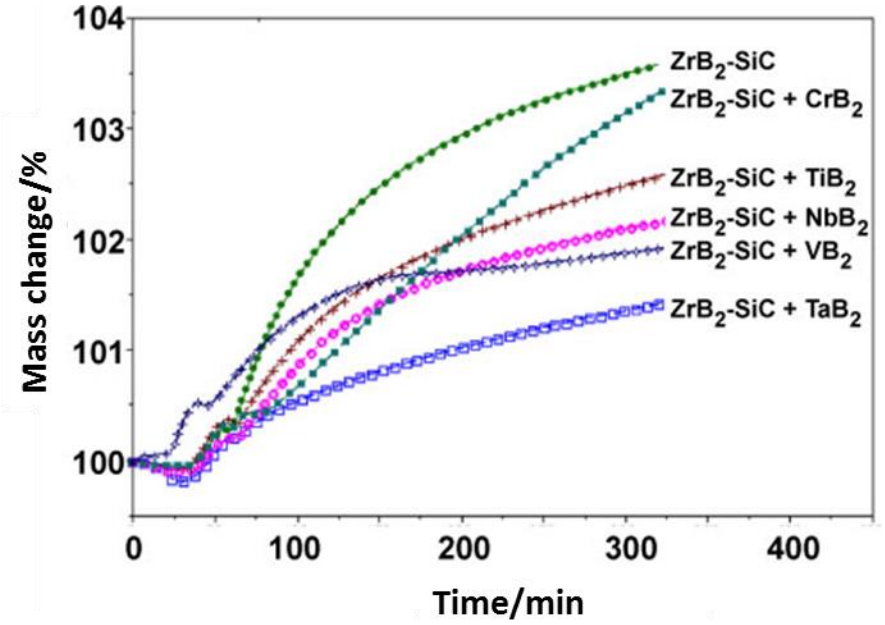

Figure 2.28 Studies of oxidation resistance of pure and additive containing ZrB_2-SiC ceramics – comparison of mass gain versus time at 1500°C [84]

Other additives have been used in combination with SiC to further improve the oxidation resistance of ZrB_2 and HfB_2. Levine et. al [157] added 20 vol% $TaSi_2$ to ZrB_2-SiC and HfB_2-SiC and reported an improved oxidation resistance of the ceramics at 1627°C, but poor performance at temperatures above 1927°C, which is due to the evaporation of the glassy layer and the melting of Ta_2O_5. Talmy et. al [21], [158] investigated additions of 10 vol% Cr-, Ti-, Nb-, V- and Ta-borides to ZrB_2-25 vol% SiC and found that all the additives improved oxidation resistance over the base composition, with TaB_2 additions being the most effective, as shown in Figure 2.28. It is because Ta compounds have the highest cation field strength (defined as Z/r^2, where Z is the valence of the cation and r is the ionic radius), which retains borosilicate glass, and hence results in reduced oxygen diffusion rates. Peng et. al also added TaB_2 and $TaSi_2$ to modify the microstructure of ZrO_2 [19], [230]. They found that with the additions of a few mole percent, e.g. 3.3 mol%, the grains of the oxide scale displayed a more equiaxed morphology which increased retention of the borosilicate glass and hence improved oxidation resistance [230]. However, with higher contents of Ta

based compounds, the additions appeared to promote coarsening of the crystalline phases in the oxide scale and the formation of ZrO_2 dendrites that penetrated the outer glassy layer, both of which degraded oxidation resistance.

Diboride based ceramics with SiC additions have been researched extensively, but silicides and other Si containing additives also produce a glassy silica rich surface layer during oxidation. For example, $MoSi_2$ was originally reported as a sintering aid for the pressureless sintering of ZrB_2 and HfB_2 [17], [30], [212], [231]. Subsequent oven oxidation tests of the ZrB_2-20 vol% $MoSi_2$ revealed that, as for SiC, the addition of $MoSi_2$ lead to the formation of a SiO_2-rich outer oxide layer at 1200^{o}C [231]. Moreover, the advantage of using $MoSi_2$ is that the formation of gaseous CO during oxidation from SiC was avoided, leading to a denser ZrO_2 layer. The addition of other silicides, such as $ZrSi_2$, $TaSi_2$ and Ta_5Si_3, showed similar effects on the oxidation behaviour of ZrB_2 at temperatures below 1900^{o}C [172], [223], [230]. However, these silicide-containing composites faced the same issues related to the evaporation of silica at higher temperatures.

As the oxidation resistance of ZrB_2 and HfB_2 is controlled by the oxygen transport through the oxide scale rather than through other glassy layers at elevated temperature, other ceramic additives, such as WC, WB_2, TaB_2 and LaB_6 have been investigated to understand their effect on the structure of the crystalline oxide scale, without forming an outer silica layer. Zhang et. al [173], [174] added up to 8 mol% WC to ZrB_2 and showed that W dissolved into the ZrB_2 matrix and reduced both mass gain and oxide scale thickness compared to nominally pure ZrB_2 at 1500 and 1600^{o}C. The improved oxidation resistance was attributed to the formation of a ZrO_2 scale with a crystalline, equiaxed microstructure and retention of a combination of WO_3 and B_2O_3 in the scale, as shown in Figure 2.29 [173]. Further, mass gain kinetics appeared to be parabolic at 1500 and 1600^{o}C [173], [174] Thus, the work suggested that oxidation

behaviour can be improved solely by manipulating the morphology of the crystalline phase in the oxide scale, whereas most studies have focused on the effect of the outer glassy layer.

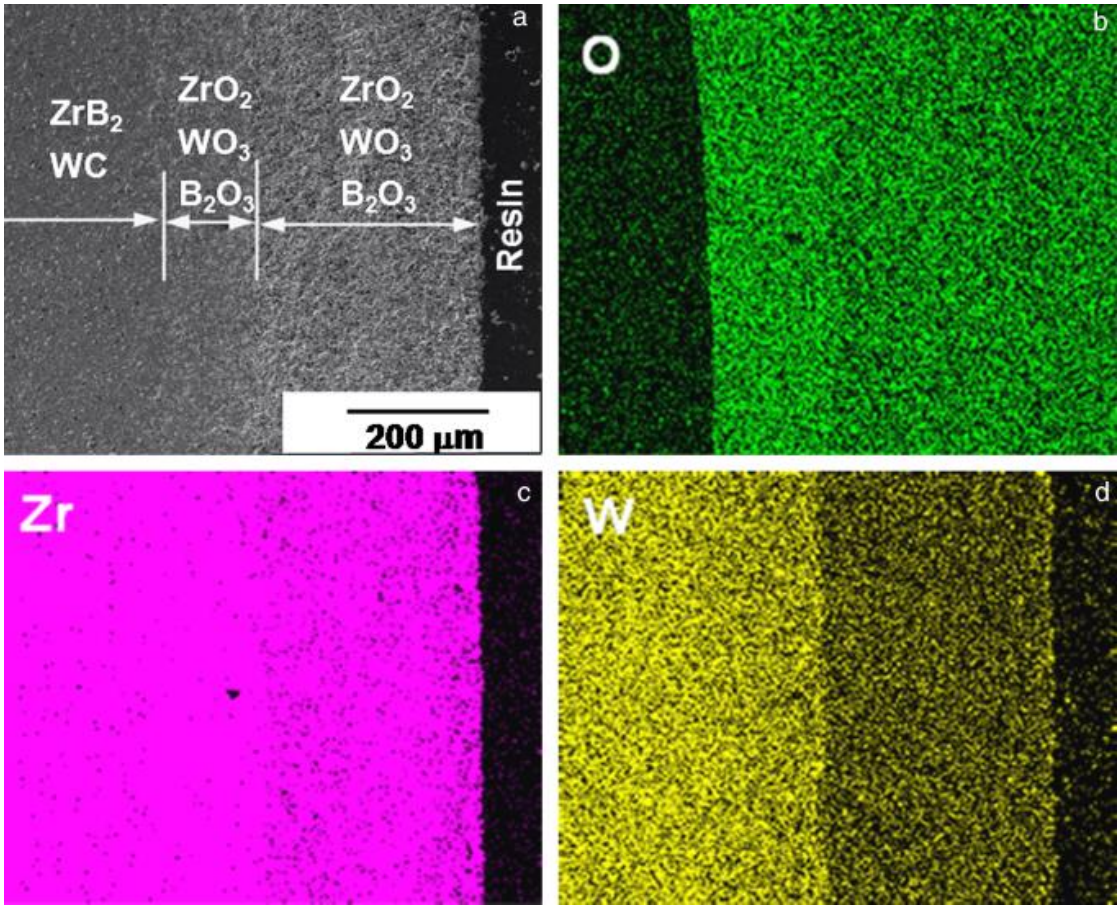

Figure 2.29 Cross-section (a) of ZrB_2-6 mol% WC oxidized at 1600°C for 3 h along with EDS element maps for O (b), Zr (c), and W (d). The SEM image showed a two-layer oxide scale. The EDS maps showed that the outer scale had lower W (d) and O (b) contents than the inner layer, indicating depletion of WO_3 and probably B_2O_3 from the outer layer [173]

Although ZrB_2 and HfB_2, both have significantly better oxidation protection than other diborides such as TiB_2, TaB_2 and NbB_2 [40], small amounts of the latter were added to ZrB_2 and HfB_2 to modify the structure of the crystalline oxide scale. Opila et. al [232] added TaB_2 into HfB_2 and reported an increase in oxide scale density at 1500°C compared with phase-pure HfB_2. This was attributed to

the tantalum-stabilized zirconia circumventing the tetragonal/monoclinic phase transformation and reducing cracking and spalling of the oxide scale [233]. However, a potential issue with the use of tantalum compounds is caused by the formation of the intermediate $Ta_2O_5 \cdot 6ZrO_2$ phase, which has a lower melting point than either oxide.

Based on the static furnace oxidation test results discussed in this chapter, even though the oxidation mechanisms of ZrB_2 and HfB_2 with various dopants have been investigated, it is still difficult to conclude which additives show the most improvement. Some additives, such as SiC, only work over limited temperature ranges, e.g. 1100-1600°C.

Table 2.11 Comparison of the oxidation behaviours of some refractory borides based ceramics

Materials	Mass gain /mg cm^{-2}	Temperature /°C	Reference
ZrB_2	11	1500	[19]
TaB_2	20	1500	[234]
TaB_2+20 vol% SiC	4	1450	[235]
ZrB_2+20 vol% SiC	2.7	1400	[154], [222]
ZrB_2+20 vol% $MoSi_2$	6.5	1400	[231]
ZrB_2+4 mol% WC	8	1600	[19]
ZrB_2+20 vol% SiC+ 10 vol% TaB_2	1.5	1400	[236]

The mass gain of ZrB_2- and TaB_2-based ceramics at different temperatures are summarized in Table 2.11 for comparison. The results again proved that the additives can significantly improve the oxidation resistance of ZrB_2. It should be noted that the higher mass gain for ZrB_2–$MoSi_2$ and ZrB_2-WC was attributed to retention of Mo and W in the oxide scale as compared to SiC, which releases carbon as CO during oxidation [231]. Therefore, added mass gain may not be an indication of more severe oxidation. The maximum testing temperature of these static testing methods is reported as 2100°C due to the limitation of the

working temperature of heating elements [107], [226]. Since the specimen can be maintained at a high temperature for as long as the furnace will allow, the static methods are suitable for understanding the oxidation mechanism and the oxidized products of the UHTC materials.

2.6.3.2 Arc-jet testing

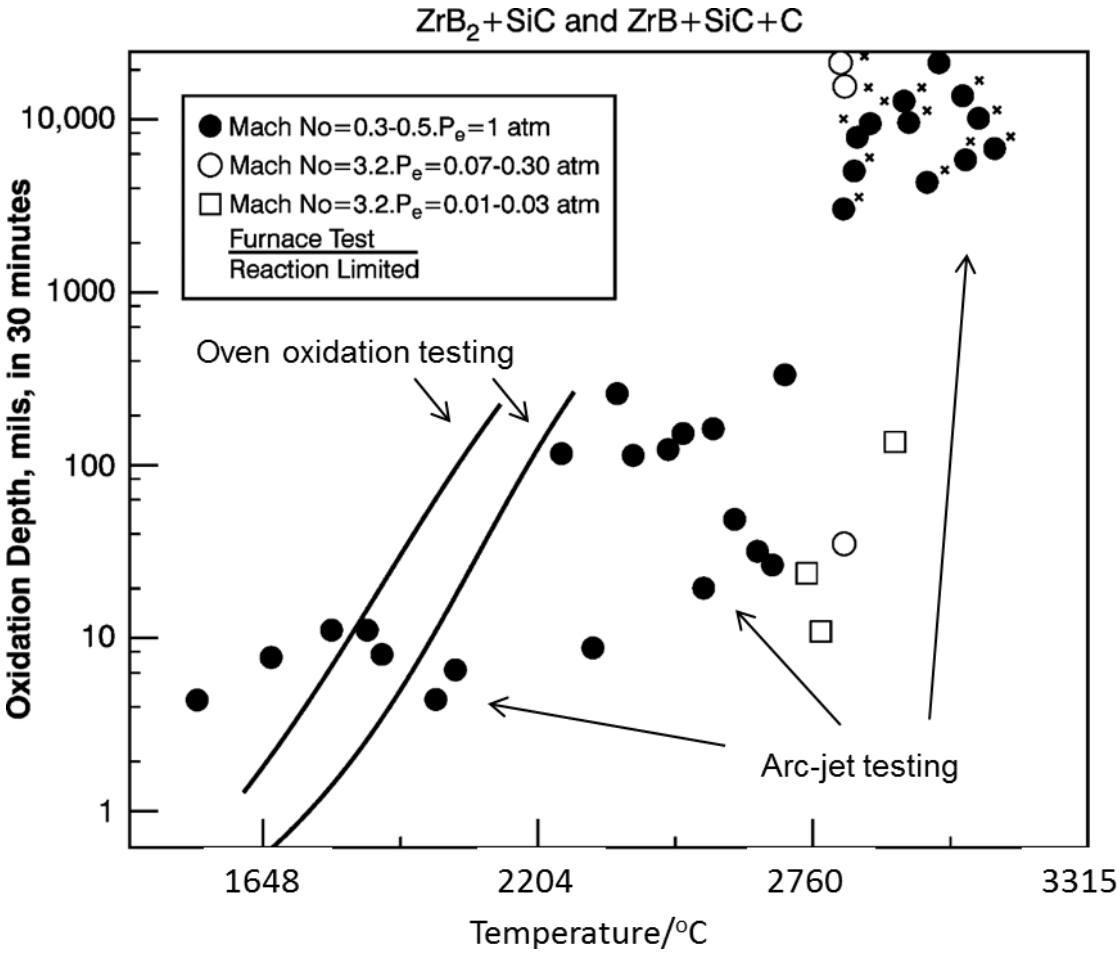

Figure 2.30 Simulation of hypersonic flow conditions in arc-jet testing [236]

The arc-heater facilities reported are capable of generating heat fluxes in the range of 2 - 14 MW m^{-2} and reaching a maximum temperature of 2400°C with a maximum duration of 10 min [10], [20], [34], [35]. The oxidation behaviour of various ZrB_2 and HfB_2 based composites measured by arc-jet testing exhibited

similar oxidation mechanisms as by static furnace oxidation, but the former exhibited lower oxidation rates [33], [35], [177], [237], [238]. For example, as shown in Figure 2.30, ZrB_2-SiC exhibits better oxidation resistant (with a thinner oxidized layer) under arc-jet testing than after oven oxidation testing [236], [237]. Parthasarathy et. al [10] claimed the reason was due to the presence of sharp thermal gradients in the specimen and the blow-off of the surface oxides during arc-jet testing reduced the measured thickness of oxide scale.

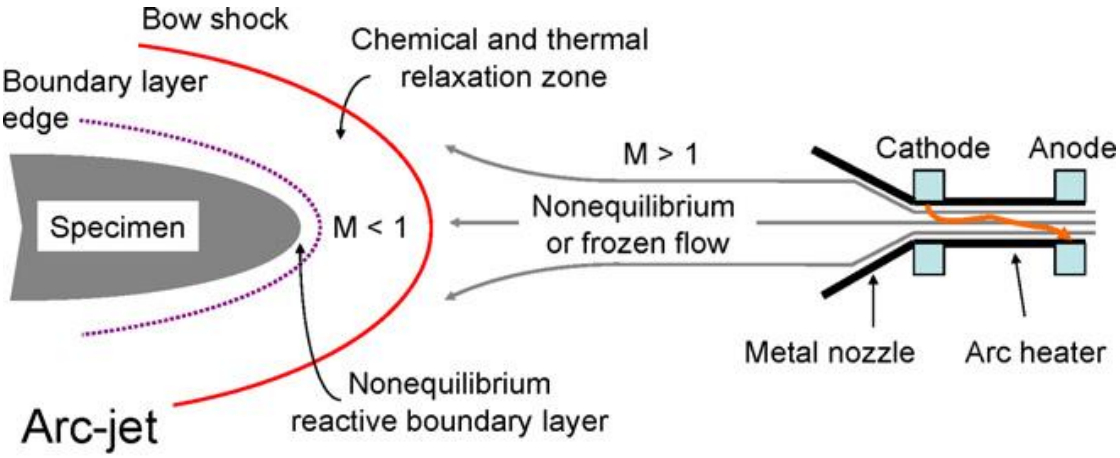

Figure 2.31 Oxidized layer thicknesses versus temperature of ZrB_2-SiC after arc-jet and oven oxidation testing [239]

In order to investigate the oxidation resistance of UHTCs under more realistic conditions for hypersonic flights, testing has been performed under simulated hypersonic flow in arc-jet facilities. These represent the best ground based simulation of a re-entry environment because of their high heat fluxes, low pressure dissociated atmosphere (i.e. O instead of O_2), and high gas velocities, despite of the cost of arc-jet testing is no less than £25K per run [20], [33]–[35], [176], [240]. The setup of an arc-jet facility is shown in Figure 2.31. In the arc-heater, current passes directly through the gas flow, which then impinges onto the surface of the specimen to be tested, achieving supersonic flow conditions, with the testing temperature reaching over 2200^{o}C. Due to the relative fluid dynamic and chemical relaxation time scales, the gas interacting directly with

the specimen is not in chemical equilibrium, resulting in a large temperature difference between the specimen and the boundary layer.

2.6.3.3 Oxyacetylene torch testing

Compared to arc-jet testing, oxyacetylene torch testing is a quick and inexpensive method to study the oxidation behaviour of UHTCs at high temperature. This technique uses a steady flow of hot gas provided by an oxyacetylene torch which generates significant heat fluxes (up to 170 W cm^{-2}) with gas velocities estimated at around Mach 1. Marra et. al [241] modelled the temperature distribution during oxyacetylene torch testing, as shown in Figure 2.32, showing that the sample temperature can be controlled by the distance from the sample to the flame.

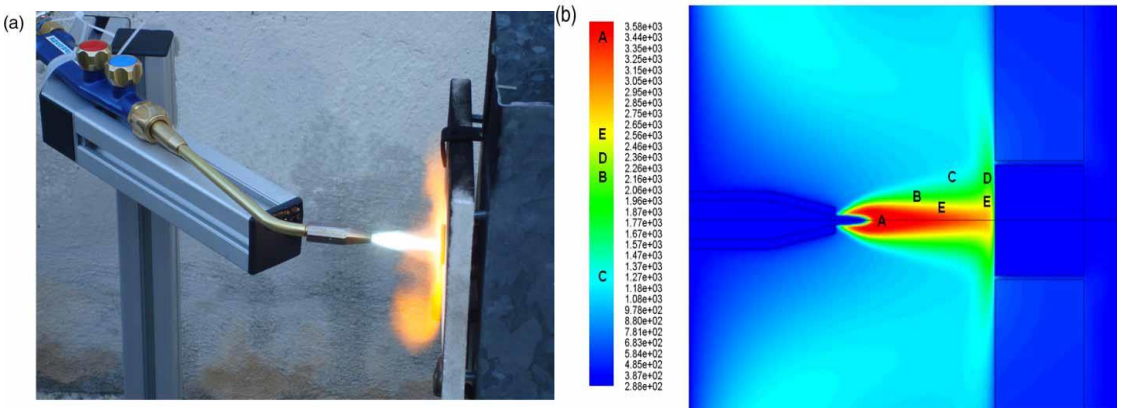

Figure 2.32 Heat flux evaluation: (a) real test and (b) simulated temperature field [241]

No ZrB_2- and HfB_2-based composites using additives other than SiC have yet been tested by this technique [36], [38], [242]. Zhang et. al [156] investigated the oxidation behaviours of ZrB_2-20 vol% SiC and ZrB_2-20 vol% SiC-10 vol% LaB_6 using oxyacetylene torch testing, which reached a peak temperature of 2400°C. Substantial enhancement of oxidation resistance was reported, as a result of the stabilization of the tetragonal ZrO_2 oxidation product and the

formation of an outer, oxygen penetration resistant $LaZr_2O_7$ layer [156]. Han et. al [37] used a similar technique to test ZrB_2-SiC composite at ~2200^oC. The materials again showed similar oxidation behaviours as static furnace oxidation.

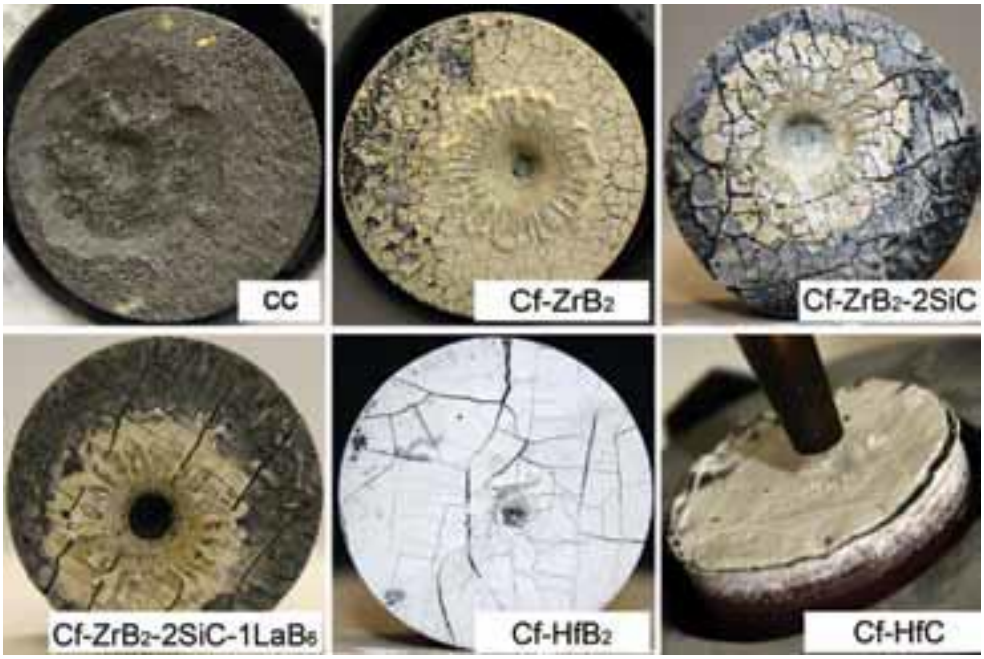

Figure 2.33 Various UHTC/carbon fibre composites after 60 s oxyacetylene testing. Diameter of the composites was 30 millimetres [14]

Paul et. al [14] reported an oxyacetylene-torch-testing, that heated specimens up to 2500^oC at a rate of 500^oC/s by employing an oxygen rich oxyacetylene flame (the ratio of acetylene: oxygen is 1:1.35) to ablate the specimen surface. ZrB_2, HfB_2, HfC, ZrB_2-20 vol% SiC and ZrB_2-20 vol% SiC-10 vol% LaB_6 carbon preform composites were tested at the maximum temperature for 60 s, as shown in Figure 2.33. The thermal shock resistance of all the composites except Cf-HfC was found to be excellent and Cf-HfB_2 exhibited the best oxidation resistance. However, the LaB_6 or SiC addition did not show any improvement in the resulting oxidation resistance compared to the pure ZrB_2 impregnation. This could be due to the ablation of the liquid La-containing oxide phase during the oxyacetylene torch test. Recently, the maximum testing temperature for the

oxyacetylene torch test apparatus at UoB was found reaching ~2800°C for HfB_2-based sample and the emphasis of UoB's research has moved to preparing HfB_2/carbon preform composite with complex shape for the test.

2.6.3.4 Other oxidation testing facilities

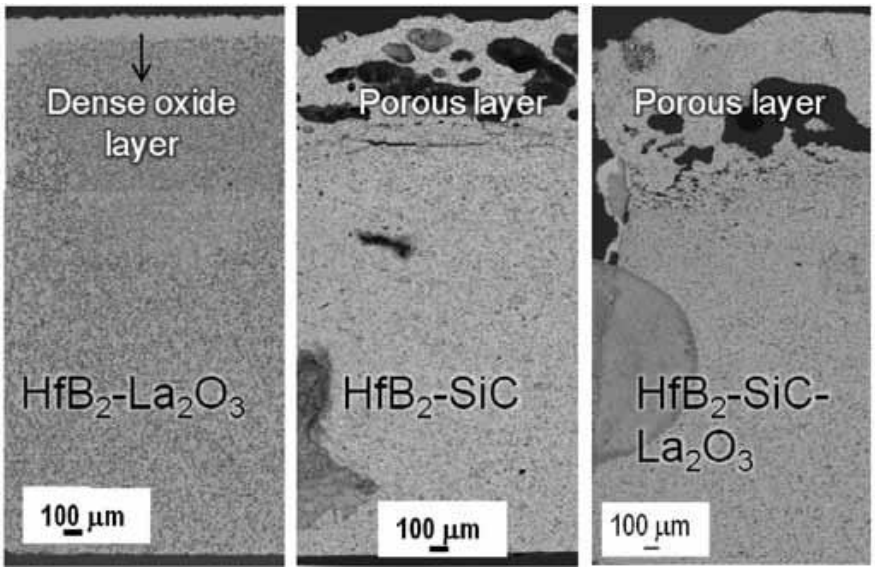

Figure 2.34 SEM images of cross section of three samples laser tested at 44 MW m^{-2} for 1 second using a defocused ytterbium laser [243].

Laser testing has also been used to evaluate the high-temperature performance of UHTCs [178], [243], [244]. The Institute for Trans Uranium Element (ITU) in Karlsruhe, Germany, developed a technique with a 4.5 kW Nd:YAG laser for melting and a second low power Ar laser to detect oscillations from the surface liquid to reveal the onset of melting for studying the oxidation behaviour of materials [245]. Rapid heating rates and extremely high testing temperatures, e.g. 4000°C, can be achieved with the method [243]. Jayaseelan et. al [243] reported laser testing of HfB_2 and HfB_2-20vol% SiC with and without 2 wt% LaB_6 additions. The laser testing was carried out using an extremely high heat flux of 44 MW m^{-2} and temperatures >3000°C but no gas flow. All the specimens,

except HfB_2-LaB_6, were severely damaged, losing their shape and uniformity after 1s laser testing. The cross section analysis of the specimen revealed the formation of a dense oxide layer in HfB_2-LaB_6 that effectively reduced oxygen penetration, Figure 2.34. Note that solar energy has also been used as an alternative heating method, heating a ZrB_2-SiC-Si_3N_4 sample to ~2000^oC [246].

Table 2.12 Comparison of the ground based testing facilities for UHTCs

Testing method	Heating mode	Maximum temperature /^oC	Maximum heat flux /MW m^{-2}	Atomic oxygen	High speed gas flow
High-temperature furnace [226]	Radiative & convective	2100	n/a	Poor	n/a
Oxyacetylene torch [238]	Convective	>2500	>8	Poor	Fair
Solar [246]	Radiative	>2600	3-8	Poor	n/a
Laser [243]	Radiative & convective	>3000	>40	Poor	n/a
Arc-jet plasma tunnel [33]	Convective /some radiative	2200	>3	Good	Good

According to the comparison of various oxidation methods, Table 2.12, the main advantage of laser and solar energy testing compared to static furnace oxidation is the higher maximum temperature they can provide. It can be concluded the arc-jet plasma tunnel shows the best simulation of the re-entry environment and the oxyacetylene torch testing, to some extent, is capable of providing high speed gas flow along with high heat flux.

2.6.4 Physical properties of UHTC composites

The thermal conductivity is a key physical property of UHTCs required for hypersonic applications, as good thermal conductivity can minimize the thermal

gradient of the UHTC component and reduces its surface temperature. Most previous studies [65], [247]–[249] have measured room temperature (RT) thermal conductivity using the radial heat flow method, showing that the thermal conductivity of ZrB_2 and HfB_2 based ceramics is ~100 W ms^{-1}, which is higher than that of other refractory carbides and oxides. The high temperature conductivities of UHTCs can be measured by laser flash techniques, which measures the thermal expansion coefficient, specific heat capacity and thermal diffusivity of the samples to calculate their thermal conductivity values, at temperatures lower than 2000°C [250]–[254]. Zimmermann et. al [254] observed that the addition of SiC reduced the thermal conductivity of ZrB_2 at temperatures close to 1550°C, as shown in Figure 2.35. Researchers from Imperial College London [250] reported a similar thermal conductivity change for ZrB_2 and ZrB_2-20 vol% SiC from 1500°C to 1900°C. The reduced conductivity may be due to the CTE mismatch of ZrB_2 and SiC, causing loss of contact between ZrB_2 and SiC grains during the thermal conductivity measurement.

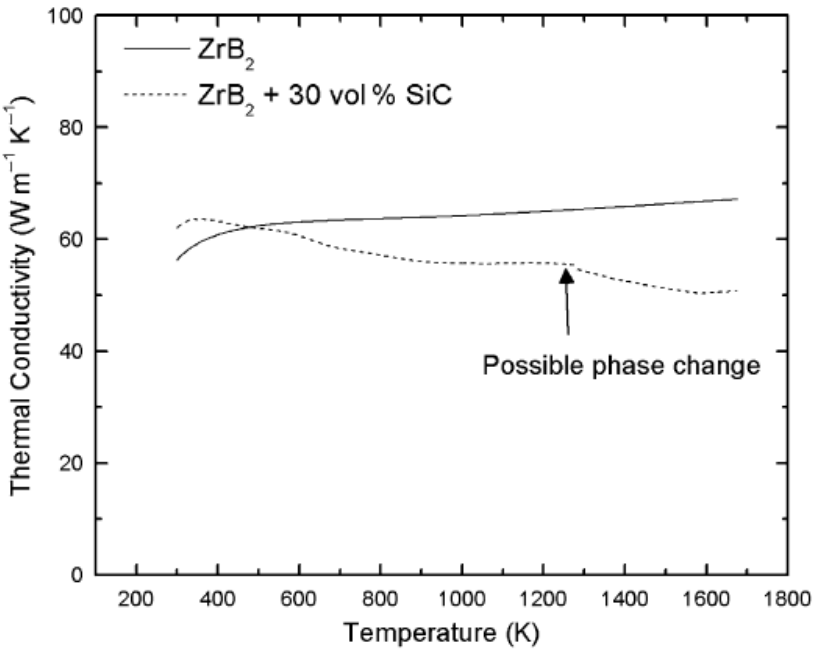

Figure 2.35 Thermal conductivity as a function of temperature for ZrB_2 and ZrB2-30 vol% SiC [254]

Like most ceramics, higher strengths are reported for diborides with finer grain sizes [255], [256]. Hence, additives such as SiC, $MoSi_2$, which reduce the densification temperature and grain size of ZrB_2 and HfB_2, can significantly improve the mechanical properties of the borides [76], [77]. Chamberlain el al. showed that hot-pressed pure-phase ZrB_2 had a strength of 565 MPa and the addition of 10, 20 or 30 vol% SiC or $MoSi_2$ reduced the average grain size to 2-3 μm, which increased strength to 700-1000 MPa, all based on room temperature testing. In fact, in a fine-grained ZrB_2-SiC composite, the grain size of SiC rather than ZrB_2 is more important in controlling the strength of the composite [76], [77]. The reason is that the smaller SiC particles reduce the tendency for microcracking and the nucleation of larger, critical flaws.

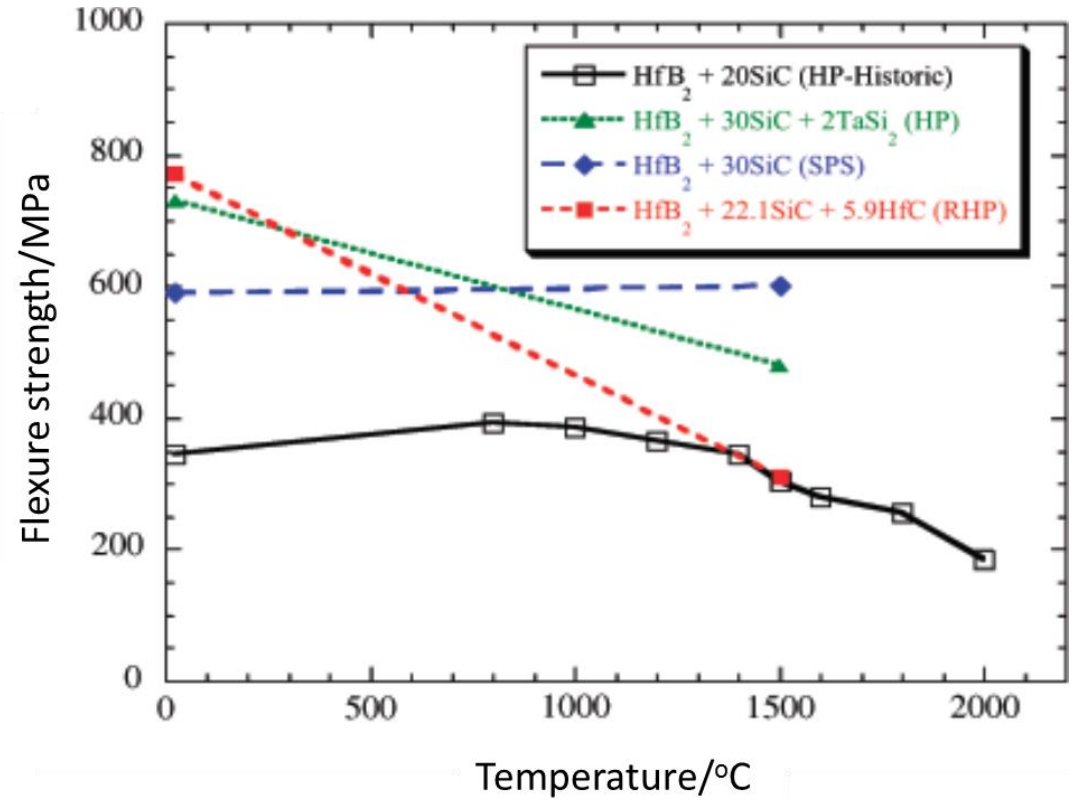

Figure 2.36 Flexure strength as a function of test temperature for hafnium diboride (HfB_2) containing 20-30 vol% SiC. The HfB_2-based samples were densified by various sintering techniques [219]

The room temperature elastic modulus, ~480 GPa, and Vickers hardness, ~28 GPa, toughness values for HfB_2 were discussed before in Table 2.3. The effect of adding SiC and $MoSi_2$ on the elastic modulus and hardness of ZrB_2 and HfB_2 is dependent on the mechanical properties of the additives themselves, e.g. E_{SiC} ~ 475 GPa, E_{MoSi2} ~ 440 GPa, Hv_{SiC} ~ 28 GPa, Hv_{MoSi2} ~ 9 GPa [257], [258], hence it scales with the volume fraction of the additive [259]. The fracture toughness of ZrB_2 was reported to increase from 3.5 MPa $m^{1/2}$ to 5.3 MPa $m^{1/2}$ by adding 30 vol% SiC, because the ZrB_2 grains was found typically failed in a transgranular manner and cracks deflected at or near ZrB_2-SiC interface [85].

However, the high temperature strength is the main concern for UHTC applications as any additives will also get oxidized at elevated temperature. According to Figure 2.36, the HP-ed HfB_2-based composites show a significant loss of strength above 1500^{o}C, while the SPS-ed composites maintain their room temperature strength up to 1500^{o}C. Monteverde et. al [32]. [160] claimed that the reduced strength is caused by the oxide impurities forming at grain boundary phases. The electrical discharge used in SPS could promote breakdown of the non-conductive oxides on the surface of the particles [260].

As a conclusion, the development of UHTCs is faced with a lot of challenges including material synthesis and ultra-high temperature testing methods. In fact, there isn’t any UHTC protection system being used for hypersonic application yet, so any improvement is good for the research of UHTCs. Therefore, a chemically modified HfB_2 system was investigated in this work, involving UHTC powder synthesis, various sintering methods and ultra-high temperature characterization techniques.

3. Experimental

This chapter deals with the details of the synthesis of HfB_2-based powders, the densification of the powders yielded and the characterisation of the sintered ceramics.

3.1 Raw materials

The chemicals used in this research and their suppliers are listed in Table 3.1.

Table 3.1 The chemicals used in this project and their suppliers

Chemicals	Details	Suppliers
Hafnium tetrachloride	Powder, chemical formula $HfCl_4$, purity: 98%	Sigma-Aldrich, UK
Boric acid	Powder, chemical formula H_3BO_3, purity: >99.5%	Fisher Scientific, UK
Boron	Powder, amorphous B, purity: 95-97%	Fisher Scientific, UK
Ethanol	Absolute ethanol, C_2H_5OH, purity: >99.9%	Fisher Scientific, UK
Powder phenolic resin (PPR)	Novolak phenolic resin, $[(HOC_6H_4)_2CH_2]_n$, carbon content: 51 wt%	Crios resins, SI group, Inc, Brazil
Graphite	Powder, C, <20 μm, synthetic	Fisher Scientific, UK
Yttrium nitrate hexahydrate	Linear formula $Y(NO_3)_3 \cdot 6H_2O$, purity: 99.8%	Sigma-Aldrich, UK
Tantalum pentachloride	Linear formula $TaCl_5$, purity: >99.8%	Sigma-Aldrich, UK
Argon	Pureshield argon, purity: >99.99%	BOC, UK
Ammonia hydroxide solution	>25% in H_2O	Sigma-Aldrich, UK

3.2 Characterisation of raw materials

The carbon content of PPR was 51%, which was obtained from the char weight percentage of this material, measured by TGA in argon at temperature of 1000^{o}C.

$$HfCl_4 + H_2O \rightarrow HfClO_2 \cdot nH_2O + HCl \quad (2\text{-}1)$$

Hafnium chloride was easily hydrated when reacting with moisture to form $HfOCl_2 \cdot nH_2O$ ($0<n<8$) according to Equation 2.1, i.e. $HfCl_4$ was partially hydrated as soon as it was in contact with air [261]. Since the structure of partially hydrated $HfCl_4$ was difficult to predict, all the $HfCl_4$ was fully hydrated to a hydration rate of n=8 by exposing the $HfCl_4$ powder to air for 24 hours to form $HfOCl_2 \cdot 8H_2O$ (the presence of $HfOCl_2 \cdot 8H_2O$ was confirmed by XRD analysis), to improve the consistency in stoichiometric calculation of HfB_2-based ceramic preparation.

3.3 Preparations of HfB_2-based ceramic powders

3.3.1 Borothermal reduction reaction-precursors

According to Equation 2.2, phase-pure HfB_2 powder is synthesized by a borothermal reduction reaction using $HfOCl_2 \cdot 8H_2O$ and amorphous boron powder as the respective hafnium and boron sources.

$$HfOCl_2 \cdot 8H_2O(s) \xrightarrow{\triangle} HfO_2(s) \xrightarrow{+4B(s)} HfB_2(s) + 2BO(g) \quad (2\text{-}2)$$

The stoichiometry of starting powders, which significantly affected the purity of final products, was calculated as follows:

To obtain 1 g monolithic HfB_2:

$$\text{weight of } HfOCl_2 \cdot 8H_2O = \frac{1\text{g} \times \text{molecular weight (Mw) of } HfOCl_2 \cdot 8H_2O}{\text{Mw of } HfB_2 \times \text{purity of } HfOCl_2 \cdot 8H_2O}$$

$$= \frac{1\text{g} \times 409.5}{200.1 \times 98\%} = 2.09\text{g}$$

$$\text{weight of B} = \frac{1\text{g} \times \text{Mw of B}}{\text{Mw of } HfB_2 \times \text{purity of B}} \times \text{B: Hf ratio}$$

$$= \frac{1\text{g} \times 10.8}{200.1 \times 96\%} \times 4 = 0.22\text{g}$$

The effect of the non-stoichiometric amount of boron on the purity and morphology of the HfB_2 powders yielded was also investigated. Hence, the amount of boron powders required for B:Hf ratios of 3:1 and 5:1 were 0.17 g and 0.28 g, respectively.

Phase-pure TaB_2 powder was synthesized according to Equation 2.3.

$$2TaCl_5(s) \rightarrow Ta_2O_5(s) \xrightarrow{+9B(s)} 2TaB_2(s) + 5BO(g) \quad (2\text{-}3)$$

The stoichiometric calculation for obtaining 1 g of the TaB_2 powders was as follows:

$$\text{weight of } TaCl_5 = \frac{1\text{g} \times \text{Mw of } 2TaCl_5}{\text{Mw of } 2TaB_2 \times \text{purity of } TaCl_5}$$

$$= \frac{1\text{g} \times 716.4}{405.0 \times 99.8\%} = 1.77\text{g}$$

$$\text{weight of B} = \frac{1\text{g} \times \text{Mw of B}}{\text{Mw of TaB}_2 \times \text{purity of B}} \times \text{B: Ta ratio}$$

$$= \frac{1\text{g} \times 10.8}{202.5 \times 96\%} \times 4.5 = 0.25\text{g}$$

To obtain 1 g TaB_2-doped HfB_2 powders, the stoichiometric calculation is shown below; 10 wt% TaB_2 doped HfB_2 is used as an example. The amount of the starting materials required to synthesize 5 and 15 wt% TaB_2 doped HfB_2 was calculated using the same equations.

$$\text{weight of HfOCl}_2 \cdot 8\text{H}_2\text{O} = 90\% \times \text{weight of HfOCl}_2 \cdot 8\text{H}_2\text{O to obtain 1 g HfB}_2$$

$$= 90\% \times 2.09\text{g} = 1.88\text{g}$$

$$\text{weight of TaCl}_5 = 10\% \times \text{weight of TaCl}_5 \text{ to obtain 1 g TaB}_2$$

$$= 10\% \times 1.77\text{g} = 0.18\text{g}$$

$$\text{weight of B} = 90\% \times \text{weight ofB to obtain 1 g HfB}_2 +$$

$$10\% \times \text{weight of B to obtain 1 g TaB}_2$$

$$= 90\% \times 0.22\text{g} + 10\% \times 0.24\text{g} = 0.22\text{g}$$

All the precursors prepared for borothermal reduction reaction and their corresponding sample names are listed in Table 3-2. The process to prepare HfB_2 precursor powders is shown in Figure 3.1. $HfOCl_2{\cdot}8H_2O$ was used as the Hf source and dissolved in ethanol to achieve a given ratio, viz. 1 g per 30 ml ethanol. The resulting transparent $Hf(OR)_4$† solution and ammonia hydrate solution (NH_3OH, 35%) were simultaneously added drop-wise into a beaker with deionized water, while continuous stirring was applied to maintain the pH at ~8.5 ($\pm$0.3) to promote the formation of white $Hf(OH)_4$ precipitates. The effect of the

† R=C_2H_5

pH values on the precipitate formation was investigated and will be discussed in Chapter 4. The resultant precipitates were filtered and rinsed at least 3 times with deionized water (pH~5.6) to remove NH_4R residues and then the rinsed precipitates were dispersed in 50 ml ethanol (EtOH). Boron powders were also added to the $Hf(OH)_4$/EtOH suspension, followed by ultrasonication for 10 min via a KS150 ultrasonicator ‡ (Kerry Ultrosonics Ltd., Skipton, UK). The B+$Hf(OH)_4$/EtOH suspension was dried at 100^{o}C for 24 h in an oil bath with a magnetic stirrer running all the time. The resultant dried mass was gently ground using a pestle and mortar and then sieved to remove agglomerates with a particle size larger than 100 μm.

Table 3.2 Composition of the precursors used for borothermal reduction

Samples	**Elemental Stoichiometry**			**Remarks**
	Hf	B	Ta	
3HfB	1	3	-	Boron 25% less than stoichiometric, as Equation 2-2
4HfB	1	4	-	Exact stoichiometry, as Equation 2-2
5HfB	1	5	-	Boron 25% excess B, as Equation 2-2
TaB	-	4.5 (B:Ta)	1	Exact stoichiometry, as Equation 2-3
5TaHfB	0.95	4	0.05	Exact stoichiometry, 5 wt% Ta-dopants
10TaHfB	0.9	4	0.1	Exact stoichiometry, 10 wt% Ta-dopants
15TaHfB	0.85	4	0.15	Exact stoichiometry, 15 wt% Ta-dopants

‡ This is a probe ultrasonicator working at the power of 75 W and the amplitude of 14 mm. The output power and amplitude were kept the same for all the ultrasonic dispersions involved in this study.

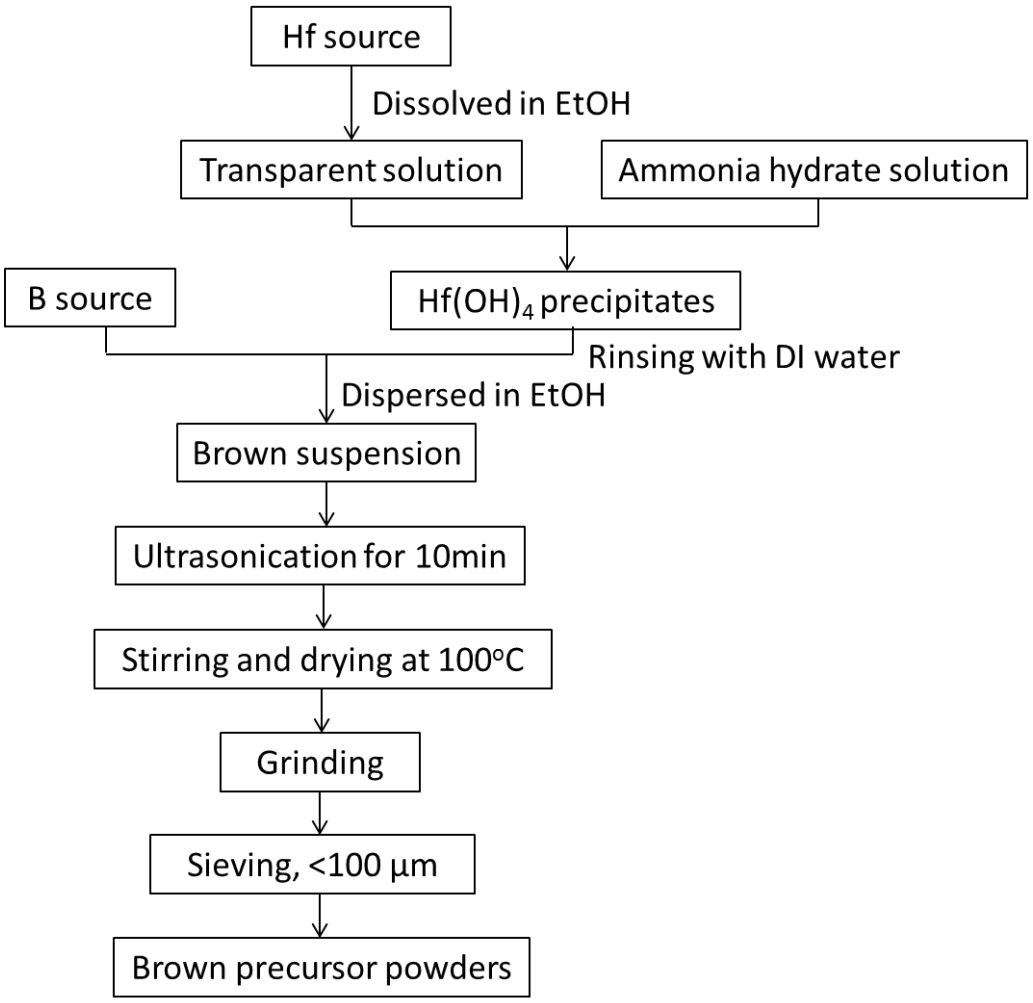

Figure 3.1 Flowchart of preparing HfB_2 precursor powders

The process to prepare TaB_2 precursor powders was exactly the same as that for preparing the HfB_2 precursor powders, but using $TaCl_5$ instead of $HfOCl_2 \cdot 8H_2O$ as the Ta source. As $TaCl_5$ can react with moisture to form $Ta(OH)_5$ before processing, the $TaCl_5$ powder was kept in a desiccator and anhydrous EtOH was used as the solvent. The process to prepare Ta-doped HfB_2 precursor powders is also quite similar. The stoichiometric amount of $HfOCl_2 \cdot 8H_2O$ and $TaCl_5$, as shown in Table 3.2, were dissolve in EtOH to obtain a transparent Hf-Ta mixture solution. The subsequent procedures were the same as that for preparing HfB_2 precursor powders.

3.3.2 Carbothermal reduction reaction precursors

According to Equation 2.4, another method to synthesize phase-pure HfB_2 powder is the carbothermal reduction reaction, which involved $HfOCl_2{\cdot}8H_2O$, boric acid (H_3BO_3) and phenolic resin as the respective hafnium, boron and carbon sources.

$$HfOCl_2 \cdot 8H_2O(s) \rightarrow HfO_2(s) \xrightarrow{+B_2O_3(s) + 5C(s)} HfB_2(s) + 5CO(g) \quad (2\text{-}4)$$

The stoichiometric elemental ratio of Hf:B:C for carbothermal reduction reaction is 1:2:5, thus the stoichiometric calculation for obtaining 1 g of HfB_2 powder was as follows:

$$\text{weight of } HfOCl_2 \cdot 8H_2O = \frac{1\text{g} \times \text{molecular weight (Mw) of } HfOCl_2 \cdot 8H_2O}{\text{Mw of } HfB_2 \times \text{purity of } HfOCl_2 \cdot 8H_2O}$$

$$= \frac{1\text{g} \times 409.5}{200.1 \times 98\%} = 2.09\text{g}$$

$$\text{weight of } H_3BO_3 = \frac{1\text{g} \times \text{Mw of } H_3BO_3}{\text{Mw of } HfB_2 \times \text{purity of } H_3BO_3} \times \text{B: Hf ratio}$$

$$= \frac{1\text{g} \times 62}{200.1 \times 99.5\%} \times 2 = 0.62\text{g}$$

$$\text{weight of PPR} = \frac{1\text{g} \times \text{Mw of C}}{\text{Mw of } HfB_2 \times \text{carbon content in LPR}} \times \text{C: Hf ratio}$$

$$= \frac{1\text{g} \times 12}{200.1 \times 52\%} \times 5 = 0.59\text{g}$$

In order to investigate the effect of boron loss (due to the evaporation of B_2O_3 at temperature above 1200°C) on the purity and microstructure of the HfB_2 powders yielded, excess B_2O_3 was needed, hence different molar ratios of

Hf:B:C was used, i.e.1:3:5 and 1:4:5. The stoichiometric ratio of 1:2:5 of Hf:B:C did not result in single phase HfB_2 powders, see section 4.2.1. In this case, the corresponding amount of boric acid required was 0.93 g and 1.24 g, respectively.

To obtain 1 g Y-doped HfB_2, 8 wt% yttrium nitrate hexahydrate was added into the system, its stoichiometric mass was calculated as follows:

$$\text{weight of } Y(NO_3)_3 \cdot 6H_2O = \frac{1\text{g} \times \text{Mw of } Y(NO_3)_3 \cdot 6H_2O}{\text{Mw of } HfB_2} \times \text{wt\% Y}$$

$$= \frac{1\text{g} \times 383}{200.1} \times 8\% = 0.15\text{g}$$

Table 3.3 Composition of the precursors used for carbothermal reduction

Samples	Elemental ratio					Remarks
	Hf	B:Hf	C:Hf	Y:Hf	Ta:Hf	
HfBC	1	2	5	-	-	Exact stoichiometry, according to Equation 2-3
Hf3BC	1	3	5	-	-	50% excess B, according to Equation 2-3
Hf4BC	1	4	5	-	-	100% excess B, according to Equation 2-3
8YHFBC	0.92	3	5	0.08	-	8 wt% Y-dopants
5TaHfBC	0.95	3	5	-	0.05	5 wt% Ta-dopants
10TaHfBC	0.9	3	5	-	0.1	10 wt% Ta-dopants
15TaHfBC	0.85	3	5	-	0.15	15 wt% Ta-dopants

In the next series of experiments, 5, 10 and 15 wt% $TaCl_5$ were added into the system to obtain Ta-doped HfB_2. The stoichiometric mass of $TaCl_5$ to obtain 1 g Ta-doped HfB_2 was calculated as follows, again using 10 wt% Ta-dopants as an example;

$$\text{weight of } TaCl_5 = \frac{1\text{g} \times \text{Mw of } TaCl_5}{\text{Mw of } HfB_2} \times \text{wt\% Ta}$$

$$= \frac{1\text{g} \times 358.2}{200.1} \times 10\% = 0.18\text{g}$$

Similarly, the mass of $TaCl_5$ required for the synthesis of 5 and 15 wt% Ta-doped HfB_2 was 0.09 and 0.27 g, respectively. The corresponding mass of $HfOCl_2 \cdot 8H_2O$ required for the synthesis of 5, 10 and 15 wt% Ta-doped HfB_2 was 1.99, 1.88 and 1.78 g. All the precursors prepared for carbothermal reduction reaction are listed in Table 3.3.

3.3.2.1 Sol-gel approach to prepare pre-ceramic powders

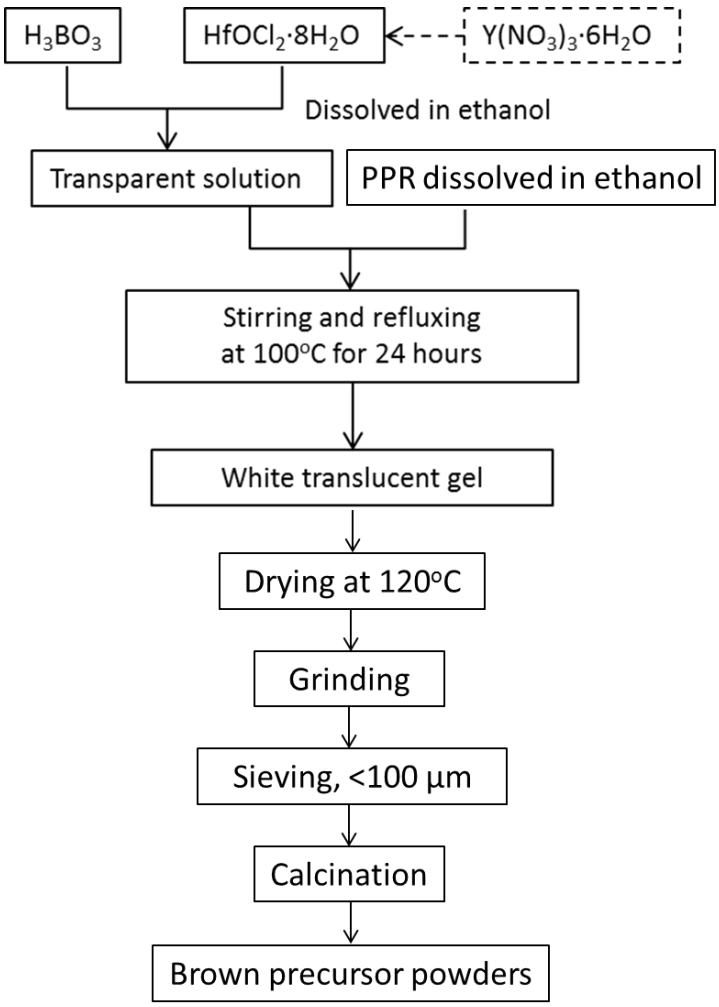

Figure 3.2 Flow chart of mixing different starting powders in sol-gel approach

The sol-gel approach which was developed by Venugopal et. al [141] for the synthesis of HfB_2 pre-ceramic powders, was used in the early stage of this project to prepare HfB_2 and Y-doped HfB_2 pre-ceramic powders.

In order to prepare the HfB_2 pre-ceramic powders by the sol-gel approach, as shown in Figure 3.2, boric acid was placed in a 500 ml flask and 50 ml of ethanol per gram of boric acid was added to achieve a solution. A heated oil bath held at 100^{o}C was used to increase the solubility of boric acid. Subsequently, $HfOCl_2 \cdot 8H_2O$ was dissolved in ethanol (1 g per 30 ml ethanol) and added into the boric acid solution. Mechanical stirring was applied for half an hour to improve the homogeneity of the solution. Then, PPR/ethanol solution (1 g per 30 ml ethanol) was added into the binary transparent solution. The latter turned yellow with a white translucent gel after stirring and refluxing at 100^{o}C for 24 h. For the preparation of 8 wt% Y-doped HfB_2 pre-ceramic powders, yttrium nitrate hexahydrate (soluble in ethanol), was directly dissolved into the ternary solution (Hf, B and C) to achieve good mixing.

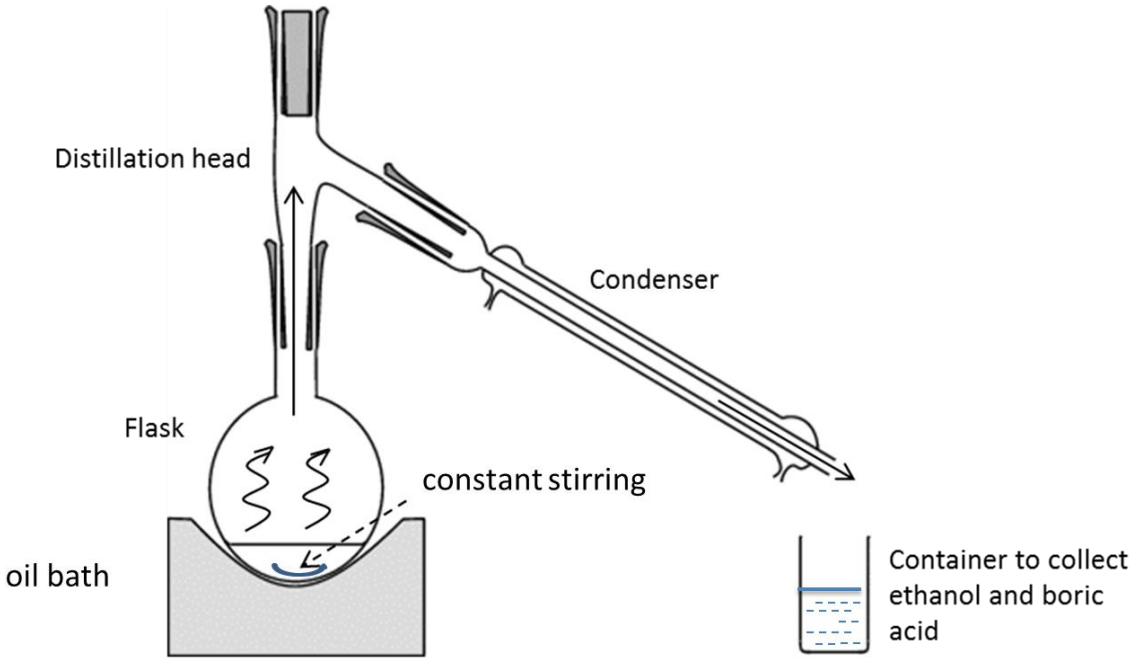

Figure 3.3 Schematic of the experimental system used for the sol-gel approach

The gel yielded by the sol-gel approach was dried at 120°C on a hot stage for 6 h, using the set up shown in Figure 3.3. The volatiles were collected to stop B_2O_3 going to the ventilation system, since B_2O_3 could be carried by ethanol vapour. The resulting solid precursors were gently ground using a pestle and mortar and sieved to remove the large particles. In order to remove residual chlorine ions from the precursor, the latter was calcined in a chamber furnace (RHF 1450, Carbolite, UK) in air at various temperatures and times, as listed Table 3.4, to understand the efficiency of removing Cl^- from the system.

Table 3.4 Various calcination temperatures and time for Cl- removal in HfB_2

Calcination temperatures/°C	Calcination time/h
350	1
350	3
400	1
400	3

3.3.2.2 Precipitation approach to prepare pre-ceramic powders

The precipitation approach involved $HfOCl_2 \cdot 8H_2O$, $TaCl_5$, boric acid and phenolic resin as Hf, Ta, B and C sources. To obtain phase-pure HfB_2, as shown in Figure 3.4, $HfOCl_2 \cdot 8H_2O$ was dissolved in EtOH (1 g per 30 ml ethanol) and then reacted with 35% ammonia hydrate to form white $Hf(OH)_4$ precipitates at a pH of ~8.5. The resultant precipitates were filtered, rinsed by DI water and dispersed again in EtOH. The white suspension yielded was mixed with boric acid/EtOH (1 g per 50 ml ethanol) and phenolic/EtOH solution (1 g per 30 ml ethanol), followed by ultrasonication, drying, grinding and sieving, which were similar as the procedures for the borothermal reduction reaction route. The entire process for the precipitation process was carried out in an extraction fume hood, as ammonia and HCl were produced during mixing.

For the preparation of Ta-doped HfB_2 preceramic powders, calculated amounts of $HfOCl_2 \cdot 8H_2O$ and $TaCl_5$ were dissolved in EtOH and mixed using a magnetic stirrer. The resultant transparent Ta- and Hf- binary solution was added drop-wise into 10% ammonia hydrate solution. According to the findings of this study, the key factor to improve the homogeneity of the precipitates was to make sure that the $Hf(OH)_4$ and $Ta(OH)_5$ co-precipitated at the same time. Hence, the pH value had to be controlled within a narrow range, i.e. 8.5 ± 0.3.

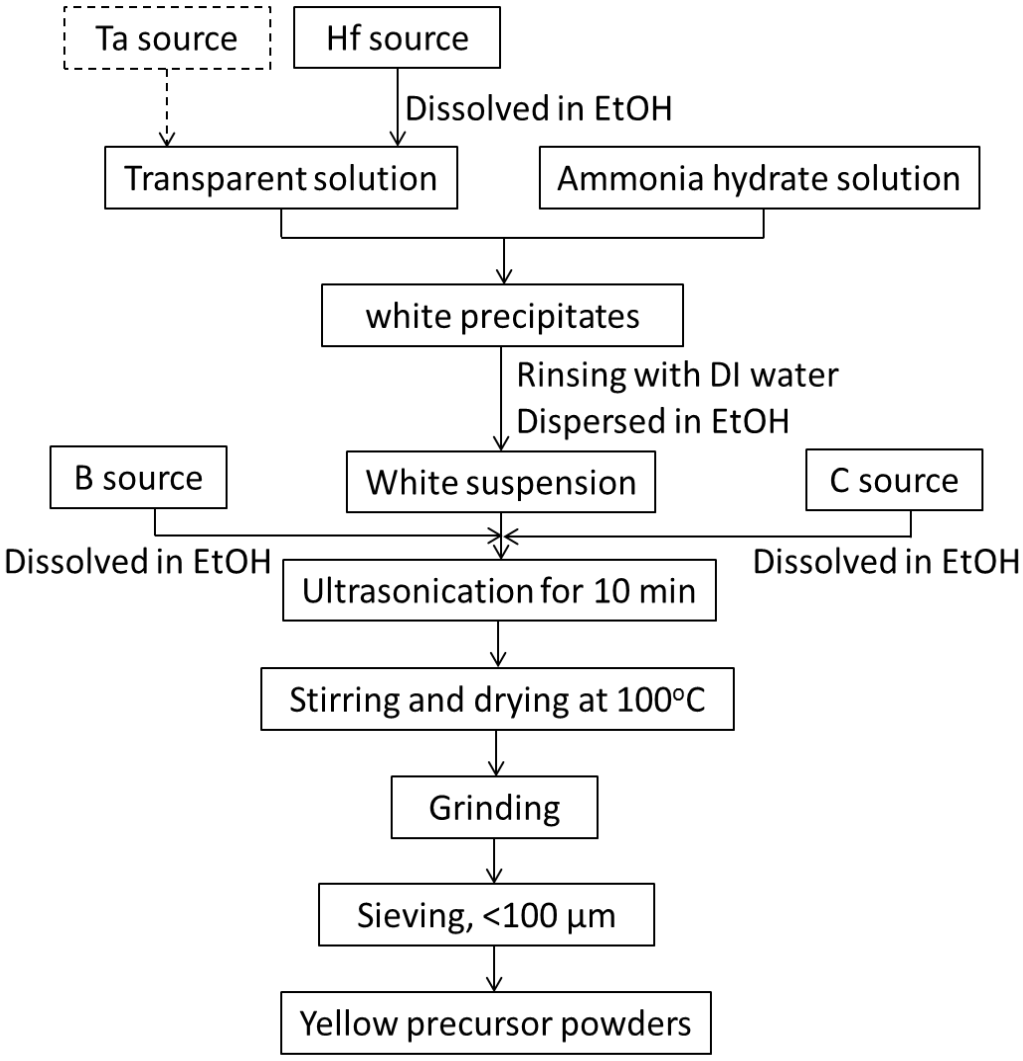

Figure 3.4 Flow chart of mixing different starting powders for precipitation approach.

3.4 Heat treatments of the precursors

The precursors from the sol-gel and the precipitation approach were converted into HfB_2 and TaB_2-based ceramic powders via borothermal reduction or carbothermal reduction reactions, which were carried out by heat treatment in a high temperature horizontal tube furnace (TSH17/75/450, Elite Thermal System Ltd, UK) fitted with an alumina tube (99.9% pure, OD x ID x L=60mm x 50mm x 120mm, Elite Thermal System Ltd, UK), as shown in Figure 3.5. Stainless steel end caps with double silicon rings were used to seal the tube. An air tight silicone oil container was connected to the outlet of the tube to prevent air ingress and to trap the bi-products of the borothermal and carbothermal reduction reactions, e.g. B_2O_3, if any from the outlet gas. Before heat treatment, the tube was evacuated to 10^{-3} Torr using a rotary pump to remove all oxygen and then Pureshield argon (>99.99%) was continuously passed through the tube at the rate of 100 cm^3min^{-1}.

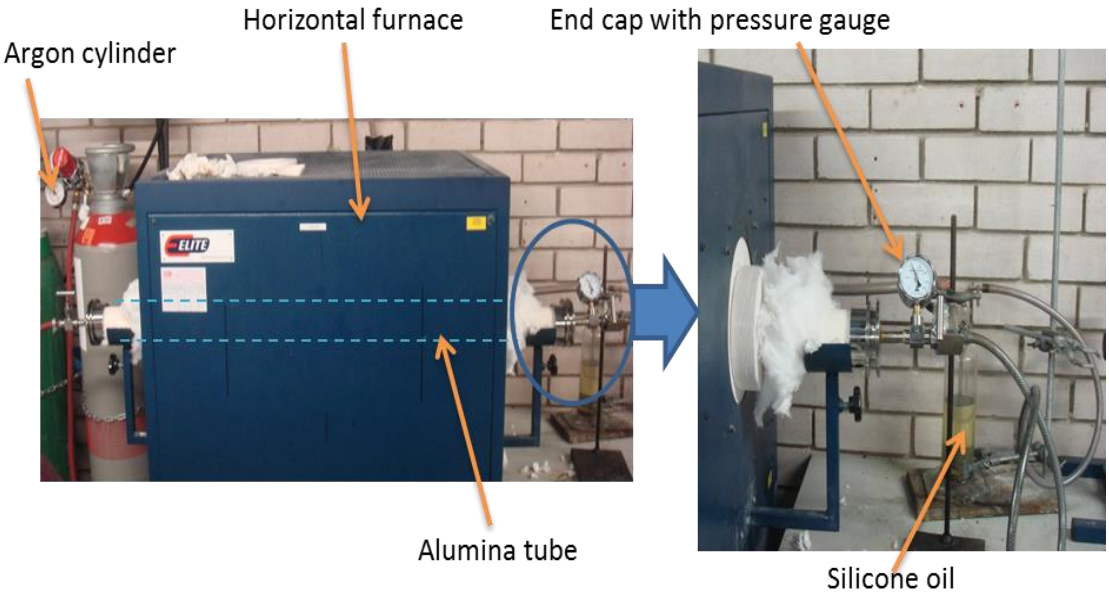

Figure 3.5 High temperature tube furnace and alumina tube used for the synthesis of HfB_2-based powders

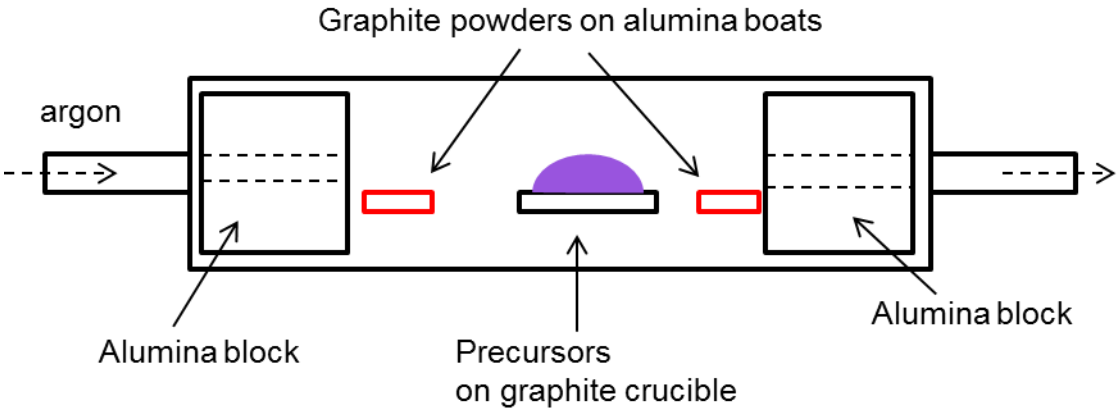

Figure 3.6 Schematic of the experimental arrangement used for the synthesis of HfB_2-based powders

Table 3.5 Various heat treatment profiles for HfB_2 powder synthesis

Heat treatment temperatures/°C	Dwell time/h
1300	25
1600	5
1600	2
1600	1

The precursor powders were placed in a graphite crucible, which was laid in the centre of the alumina tube. Alumina boats containing graphite powders placed on both sides of the precursors were used to absorb residual oxygen and to improve the purity of HfB_2 products, as shown in Figure 3.6. Alumina blocks were placed near the inlet and outlet ends to protect the tube from thermal shock and limit the heat dissipation to the end caps. It should be noted that the alumina tubes are vulnerable from thermal shock and thus the heating and cooling rates were maintained at 5°C/min at temperature below 1000°C and 2°C/min at temperatures above 1000°C in all cases. Another issue with the alumina tubes was the creep strain, which was caused by the weight of the samples and lack of support for the tube inside the heating zone of the furnace, especially at temperatures above 1500°C. Hence the tube was rotated 90° each time after

use to avoid bending. To obtain HfB_2 and TaB_2-based ceramic powders, various heat treatment temperatures and dwell times, as listed in Table 3.5, were used to study their effects on the purity and particle size of the final products.

3.5 Densification of HfB_2-based ceramics

3.5.1 Pressureless sintering of HfB_2-based ceramics

Before the microwave sintering was conducted for the HfB_2-based powders, their dielectric properties were measured at Nottingham University, with the help of Dr. Dimitrakis. The dielectric measurements involved an open-end coaxial line terminating to a probe with an annular aperture, while the other end of the coaxial line was connected to an Agilent 8753ES Vector Network Analyzer (VNA) with a frequency range 30 kHz–6 GHz. During the measurement, the powder samples were dispersed in ethanol. A swept frequency signal was transmitted from the VNA into the ethanol media via the coaxial line and the reflection coefficient Γ was recorded. The dielectric constant, ε', and loss factor, ε'', were calculated from the amplitude and the phase of Γ via a computer programme [262], for the HfB_2-based powders measured at 910 and 2470 MHz.

The microwave sintering furnace, Figure 3.7, with a maximum power output of 6 kW was designed and built by Microwave Heating Ltd. at Loughborough University. HfB_2 and 10 wt% Ta-doped HfB_2 powders were initially die pressed using a 10 mm diameter die at 100 MPa and then placed on an alumina holder with microwave absorbing ceramic paste (US patent, 60/262.206, D.Agrawal, R.Roy and B.Vaidhyanathan, 2002) surrounding the sample to promote the absorption of microwave. Only one sample could be loaded into the microwave furnace at a time. Samples were loaded and placed in the centre of the furnace. The power output of the furnace started at 15% with a 1% increase every 3 minutes until a 50% power output was reached. The microwave sintering was

conducted in argon by passing Pureshield argon through the furnace at a flow rate of 200 cm^3 min^{-1}. The argon flow started 30 minutes before the start of the microwave sintering, and was continued during the entire process. The temperature analysis of the sample was achieved using a thermal imagine camera (FLIR Thermovision A40, FLIR Systems, West Malling, UK). It is important to note that the emissivity of HfB_2 is 0.78 and that of quartz (the material used as a furnace window) is 0.93, making a corrected emissivity value of 0.73.

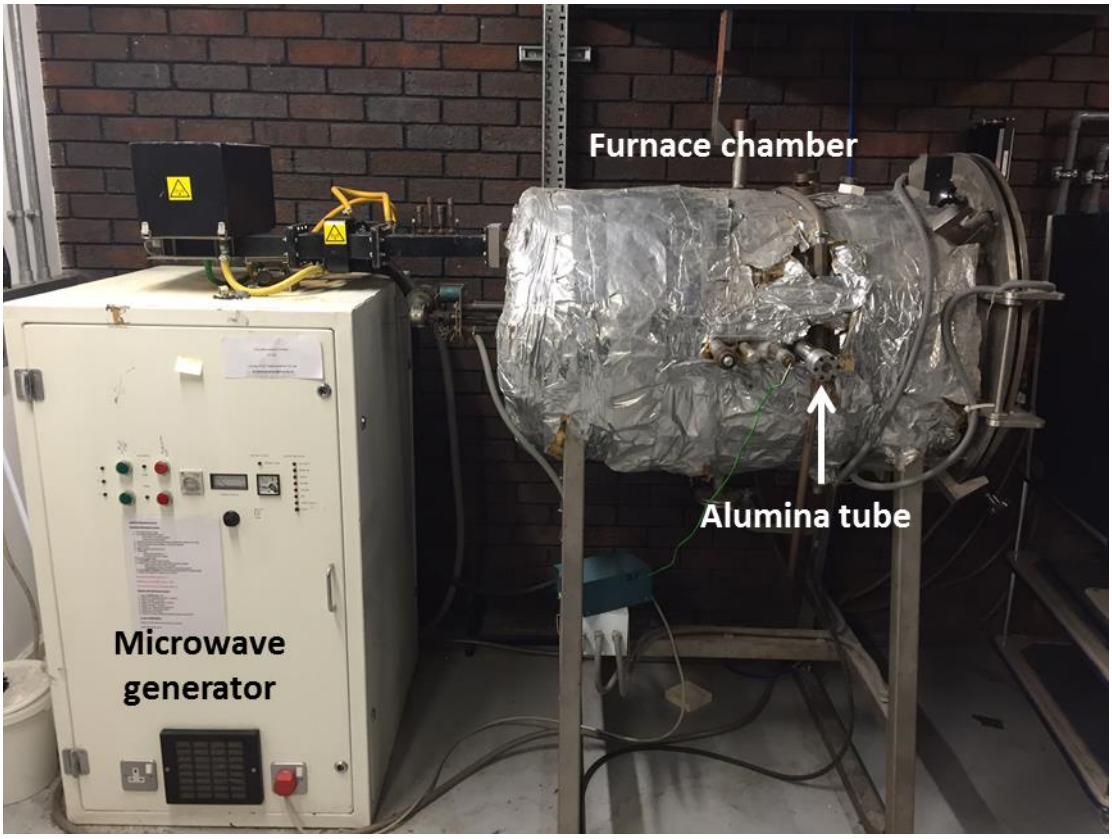

Figure 3.7 Schematic of the microwave furnace for the densification of HfB_2-based ceramics

The flash sintering apparatus used was also designed and built at Loughborough University, utilising an alumina tube furnace (LTF/16, Lenton Thermal Designs, UK). HfB_2 and 10 wt% Ta-doped HfB_2 green samples from die pressing (10 mm ∅ × 3 mm high pellet) were coated with silver paste, which

was cured at 450ºC for 1 h. The samples were then placed between the electrodes, with graphite sheet and platinum mesh on both the top and the bottom surfaces of the sample, as shown in Figure 3.8, to improve its contact with the electrodes.

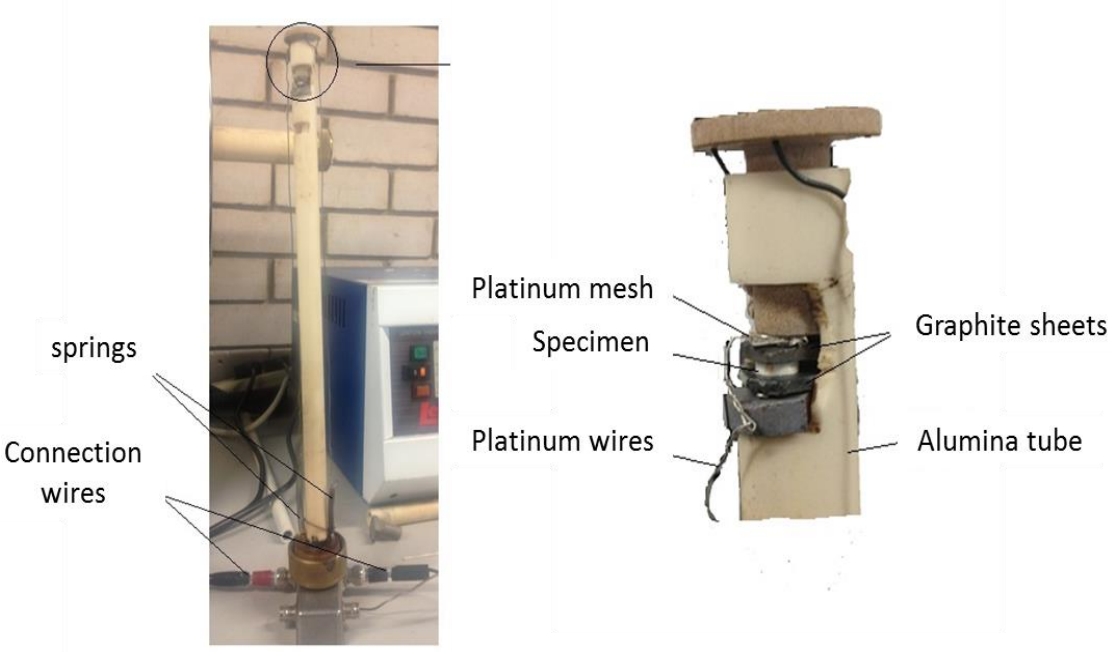

Figure 3.8 Schematic of the sample holder for flash sintering of HfB_2-based specimen

The DC field power of ~20 V cm^{-1}, generated by a rectifier (150V Multi-Mode Dual Bench Power Supply, TTi, UK), was applied on the sample and the sample was initially heated up to 900°C with a heating rate of 10º min^{-1}. A voltage sufficient to supply a current of 4A was subsequently applied to the sample. The voltage and current were recorded, and the sample temperature was monitored by a two-colour pyrometer (Marathon MR1SCSF, Raytek GmbH, Berlin, Germany). Similar to the microwave sintering, the flash sintering was also conducted in argon atmosphere with a flow rate of 120 cm^3 min^{-1}.

3.5.2 Pressure assisted densification: spark plasma sintering

Since long duration hot pressing generally leads to large grains in the sintered UHTCs (see section 2.6.2), the HfB_2 and Ta-doped HfB_2 were densified using SPS. This is a fast sintering technique that can limit the grain growth of the sintered ceramics. The SPS trials for phase-pure HfB_2 and 5, 10 and 15 wt% Ta-doped HfB_2 were performed at Queen Mary University, London using an FCT HP D20 model flash spark plasma sintering facility, FCT Systeme GmbH, Germany, which was also computerised for data processing. As shown in Figure 3.9, 10 g of the HfB_2 based ceramic powders were cold pressed at the pressure of 50 MPa and placed in a 20 mm diameter graphite die. Graphite sheets were applied on both the top and the bottom surfaces of the powders to avoid interaction with the graphite punches. Then the die was placed in the SPS cavity, which was maintained in vacuum through the entire SPS cycle.

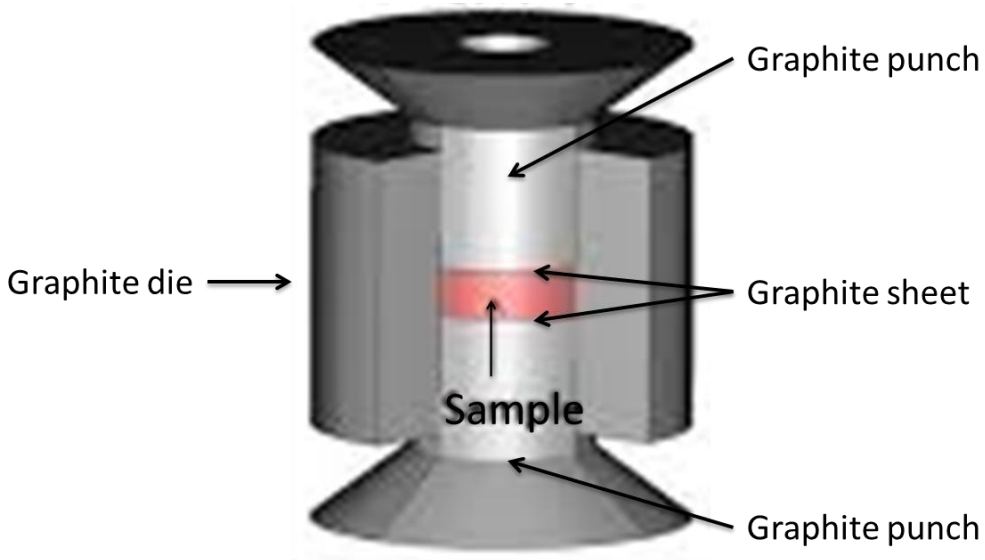

Figure 3.9 The graphite die used for SPS, Queen Mary University, London

A load of 19 kN, which resulted in ~60 MPa pressure on the 20 mm diameter samples, was applied during sintering. The heating and the cooling rates were kept as 100^{o}C min^{-1} and 50^{o}C min^{-1}, respectively. The samples were initially

heated to 1800°C and soaked for 30 min to allow any potential volatiles to escape. The samples were subsequently heated to the sintering temperature and soaked for another 30 min. 4 different sintering temperatures, 1900, 2000, 2100 and 2150°C were employed to investigate the effect of temperature on the densification of the HfB_2-based ceramics. Other than temperature and pressure, the linear change in shrinkage for the samples during sintering was recorded, by monitoring the displacement of the sample along the pressing direction. It should be noted that the optical pyrometer monitored the temperature on the surface of the graphite die rather than directly on the sample, which in turn gave rise to a difference between the temperature of the die and that of the sample, especially at the faster heating rates.

3.6 Oxidation testing of HfB_2-based ceramics

3.6.1 Static furnace oxidation

Table 3.6 HfB_2-based samples for furnace oxidation testing at various temperatures with 10 min dwelling time

Samples	Composition	Temperature/°C
Powders	HfB_2, 8 wt% Y_2O_3 doped HfB_2 5, 10 and 15 wt% Ta-doped HfB_2	1600 (LU)
Sintered ceramic	HfB_2, 5, 10 and 15 wt% Ta-doped HfB_2	1000 (LU)
		1300 (LU)
		1600 (LU)
		1700 (AFRL)
		1800 (AFRL)
		1900 (AFRL)

The oxidation studies of both powder and sintered phase-pure HfB_2, Y-doped and Ta-doped HfB_2, details shown in Table 3.6, were carried out in a box furnace (Elite 1600 Laboratory Chamber Furnace, with alumina insulation) at 1000, 1300 and 1600^oC. The oven oxidation testing at 1700, 1800 and 1900^oC for only sintered HfB_2 and Ta-doped HfB_2 were carried out in a zirconia element furnace (ZrF-25: Shinagawa Refractories Co., Tokyo, Japan) at Air Force Research Laboratory (AFRL), US, with the help of Dr. Carney. The heating and cooling rates for all the furnace oxidation testing was 5^oC min $^{-1}$, which was limited by the furnace, and all the samples were soaked at the testing temperature for 10 min.

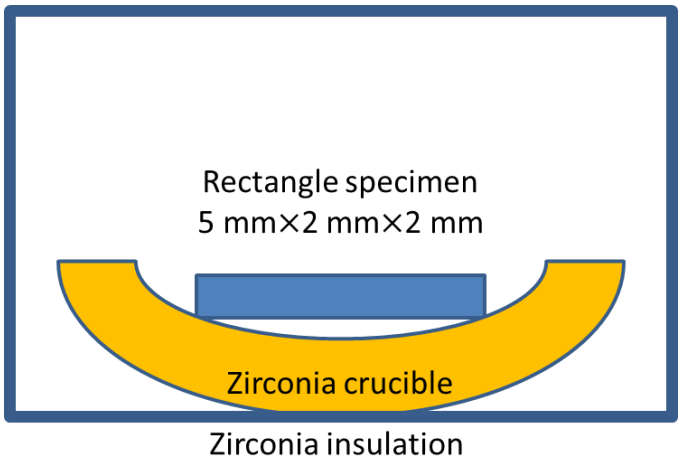

Figure 3.10 Schematic of HfB_2-based specimens tested in the zirconia element furnace

The dimension of the sintered samples was 5 mm × 2 mm × 2 mm rectangles and all the sides of the samples were polished to a 1 µm finish using diamond slurry before being put into the furnace. As shown in Figure 3.10, the HfB_2-based ceramic samples were placed on a concave ZrO_2 crucible to limit contact between the sample and the crucible. The masses of the samples pre- and post-testing were recorded to study the oxidation rate and then the oxidized samples were cut and polished for further microstructural analysis.

3.6.2 Oxyacetylene torch testing

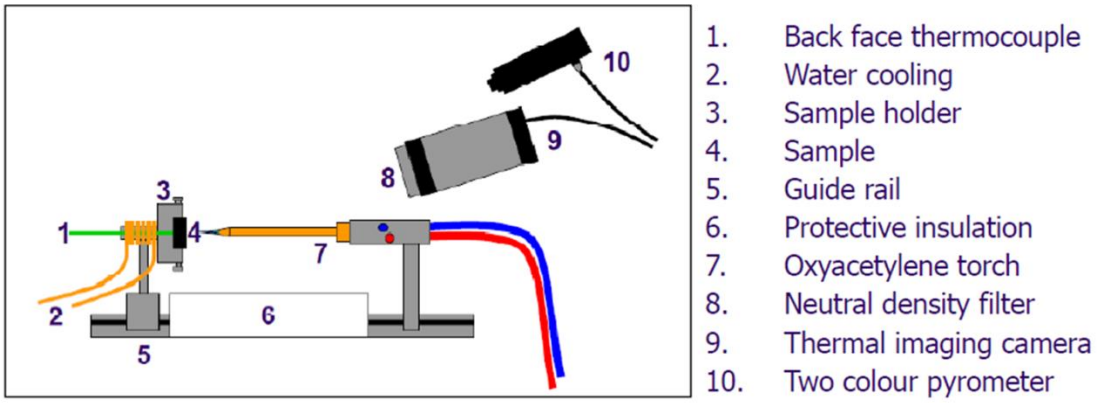

Figure 3.11 Oxyacetylene torch test set up [14], [263]

Compared to the static oven oxidation test, the dynamic oxidation test, e.g. oxyacetylene torch test can provide more information of the oxidation behaviours of the sample with the present of high gas flow speed. The oxyacetylene torch testing for pure and 10 wt% Ta-doped HfB_2 was performed at the University of Birmingham using the facility shown in Figure 3.11. 20 mm diameter disc specimens were placed in a graphite insert (outer diameter 35 mm), which was then fixed inside the water-cooled graphite sample holder. During the test, an oxygen rich flame (1:1.35 acetylene to oxygen ratio) was focused on the specimen resulting in a heating rate of >100^{o}C s^{-1}. The peak temperature and the temperature distribution on the front surface of the specimen were recorded by using a two colour pyrometer (METIS M311, Sensortherm GmbH, Hauptstrabe, Germany) and a modified infrared thermal imaging camera (Thermovision A40, FLIR System AB, Danderyd, Sweden). The two colour pyrometer was capable of recording a temperature from 1100 to 3300^{o}C and the thermal imaging camera could record a temperature up to 2800^{o}C when combined with a neutral density filter. For each specimen, distances of 10 and 20 mm between the specimen and nozzle were used to

alter the peak temperatures and heating profiles. Since the aim of the test was to understand the effect of Ta dopants on the oxidation mechanism of HfB_2, the test was carried out for 240 seconds to allow a relatively thick, >10 μm oxide scale to form. The mass change of each sample after testing was recorded. The oxide products were further characterized using XRD, SEM and TEM.

3.7 Sample preparation and characterization techniques used

3.7.1 Fourier transform infra-red (FTIR) spectroscopy

The functional groups present in the HfB_2-based precursor powders containing PPR, boric acid and $HfOCl_2$ were analysed using FTIR (FTIR 8400S, Shimadzu, Maryland, USA). The amount of the precursor powders (~1 mg) were mixed with 1 g of potassium bromide (KBr) using a pestle and mortar. 100 MPa was applied to the powder mixture to make thin pellets of 12 mm diameter for FTIR analysis. A pure KBr pellet pressed under the same conditions was used as a reference to obtain the background curve, which was then subtracted from the scans of the HfB_2 samples.

3.7.2 BET surface area measurements

An automated gas adsorption analyser (TristarTM 3000, Micromeritics Instrument Corporation, Norcross, USA) was used to measure the BET surface area of the synthesized HfB_2 and Ta-doped HfB_2 powders. The value of the surface area obtained was also used to calculate the specific particle size, via Equation 2-5 and estimate the extent of agglomeration.

$$\text{Particle size} = \frac{6}{\rho \times S} \times 1000 \qquad (2\text{-}5)$$

Where S is the specific surface area and ρ is the theoretical density of the material.

Approximately 1 g of HfB_2-based ceramic powders were initially degassed in a nitrogen atmosphere at 150^oC for 60 min before testing, followed by evacuating to less than 20 μm Hg vacuum and cooling down to -196^oC using liquid nitrogen. After that the samples were exposed to high purity (>99.99%) nitrogen. The amount of nitrogen adsorbed on the particle surface at -196^oC was recorded using the ratio of the relative pressure to the saturation vapour pressure, to estimate the surface area of the particles.

3.7.3 Mastersizer

A Mastersizer 2000 (Malvern, UK) was used to study the particle size distribution of the HfB_2-based powders. This instrument used the laser diffraction technique, i.e. calculation on the diffraction angle when the particles were passed through the laser beam, to measure the particle size and had a measurement range from 20 nm to 2000 μm. The powders to be measured were dispersed in ethanol (>99.7%, Fisher Scientific, UK) and subjected to ultrasonication for 20 min to break the soft agglomerates before the measurements. The dilute suspension was then circulated into the cell. Both the volume and number particle size distribution were recorded for each sample.

3.7.4 X-ray diffraction (XRD)

The crystalline structure of materials can be determined by the elastic scattering of X-rays from the individual atoms. A D2 Desktop Diffractometer (Bruker Instruments, UK) equipped with an integrated PC and a flat screen monitor, supplemented with an easy-to-use workflow software DIFFRAC-SUITE, was used to identify the crystalline structures of the synthesized HfB_2-based ceramic

powders. The accuracy of the instrument was ±0.02° throughout the entire measuring range and the achievable peak width was <0.05°. However, the instrument was not sufficiently sensitive to detect a phase at <3 atom%. The voltage and current used to generate the X-rays were 40 kV and 35 mA respectively. Nickel filted CuKα radiation with a wavelength of 0.154 nm was irradiated onto the powder samples. For general scanning, the samples were analysed at a scan speed of 1^o min^{-1} and with a step size of 0.02^o from 20^o to 80^o 2θ range, whilst for high resolution scanning, the scan speed and step size were reduced to 0.5^o min^{-1} and 0.005^o, respectively. The information, such as diffraction peak position, intensity and shape, was related to the International Centre for Diffraction Data (ICDD) cards to identify the phase of the as-synthesized powders.

3.7.5 X-ray photoelectron spectroscopy (XPS)

XPS was used for the element identification of the HfB_2-based powders, especially for the light atom and amorphous phase, e.g. B_2O_3, which was difficult to detect either by XRD or SEM-EDX. The XPS analysis was carried out by a K-alpha surface analyser (Thermo scientific, UK) with an Al Kα X-ray source (1486.6 eV) in vacuum. Only several milligrams of powders were required for analysis. In XPS, the surface of the powder samples is irradiated with X-rays. The resulting photoelectrons emerging from the surface are collected and then energy analysed. Each element gives rise to a set of peaks at characteristic energies. Hence the photoelectron spectrum allows identification of the elements present on the surface of the sample. The concentrations of these elements can be calculated from the relative intensities of the photoelectron peaks, with a sensitivity of 0.1-1 atom%. In addition, the emitted electrons are of such an energy that only those from the top few atomic layers have a significant chance of escaping from the surface without losing energy, hence the technique is highly surface sensitive (5~10 nm depth). One general scan

was performed for each HfB_2-based sample to identify all the elements on the sample surface and a few high resolution scans were performed for elements such as Hf, Ta, B and O to identify the corresponding compounds.

3.7.6 Thermal gravimetric analysis (TGA)

The onset temperature of the carbothermal and borothermal reduction reactions were analysed by TGA which was carried out using a Netzsch Simultaneous Thermal Analyser (STA 449C, Netzsch Group, Selb, Germany). The sensitivity of the equipment used was 0.1 µg and the maximum loading was 0.2 g. The heating rate of the chamber could be selected from 0.1 – 500°C/min up to 1600°C in air or controlled atmosphere. Approximately 10 mg of HfB_2 precursors was heated at the rate of 5^{o}C/min from room temperature to 1000^{o}C and 3^{o}C/min from 1000^{o}C to 1600^{o}C in an argon atmosphere. The weight and the difference in heat flow as a function of temperature were recorded to show the exothermic and endothermic reactions associated with the weight loss of the precursors. A STA 449 F5 Jupiter Netzsch Thermal Analyser was used to investigate the oxidation rate of the large sintered HfB_2-based specimen. The mass gain of the samples, which were due to the oxidation of HfB_2, was recorded between 25 and 1600^{o}C. For the large specimen, there was always a lag between the samples' temperature and the programme temperature due to the lack of dwell time, hence the maximum temperature the sample reached was in the range of 1500-1550^{o}C.

3.7.7 Sample mounting and polishing

The sintered HfB_2-based ceramics needed to be mounted and polished for further oxidation testing and microstructural analysis. The samples were mounted using epoxy resin and its corresponding hardener mixture (Epofix,

Struers Ltd., Solihull, UK) with a weight ratio of 25:3. The epoxy resin was left at room temperature for 12 hours to cure. The samples were then polished using a semi-automated polishing machine equipped with an automatic diamond slurry feeding system (Tegramin-25, Struers Ltd., Solihull, UK). The polishing cycle for the HfB_2-based ceramics is shown in Table 3.7. The first step was grinding, removing the epoxy that covered the specimens. It should be noted that the specimen edges were rounded off to avoid damaging the polishing discs. After each step, the specimens were rinsed with deionized water and, in addition, the specimen surface was wiped with acetone after the final step.

Table 3.7 Grinding and polishing cycle for sintered HfB_2-based ceramics

Step	Polishing disc	Polishing Media	Force /N	Duration /min
1	MD-Piano 220	water	30	15
2	MD-Piano 600	water	20	5
3	MD-Piano 1200	water	20	5
4	MD-Plan	DP-suspension (9 μm finish)	15	5
5	MD-Dac	DP-suspension (3 μm finish)	15	5
6	MD-Floc	DP-suspension (1 μm finish)	10	10

3.7.8 Cutting of the sintered ceramics

Since sintered ceramics can be difficult to be cut, a Struers Accutom-5 cutting machine equipped with a diamond wafer blade (Buehler, Düsseldorf, Germany) was used to cut the HfB_2-based ceramics. The blade rotary speed was 2500 rpm and the sample feeding rate was less than 0.005 mm s^{-1}. The cutting machine was capable of making rectangle samples for oxidation testing, however, in order to obtain a complex shape, the samples were cut with a wire electro-discharge machine (EDM) into cylinders in the School of Metallurgy and Materials, University of Birmingham.

3.7.9 Density measurements

The green density of the HfB_2-based pressed pellets was measured using the geometrical method according to Equation 2.6.

$$\text{Green density (GD)} = \frac{\text{mass}}{\text{volume}} = \frac{\text{m}}{\pi r^2 h} \quad (2\text{-}6)$$

where, the r is the sample radius and h is the samples thickness, measured by a Vernier calliper and screw gauge respectively. The density of the sintered HfB_2-based ceramics was measured using the Archimedes water displacement method. Equation 2.7 gives the bulk density of the samples.

$$\text{Bulk density (BD)} = \frac{M_d \times \rho}{M_d - M_w} \quad (2\text{-}7)$$

where, M_d is the dry weight of the sample, M_w is the weight of the sample in deionized water and ρ is the density of water at room temperature. The relative density of the sintered samples was calculated using Equation 2.8.

$$\text{Relative density} = \frac{\text{GD or BD}}{\text{Theoretical density of the samples}} \times 100 \quad (2\text{-}8)$$

where, 10.50 and 11.15 g cm^{-3} were taken as the theoretical density of HfB_2 and TaB_2, respectively.

3.7.10 X-ray fluorescence analysis (XRF)

The content of Hf and Ta in the sintered Ta-doped HfB_2 ceramics was analysed using Micro-XRF (Edax Orbis X-ray fluorescence spectrometer). The X-ray source was set at 40 keV and 1000 mA and focused to a 3mm spot size using

X-ray optics with capillary. The XRF spot analysis was performed on the fracture surface of the sintered ceramics in vacuum.

3.7.11 Thermal and electrical conductivity measurements

The thermal diffusivity and specific heat capacity of the pure and 15 wt% Ta-doped HfB_2 was measured by Laser Flash analysis using a LFA 427 device (Netzsch). The surface of sintered ceramic samples (12.5 mm in diameter and 2 mm in thickness) was polished to 1 μm finish and then coated with graphite to prevent the direct transition of the laser beam and to help the energy transfer to the sample. The measures were conducted from ambient temperature to 1500°C in argon. The thermal conductivity values for the pure and Ta-doped HfB_2 were calculated via Equation 4.13,

$$K=\alpha\rho C_p \quad (4\text{-}13)$$

where K is thermal conductivity, ρ is density and C_p is specific heat capacity.

The electric conductivity of the pure and 15 wt% Ta-doped HfB_2 was measured by a 2-point DC method. The top and bottom surface of the sintered ceramic samples, which was used for thermal conductivity measurements, was coated with silver paste and connected to electrodes. The voltage and current change of the samples (measured by Impedance Analyser, SI 1260, Solartron, UK) against temperature were recorded to calculate the electric resistance R of the sample and then transferred into electrical conductivity σ, via Equation 2.10,

$$\sigma = \frac{L}{RA} \quad (2\text{-}10)$$

where, L and A are the thickness and top/bottom surface area of the cylinder sample.

3.7.12 Field emission gun scanning electron microscopy

The morphology of the synthesized powders, the fracture surface of the sintered ceramics and the microstructure of the oxidized samples were observed by field emission gun scanning electron microscopy (FEG-SEM, Leo 1530VP, Carl Zeiss NTS Ltd., Cambridge, UK). The FEG-SEM had a higher resolution and better contrast compared to a conventional SEM and was capable of analysing nano grain-sized samples. The samples were mounted onto aluminium stubs with conductive carbon disc tapes (Agar Scientific, UK) and coated with Au/Pd using a Polaron Emitech SC7640 sputter coater (Quorum Technologies Ltd, UK). The secondary electron (SE2) detector was operated with a 5kV accelerating voltage and 30 μm aperture to obtain SEM images for all the samples.

The Leo FEGSEM was also equipped with an energy dispersive x-ray analysis (EDX, EDAX Inc., NJ, USA) allowing compositional analysis of the samples. In EDX analysis, besides the employment of high current, the accelerating voltage remained 5 kV and the aperture size was increased to 120 μm to enhance the signal from the low molecular weight atoms, e.g. boron. The orientation of the grains in the sintered samples were observed by JEOL 7800F FEG-SEM (JOEL Ltd., Tokyo, Japan) with electron backscattered diffraction (EBSD) imaging system (Hikari hi-speed camera).

3.7.13 Focused ion beam (FIB)

To prepare a TEM specimen from the sintered Ta-doped HfB_2, a Dual Beam FIB (Nanolab 600, FEI), which combined a focused ion beam microscope and FEGSEM, was used to carry out the lift-out. Similar to the SEM sample preparation, the Ta-doped HfB_2 sample was coated with Au/Pd and fixed onto an aluminium stub using silver paste. During lift-out, the sample was tilted at 52^{o}

and the gun voltage maintained at 30 kV. A thin layer of Pt was initially deposited on the surface of the selected area. Then a gallium ion beam, operating at 20 nA, was used to remove material from both sides of the selected area to form a ~500 nm thick rectangular specimen. This was attached to a TEM grid using Pt as an adhesive and was further thinned using the ion beam with gradually reduced current (from 7 to 5 nA and finally to 3 nA) until a final thickness of ~100 nm was achieved.

3.7.14 Transmission electron microscopy (TEM)

The morphology of the HfB_2 based powders and the composition of the grains in the sintered Ta-doped HfB_2 were analysed using transmission electron microscopy (TEM, JEOL JEM 2000FX, JEOL Ltd., Japan). Sample preparation is critical in TEM analysis as the sample has to be electron transparent, i.e. thin enough for the beam to pass through. Powder samples were dispersed in ethanol, followed by ultrasonication for 20 min to break soft agglomerates. A drop of the resultant suspension was placed on a copper grid covered with carbon film, which was loaded into a single tilt TEM holder. For the sintered ceramic samples, FIB lift-out was required to cut the sample and thin it down to 100-150 nm, and then the resulting sample was loaded into a double tilt holder to obtain TEM images at an operating voltage of 200 kV and with various magnifications and diffraction patterns. In addition, the elemental distribution within two adjacent grains of the sintered Ta-doped HfB_2 was analysed using EDX with a field emission gun-TEM (Tecnai F20, FEI).

4. Results and discussion

This chapter discusses the results of the synthesis of pure and doped HfB_2 powders, the subsequent densification process and the characterisation of the sintered ceramics. Before making doped HfB_2, it is important to understand the optimized conditions to synthesize phase-pure HfB_2. At the early stage of this work, a sol-gel approach, which was developed at Loughborough University, was first selected to synthesize pure HfB_2 as it was reported to be capable of yielding sub-micron sized powder which was beneficial for impregnating HfB_2/carbon preform composites. However, based on extensive investigation, the drawback of the sol-gel approach was found to be the presence of impurities such as HfC and free carbon that were difficult to remove from the resultant HfB_2. Since the ultimate aim of this work was to investigate the effect of dopants on the oxidation behaviour of HfB_2-based ceramics, the purity of the powders was more critical than the particle size. Hence, a precipitation approach was subsequently developed to synthesize both pure and doped HfB_2 powders. The sinterability of the HfB_2-based powders prepared by the different approaches was compared. Static furnace oxidation and dynamic oxyacetylene torch tests were also performed on the sintered ceramics to study their oxidation behaviour and mechanisms.

4.1 Synthesis of pure and doped HfB_2 powders by carbothermal reduction reaction method

4.1.1 Characterization of the starting materials

As the stoichiometric ratio of the starting materials is a critical factor to control the purity of the HfB_2 powders yielded from either carbothermal or borothermal reduction reactions, it is important to understand the stability and reactivity of

the starting materials.

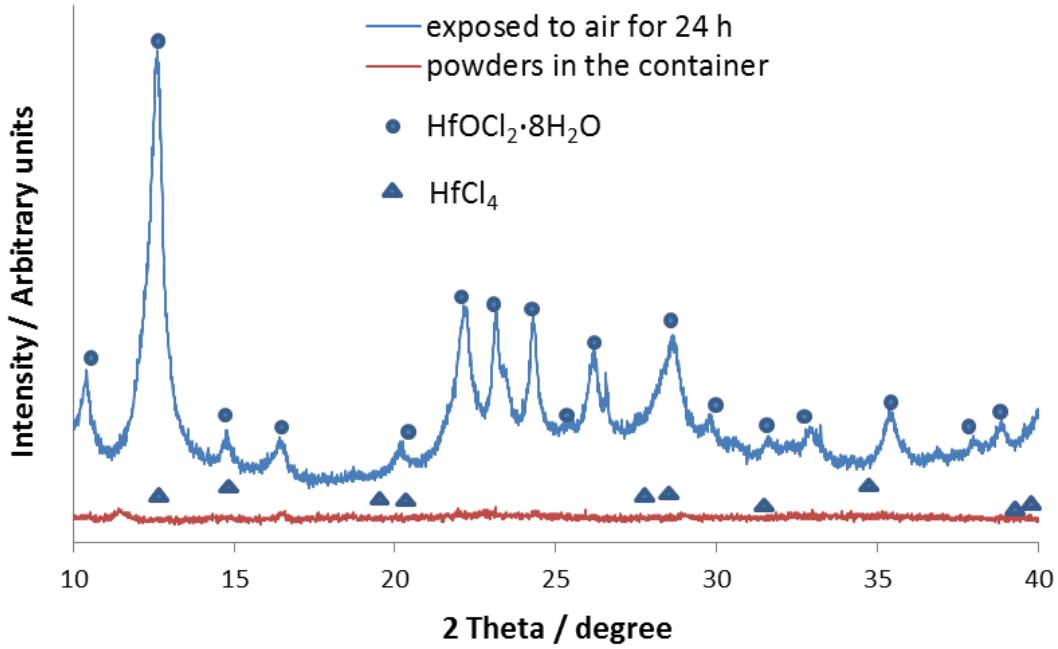

Figure 4.1 XRD patterns of $HfCl_4$ powder after exposing to air for 24 hours indicating mainly $HfOCl_2 \cdot 8H_2O$

$$HfCl_4 + (n+2)H_2O \rightarrow Hf(OH)_2Cl_2 \cdot nH_2O + 2HCl \rightarrow HfOCl_2 \cdot nH_2O + 2HCl + H_2O \quad (4\text{-}1)$$

The $HfCl_4$ powder for HfB_2 synthesis was kept in a storage bottle closed under air since the powders could undergo hydration before use. According to Figure 4.1, the XRD pattern of the powders after several months' storage indicates the presence of a low-crystallinity phase, which may be due to the combined presence of $HfCl_4$ and $HfOCl_2 \cdot nH_2O$ ($0<n<8$) in these powders. $HfCl_4$ has a monoclinic AB_4-type structure and consists of a zig-zag chain of $HfCl_6$ octahedrons, as shown in Figure 4.2. Every Hf atom shares two chlorine ions with each of its two Hf neighbours. The other two chlorine ions, which are linked to Hf atoms by single bonds, are highly reactive with OH^-, thus hafnium chloride is easily hydrated when exposed in moist air and becomes $HfOCl_2 \cdot nH_2O$ ($0<n<8$) following Equation 4.1, where n depends on the hydration rate. $HfCl_4$ particles

started to hydrate as soon as in contact with moisture, leading to the cracking of the hydrated outer shell of particles, which allowed further inward diffusion of water molecules to take place. As shown in Figure 4.2, the resultant partially hydrated $HfCl_4$ particles were heterogeneous with a positive hydration gradient from an anhydrous $HfCl_4$ core to an outer hydrated $HfOCl_2$ surface layer [261].

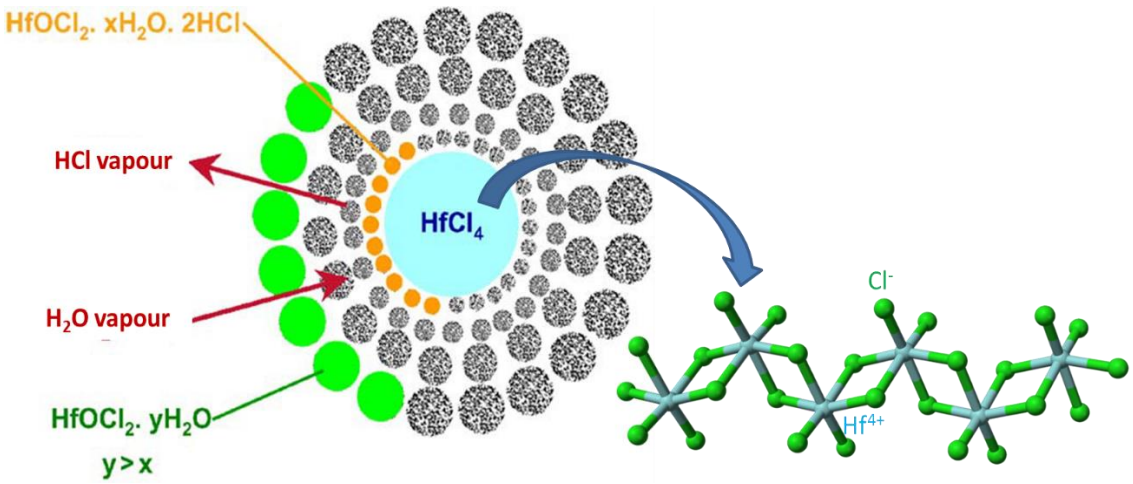

Figure 4.2 Octahedral chain structure of $HfCl_4$ and the composition of a partially hydrated $HfCl_4$ particle [261]

Since the number of water molecules in partially hydrated $HfCl_4$ powders was difficult to estimate, in order to improve the consistency of the stoichiometric calculation for the synthesis of HfB_2 powder, the partially hydrated $HfCl_4$ powder was further hydrated to a maximum hydration rate of n=8, by deliberately exposing to air for an extended time. Based on Figure 4.1, it was found that $HfOCl_2{\cdot}8H_2O$ (JCPDS cards: 00-015-0348) was the dominant phase for the powders after 24 h exposure to air. Hence, $HfOCl_2{\cdot}8H_2O$ instead of $HfCl_4$ was used as the starting Hf source. The thermal decomposition analysis, Figure 4.3, also showed that fully hydrated $HfOCl_2{\cdot}8H_2O$ was obtained after exposing $HfCl_4$ to air for 24 h; the mass change for the $HfCl_4$ powder heated to 1400°C in air was ~33.2%, which corresponded to the loss of all H_2O molecules in $HfOCl_2{\cdot}8H_2O$, whilst the mass change from 140-550°C was mainly due to the reaction of $HfOCl_2$ with oxygen via Equation 4.2. HfO_2 was the final product of $HfOCl_2$ decomposition. For the $HfCl_4$ powder heated under argon, the greatest

mass change happened at temperatures <140°C as $HfOCl_2$ was found to be the final product. The residual Cl present in $HfOCl_2$ could lead to serious errors during HfB_2 synthesis and the removal of Cl from the system was required.

$$2HfOCl_2 + O_2 \rightarrow 2HfO_2 + 2Cl_2 \quad (4\text{-}2)$$

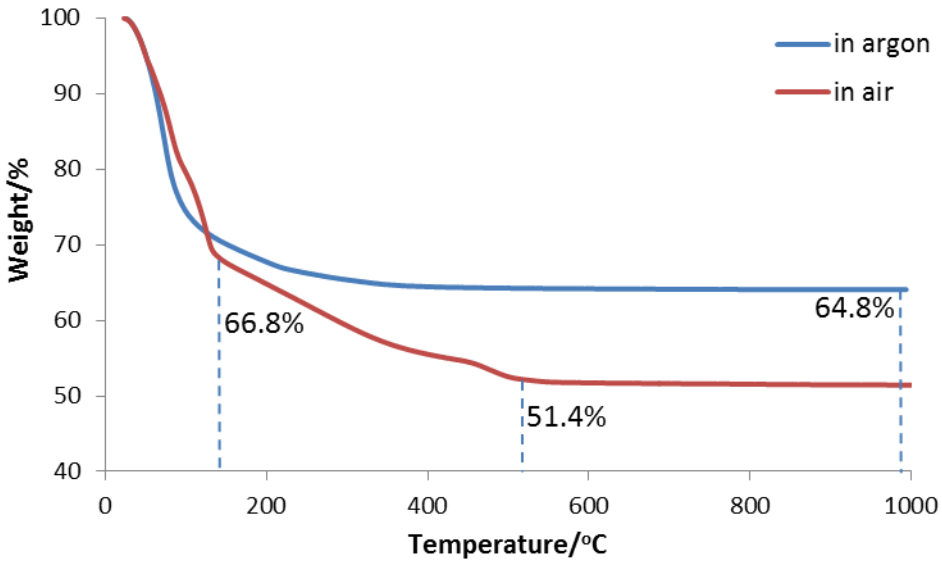

Figure 4.3 Thermal decomposition of $HfOCl_2 \cdot 8H_2O$ from ambient temperature to 1000°C

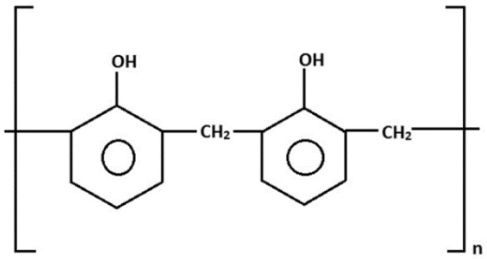

Figure 4.4 Molecular structure of novolac phenolic resin

Novolac phenolic resin[d], the structure of which displayed in Figure 4.4, was used as the carbon source for HfB_2 synthesis since a carbon residue was obtained

[d] Novolacs are phenol-formaldehyde resins with a formaldehyde to phenol molar ratio of less than one. Thus the polymerization can be completed by using acid-catalysis, e.g. hydrochloric acid.

after the thermal degradation of phenolic resin in argon. The carbon content of the novolac phenolic resin was measured by TGA. As indicated in Figure 4.5, the mass change of the resins below 200°C corresponded to the loss of water, after which the curve tended to be stable due to the heat-imposed curing of the resins until 400°C, when the cured resins started to degrade, releasing volatile compounds such as 2,4-xylenol, phenol and CO. The residual content, which was ~41%, was recorded as the carbon content for the synthesis of HfB_2, as all the residue disappeared when the TGA for the same powder was conducted in air.

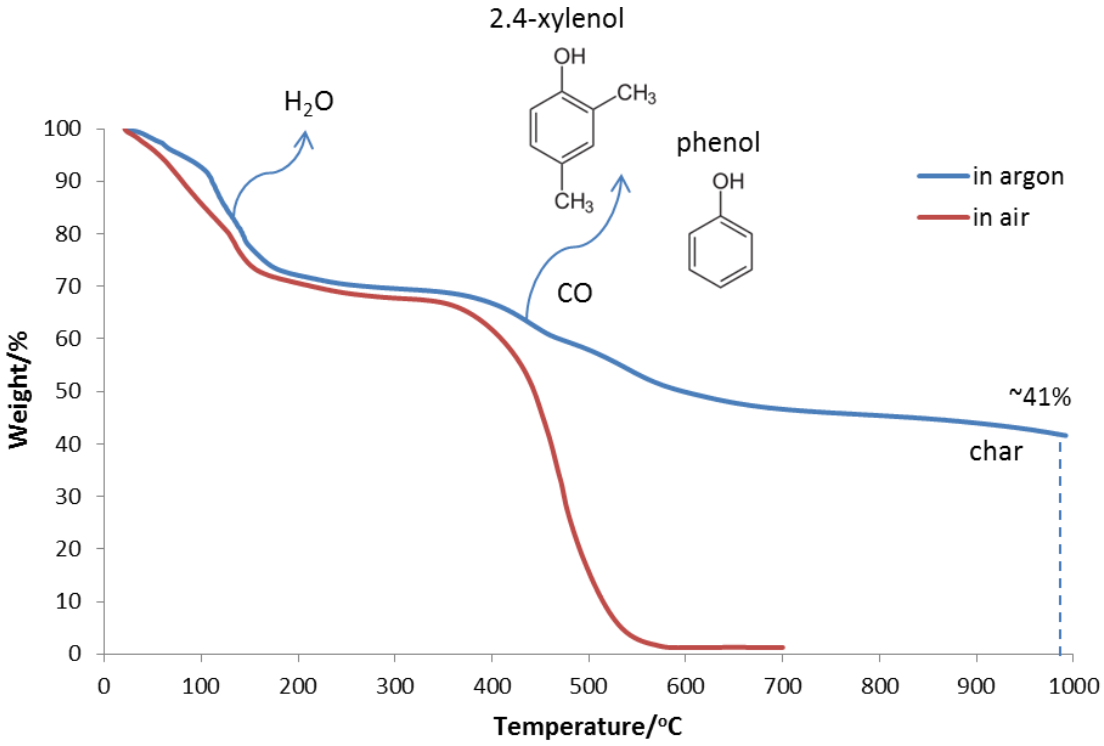

Figure 4.5 TGA of novolac phenolic resin from ambient temperature to 1000°C in different atmosphere

Boric acid was used as the boron source for HfB_2 synthesis due to its good solubility in water and alcohols, which is beneficial for subsequent solution-based processing approaches. It was seen from Figure 4.6 that boric acid was stable at temperatures <100°C and then gradually lost 3 water molecules, which was 55.8 wt% of the original boric acid, to form B_2O_3.

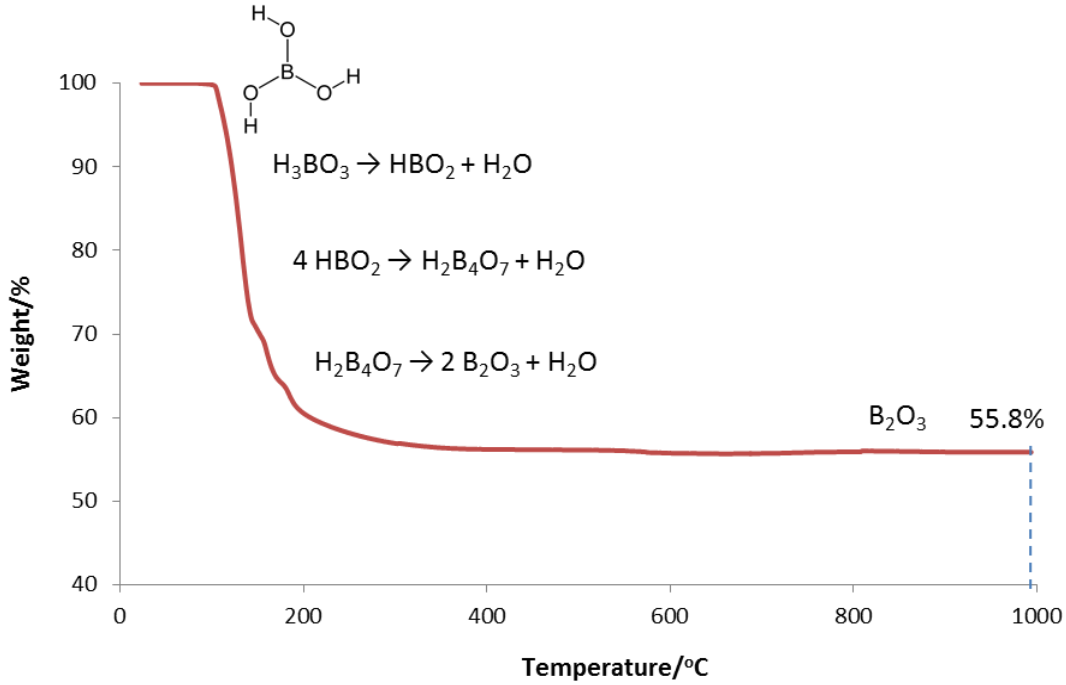

Figure 4.6 TGA of boric acid from ambient temperature to 1000°C in argon

4.1.2 Synthesis of HfB_2 powders by carbothermal reduction reaction from sol-gel derived precursors

The synthesis of HfB_2 by carbothermal reduction was based on Equation 4.3, using carbon as a reducing agent to remove oxygen from HfO_2 and B_2O_3. In order to achieve high purity of the resultant HfB_2 powder, a sol-gel approach was used to improve the mixing of the reactants. $HfOCl_2$, H_3BO_3 and novolac phenolic resin, which were all soluble in ethanol, were used as hafnium, boron and carbon sources, respectively.

$$HfO_2 + B_2O_3 + 5C \rightarrow HfB_2 + 5CO \qquad (4\text{-}3)$$

4.1.2.1 Characterization of the sol-gel derived precursors

Ethanol solutions of $HfOCl_2$, H_3BO_3 and phenolic resin were mixed by using a magnetic stirrer, but in the sol-gel approach, the more critical factor designed to retain the molecule-level mixing during drying relied on gelation, which was

attributed to the cross-linking of the novolac phenolic resin. The mixture solution of $HfOCl_2$, H_3BO_3 and novolac phenolic resin was stirred at 100°C for 24 h to form a milky gel and the resultant gel was dried at 120°C to obtain the precursor powders.

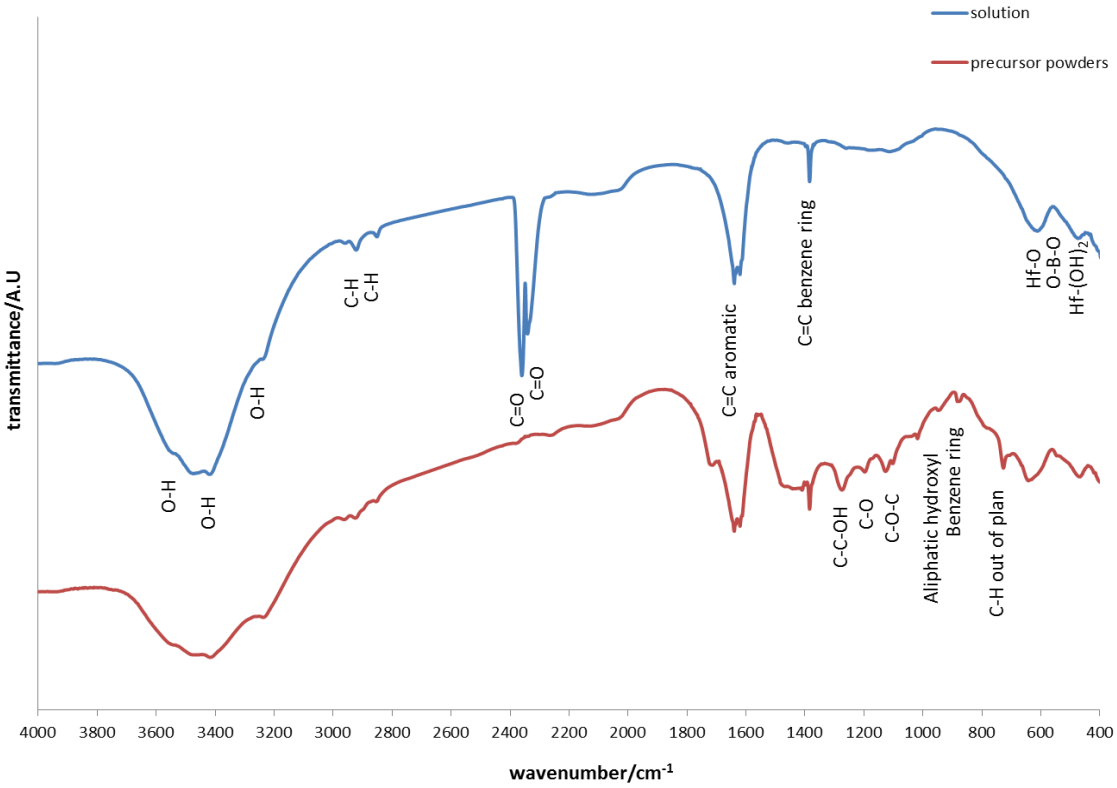

Figure 4.7 FTIR spectra of $HfCl_4$, H_3BO_3 and novolac phenolic resin solution and dried precursor powders

The FTIR transmission spectrum from 4000-400 cm^{-1} for $HfCl_4$, H_3BO_3 and novolac phenolic resin solution and the precursor powders is plotted in Figure 4.7. According to the NIST standards database [264], the broad peak around 3400 cm^{-1} corresponds to O-H stretching vibrations, which occurs due to the hydroxyl groups in the phenolic resin, boric acid and the $Hf(OH)_2Cl_2$. The small peaks at 2845 and 2920 cm^{-1} are due to C-H stretching vibrations from the phenolic resin. For the mixture solution, the strong peaks at 2330 and 2360 cm^{-1} are associated with C=O stretching vibrations from ethanol. The peaks at 1630 and 1450 cm^{-1} represent the aromatic C-H deformation and C=C vibrations from

the benzene ring, respectively. The peaks at 470 and 626 cm^{-1} are due to Hf-$(OH)_2$ and Hf-O stretching vibrations. The peak at 520 cm^{-1} is associated with O-B-O stretching from H_3BO_3. For the precursor powders, the peaks corresponding to ethanol disappear while several small peaks associated with the asymmetric stretch of phenolic C-C-OH, C-O stretch, asymmetric stretching vibration of C-O-C, aliphatic hydroxyl and 1,2,4-substituted benzene are seen at 1237, 1100, 1000 and 976 cm^{-1} [265], respectively, indicating the cross-linking of the novolac phenolic resin.

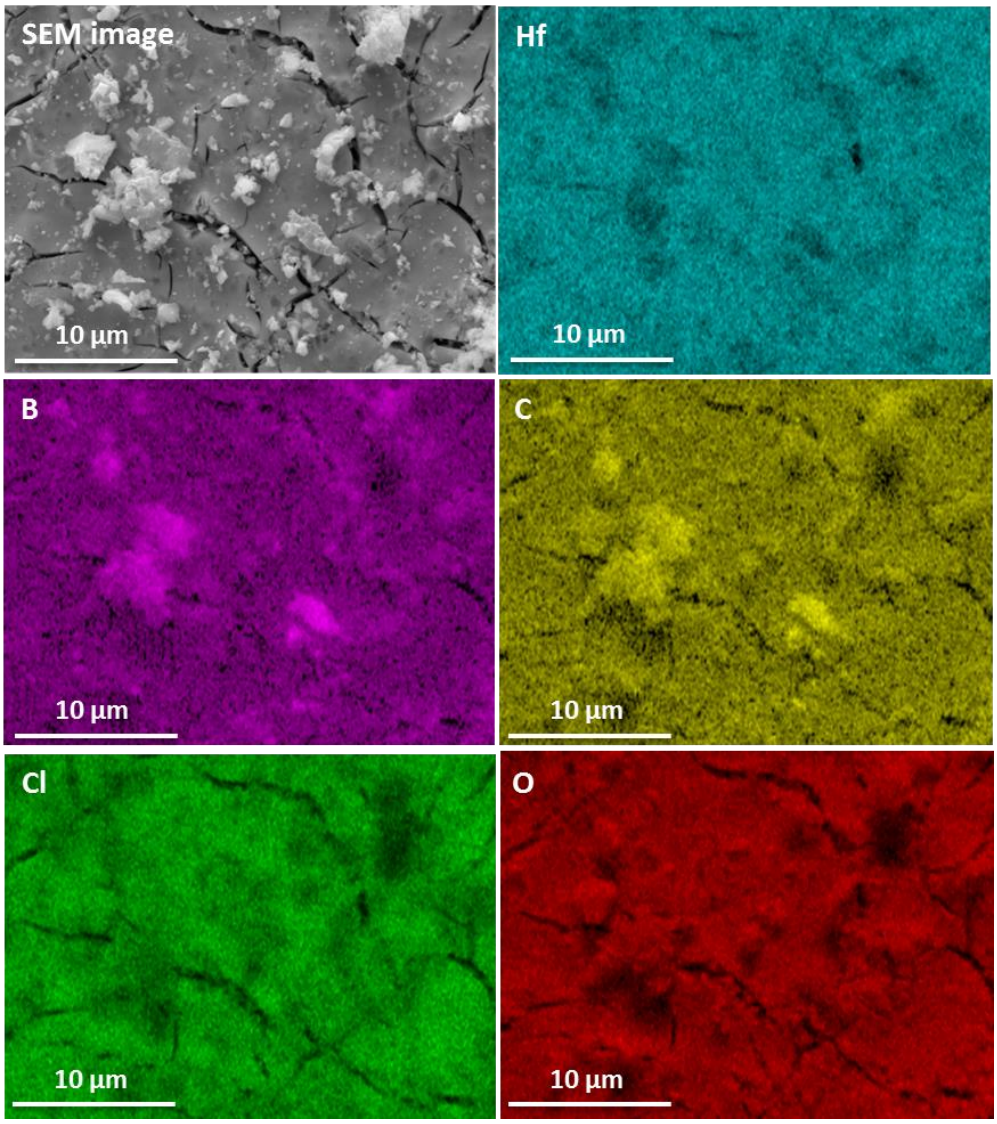

Figure 4.8 SEM-EDX images of the precursor powders obtained from $HfOCl_2$, H_3BO_3 and novolac phenolic resin solution

The homogeneity of the precursor powders was checked by SEM-EDX mapping. It can be seen from Figure 4.8 that the $HfOCl_2$, H_3BO_3 and phenolic resin were well-mixed in the precursor without any rich areas of singe elements.

Table 4.1 Thermal degradation temperature and products of $HfOCl_2 \cdot 8H_2O$, H_3BO_3 and novolac phenolic resin, summarized from Figure 4.3, 4.4 and 4.5

	Degradation Temperature /°C	**Products**
$HfOCl_2 \cdot 8H_2O$	20-140	H_2O
	140-550	HfO_2, Cl_2
H_3BO_3	100-300	H_2O, B_2O_3
phenolic resin	20-150	H_2O
	400-650	2,4-xylenol, phenol and carbon char

Table 4.2 XPS composition analysis of the HfB_2 precursor powders before and after calcined at 400°C for 3 h in air

Element	**Before calcination /atomic %**	**After calcination /atomic %**
B 1s	8.78	11.94
C 1s	37.63	39.77
Cl 2p	11.56	1.24
Hf 4f	5.94	7.11
O 1s	36.09	39.94

The chlorine from $HfOCl_2$ in the precursor had to be removed because it can react with B_2O_3 to cause extra boron loss during the subsequent carbothermal reduction reaction and is also harmful to the furnace end caps, which were made of aluminium. As discussed earlier, chlorine in $HfOCl_2$ was not able to be removed at temperatures <1000°C in argon, therefore, the precursor powders were calcined in air at 400°C for 3 h to remove chlorine. As shown in Table 4.1, the calcination temperature used was beyond the degradation temperature of $HfOCl_2$, but below that of phenolic resin to avoid the oxidation of carbon. Table

4.2 suggests that precursor powders without calcination contained 11.56% chlorine, whilst after calcination, it was significantly reduced to 1.24% without any weight loss associated with boron or carbon. Based on the TGA results of the calcination of $HfOCl_2 \cdot 8H_2O$, Figure 4.9, 45.2% weight loss was found after the calcination, meaning that more than 80% of the chlorine was removed from the system. The effect of the small amount of residual chlorine on the purity of the HfB_2 yielded from carbothermal reduction reaction will be discussed in section 4.1.2.4.

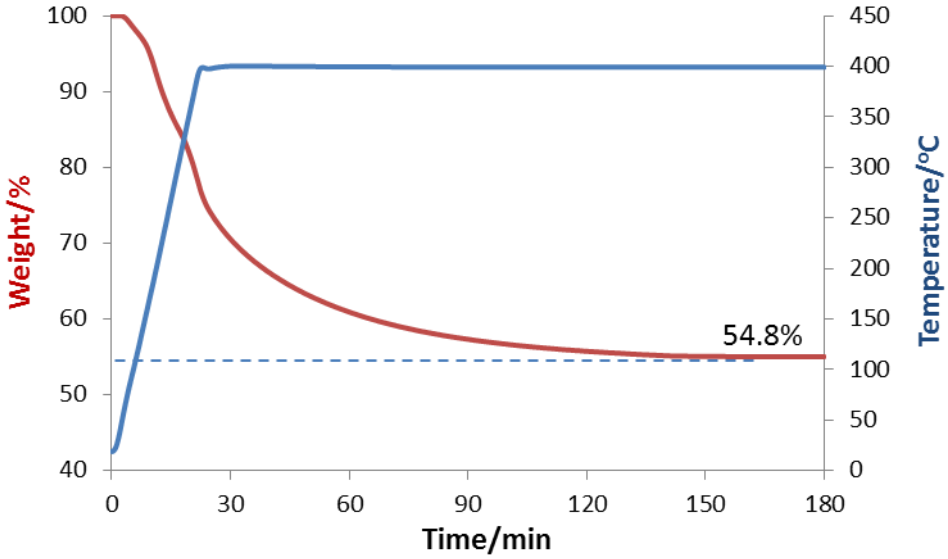

Figure 4.9 Thermal degradation of $HfOCl_2 \cdot 8H_2O$ in air, at 400°C for 3 h

4.1.2.2 Study of carbothermal reduction reaction

According to the thermal dynamic calculation for Equation 4-3 using Factsage 6.1, the carbothermal reduction reaction becomes thermal-dynamically favourable at temperatures >1523°C. However, it was found that HfB_2 powders formed at temperature far below the calculated value. Figure 4.10 shows the TGA-DTA curves of the sol-gel derived precursor (elemental ratio of Hf:B:C=1:3:5). As confirmed by the TGA analysis of the raw materials in Section 4.1.1, the weight loss occurring below 700°C was due to the degradation of

$HfOCl_2 \cdot 8H_2O$, boric acid and phenolic resin. Therefore, at temperatures < 700°C, the precursor powders consisted of un-reacted but intimately mixed B_2O_3, HfO_2 and C. At temperature above 1300°C, the weight loss accelerates and tends to stabilize after 1600°C, which was believed to be related to the process of the carbothermal reduction reaction. The residual mass was approximately 50%. With regard to the DTA results, the endothermic peak at 1226°C suggests the beginning of the carbothermal reduction reaction. The reason why its practical onset temperature was lower than the calculated reaction threshold temperature of 1523°C might be due to the formation of the intermediate products, such as highly reactive boron or boron sub-oxide, which could react with HfO_2 to form HfB_2 at lower temperature, as shown in Equation 4.4, since this reaction is favourable at 1350°C according to thermodynamic calculations.

$$HfO_2 + 2B \text{ or } B_2O_2 + 2C \rightarrow HfB_2 + 2CO \text{ or } 4CO,\ \Delta G < 0 \text{ at } 1350^oC \quad (4\text{-}4)$$

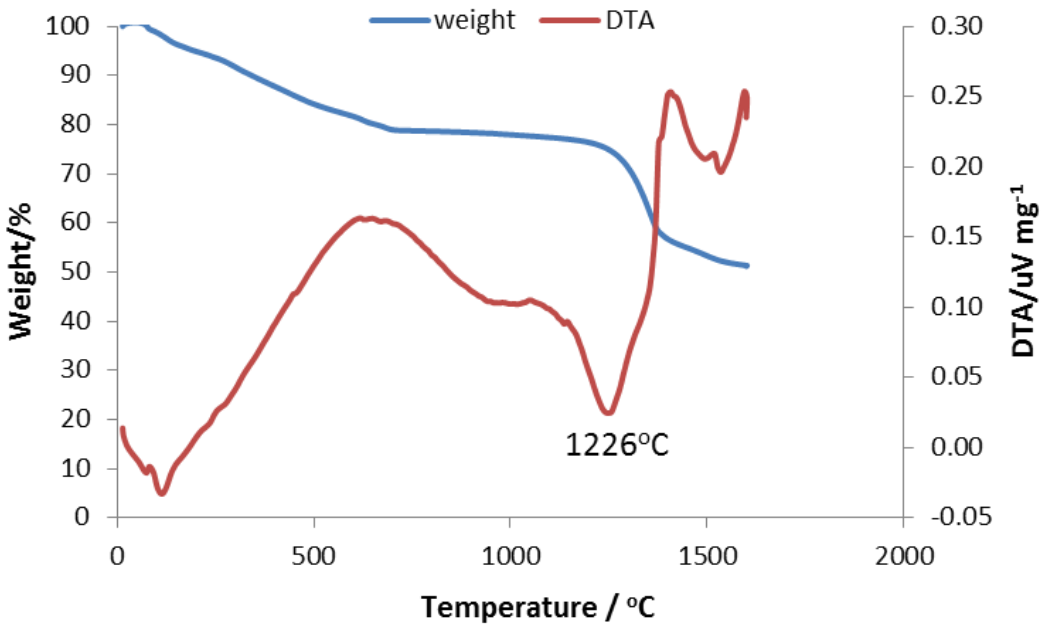

Figure 4.10 TGA-DTA curve of the sol-gel derived precursor, the elemental ratio of Hf:B:C=1:3:5

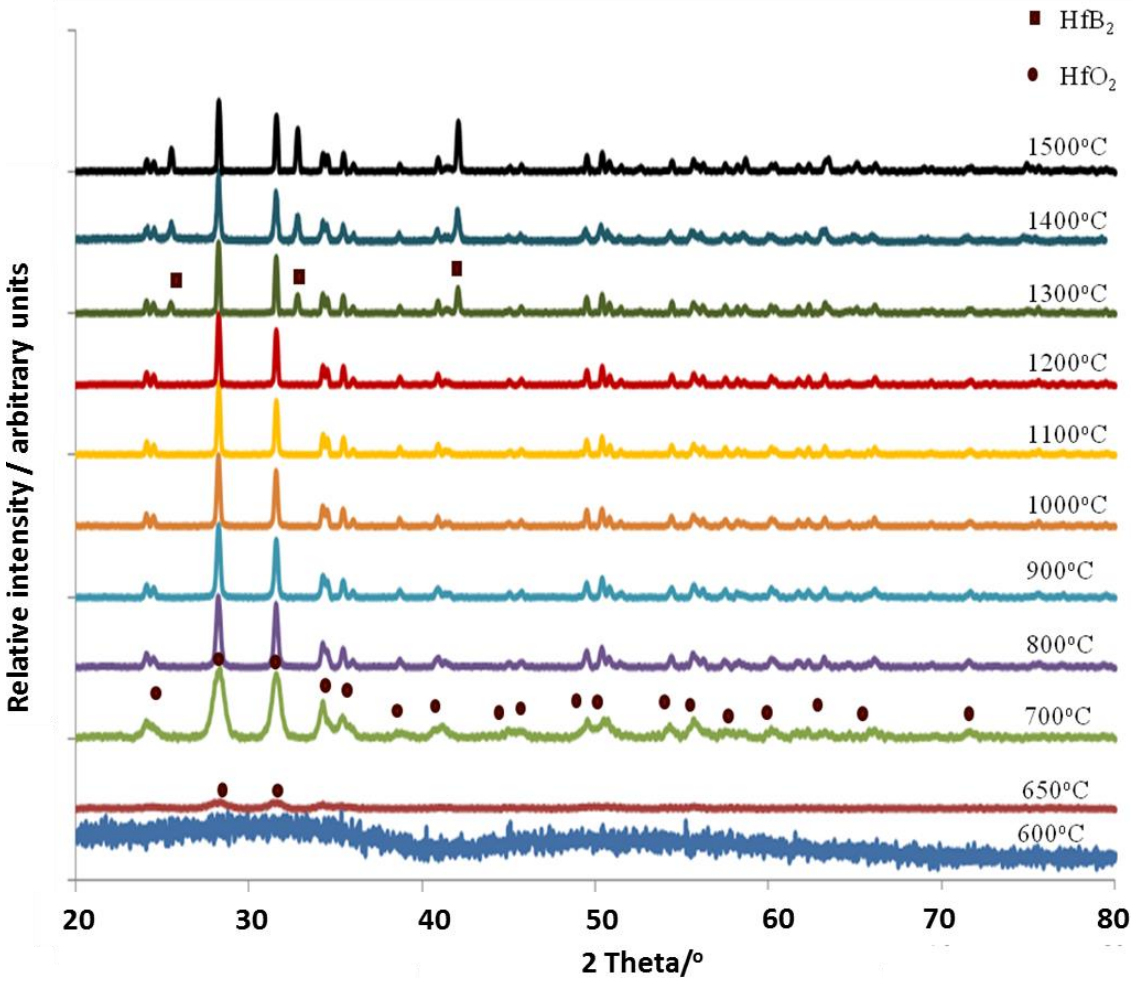

Figure 4.11 XRD patterns of the HfB_2 precursor powders, elemental ratio of Hf:B:C=1:3:5, heated from 600°C to 1500°C with 0.1 h dwell in argon (analysis done by Dr. Venugopal)

Figure 4.11 shows the high-temperature XRD patterns for the precursor powders with the elemental ratio of Hf:B:C=1:4:5, heated from 600°C to 1500°C with a 0.1 h dwell. Diffraction peaks of HfO_2 were detected at 650°C, which was in agreement with the previous TGA analysis of the precursors. The peaks associated with HfB_2 appeared at 1300°C. As the XRD apparatus (D2 Phaser) was only capable of identifying phases of >5 mol%, there was a lag between the true HfB_2 formation temperature and the temperature when the diffraction peaks due to HfB_2 were detected. Therefore, the high temperature XRD study again showed that the onset temperature of the carbothermal reduction reaction was below 1300°C. However, HfO_2 instead of HfB_2 was the major phase in the

precursors heat treated at 1500°C for 0.1 h.

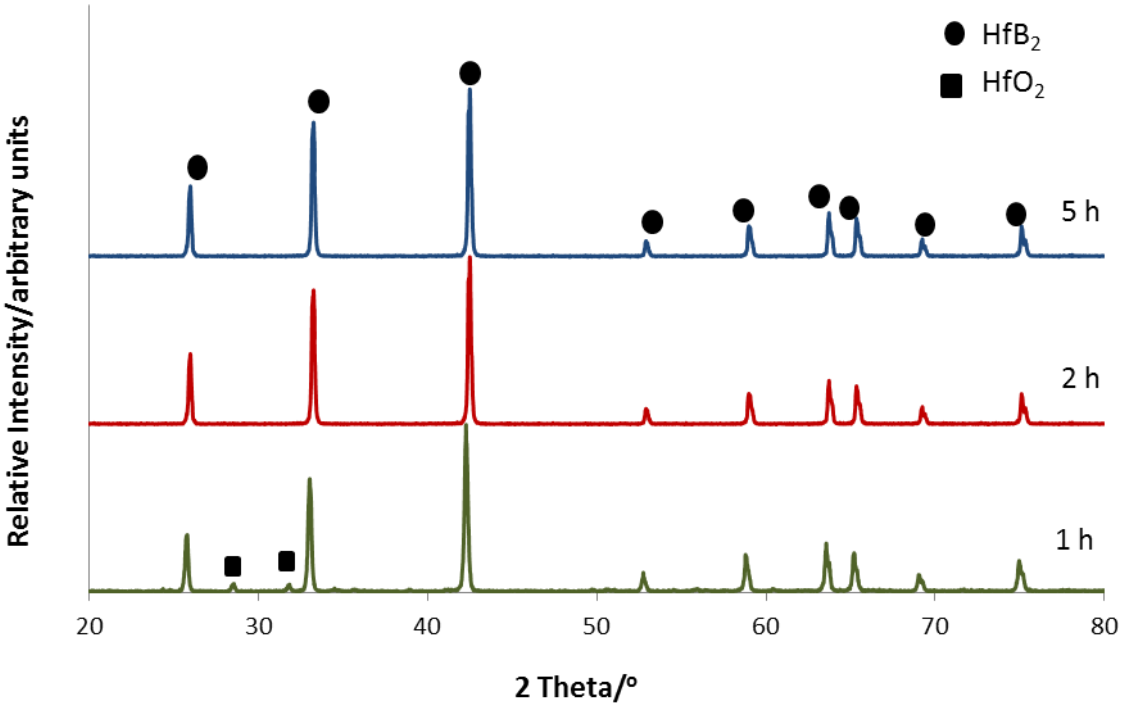

Figure 4.12 X-ray diffraction patterns of the precursors (elemental ratio of Hf:B:C=1:4:5) heat treated at 1600°C with various dwell time

The carbothermal reduction required higher temperatures or longer dwell times to achieve pure HfB_2 powders. Venugopal et. al [265] reported high-purity HfB_2 powders were formed after heat treatment at 1300°C for 25 h, which was probably too long for economic industrial use. Therefore, the precursors with the elemental ratio of Hf:B:C=1:4:5 were heat treated at 1600°C for 1 h, 2 h and 5 h, and the resulting powders were analysed by XRD. Figure 4.12 shows that dwell time of a 1 hour at 1600°C was still insufficient for the carbothermal reduction reaction to complete as small peaks arising from monoclinic HfO_2 were found, whilst dwell time of 2 hours resulted in nominal single-phase HfB_2 powders based on XRD analysis. It was believed that the carbothermal reduction reaction rate was improved by using the well-mixed $HfOCl_2$, boric acid and phenolic resin precursors prepared by the sol-gel approach.

For the carbothermal reduction reaction, use of excess boron oxide to compensate for the boron loss during HfB_2 synthesis was vital if pure HfB_2 powder was to be achieved. According to the original carbothermal reduction reaction, Equation 4.3, the elemental ratio of Hf:B:C=1:2:5 was the exact stoichiometric ratio, which in fact resulted in the formation of HfC rather than HfB_2. HfC was obtained by the side reaction between HfO_2 and carbon via Equation 4.5, which has been reported to occur at temperatures >1573°C [141]. Generally, the carbothermal reduction reaction of HfO_2, Equation 4.3, is thermodynamically favourable compared to Equation 4.5. However, the boron loss during HfB_2 synthesis led to unreacted HfO_2 and C being able to react to form HfC after the heat treatment at 1600°C.

$$HfO_2 + 2C \rightarrow HfC + CO \quad (4\text{-}5)$$

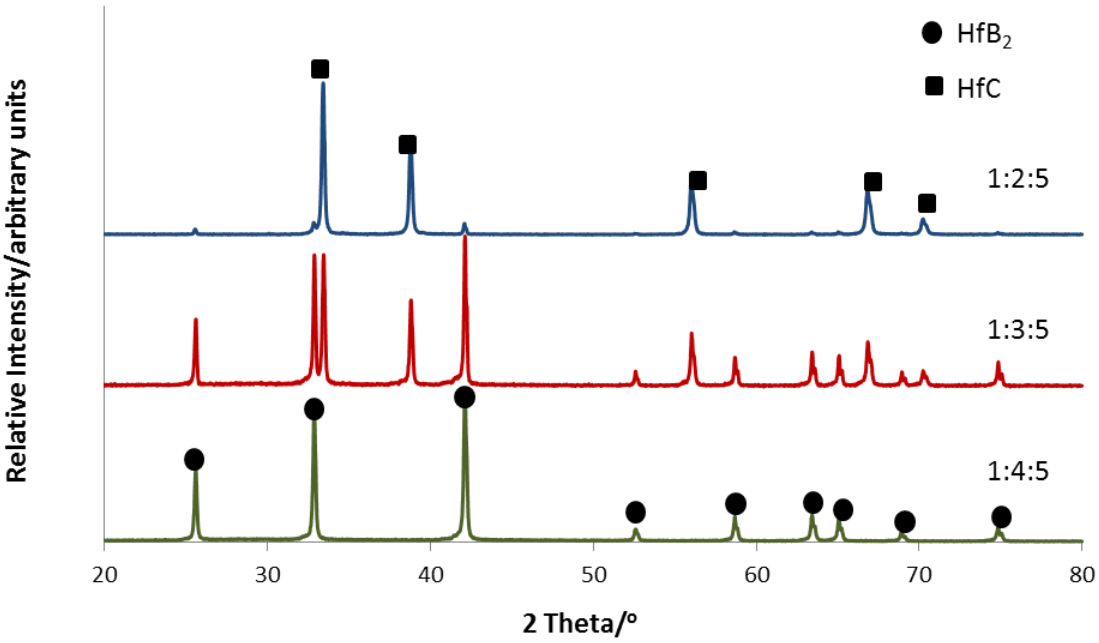

Figure 4.13 XRD patterns of the powders synthesized with various Hf:B:C ratio, 1:2:5, 1:3:5 and 1:4:5, at 1600°C for 2 h

As seen from Figure 4.13, the content of HfC in the resultant powders from the precursors with different Hf:B:C ratio was significantly reduced by adding 50%

and 100% excess boron to compensate for the boron loss, i.e. changing the elemental ratio of Hf:B:C of the precursors from 1:2:5 to 1:3:5 and 1:4:5. The mass fraction of HfB_2 in these powders was calculated via Equation 4.6,

$$\text{wt\% } HfB_2 = \frac{1}{1 + I_{HfC}K_{HfC}/I_{HfB2}K_{HfB2}} \quad (4\text{-}6)$$

where, I_{HfC} and I_{HfB2} are the relative intensities of HfC's and HfB_2's strongest diffraction peaks, and K_{HfC} and K_{HfB2} are the reference spectral intensities of HfC and HfB_2. According to the JCPDS cards number 00-039-1491 and 00-038-1398, the reference spectral intensities for cubic HfC and monoclinic HfB_2 were 16.98 and 17.70, respectively. Thus, the calculated HfB_2 mass fraction increased from 15 to 48 wt% when the ratio of Hf:B:C changed from 1:2:5 to 1:3:5 and single-phase HfB_2 was obtained from the precursors with a Hf:B:C ratio of 1:4:5.

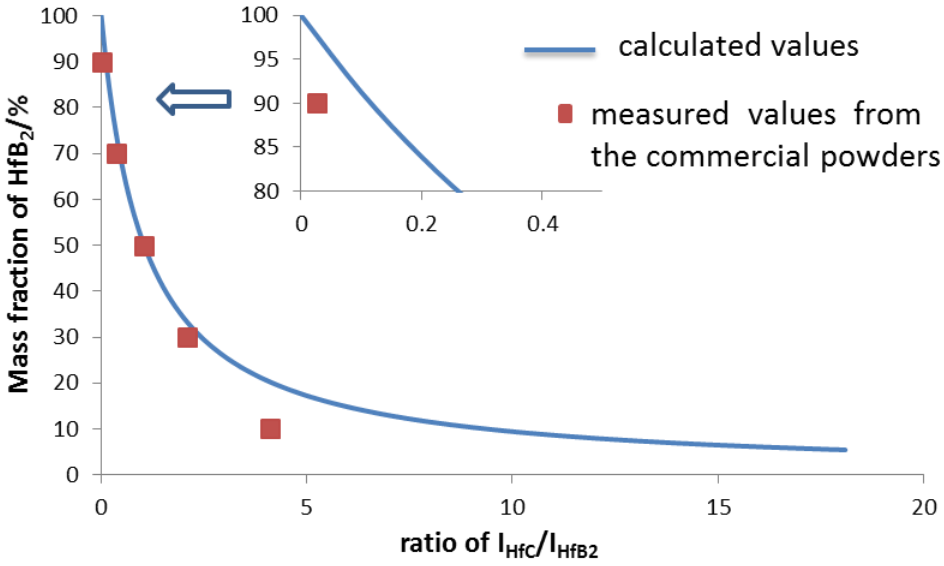

Figure 4.14 HfB_2 mass fractions vs. the intensity ratio of the strongest peaks of HfC/HfB_2

Commercial HfC (H.C. Starck, Germany) and HfB_2 (H.C. Starck, Germany) powders were used to check the validity of the curve by mixing with different mass fractions of HfB_2, viz. 10, 30, 50, 70 and 90 wt%. The measured HfC/HfB_2

intensity ratio of the strongest peaks from the XRD patterns of these commercial powder mixtures was compared with the calculated values. The commercial powder mixtures containing 30, 50 and 70 wt% HfB_2 showed good consistency with the calculated values while the ones containing 10 and 90 wt% showed significant deviation due to the limitation of XRD for identifying low mass fraction phases. Hence, it should be noted that the error for calculating the mass fraction of a phase <10 wt% can be more than 50%. This equation for calculating the mass fraction of different phases were also used for the analysis of the monoclinic/tetragonal HfO_2 fractions later.

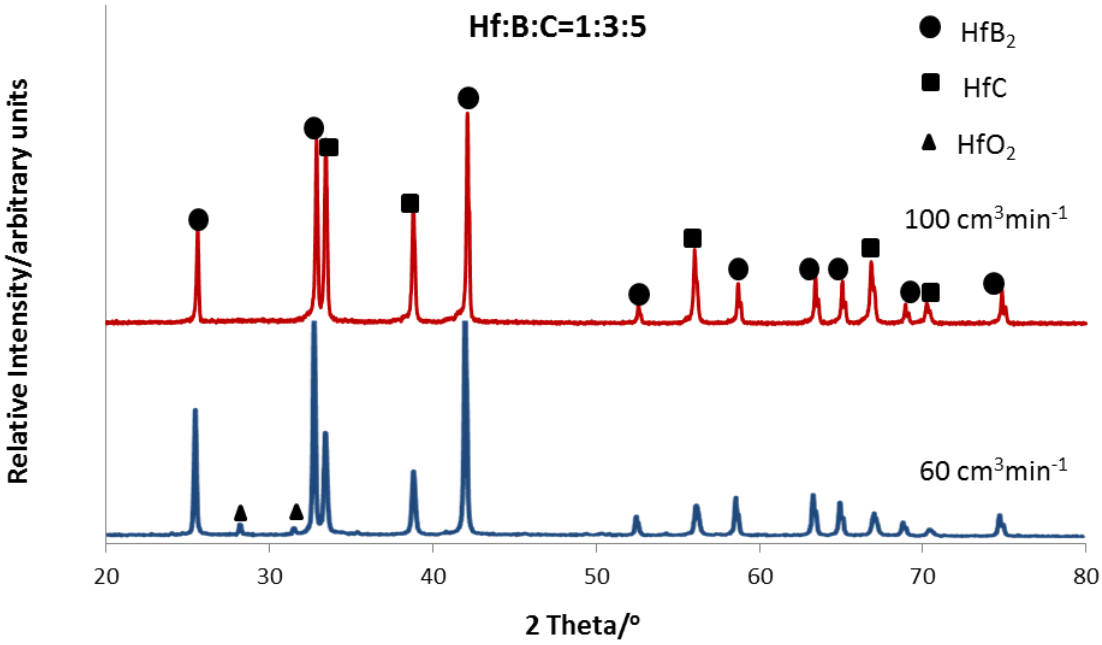

Figure 4.15 XRD patterns of the precursor powders (Hf:B:C=1:3:5) heat treated at 1600°C for 2 h, with argon flow rates of 60 and 100 cm^3min^{-1}

The main cause for the boron loss was due to the evaporation of B_2O_3; the melting point and boiling point of B_2O_3 under 1 atm vapour pressure are 450 °C and 1860°C, respectively. Hence, the B_2O_3 could readily evaporate when maintained at 1600°C for up to 2 hours and the B_2O_3 vapour was continuously removed from the reaction zone by argon flow. Figure 4.15 shows that faster argon flow rate led to a higher content of HfC impurity in the reaction products

because B_2O_3 in the precursors evaporated faster with lower B_2O_3 vapour pressure. However, if the argon flow rate was reduced too much, it became difficult to protect the reactants from oxidation. Thus, an argon flow rate of 100 $cm^3\ min^{-1}$ was chosen for all heat treatment performed in this work. The exact evaporation rate of B_2O_3 was still unknown because B_2O_3 was simultaneously consumed by the carbothermal reduction reaction. Generally, pure HfB_2 powders were reported to be successfully synthesised from HfO_2, B_2O_3 and carbon with a Hf:B:C ratio of 1:3:5 only when B_2O_3 sublimation was the predominant reason for boron loss [78].

$$B_2O_3 + 6Cl^- + 3C \rightarrow 2BCl_3 + 3CO \quad (4\text{-}7)$$

The reaction between B_2O_3 and the chlorine ion from the degradation of the precursors, Equation 4.7, was another possible reason causing boron loss. This reaction was reported to become thermodynamically favourable at 500°C [266]. Since B_2O_3 and C were the thermal decomposition products of boric acid and phenolic resin at temperatures >600°C, the boron loss due to the B_2O_3 and Cl_2 reaction could be roughly estimated: 1 mol of $HfOCl_2$ precursor released 1 mol of Cl_2, which consumed $^1/_3$ mol B_2O_3. The reaction also consumed carbon, as a result, the stoichiometry of the carbothermal reduction of HfO_2 became too complicated to be controlled.

4.1.2.3 Characterization of the powders from the sol-gel approach

Since the composition and purity of the powders from the sol-gel derived precursors had been identified by XRD, the morphology and particle size of these powders were analysed by SEM, BET and Mastersizer. As seen from Figure 4.16(a), the majority of the coarser particles in the sample with a Hf:B:C ratio of 1:2:5 were HfC, with a small amount of finer HfB_2 particles also present in this powder as confirmed by the supplemental EDX mapping. It can also be

seen from Figure 4.16(a)-(c) that the purity of HfB_2 was improved by adding excess boron to compensate for the boron loss during the carbothermal reduction reaction, in agreement with the previous XRD analysis. Although the Hf:B:C ratio was changed from 1:2:5 to 1:3:5 and 1:4:5, the sizes of the spherical HfB_2 particles obtained from the sol-gel derived precursors did not change significantly and were finer than the commercial Treibacher HfB_2 powders, as shown in Figure 4.16(d).

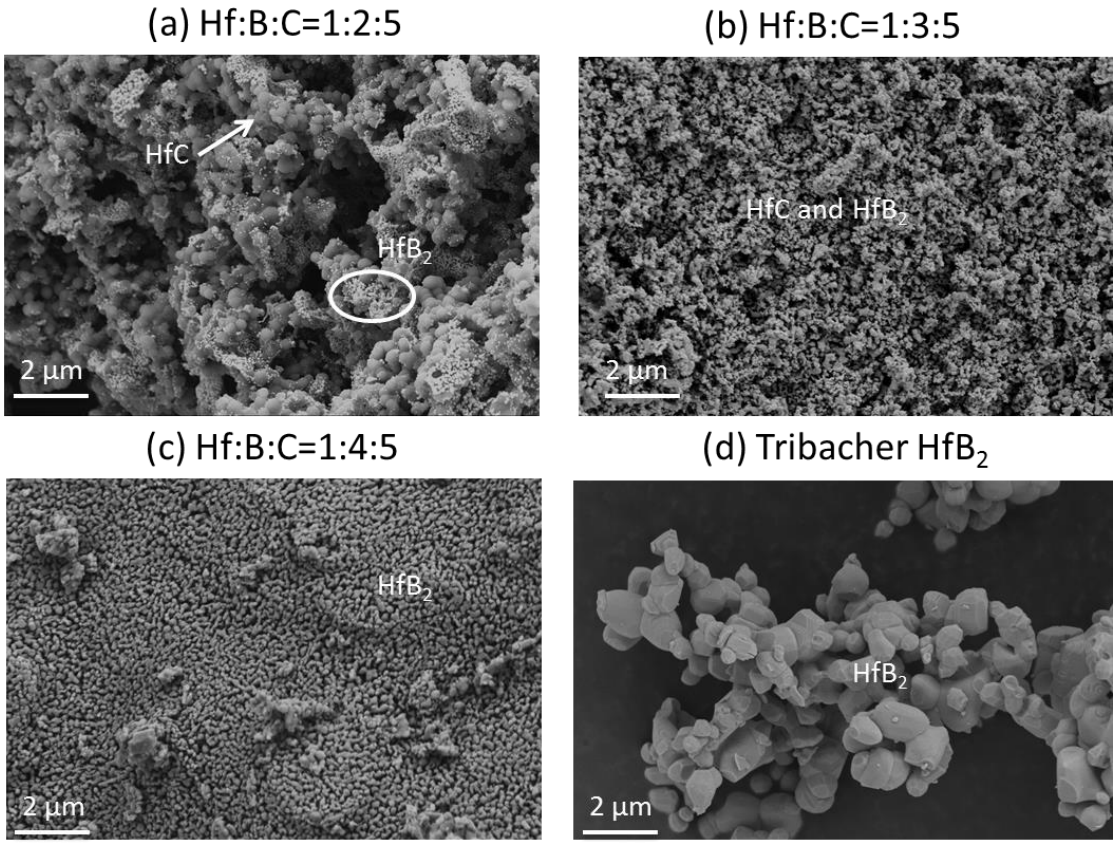

Figure 4.16 Comparison of the particle size and morphology of the (a)-(c) HfB_2 powders synthesized by carbothermal reduction reaction from sol-gel derived precursors with different Hf:B:C ratios and (d) commercial HfB_2 powders

Table 4.3 Comparison of the mean particle size and surface area between the HfB_2 powder prepared by sol-gel derived precursors and commercial HfB_2

Sample	Mean particle size/ µm	Surface area/m^2 g^{-1}
HfB_2 from sol-gel approach	0.19	2.98
Tribacher HfB_2	1.90	1.92

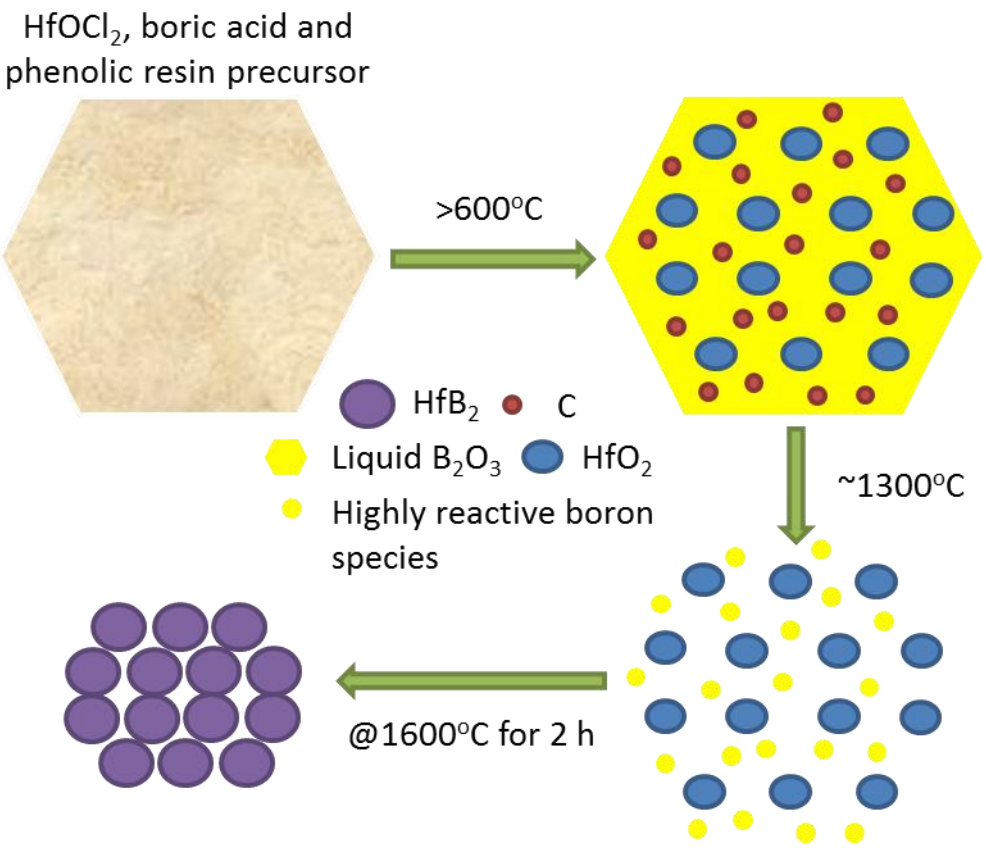

Figure 4.17 Schematic of the synthesis of HfB_2 powder via carbothermal reduction reaction, from sol-gel derived precursor to sub-micro sized HfB_2 powder

Table 4.3 gives the mean particle size and surface area of the HfB_2 powders prepared by carbothermal reduction reaction from the sol-gel derived precursors; the values were 0.19 μm and 2.98 m^2g^{-1}, respectively, whilst for Tribacher HfB_2, the mean particle size and surface area of the powder were 1.90 μm and 1.92 m^2g^{-1}. The formation of extremely fine HfB_2 particles from the sol-gel derived precursors was related to the size of HfO_2 nucleus in the precursors. As illustrated in Figure 4.17, when the sol-gel derived precursors were heated to >600°C, it is believed that HfO_2 nucleus was formed inside the precursor particles and the nuclei growth was restricted by the surrounding carbon, which was from the degradation of the cross-linked phenolic resin. Then, when the furnace temperature reached >1300°C, B_2O_3 will have been present as a liquid phase and reduced by carbon to release a highly reactive boron species [170],

which subsequently substituted for the oxygen in HfO_2 to form HfB_2. It should be noted that the HfB_2 particle growth involved solid-liquid equilibrium and excess B_2O_3 could lead to particle coarsening. Therefore, the main advantage of the sol-gel approach was the formation of sub-micron sized HfB_2 powders; the atomic-level mixing of the starting materials reduced the carbothermal reduction reaction temperature/time and the carbon from the degradation of cross-linked phenolic resin inhibited initial HfO_2 nuclei growth.

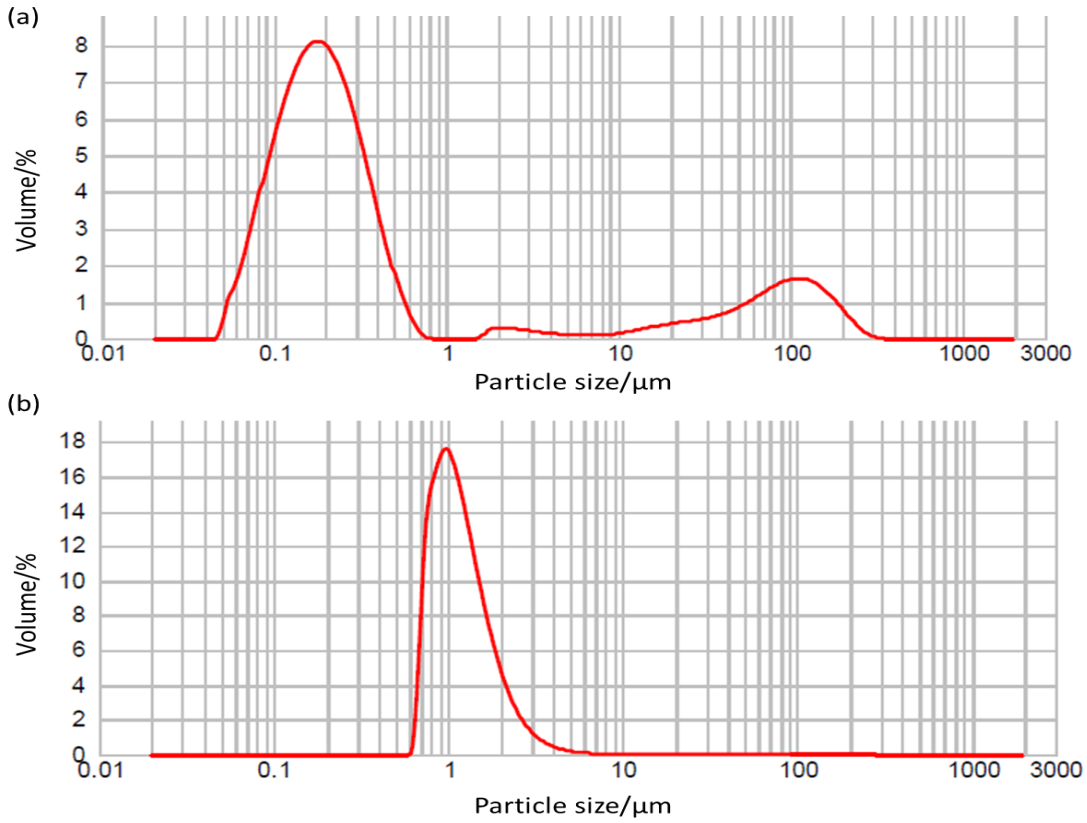

Figure 4.18 Particle size distributions of (a) the HfB_2 powder prepared by the sol-gel derived precursor with Hf:B:C ratio of 1:4:5 and (b) commercial HfB_2 powder

Although sub-micron sized HfB_2 powder was successfully synthesized by the sol-gel approach, Figure 4.18 shows the presence of large hard agglomerates, with a size of up to 100 μm. As a result, the surface area of the sub-micron powders was only 1.5 times larger than that of the commercial micron sized HfB_2 powders. The agglomeration resulted from the hard precursors formed

from drying and grinding of the cross-linked phenolic resin. As seen in Figure 4.19, the precursor powders consisting of $HfOCl_2$, boric acid and phenolic resin showed similar morphology and particle size as the agglomerates in the resultant HfB_2 powders, indicating that the nucleation and particle growth of HfB_2 took place inside the original precursor particles.

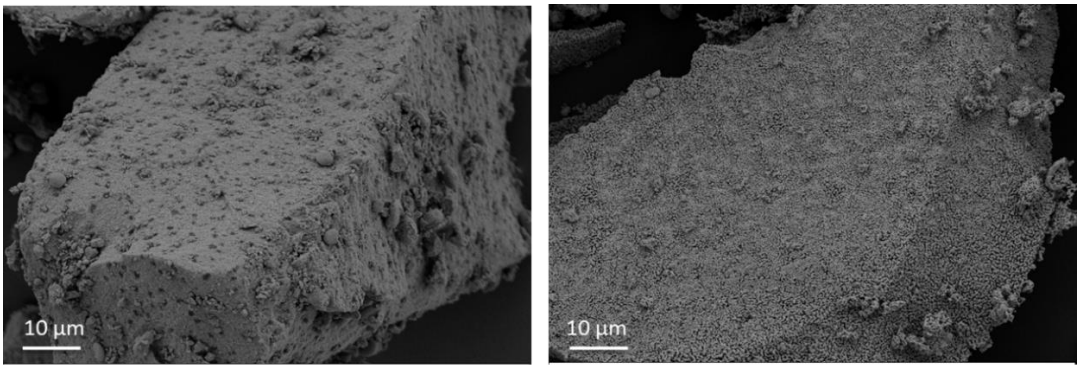

Figure 4.19 FEGSEM images of (a) the bulk $HfOCl_2$, boric acid and phenolic resin precursors with Hf:B:C ratio of 1:4:5 and (b) the hard agglomerates in the resultant HfB_2 powder

4.1.2.4 Drawbacks of using sol-gel derived precursors for carbothermal reduction reaction

The sub-micron HfB_2 powder obtained from the sol-gel derived precursors was beneficial for densification as finer particles could increase the surface energy, thus improving its sinterability, although the large agglomerates could lead to the formation of large grains. The sinterability of this powder will be discussed in Section 4.3 and compared with the HfB_2 powder synthesized by a borothermal reduction method.

The main drawback of the sol-gel approach was associated with the residual chlorine from the $HfOCl_2$, despite the fact that the precursors were calcined to remove ~80% of the chlorine. The residual chlorine not only caused extra boron and carbon loss, but could also damage the furnace in some cases. Since

chlorine, or the chlorine ion was highly reactive with metal oxide, the alumina crucible and insulation used for the synthesis was corroded after the heat treatment of the sol-gel derived precursors. As seen from Table 4.4, aluminium, oxygen and chlorine were detected on the end caps of the tube furnace, suggesting that the alumina in the crucible and tube was reacting with the chlorine and being transported through evaporation and condensation.

Table 4.4 Composition analysis of the contamination deposited on the end caps of the tube furnace after HfB_2 synthesis

Element	wt%
Al	52
O	41
Cl	5
B	2

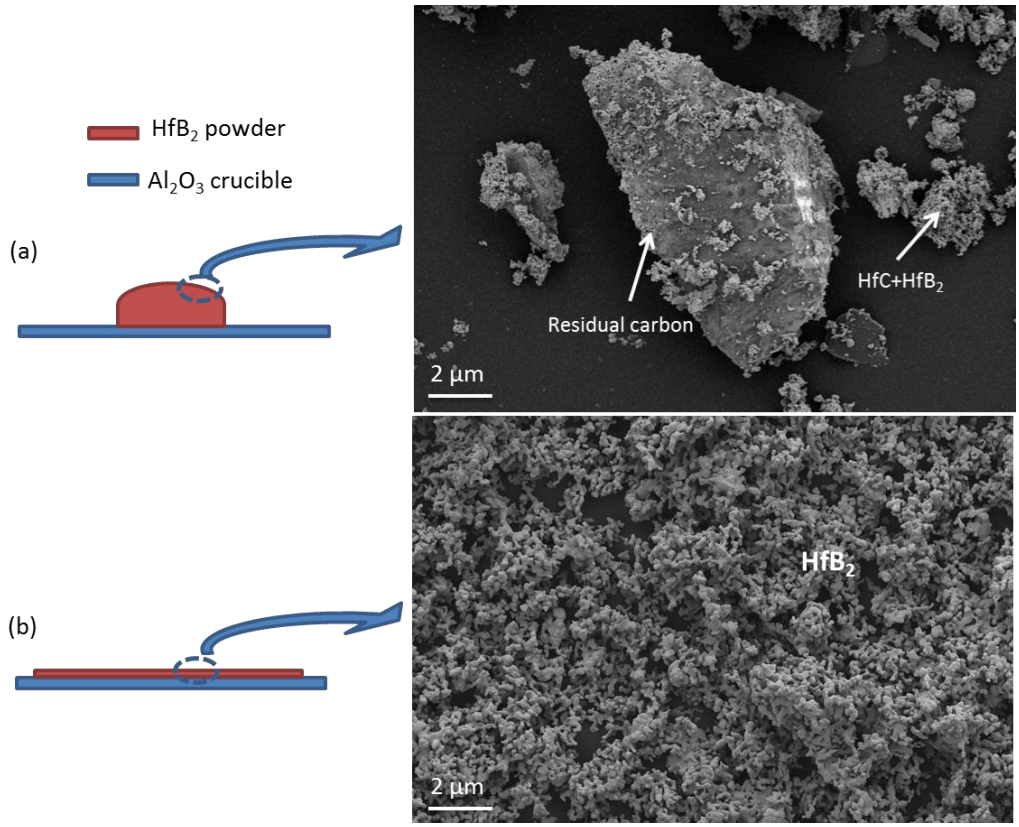

Figure 4.20 The methods of arranging the precursor powders (Hf:B:C ratio of 1:4:5) in alumina crucibles and their effect on the homogeneity of the HfB_2 powders yielded from the carbothermal reduction reaction

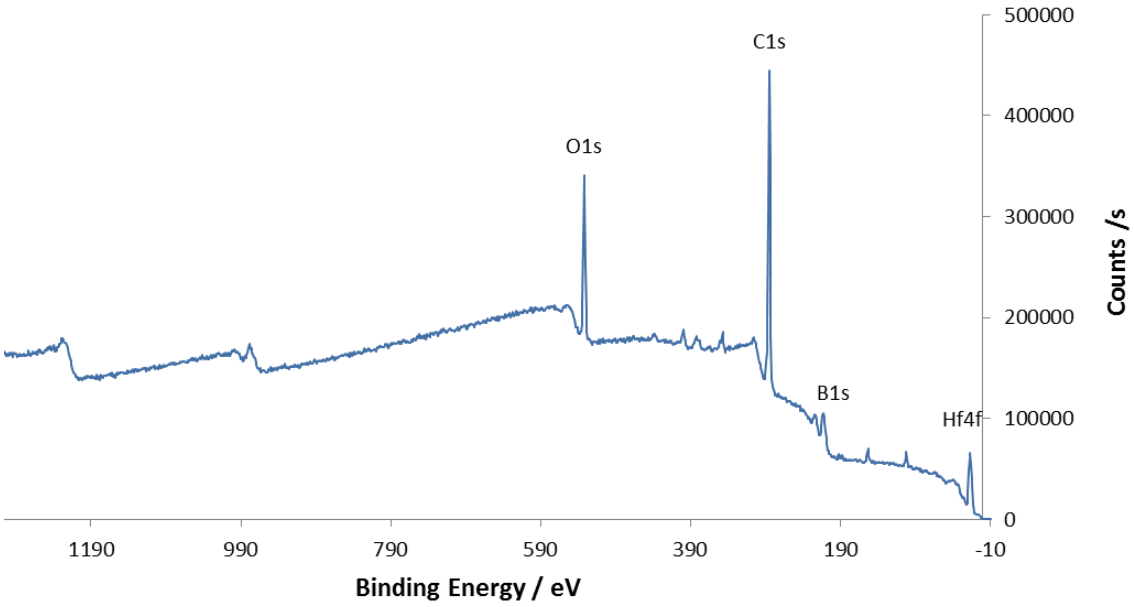

Figure 4.21 XPS elemental survey for the HfB_2 powders obtained from carbothermal reduction. The precursors were placed in alumina crucible using the method shown in Figure 4.20(a) and the HfB_2 powder at the top analysed by XPS

Another issue of the carbothermal reduction synthesis involved the presence of liquid B_2O_3. A glassy B_2O_3 layer was found on the surface of the alumina crucible after use. It suggested that the distribution of liquid B_2O_3 in the precursors might be affected by gravity during heat treatment at 1600°C. Hence, if the precursor powders (Hf:B:C=1:4:5) was simply stacked up on the crucible, as shown in Figure 4.20(a), there would be a gradient of B_2O_3 distribution along the height of the stack, resulting in the lower part of the powder bed B_2O_3-rich and leading to unreacted carbon and formation of HfC at the top. It should be noted that the amorphous carbon impurities in the HfB_2 powder could not be detected by XRD due to the crystallinity difference between carbon and HfB_2. This was why XPS was used to identify the amorphous or small fraction impurities, e.g. carbon, HfC and B_2O_3, Figure 4.21. These impurities were difficult to remove without causing HfB_2 to oxidize as the surface of sub-micron HfB_2 powder was found to be readily oxidized due to the high temperature or hot water employed for removing carbon or B_2O_3. In terms of improving the purity of the resultant HfB_2 powder,

the precursors had to be placed evenly in the crucible, with the height of the powder bed as small as possible, as shown in Figure 4.20(b), to avoid the liquid B_2O_3 settling. This could be a major issue for when scaling up the process.

4.1.2.5 Precipitation approach used for the synthesis of HfB_2 powder

Since any chlorine left in the precursor can reduce the purity of the resultant HfB_2 powder and damage the alumina tube furnace, NH_3OH was used to remove chlorine from $HfOCl_2{\cdot}8H_2O$ before the latter was with B_2O_3 and phenolic resin. The solubility constant of $Hf(OH)_4$, $\log_{Ksp}$, is only −51.8 ± 0.5, which is so low that $Hf(OH)_4$ would precipitate as soon as it is formed when NH_3OH reacts with $HfOCl_2 \cdot 8H_2O$ aqueous solution. The resulting white precipitates were filtered and rinsed by deionized water for 5 times to remove the water-soluble NH_3Cl and then calcined at 400°C for 3 h. Table 4.5 shows that chlorine was completely removed after the calcination of the precipitates, which were obtained at different pH values. In addition, $Hf(OH)_4$ precipitates were converted to HfO_2 with the loss of 2 water molecules, which was confirmed by measuring the mass change from the original $HfOCl_2{\cdot}8H_2O$ to the calcined precipitates, i.e. the molecular weight of HfO_2 was exactly 52% of that of $HfOCl_2{\cdot}8H_2O$. Hence, it can be concluded that $Hf(OH)_4$ precipitates were stable over a wide pH range of 4-10 at ambient temperature.

Table 4.5 Elemental analysis of the calcined $Hf(OH)_4$ by XPS

pH	Hf/wt%	O/wt%	Cl/wt%
5	84.6	15.4	0
6	84.5	15.5	0
7	84.9	15.1	0
8	84.5	15.5	0
9	84.5	15.5	0
10	84.8	15.2	0

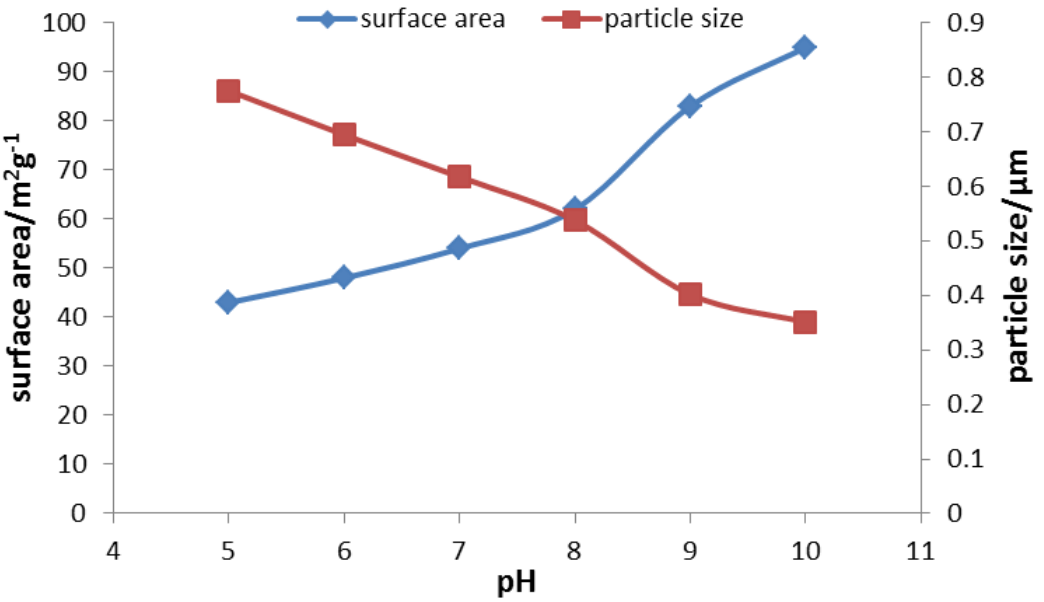

Figure 4.22 Surface area and particle size of the calcined $Hf(OH)_4$ vs. pH value

The surface area and size of the $Hf(OH)_4$ precipitates were controlled by the pH value. Figure 4.22 shows that the surface area of the calcined $Hf(OH)_4$ increased with increasing pH. The corresponding particle size was calculated using the model developed by Andre et.al. [267]. The model was reliable for predicting the particle size-surface area relationship of spherical particles. However, as the surface measurements were performed on the calcined $Hf(OH)_4$ precipitates, which had random shapes, the particle sizes plotted in Figure 4.22 just gave a rough idea that higher pH could lead to finer precipitates. Large agglomerates were found in the $Hf(OH)_4$ precipitates formed at pH >9, thus a pH of 8.5±0.3 was used to prepare $Hf(OH)_4$ precipitates with moderate size and no significant agglomerates. Figure 4.23 shows that the observed particle size of the $Hf(OH)_4$ precipitates formed at 8.5 is ~0.5 µm, which is in agreement with the calculated values based on surface area measurements. It should be noted that during HfB_2 synthesis, the precipitates in the precursors could be finer due to the presence of phenolic resin, which hindered the formation of $Hf(OH)_4$ agglomerates.

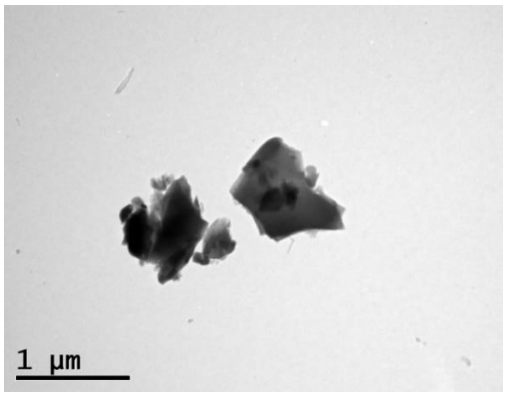

Figure 4.23 TEM image of the $Hf(OH)_4$ precipitates formed at pH of 8.5, followed by drying at 400ºC and grinding using a pestle and mortar

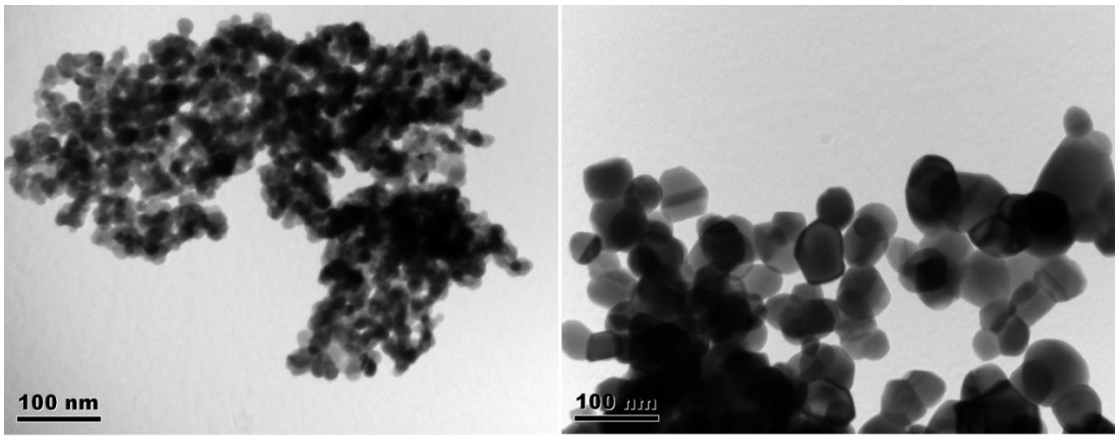

Figure 4.24 TEM images of HfO_2 nuclei formed by calcination of (a) $HfOCl_2$, H_3BO_3 and phenolic resin precursor and (b) $Hf(OH)_4$, H_3BO_3 and phenolic resin precursor at 1100ºC for 1 h in air

As discussed before, the size of the initial HfO_2 nuclei played an important role in controlling the particle size of the HfB_2 powder obtained from the carbothermal reduction reaction. The HfO_2 particles resulted from the precursors involving $HfOCl_2$ and $Hf(OH)_4$ are compared in Figure 4.24. Both the precursors were calcined at 1100ºC for 1 h in air to allow O-Hf-O to rearrange to form HfO_2 crystallites. In these precursors, phenolic resin and its degradation product carbon could inhibit the HfO_2 nuclei growth and were removed later by forming CO. B_2O_3 was removed as well by rinsing the precursors with hot water. It can

be seen that the size of the HfO_2 nuclei obtained from the original sol-gel approach was ~10 nm, while the nuclei size increased to ~50 nm for the HfO_2 prepared by the precipitation approach.

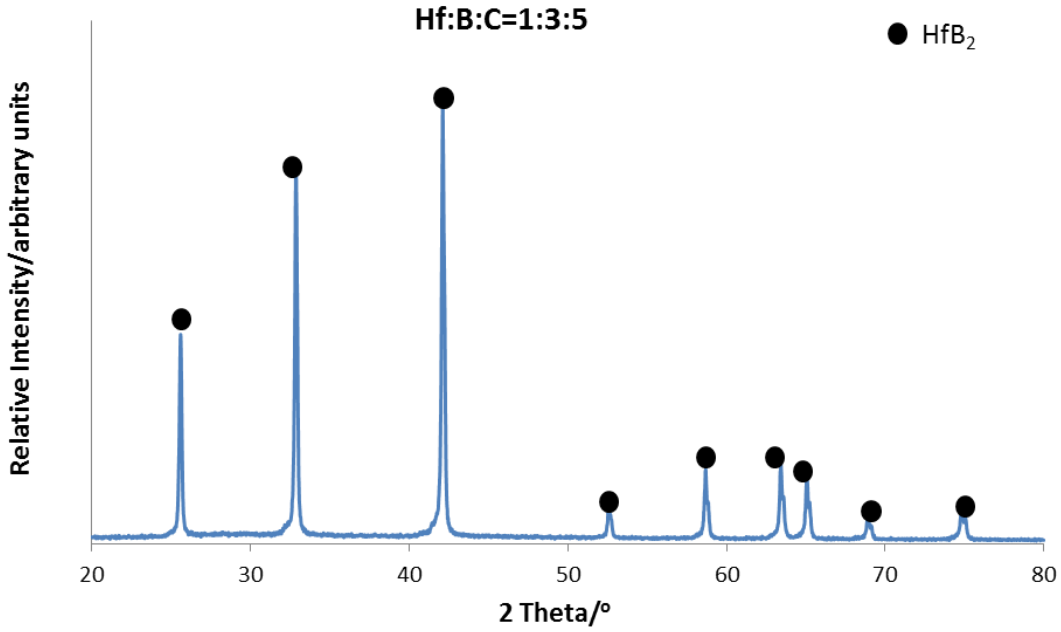

Figure 4.25 XRD of the HfB_2 powder synthesized by precipitation approach, the precursors with an Hf:B:C ratio of 1:3:5 was held at 1600°C for 2 h

Although coarser HfO_2 nuclei formed with the precipitation approach, the carbothermal reduction reaction of the precipitation-derived precursors was also completed at 1600°C for 2 h, the same as for the sol-gel derived precursors. Furthermore, the chlorine-free precipitation derived precursor reduced the boron loss due to the reaction involving chlorine, B_2O_3 and carbon. Figure 4.25 shows that HfB_2 was the only phase of the powder prepared using the precipitation-derived precursor with a Hf:B:C ratio of 1:3:5, whilst sol-gel-derived precursor required a ratio of 1:4:5 to form the same purity of HfB_2, as discussed previously. According to the morphology analysis of these powders in Figure 4.26(b), the HfB_2 powder obtained by the precipitation approach showed spherical particles with a mean particle size of ~600 nm, larger than that of the HfB_2 powder obtained by the sol-gel approach, Figure 4.26(a). The difference in

particle sizes was attributed to the difference in HfO_2 nuclei size yielded from $HfOCl_2$ and $Hf(OH)_4$, as the other processing conditions remained the same for these two approaches. For the precipitation approach, a Hf:B:C ratio of 1:3:5 was sufficient to achieve high purity HfB_2.

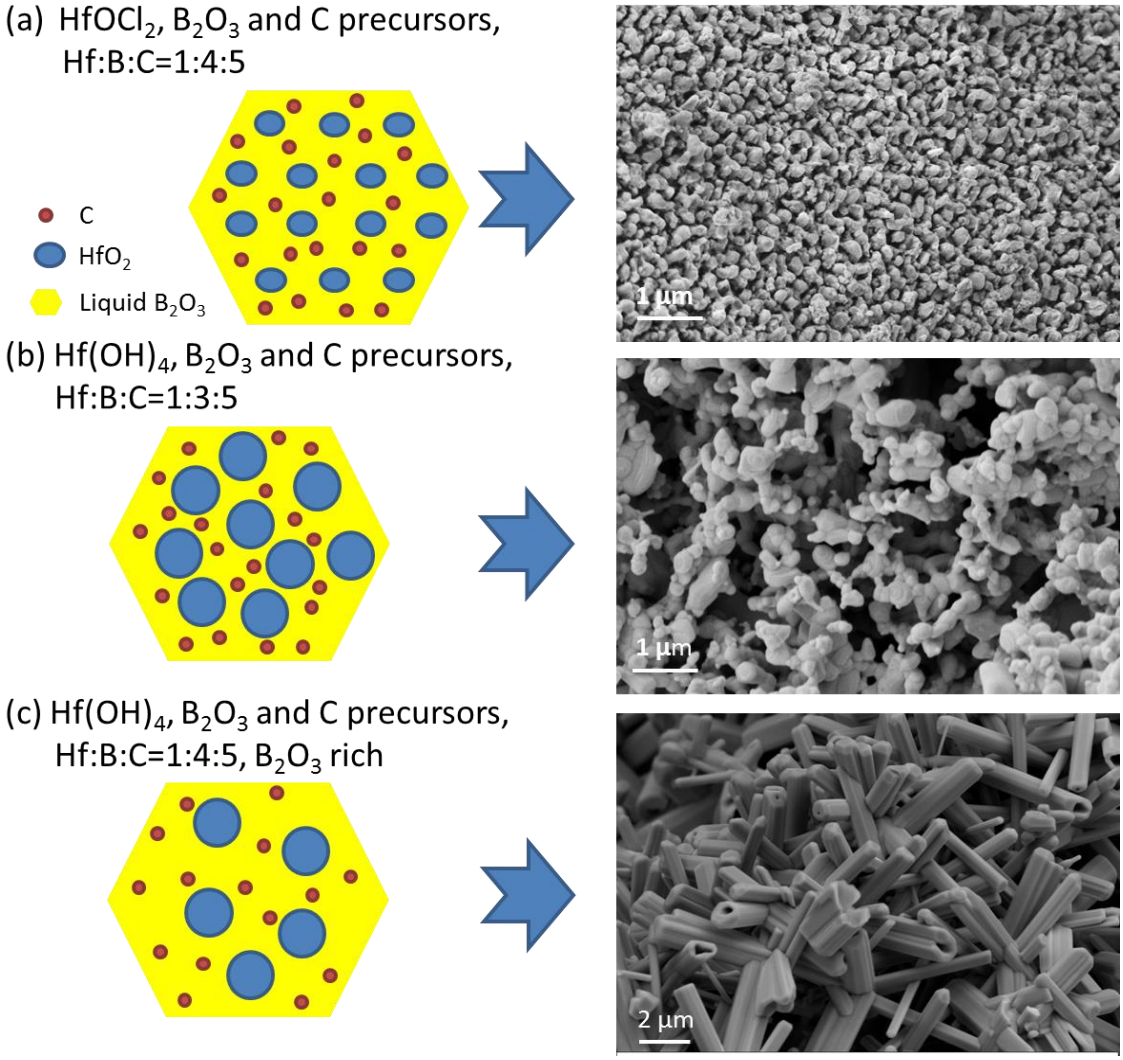

Figure 4.26 Comparison of the morphology and particle size of the HfB_2 powders yielded from (a) sol-gel derived precursors, (b) precipitation derived precursor with stoichiometric Hf:B:C ratio and (c) precipitation derived precursor with excess boron

It was interesting that the Hf:B:C ratio of 1:4:5 resulted in the formation of larger rod-like HfB_2 particles as shown in Figure 4.26(c). The anisotropic structure was

the typical product of a vapour-liquid-solid particle growth mechanism, which occurred under the condition of high concentration of liquid B_2O_3 [268]. The rod-shaped HfB_2 particles could be used to produce HfB_2 ceramics with tailored texture or preferred orientation, but may also be faced with the issue of poor sinterability due to the hollow structure. By comparing the particle morphology and size of the HfB_2 powder synthesised by various approaches, it was concluded that extremely fine HfO_2 nuclei and the presence of carbon, which inhibited HfB_2 particle growth, were critical for obtaining sub-micron HfB_2 powder, while high concentrations of B_2O_3 led to particle coarsening.

4.1.3 Synthesis of doped HfB_2 powders by carbothermal reduction reaction

4.1.3.1 Comparison of different dopants

As the primary aim of this work was to inhibit the volume change due to HfO_2 phase transformation during HfB_2-based ceramic oxidation, one way to achieve it was through doping. HfO_2 has three different metastable crystal structures. The stable low temperature phase is monoclinic hafnia (m-HfO_2), whilst tetragonal (t-HfO_2) and cubic hafnia (c-HfO_2) become stable at 1720^{o}C and 2600^{o}C, respectively. Certain phases of HfO_2 can be more favourable for some applications, for example, c-HfO_2 is used as a thermal barrier for jet engines as it has a high bulk modulus and lower thermal conductivity. Based on computational studies [269], dopant atoms that have a smaller covalent radii than that of Hf atom tend to stabilize HfO_2 in the tetragonal structure. Since four Hf-O bonds are already shorter than the others, the shorter stable dopant-oxide bonds can form with relatively small lattice distortions. On the other hand, dopant atoms with covalent radii larger than that of the Hf atom require the elongation of the bonds with nearby oxygen atoms. Cubic HfO_2, unlike monoclinic and tetragonal HfO_2, doesn't have any shorter Hf-O bonds, hence

the cubic structure is favoured by the dopants with metal atoms larger than Hf. It should be noted that the stable phase is also affected by the content of the dopant in HfB_2.

Table 4.6 Properties of several group V and VI refractory metal borides

Compound	Melting point /^oC	Crystal structure	Covalent radius of the metal atom / pm
HfB_2	3250	Hexagonal	175±10
YB_2	2220	Hexagonal	190±7
TaB_2	2850	Hexagonal	170±8
LaB_6	2250	Cubic	207±8
MgB_2	830	Hexagonal	141±7

In hypersonic applications, the oxygen permeation through the HfB_2 thermal protection system mainly depends on the diffusion rate of oxygen through the porosity inside the oxide scale rather than through the oxide itself, so it is critical to supress the HfO_2 phase transformation to avoid the resultant volume change. It was thus deemed necessary to find a compound that could form a solid solution with HfB_2. As can be seen from Table 4.6, TaB_2 possesses a melting point that is only 400^{o}C lower than that of HfB_2, showing that it can be used as a dopant at temperatures >1600^{o}C. Moreover, TaB_2 has same crystal structure as HfB_2 and the covalent radii of the Ta atom is slightly smaller than that of Hf atom, thus relatively less energy is required for the diffusion of Ta into the HfB_2 lattice. It also can be predicted that tetragonal HfO_2 should be the favourable product of the oxidation of Ta-doped HfB_2.

Although the melting point of YB_4 is 1000^{o}C lower than that of HfB_2, Y-doping was also investigated since zirconia and hafnia have a similar crystal structure and yttria doping of zirconia has been widely studied. Regarding the other metal diborides, the melting point of MgB_2 was considered too low for hypersonic applications. LaB_6 had a different crystal structure and a significantly larger

covalent radii of the metal atoms than HfB_2, as a result, it may have required extremely high energy for lanthanum to diffuse into HfB_2.

4.1.3.2 Synthesis and characterization of Y-doped HfB_2 powder

The synthesis of Y-doped HfB_2 powder involved the formation of yttria doped hafnia and its carbothermal reduction in the presence of B_2O_3. It was reported that the addition of 10 mol% Y_2O_3 can partially stabilize HfO_2 with a tetragonal crystal structure whilst 20 mol% Y_2O_3 can fully stabilize HfO_2 with cubic crystal structure [270]. A sol-gel approach was used to obtain yttria doped hafnia by mixing $Y(NO_3)_3 \cdot 6H_2O$ with $HfOCl_2 \cdot 8H_2O$ as well as boric acid and phenolic resin in their ethanol-based solution and citric acid was added as the chelation agent with a (Y+Hf)/citric acid molar ratio of 1:2. As shown in Figure 4.27, the use of citric acid improved the mixing of the Y- and Hf-compounds by bonding hafnium ions with yttrium ions to avoid the two ions precipitating at different times during the drying stage. The resultant precursors were calcined at 400°C. Figure 4.28 shows that both yttrium and hafnium were homogeneously distributed in the precursors after drying, which was considered beneficial for the diffusion of yttrium atoms into HfB_2 during the later heat treatment.

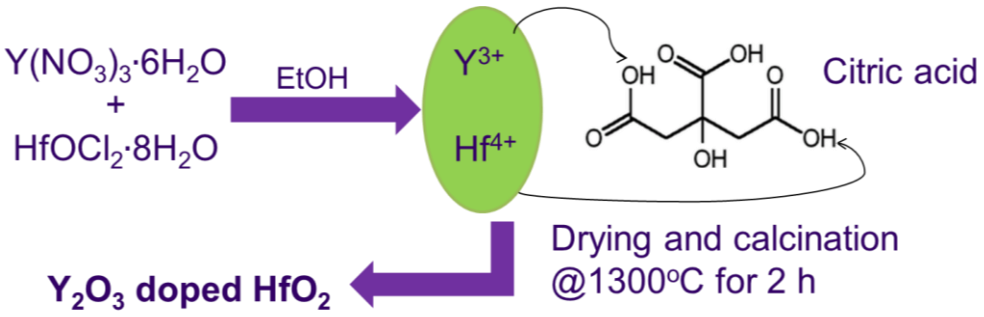

Figure 4.27 Schematic of the chelation process in the synthesis of Y_2O_3 doped HfO_2

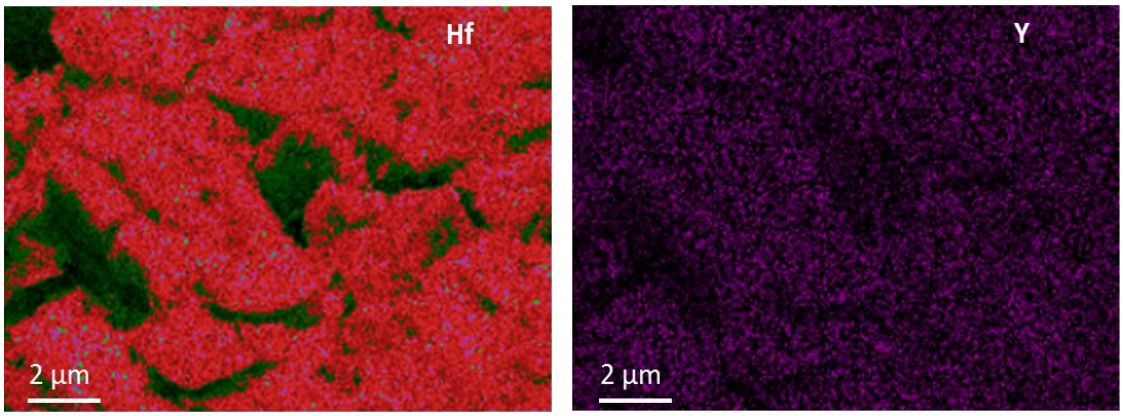

Figure 4.28 EDX mapping for hafnium and yttrium in the mixed precursors yielded from 8 wt% $Y(NO_3)_3 \cdot 6H_2O$ and $HfOCl_2 \cdot 8H_2O$

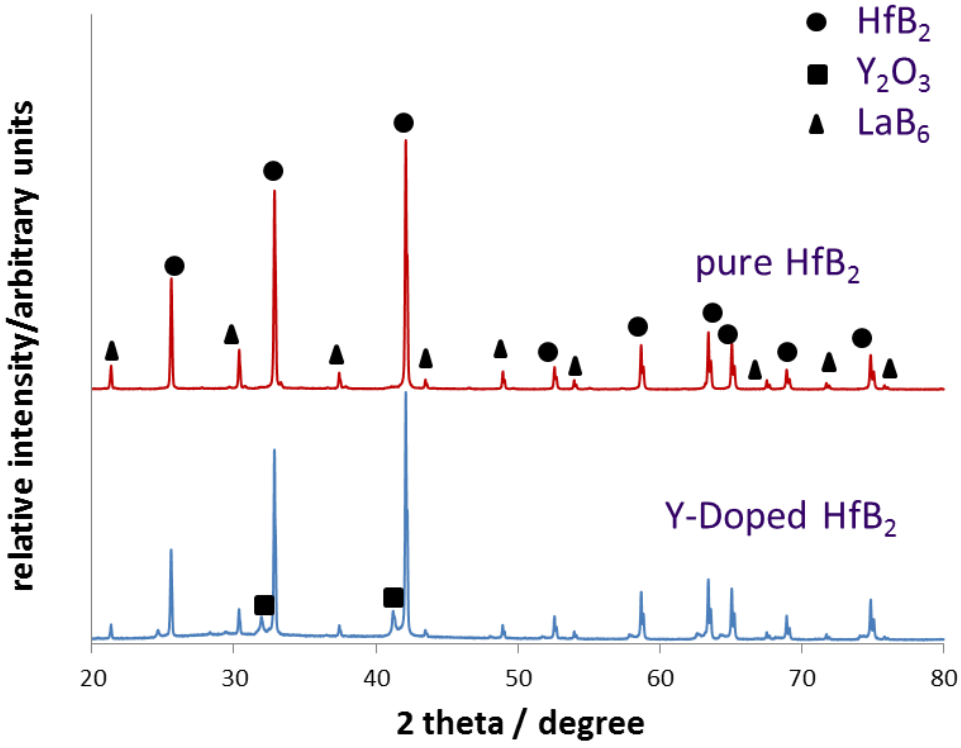

Figure 4.29 XRD patterns for pure and Y-doped HfB_2 powders obtained from carbothermal reduction synthesis. LaB_6 was used as a reference for the investigation of diffraction peak shifting.

The precursors containing mixed Y and Hf were heat treated at 1600°C for 2 h, which was under the same furnace conditions as the synthesis of pure HfB_2. It can be clearly seen from the XRD pattern of the resulting powders, Figure 4.29,

that HfB_2 was the majority phase with the presence of a small amount of Y_2O_3. In addition, no HfB_2 peak shifting was observed from Y-doped HfB_2 when compared with the pure HfB_2. The results were in agreement with the EDX mapping of Y-doped HfB_2 as shown in Figure 2.30. The Y-dopants formed a minor Y_2O_3 phase, which was segregated from HfB_2 during the carbothermal reduction reaction of the precursors. It was because YB_2 is a metastable phase and the reaction of Y_2O_3, B_2O_3 and carbon is not thermodynamically favourable at 1600°C.

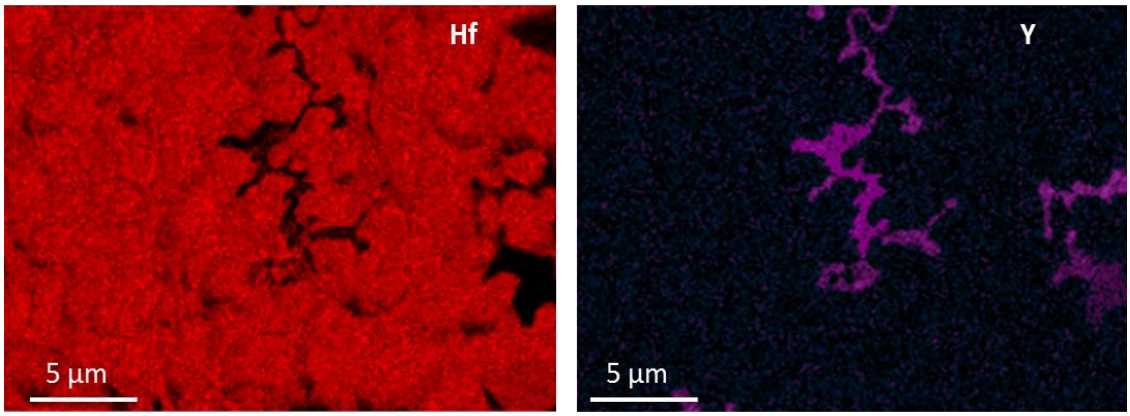

Figure 4.30 EDX mapping for hafnium and yttrium in the Y-doped HfB_2 obtained from carbothermal reduction

Static oven oxidation tests were performed for the 8 wt% Y-doped HfB_2 powders at 1600°C for 0.1 h. Figure 2.31 shows that both tetragonal and monoclinic HfO_2 was found in the oxidation products. It leads to the conclusion that the use of 8 wt% Y-dopant could partially stabilize the oxidation products of HfB_2 as tetragonal HfO_2. The diffraction pattern of monoclinic HfO_2 and tetragonal HfO_2 showed significant overlap, thus the diffraction peak at ~30° was used as the characteristic peak for the calculation of the mass fraction of tetragonal HfO_2. It can be seen that ~38 wt% tetragonal HfO_2 was formed in the oxidation product of 8 wt% Y-doped HfB_2. However, for hypersonic applications, the presence of monoclinic HfO_2 may result in cracking due to its phase transformation upon heat and cooling, so a dopant that can lead to the formation of a solid solution

and fully stabilize the oxidation products of HfB_2 as tetragonal or cubic HfO_2 was deemed to be required.

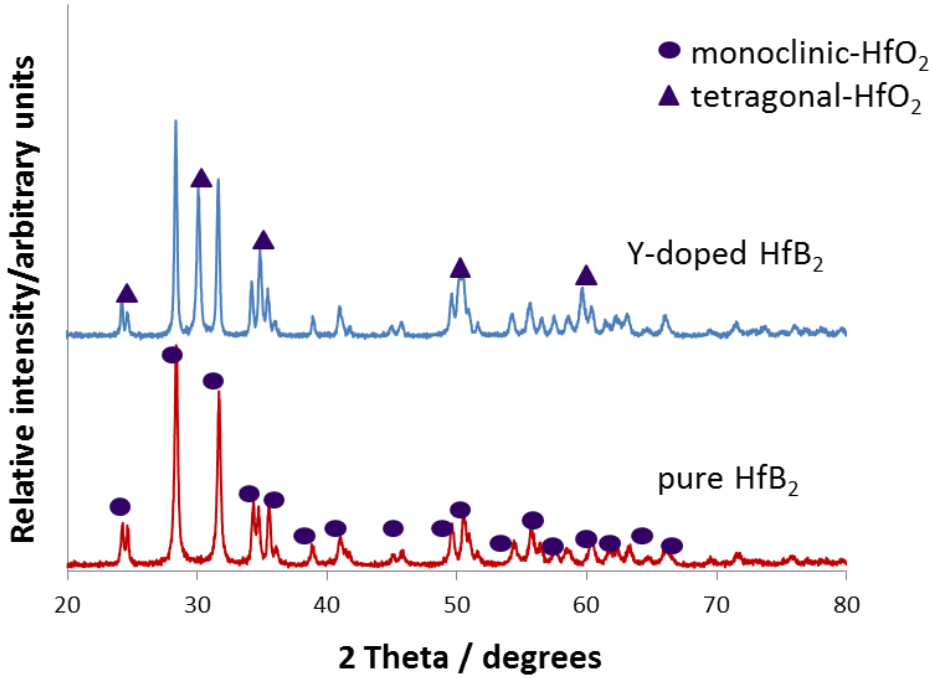

Figure 4.31 XRD patterns of the pure and Y-doped HfB_2 powders oxidized at 1600°C for 0.1 h in air

4.1.3.3 Synthesis and characterization of Ta-doped HfB_2 powder

As discussed in Section 4.1.3.2, the main reason why Y-dopant and HfB_2 cannot form solid solution is because YB_2 is a metastable phase, hence it requires more energy to transfer Y_2O_3 to YB_2 than that for carbothermal reduction of HfO_2. Thus Ta-dopant was selected as the next dopant. One of the main advantages of using Ta-dopants was that according to the thermodynamic calculation of Equation 4.8, the formation of TaB_2 was thermodynamically favourable at 1327°C, which was similar to the calculated reaction threshold temperature for the carbothermal reduction of HfB_2, 1350°C.

$$Ta_2O_5 + 2B_2O_3 + 11C \rightarrow 2TaB_2 + 11CO\,,\ \Delta G < 0 \text{ at } > 1327^{o}C \qquad (4\text{-}8)$$

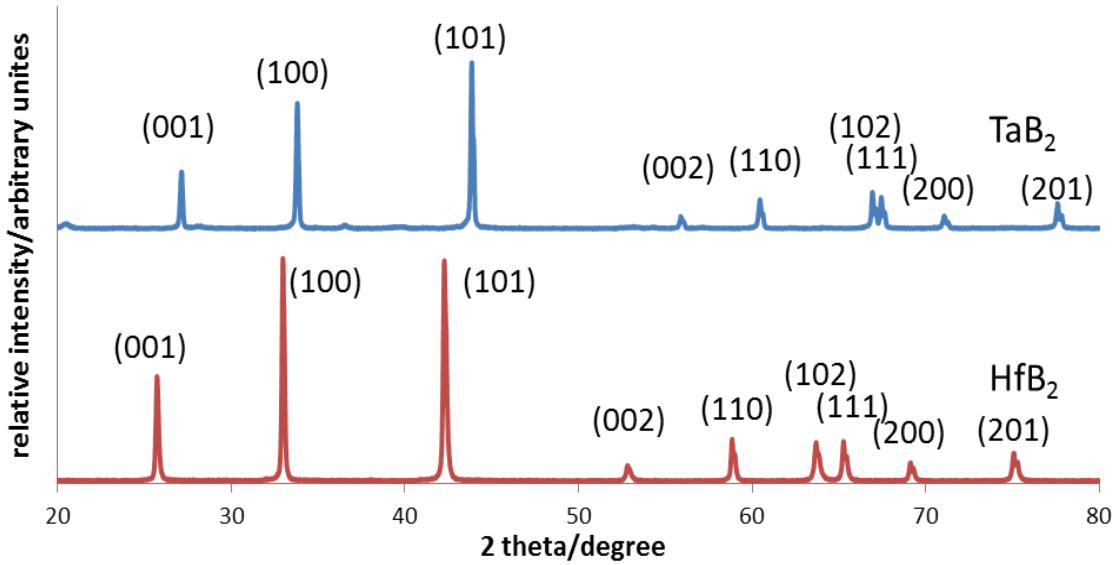

Figure 4.32 XRD patterns of the TaB_2 and HfB_2 powder synthesised by carbothermal reduction using precipitation-derived precursors. The Ta:B:C and Hf:B:C molar ratio of the corresponding precursors to yield pure TaB_2 and HfB_2 powder were 1:3:5.5 and 1:3:5, respectively

Table 4.7 Literature and measured values of the lattice parameter for pure HfB_2 and TaB_2

Lattice parameter	HfB_2 (literature)*	HfB_2 (this work)	TaB_2 (literature)#	TaB_2 (This work)
a/nm	0.314	0.314	0.306	0.309
c /nm	0.347	0.350	0.330	0.324

* JCPDS card number: 00-038-1398

JCPDS card number: 00-038-1462

To confirm the reaction process of Equation 4.8, boric acid, phenolic resin and $TaCl_5$ was used to synthesise TaB_2 powder, which was similar as the synthesis route used for HfB_2. Figure 4.32 shows that pure TaB_2 powder was obtained under the same heat treatment conditions as for the synthesis of HfB_2 powder, i.e. 1600ºC for 2 h. The XRD diffraction patterns for TaB_2 and HfB_2 were also very similar since both these materials had a hexagonal crystal structure. The difference in the diffraction peak positions for the same planes in these two diborides was due to the shorter M-B, B-B and M-M bonds in the TaB_2 compared

to HfB_2, as a result of the smaller covalent radii of Ta atoms, so the lattice parameters a (a=b in the hexagonal structure) and c of TaB_2 were smaller than that of HfB_2, as seen from Table 4.7.

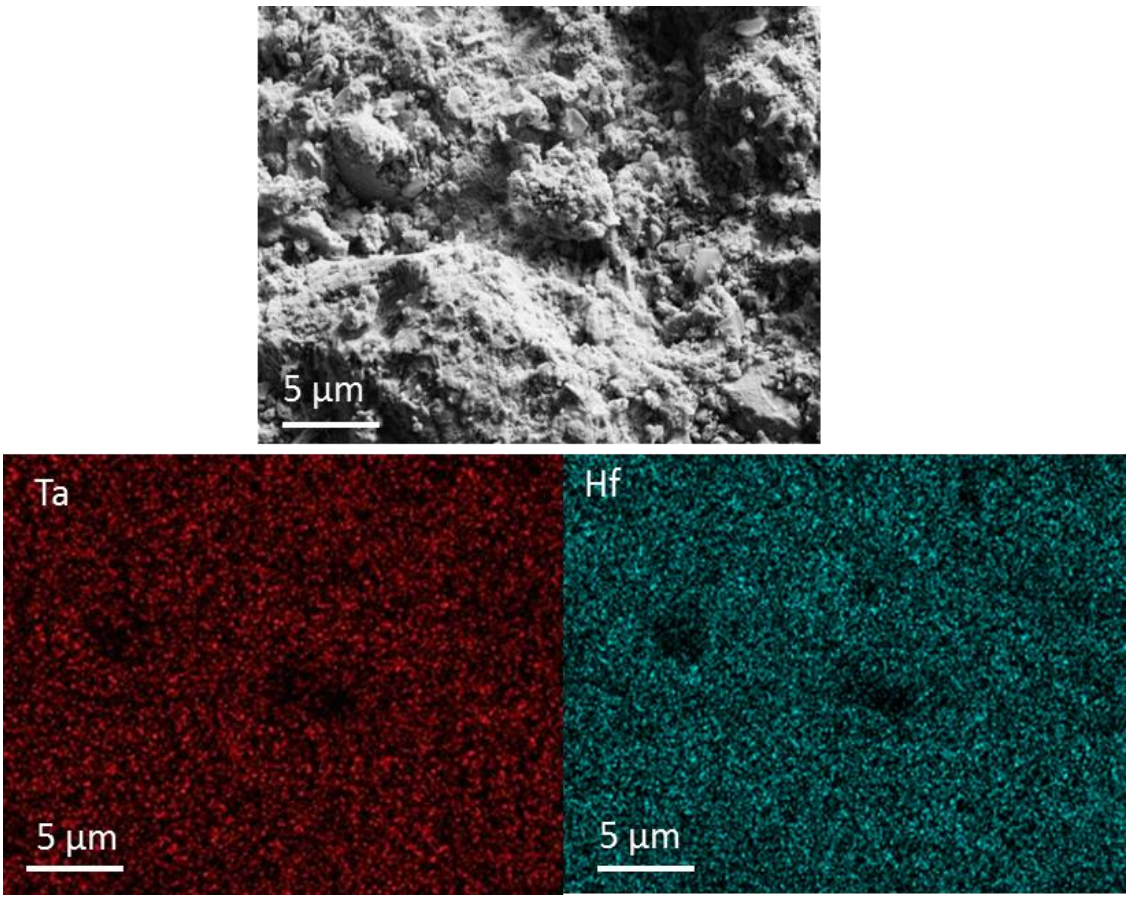

Figure 4.33 SEM image and EDX mapping of the co-precipitation derived precursors which was for the synthesis of 10 wt% Ta-doped HfB_2

Based on the similar formation temperature of TaB_2 and HfB_2, Ta-doped HfB_2 powder was prepared by in-situ synthesis which involved initial co-precipitation of $Hf(OH)_4$ and $Ta(OH)_5$ to improve homogeneity, followed by carbothermal reduction for the resultant HfO_2 and Ta_2O_5. As mentioned before, $Hf(OH)_4$ precipitates were stable over a wide pH range from 4-10, with a solubility in water of 45 mg l^{-1}. It was reported that the solubility of $Ta(OH)_5$ in water was 162 mg l^{-1} and $Ta(OH)_5$ precipitates were stable over the pH range from 6-10 [271]. Thus if $Ta(OH)_5$ and $Hf(OH)_4$ were formed at a pH within the range 6-10, they

would precipitate at the same time due to their low solubility in water. The co-precipitation pH used for the synthesis of Ta-doped HfB_2 was 8.5±0.3, which was exactly the same as that used during the synthesis of pure HfB_2, as it led to the formation of fine precipitates without significant agglomeration. The resulting $Ta(OH)_5$ and $Hf(OH)_4$ precipitates were dispersed in boric acid and phenolic resin/ethanol solution, then dried and calcined at 400°C to obtain the precursors for the synthesis of Ta-doped HfB_2 powder. Figure 4.33 shows that molecular-level mixing of Hf and Ta was achieved in the precursor prepared by the co-precipitation approach.

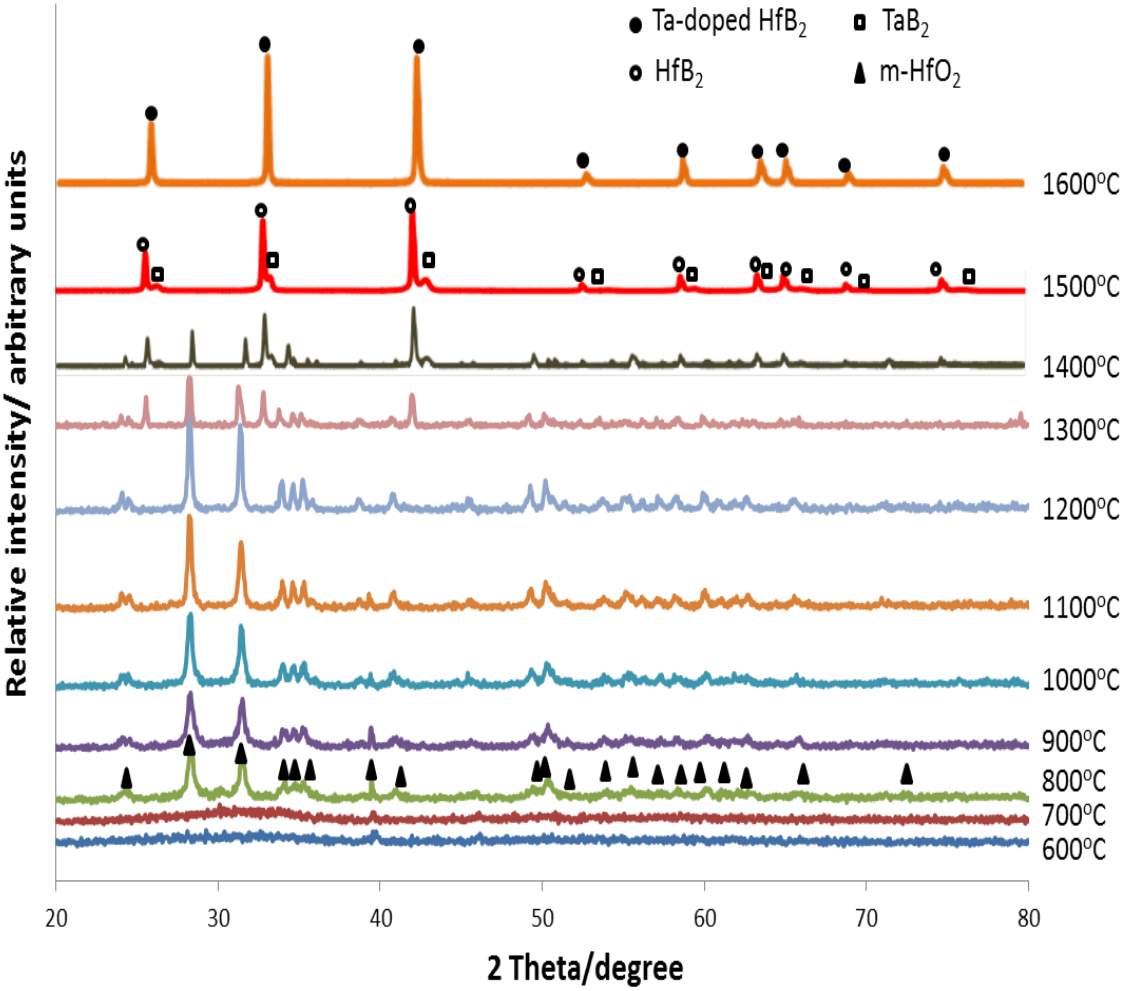

Figure 4.34 XRD patterns for the 10 wt% Ta-doped HfB_2 precursor heat treated at various temperatures. The heating rate was 5°C min^{-1} and the sample was soaked for 2 hrs at each targeted temperature.

The precursors containing $Ta(OH)_5$, $Hf(OH)_4$, boric acid and phenolic resin were heat treated at various temperatures in argon to investigate the formation mechanism of Ta-doped HfB_2. According to Figure 4.34, monoclinic HfO_2 formed at temperatures >800^oC. It was difficult to observe diffraction peaks associated with the formation of B_2O_3 and carbon as they were XRD-transparent amorphous materials. The formation of Ta_2O_5, which was polycrystalline and with only 10% mass fraction, was hardly to be seen, but since only monoclinic HfO_2 was present in the system, it revealed that the diffusion of Ta or Hf had not happened yet at this stage. Peaks due to HfB_2 and TaB_2 first appeared at 1300^oC and there was a significant increase in peak density for these phases at temperatures from 1300-1500^oC. Between 1500 and 1600^oC, $(Hf,Ta)B_2$ solid solution was formed, as evidenced by the merging of their respective diffraction peaks after heat treatment at 1600^oC.

The formation of $(Hf,Ta)B_2$ solid solution was dependent on the diffusion rate of Ta into HfB_2 or Hf into TaB_2, which was influenced by the synthesis temperature. The quantitive analysis of the diffusion rate of Ta and Hf in their corresponding borides was performed by placing a HfB_2 powder compact on a TaB_2 powder compact, followed by holding at 1600^oC for 2 hours. Figure 4.35(a) shows the fracture surface of the two powder compacts after heat treatment. It can be clearly seen that the inter-diffusion of Ta and Hf occurred, leading to a blurred boundary between TaB_2 and HfB_2. The diffusion distance of Ta into HfB_2 could be up to 7 μm after heat treatment at 1600^oC for 2 h, as measured from Figure 4.35(b). Since the observation error due to SEM resolution limitation was ~±1 μm, the inter-diffusion rate of Ta and Hf was calculated to be 0.058±0.008 μm min^{-1} at 1600^oC.

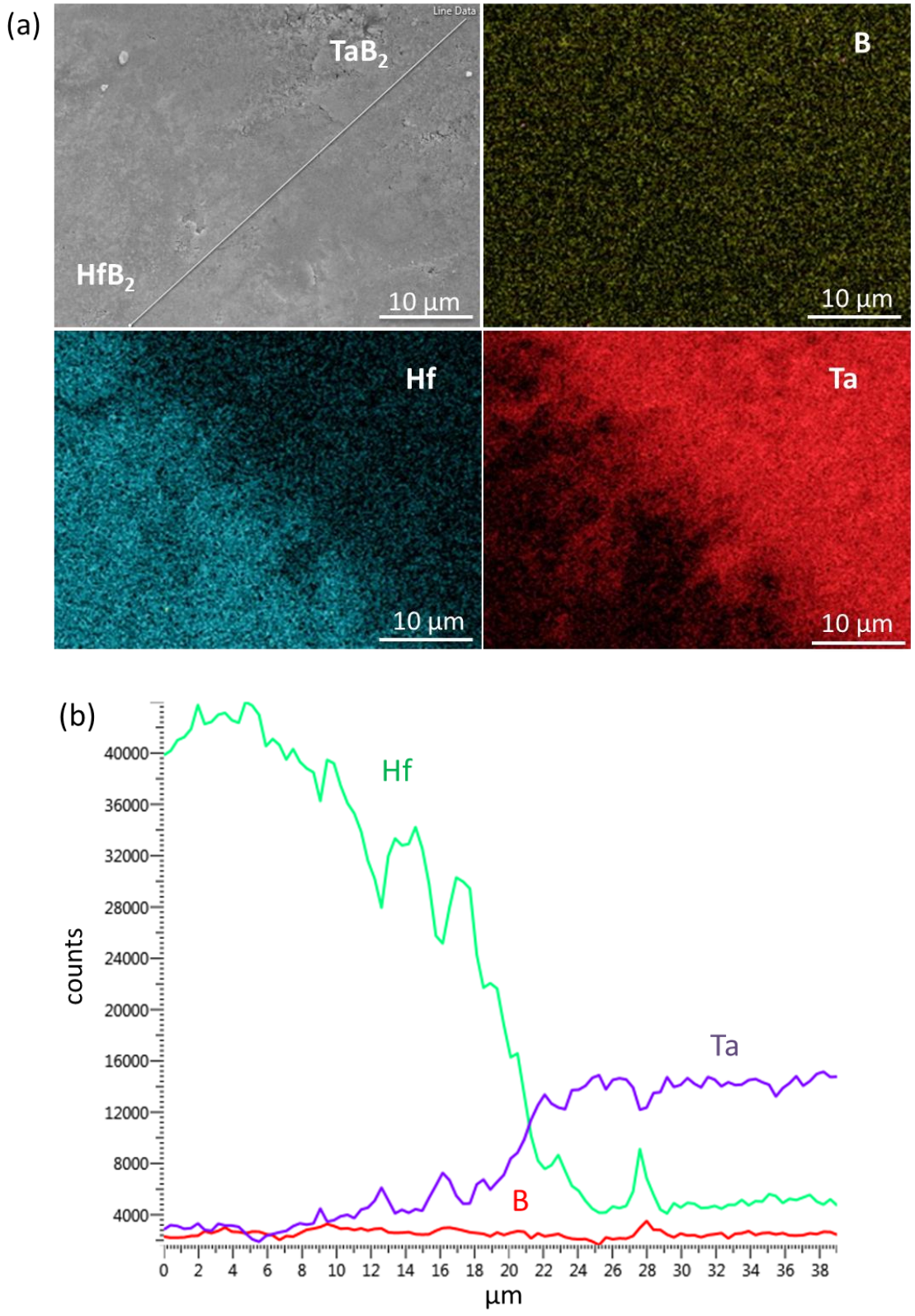

Figure 4.35 (a) SEM image and EDX mapping of the fracture surface of the powder compacts of TaB_2 and HfB_2 heat treated at 1600°C for 2 h; (b) EDX line scan was performed along the solid line shown in Figure 4.35(a)

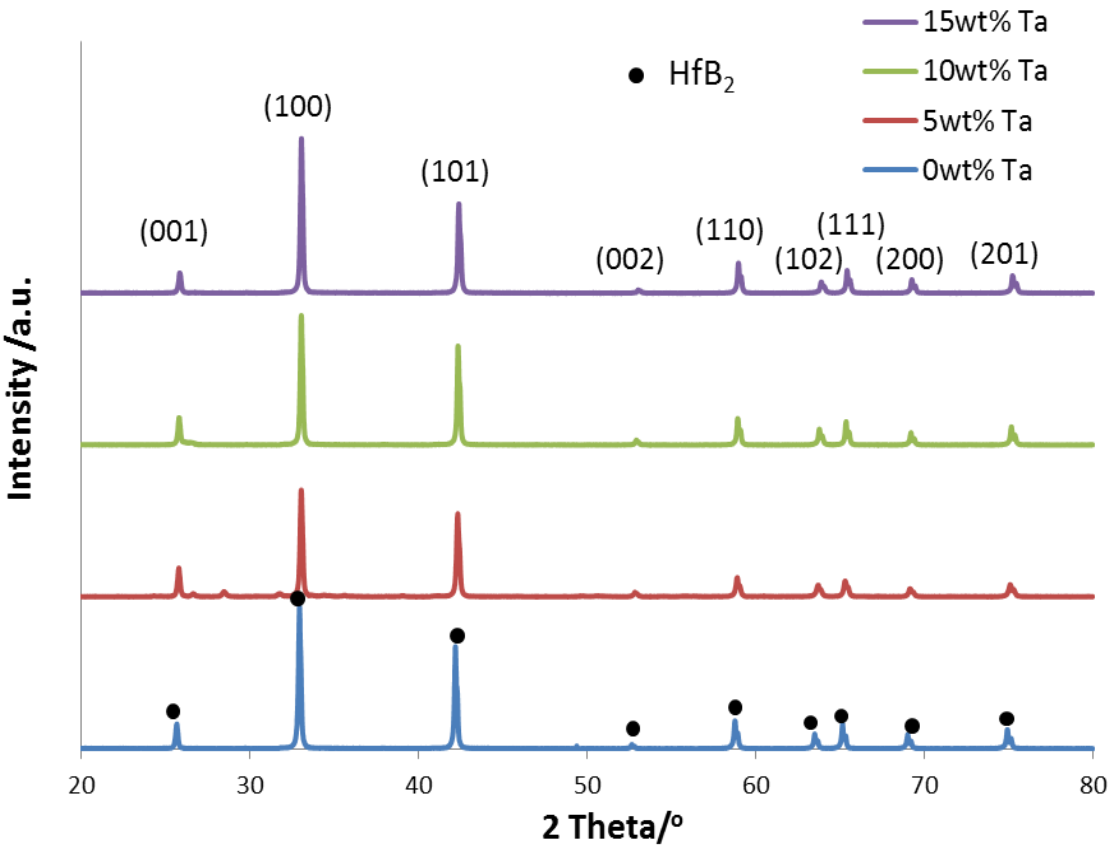

Figure 4.36 XRD patterns for pure and 5, 10 and 15 wt% Ta-doped HfB_2 powders heat treated at 1600°C for 2 hours

As pure HfB_2 and TaB_2 powder was successfully synthesized by using the Hf:B:C and Ta:B:C ratios of 1:3:5 and 1:3:5.5, these ratios were combined and employed for the synthesis of Ta-doped HfB_2 powders containing 5, 10 and 15 wt% Ta-dopant. The XRD patterns of the powders after heat treatment, Figure 4.36, indicate the formation of $(Hf,Ta)B_2$ solid solution in the Ta-doped HfB_2 samples, as only diffraction peaks for HfB_2 are visible and the greater the Ta doping level, the more the peaks shifted to higher 2θ values. This is because the doped HfB_2 lattice structure shrank with increased Ta substitution. Based on the peak shifts, the lattice parameters for the pure and Ta-doped HfB_2 were calculated and are listed in Table 4.8.

Table 4.8 Measured values of the lattice parameter for HfB_2 and Ta-doped HfB_2

Lattice parameter	HfB_2	5 wt% Ta-doped HfB_2	10 wt% Ta-doped HfB_2	15 wt% Ta-doped HfB_2
a/nm	0.3142	0.3140	0.3139	0.3138
c/nm	0.3470	0.3468	0.3466	0.3464

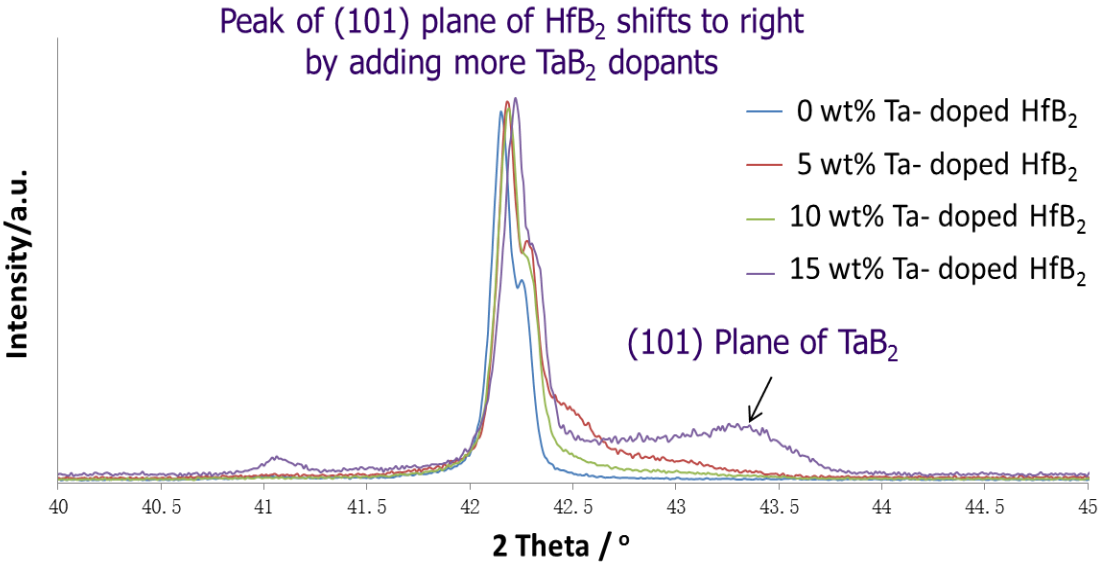

Figure 4.37 High-resolution XRD patterns for the diffraction peak associated with (101) plane in pure and Ta-doped HfB_2.

Figure 4.37 shows the high resolution XRD evaluation of the (101) plane of the pure and Ta-doped HfB_2 samples, revealing clearly the displacement of the diffraction peaks. In addition, the (101) peak associated with TaB_2 can be seen in the diffraction pattern for the 15 wt% Ta-doped HfB_2, which may be due to exceeding the solution limit of Ta dopant in HfB_2 at 1600°C. The TaB_2-HfB_2 and TaB_2-ZrB_2 phase diagrams hasn't been reported yet, so more work needs to be done to determine the solution limit for TaB_2 in HfB_2 at different temperatures. In subsequent spark plasma sintering experiments, which involved a maximum temperature of 2150°C, higher diffusion rates and solubility of Ta dopants in HfB_2 was found. The details will be discussed in Section 4.3.2.2.

The key factor promoting the formation of (Hf,Ta)B_2 solid solution at 1600°C was the excellent mixing of Hf and Ta achieved by the co-precipitation approach. The

FEG-SEM images and supplemental EDX mapping of the 10 wt% Ta-doped HfB_2 powders yielded after heat treatment at 1600°C for 2 h confirm that the homogeneous distribution of Hf and Ta in the precursors, Figure 4.33, was retained in the resultant Ta-doped HfB_2 powders, Figure 4.38.

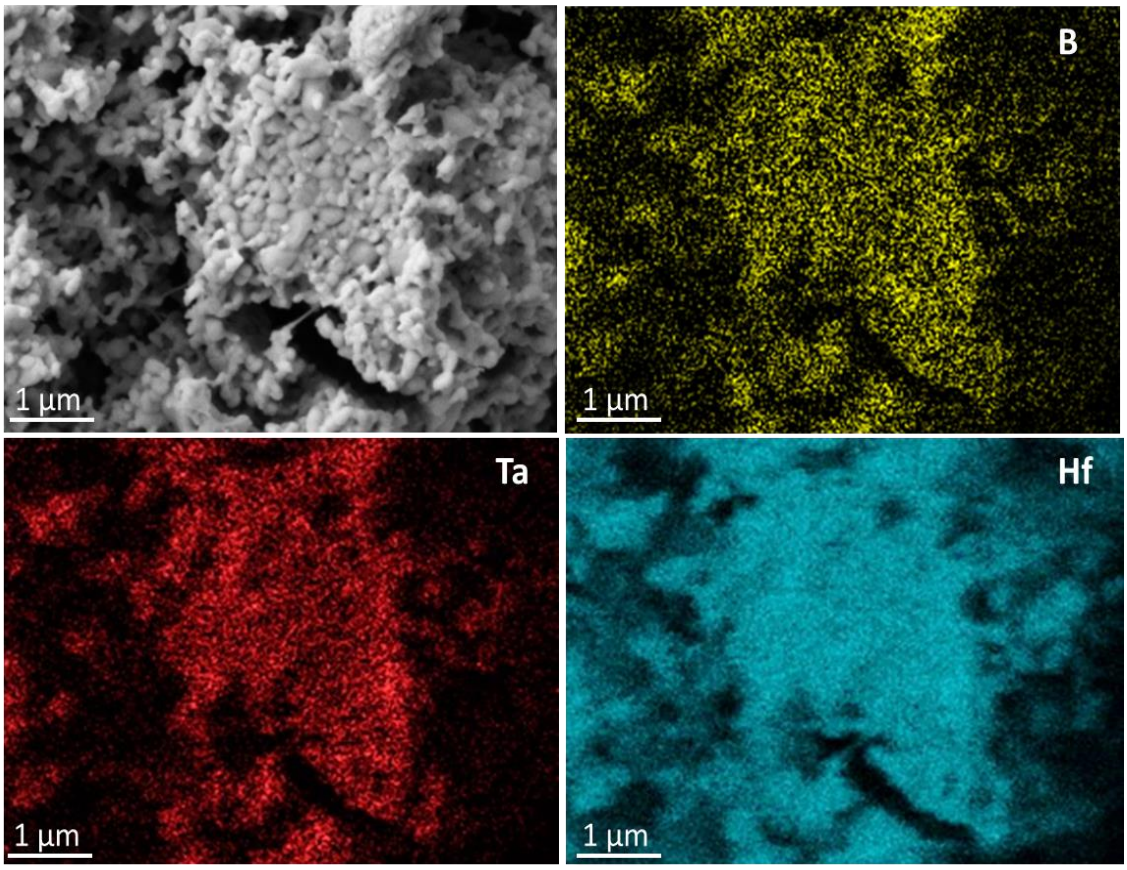

Figure 4.38 SEM image and EDX mapping of the 10 wt% Ta-doped HfB_2 powder

The use of Ta-dopant did not significantly change the particle size and morphology of the HfB_2-based powders yielded by carbothermal reduction reaction. Figure 4.39 shows that the particle size of the 5, 10 and 15 wt% Ta-doped HfB_2 powders are all in the range of 400-800 nm, which is similar to that of the pure HfB_2 powder synthesized under the same conditions. It was difficult to separate TaB_2 particles from HfB_2 particles using SEM-EDX due to the resolution limitation of the equipment as these particles were smaller than 1 µm,

but based on previous XRD analysis, the 5 and 10 wt% Ta-doped HfB_2 powders yielded by carbothermal reduction synthesis at 1600°C for 2 h can be regarded as $(Hf_{0.95}Ta_{0.05})B_2$ and $(Hf_{0.9}Ta_{0.1})B_2$, respectively.

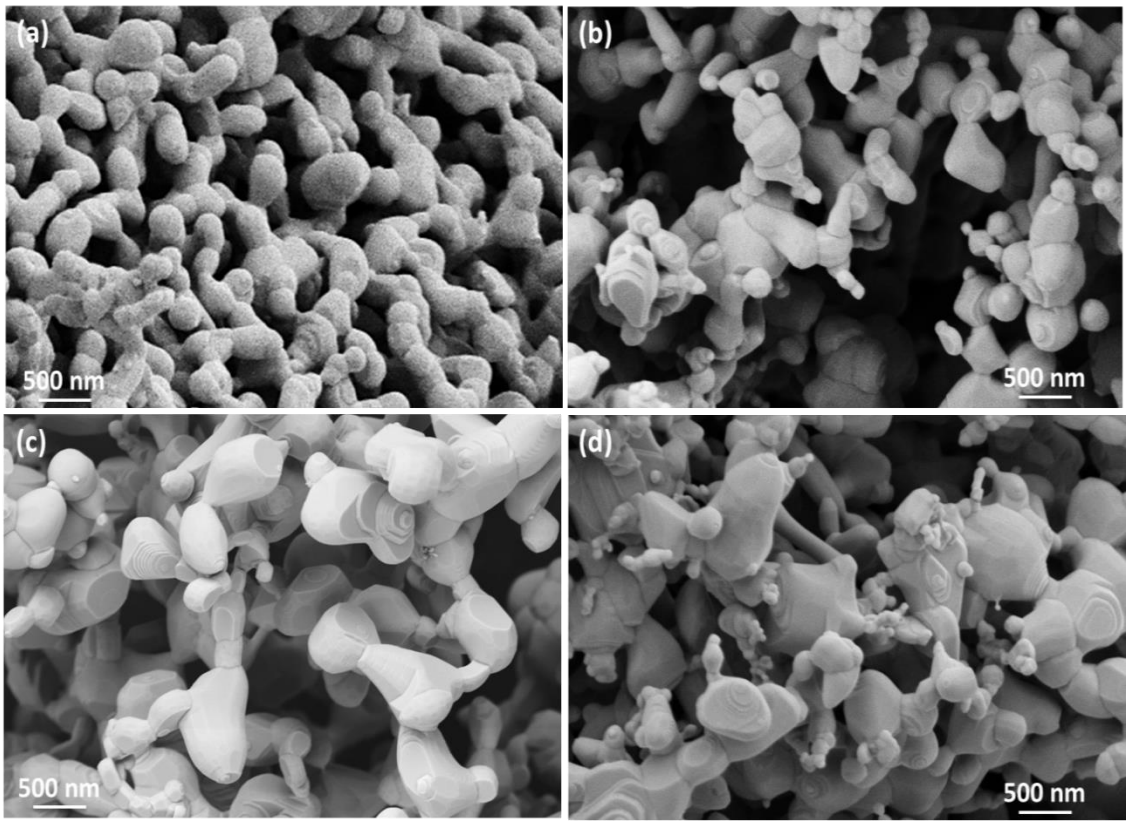

Figure 4.39 SEM images of the (a) 0, (b) 5, (c) 10 and (d) 15 wt% Ta-doped HfB_2 powders synthesized by carbothermal reduction reaction

4.2 Synthesis of pure and Ta-doped HfB_2 powder by borothermal reduction reaction

Pure and Ta-doped HfB_2 powders were also synthesised from $Hf(OH)_4$ and boron via borothermal reduction to understand the effect of a different HfB_2 formation mechanism on the purity and particle size of the resulting powders. As for the carbothermal reduction synthesis, the Ta- and Hf- compounds were mixed by the co-precipitation approach as well in the borothermal reduction synthesis. Boron powder instead of boric acid was used as the boron source.

4.2.1 Synthesis of HfB_2 powder by borothermal reduction reaction

To assess the borothermal reduction process, the weight and heat flow changes of the $Hf(OH)_4$ and boron precursors were measured as a function of the synthesis temperature and are shown in Figure 4.40. The weight loss at temperatures <500°C was in agreement with the calculated weight loss of 18%, which was due to the loss of H_2O molecules from thermal decomposition of $Hf(OH)_4$. According to thermodynamic calculation, the Gibbs free energy of Equation 4.9 is -13kJ/mol at 1300°C, which shows the borothermal reduction reaction can happen at lower temperatures than the carbothermal reduction reaction.

$$3\mathrm{HfO_2(c)} + 10\mathrm{B(c)} \rightarrow 3\mathrm{HfB_2(c)} + 2\mathrm{B_2O_3(l)} \quad (4\text{-}9)$$

In the TGA analysis, the endothermic peak at 1230°C demonstrates the practical onset temperature of the borothermal reaction. At 1600°C, the weight loss reached a maximum of 34% and no additional weight loss was measured at higher temperatures, suggesting that all volatile products had been removed from the system. Since the previous TGA analysis for carbothermal reduction synthesis of HfB_2, Figure 4.10, showed that the carbothermal reduction reaction precursors were still losing weight at 1600°C, it suggested that the borothermal reduction reaction could be completed with a lower temperature and/or shorter time, but for consistency, the $Hf(OH)_4$ and boron precursors were also heat treated under the same conditions as for the carbothermal reduction, i.e. 1600°C for 2 h. Phase-pure HfB_2 powder was successfully obtained by the borothermal reduction reaction as well. Another advantage of performing the heat treatment at such a temperature was that it allowed the residual B_2O_3 to evaporate.

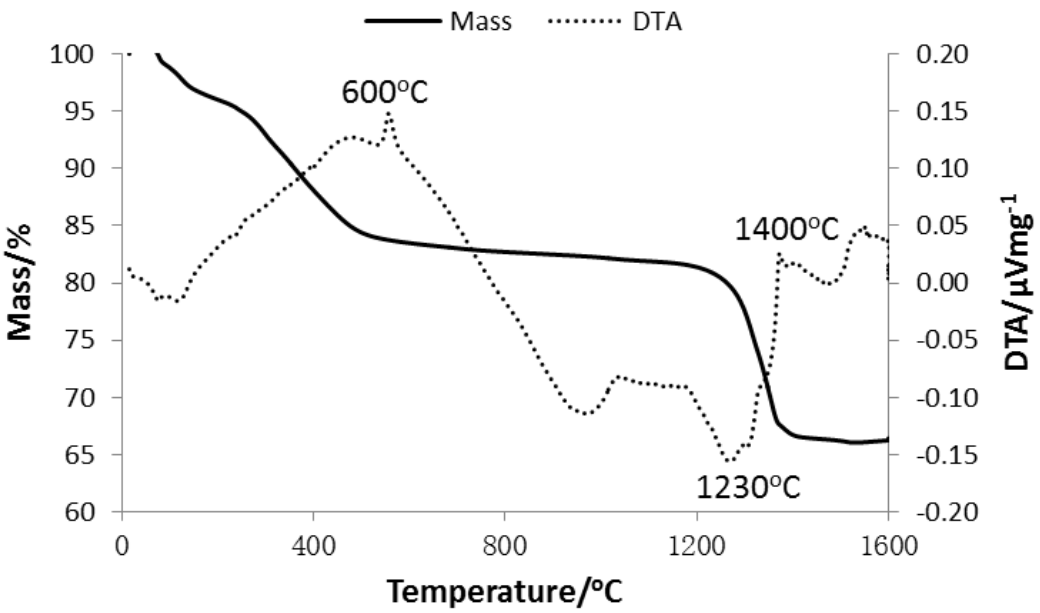

Figure 4.40 The weight and heat flow changes for the mixture of $Hf(OH)_4$ and boron (molar ratio of Hf:B=1:4) as a function of temperature

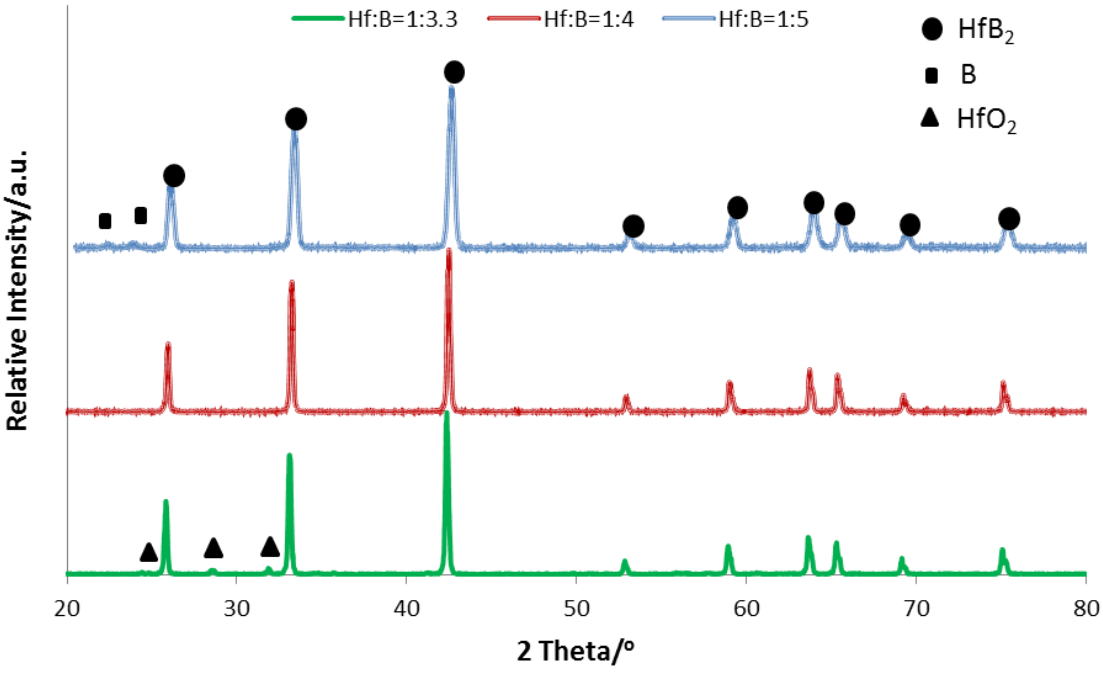

Figure 4.41 XRD patterns of the $Hf(OH)_4$ and boron precursors with different Hf:B ratios, 1:3.3, 1:4 and 1:5. The precursors were heat treated at 1600°C for 2 h in argon

A stoichiometric study of the borothermal reduction was carried out by mixing $Hf(OH)_4$ and boron in various Hf:B molar ratios, viz. 1:3.3, 1:4 and 1:5. The $Hf(OH)_4$ and boron precursors were heat treated at 1600°C for 2 h. The XRD patterns of the powders produced after heat treatment, Figure 4.41, shows that although the stoichiometric Hf:B ratio was 1:3.3 according to Equation 4.9, impurities such as unreacted HfO_2 were found in the resultant HfB_2 powder. When the Hf:B ratio used was increased to 1:4, HfB_2 was the only crystalline phase in the resultant powder. Residual boron was detected by XRD when the Hf:B ratio was further increased to 1:5. Single phase HfB_2 obtained from the precursor with Hf:B ratio of 1:4 showed that excess boron was required during the borothermal reduction process, presumably because boron could react with B_2O_3, which was the side product of Equation 4.9, to form boron suboxide gases such as B_2O_2(g) and BO(g) via Equation 4.10 and 4.11 [140], [272].

$$2B_2O_3 + 2B \rightarrow 3B_2O_2 \quad (4\text{-}10)$$

$$B_2O_3 + 2B \rightarrow 3BO \quad (4\text{-}11)$$

In order to identify the formation of these boron suboxides, B_2O_3 was mixed with boron powder with the molar ratio of 1:5 and heated up to 1000°C. It can be seen from Figure 4.42 that the atomic concentration of B_2O_3 was slightly reduced and two weak peaks due to boron suboxides, e.g. B_2O_2 and BO, were detected after the heat treatment. It was difficult to estimate the reaction rate due to the volatile nature of the boron oxide species. Since the reaction between B_2O_3 and boron was more thermodynamically favorable than the borothermal reduction of HfO_2, the B_2O_3 will have reacted with boron immediately after its formation. Therefore, the borothermal reduction reaction to form HfB_2 in fact should follow Equation 4.12, which is the combinations of Equation 4.9 and 4.10.

$$HfO_2(c) + 4B(c) \rightarrow HfB_2(c) + 2B_2O_2(g) \quad (4\text{-}12)$$

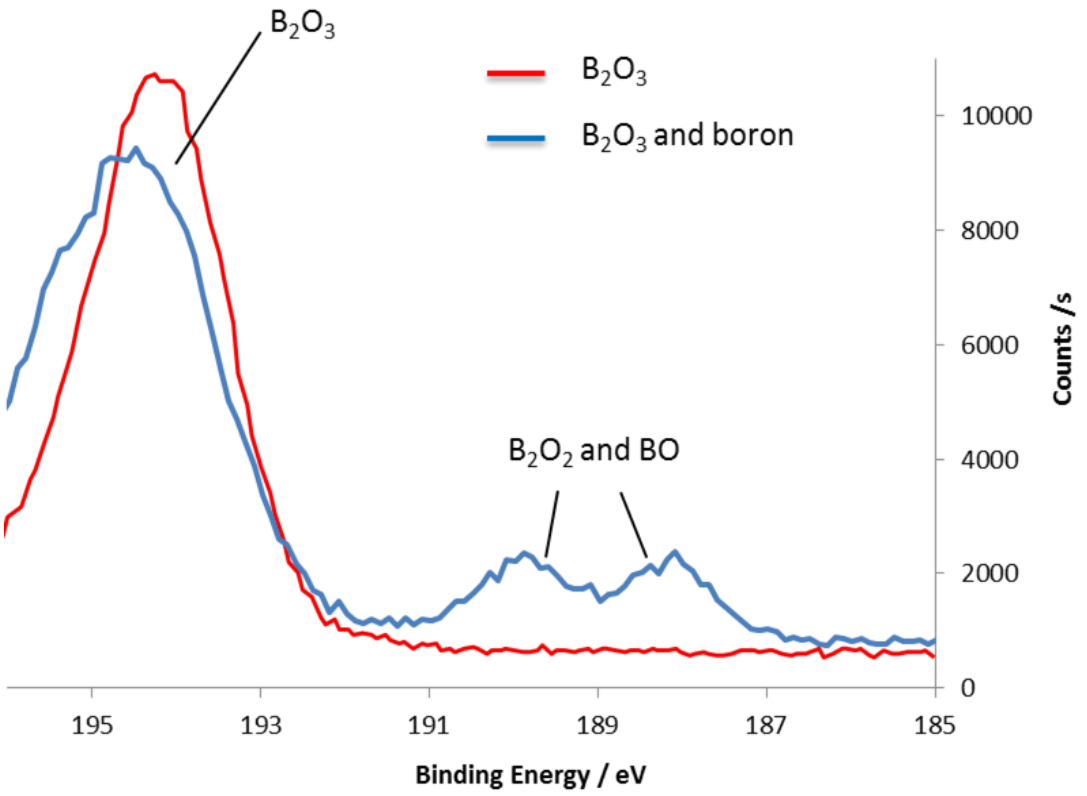

Figure 4.42 High-resolution XPS scan of the boron species for B_2O_3 and B powder mixture after heat treatment at 1000°C for 1 h

The morphology and particle size of the HfB_2 powders obtained from different Hf:B ratios were analysed by FEG-SEM. Figure 4.43(a) shows that the powders obtained from Hf:B=1:3.3 exhibited a faceted morphology due to the presence of unreacted HfO_2 as well as HfB_2. The powders obtained from Hf:B=1:4, Figure 4.43(b), had a nearly spherical morphology. Although boron was detected in the powders from Hf:B=1:5, it was difficult to tell the boron and HfB_2 particles apart due to their similar particle size and the limitation of EDX. The particle size of the single phase HfB_2 powder was in the range of 0.5-2 μm, based on size measurement of the particles from the SEM images using ImageJ. It can be seen from Figure 4.43(c) that the excess boron used in the borothermal reduction reaction did not lead to the formation of anisotropic HfB_2 particle growth due to the absence of a liquid B_2O_3 phase which was effectively removed

by reaction with boron at temperatures >1000°C.

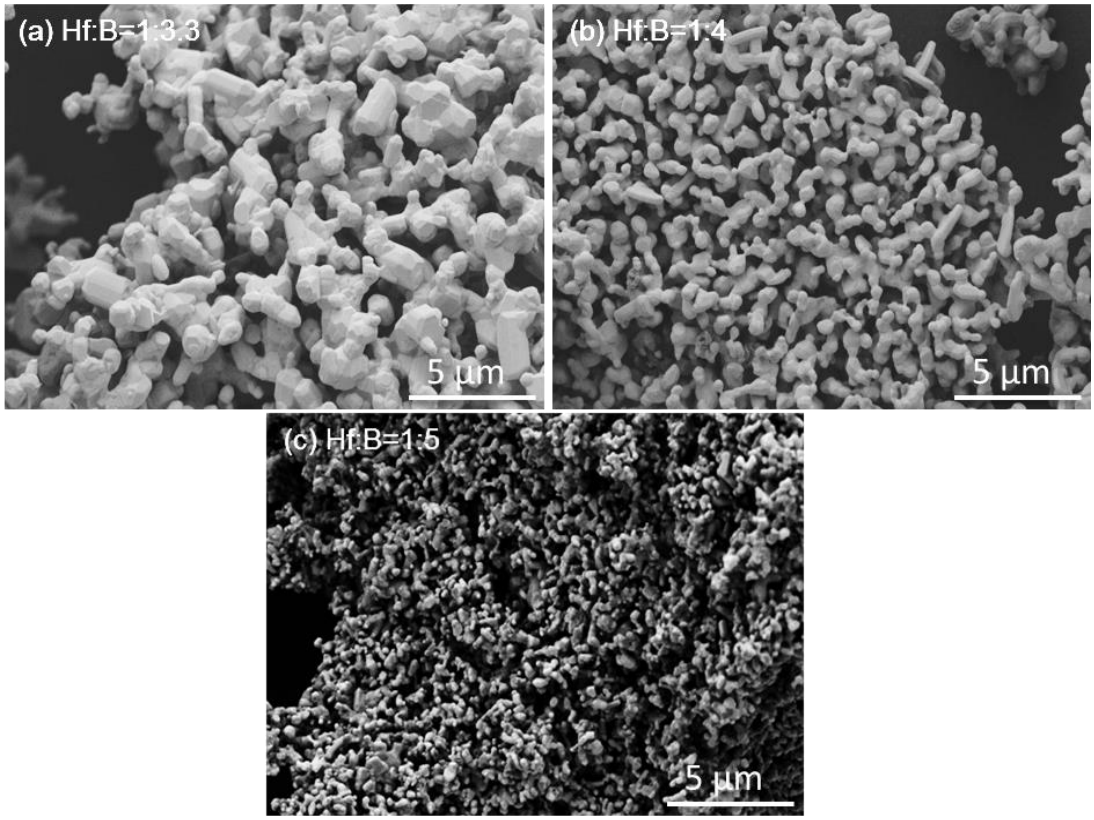

Figure 4.43 The morphology and particle size of the HfB_2 powders with different Hf:B ratios (a) 1:3.3, (b) 1:4 and (c) 1:5, synthesized by borothermal reduction reaction at 1600°C for 2 h.

4.2.2 Synthesis of Ta-doped HfB_2 powders by borothermal reduction reaction using co-precipitation-derived precursors

To synthesize Ta-doped HfB_2 powders by borothermal reduction, the co-precipitates $Hf(OH)_4$ and $Ta(OH)_5$ were used instead of only $Hf(OH)_4$. The surface composition of the resultant Ta-doped HfB_2 powder was checked by XPS and compared with the powders synthesized by carbothermal reduction. Figure 4.44 demonstrates that for 10 wt% Ta-doped HfB_2 powders synthesized by carbothermal reduction, a strong carbon peak was observed, showing the carbon impurity issue which was faced by the carbothermal reduction synthesis

of pure HfB_2 as well. In addition, oxygen impurities, which were associated with surface oxidation of HfB_2, and residual B_2O_3, were detected in both powders. Although the oxidation of HfB_2 ceramics happens at temperatures >600°C based on the subsequent oxidation testing results, the sub-micron HfB_2-based powders can be gradually oxidized when exposed to air at room temperature, hence the powders have to be stored in vacuum or inert gas for long-term use.

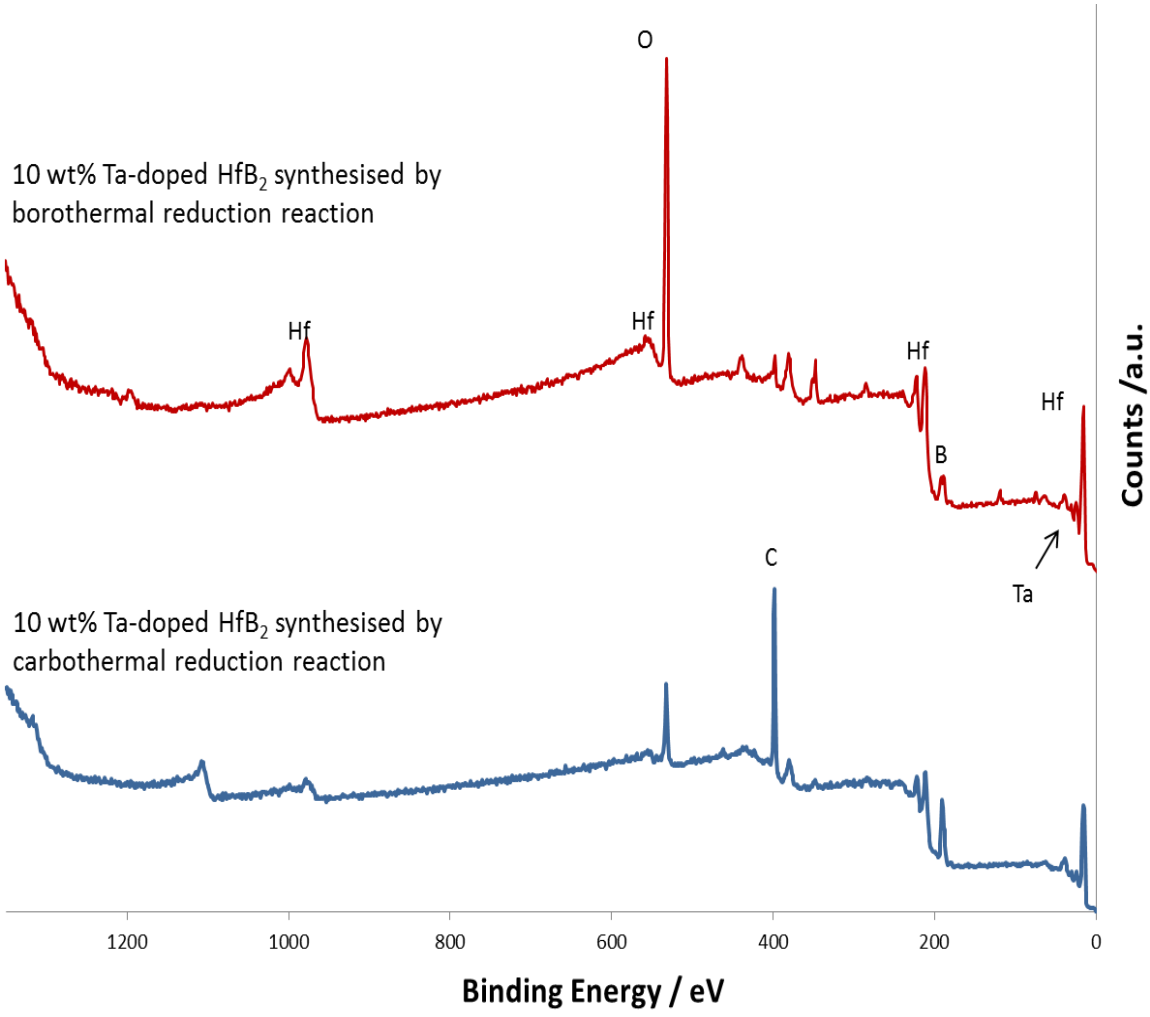

Figure 4.44 XPS analysis of the 10 wt% Ta-doped HfB_2 powders synthesized by borothermal and carbothermal reduction reaction, both at 1600°C for 2 h

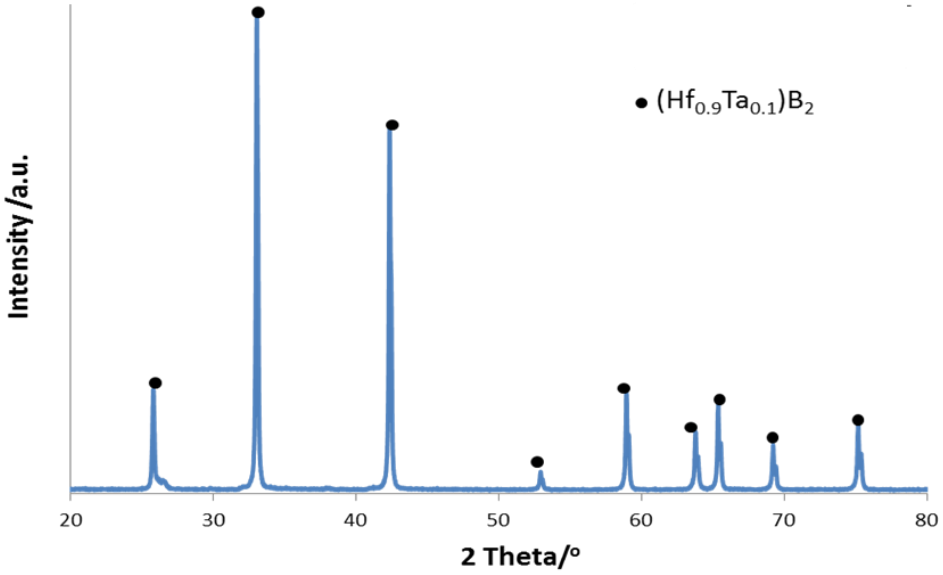

Figure 4.45 XRD patterns of the 10 wt% Ta-doped HfB_2 powders synthesized by borothermal reduction reaction at 1600°C for 2 h

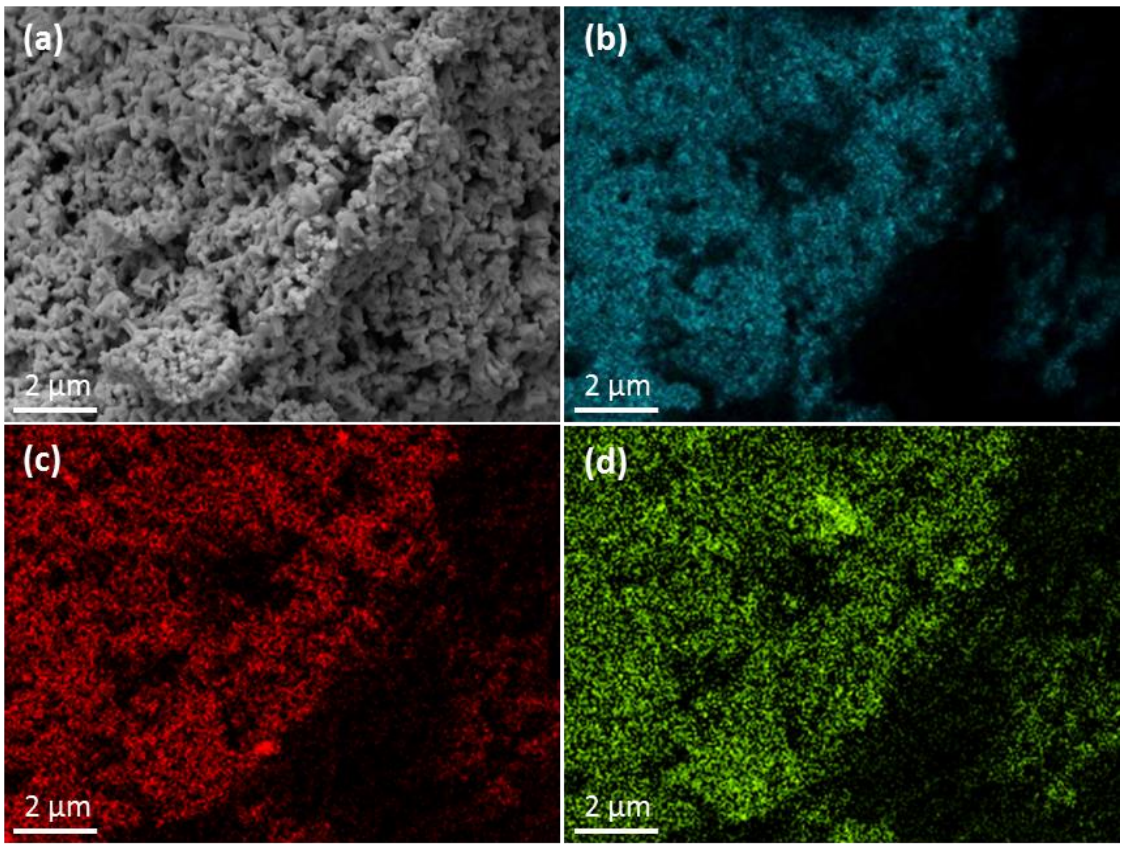

Figure 4.46 (a) SEM image of the 10 wt% Ta-doped HfB_2 powders synthesized by borothermal reduction reaction at 1600°C for 2 h and the distribution of (b) Hf, (c) Ta and (d) B in the powders

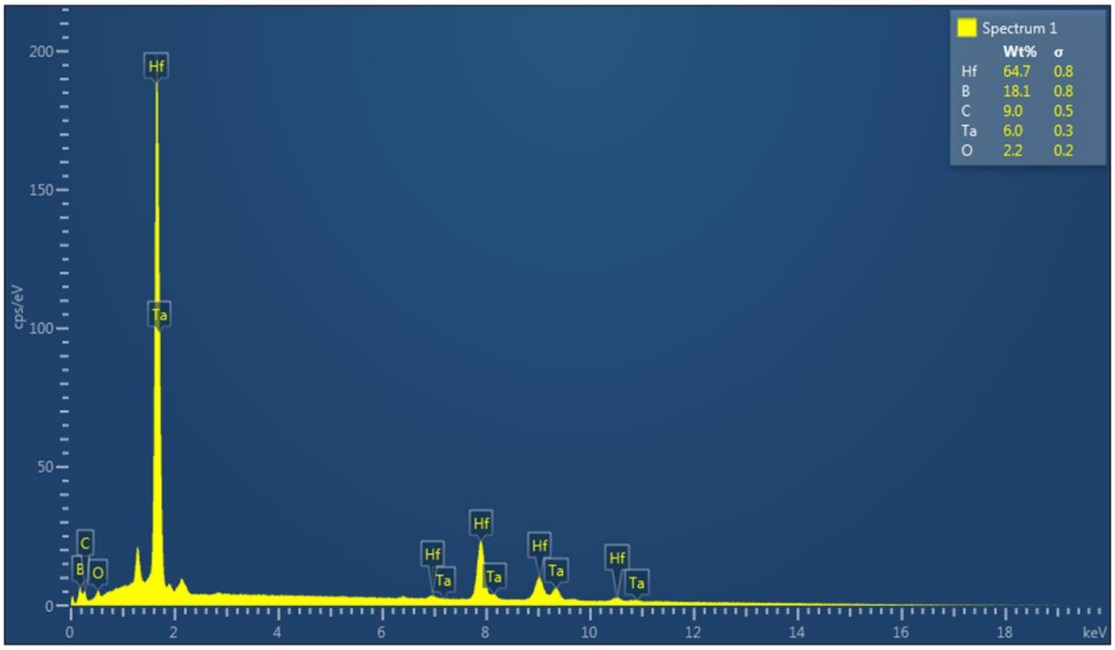

Figure 4.47 Area analysis of the composition of 10 wt% Ta-doped HfB_2 powders synthesized by borothermal reduction reaction at 1600°C for 2 h

Table 4.9 Hf/Ta atomic ratio measurement by XRF for the pure and Ta-doped HfB_2

Samples	Hf/at%	Ta/at%
HfB_2	100	-
5 wt% Ta-doped HfB_2	94.6	5.4
10 wt% Ta-doped HfB_2	89.1	10.9
15 wt% Ta-doped HfB_2	83.9	16.1

The formation of $(Hf,Ta)B_2$ solid solution was confirmed by Figure 4.45 for the Ta-doped HfB_2 powders synthesized by borothermal reduction reaction at 1600°C for 2 h. Furthermore, the homogeneous distribution of Ta in the borothermal reduction synthesis precursors was maintained in the resultant Ta-doped HfB_2 powders, as displayed in Figure 4.46 and Figure 4.47. SEM-EDX was not suitable for quantitive analysis of the exact composition of the samples, hence XRF was employed to confirm that the Ta contents in the resultant Ta-doped HfB_2 powders were consistent with the initial ratio of the starting materials

used for the synthesis of Ta-doped HfB_2. The results are shown in Table 4.9. This confirms that there was no tantalum or hafnium loss during the precipitation process and subsequent heat treatment.

Figure 4.48 shows that the mean particle size of the 10 wt% Ta-doped HfB_2 powders synthesized by borothermal reduction reaction is ~0.6 μm, which is significantly larger than that of the carbothermal reduction-derived powders. The coarser particles were believed to be due to the absence of carbon in the former; the HfB_2 particle growth was only controlled by heat treatment temperature and time. This led to the conclusion that in general finer particles were yielded from by carbothermal reduction reaction, despite the presence of some large agglomerates and carbon impurities. The sinterability of the pure and Ta-doped HfB_2 powders synthesized by these two methods will be discussed in the next section.

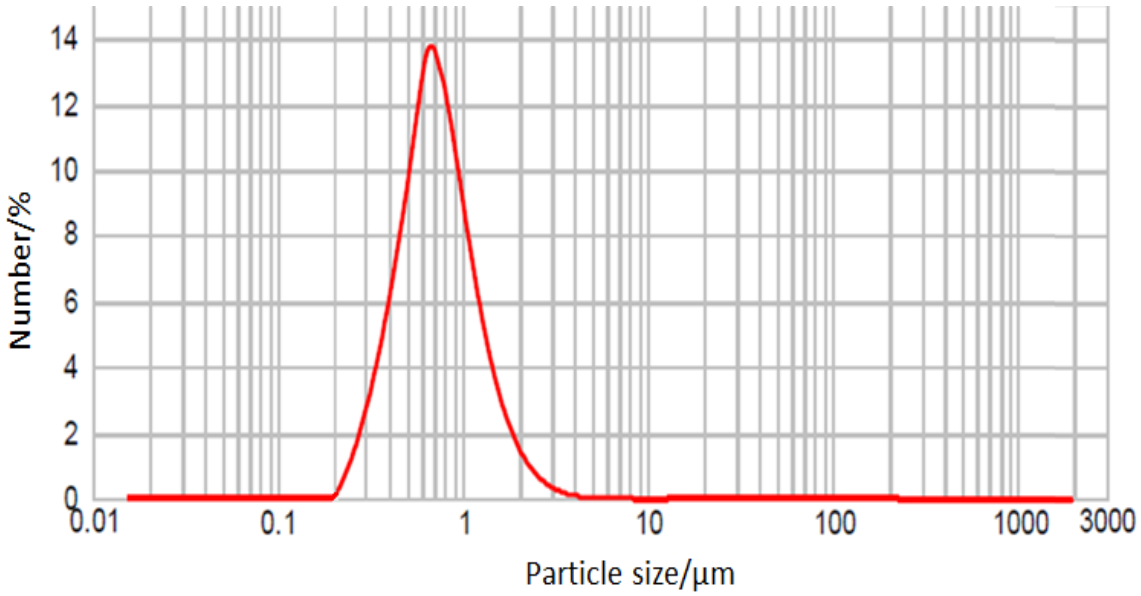

Figure 4.48 Particle size distributions of the 10 wt% Ta-doped HfB_2 powders synthesized by borothermal reduction reaction at 1600°C for 2 h

4.3 Densification of the HfB_2-based ceramics

4.3.1 Pressureless sintering

Pressureless sintering is the first choice for densifying ceramics since it is generally cheap and can be used to produce ceramics with complex shape without requiring extensive machining. It was reported that the highest density achieved by conventional pressureless sintering for HfB_2 was ~98%, with 2 wt% B_4C used as a sintering and the sintering condition was 2200°C for 2 h [218]. In this work, microwave and flash sintering technique were used instead of conventional sintering since they have been reported to be capable of sintering ceramics at significantly lower temperature than by conventional sintering [273].

4.3.1.1 Microwave sintering trials

Microwave sintering requires the materials to absorb microwave radiation and transfer the energy into heat. The dielectric properties of HfB_2-based powders were measured to check the feasibility of using microwave sintering for these powders. Figure 4.49(a) demonstrates that the change of dielectric constant ε' of HfB_2-based powders is slight at temperatures <1000°C. As the dielectric permittivity of water at room temperature is 80.4, it suggests HfB_2-based ceramic is not good at storing electric energy. More importantly, Figure 4.49(b) shows that the HfB_2-based materials have very high dielectric loss at the frequency of 2470 MHz, which is in the microwave frequency range. Furthermore, the dielectric loss is enhanced by the addition of Ta dopant. A high dielectric loss can lead to a better ability of transfer microwave energy into heat, thus the Ta-doped HfB_2 was believed to be a good candidate for microwave sintering, despite that very limited paper has reported microwave sintering for UHTCs [274].

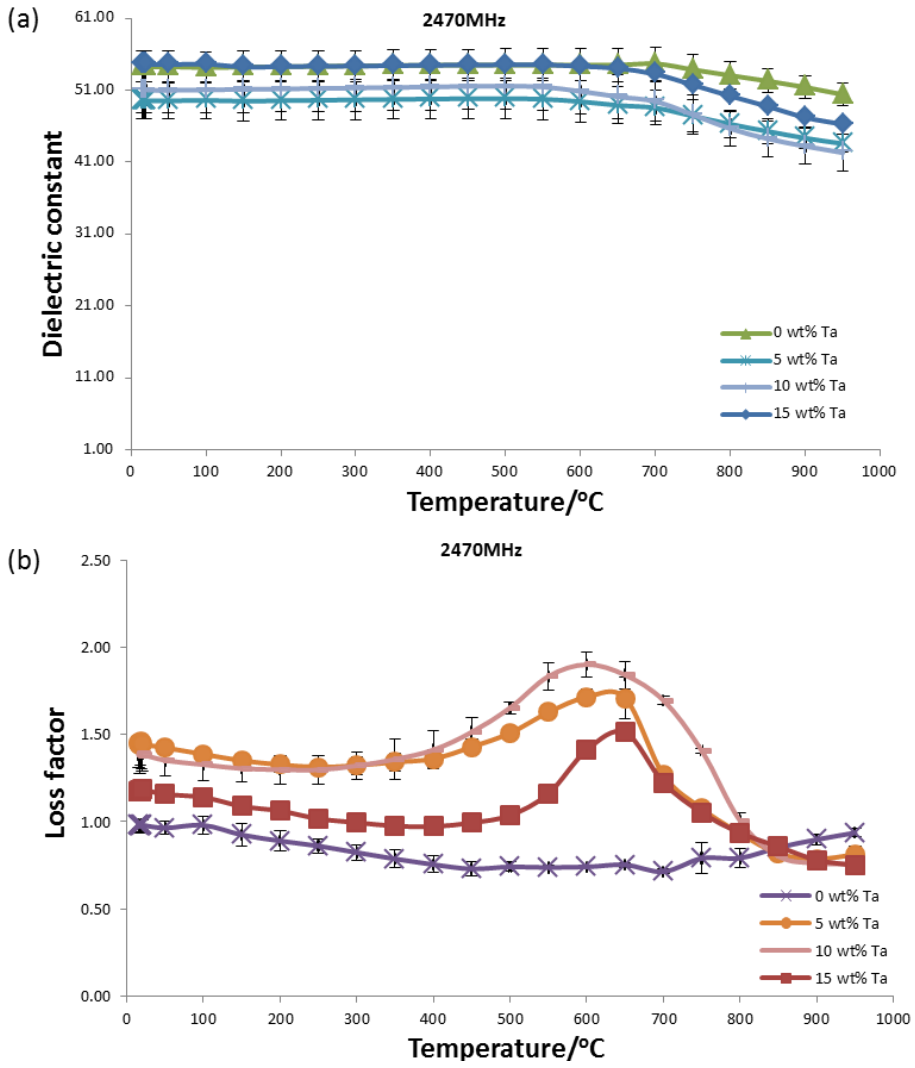

Figure 4.49 (a) Dielectric constant vs. temperature and (b) dielectric loss vs. temperature for pure and Ta-doped HfB_2, measured at 2470MHz. Thanks Dr. Dimitrakis from Nottingham University for conducting the measurements

During microwave sintering, the Ta-doped HfB_2 powder compacts were placed into an alumina tube furnace. As alumina absorbed very limited amounts of microwaves, extremely high sample temperatures could be achieved without over heating the tube and furnace during sintering. 10 mm ø × 3 mm high 10 wt% Ta-doped HfB_2 powder compacts prepared by die pressing were heated up in the microwave furnace using a ceramic paste (US patent 60/262.206) to assist in absorbing microwaves at low temperature. Figure 4.50 shows that the use of the ceramic paste around the 10 wt% Ta-doped HfB_2 significantly improved the latter's ability to heat through conduction and radiation. However,

the microwave trials had to stop at 33% of the power output due to the formation of a very large plasma inside the alumina tube furnace.

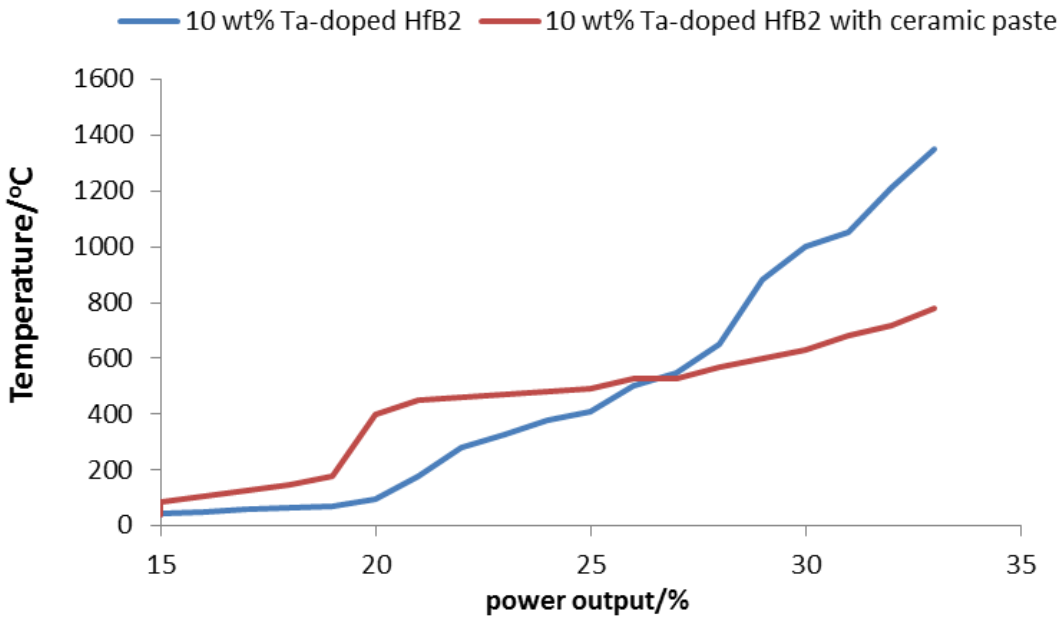

Figure 4.50 Sample temperatures vs. powder output of the microwave furnace for 10 wt% Ta-doped HfB_2. Argon was continuously passing through the tube furnace with a flow rate of 200 cm^3 min^{-1}

Plasma is an ionized gas, in other words, the ions and electrons are separate from each other. It has been reported that no plasma would occur when passing microwaves through air under normal atmospheric conditions [275]. However, microwaves passing through an argon atmosphere create conditions for plasma to occur. Lynch et.al. [276] found that plasma can form on the surface of samples with an argon flow rate of 120cm^3/min. Since an argon flow rate of 120cm^3/min was low enough for plasma to form and the plasma formation may also be sample dependent, 200cm^3/min was used in this work. However, this level of argon flow just slightly delayed the plasma occurrence from 28% to 33% powder output.

The maximum sample temperature observed in the microwave sintering trial was 1500°C, which was too low for the refractory metal borides to be densified.

This is the first time that microwaves have been explored for the densification of HfB_2-based ceramics, hence more work needs to be done to improve the maximum temperature which the HfB_2–based samples can reach during microwave sintering. Further efforts are currently underway in another project.

4.3.1.2 Flash sintering trials

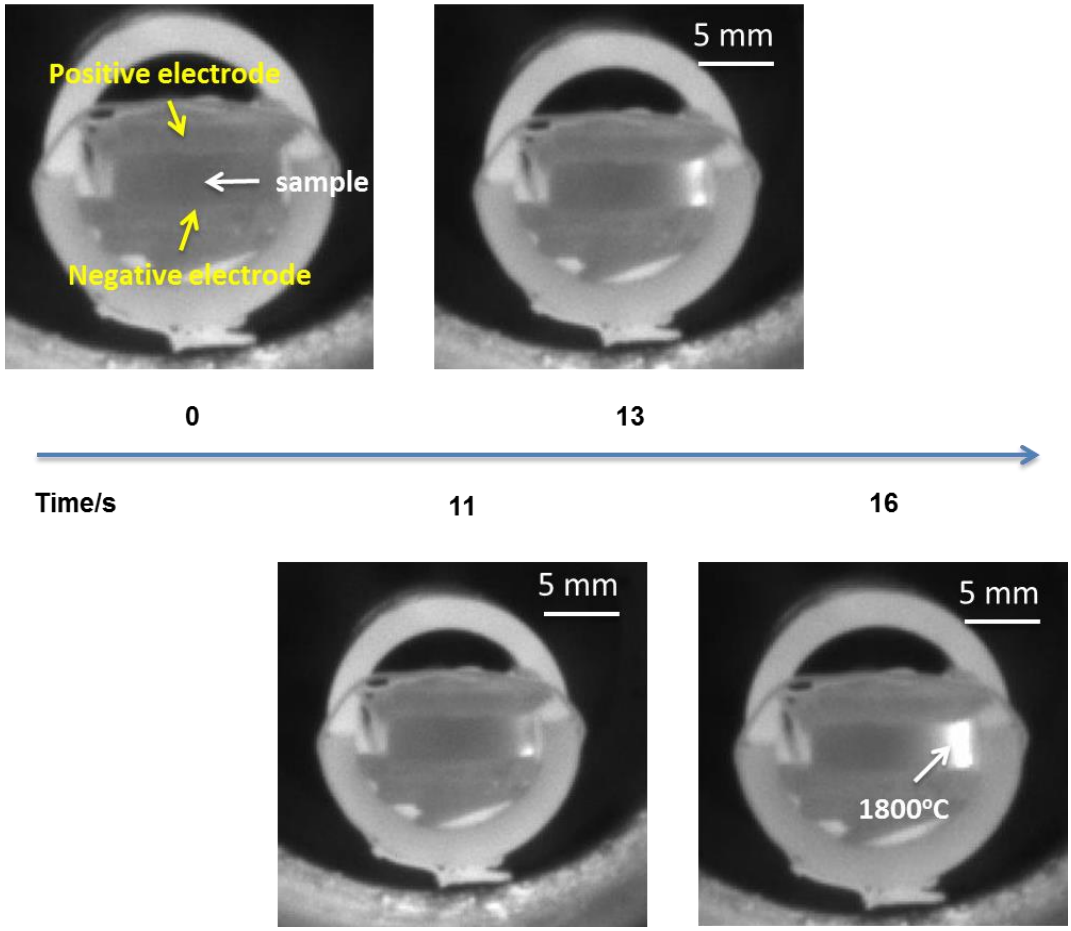

Figure 4.51 IR camera images for the 10 wt% Ta-doped HfB_2 with furnace temperature of 1450°C during flash sintering

The 10 wt% Ta-doped HfB_2 powder compact used for flash sintering had the same dimensions as the sample used for microwave sintering. For the densification of HfB_2-based powders, the furnace temperature was initially increased to 900°C and a power field of 20 V cm^{-1} was applied on the 10 wt% Ta-doped HfB_2 powder sample. A 'flash' was observed when the furnace

temperature reached 1450°C. Figure 4.51 shows that the flash initially occurred on the edge of the sample and started from the negative electrode, then expanded to the positive electrode within a few seconds. The maximum temperature reached during the flash was ~1800°C. However, the flash was not activated in other areas of the sample, probably due to the loss of contact between the sample and the electrodes. In pressureless flash sintering, the samples were placed on the electrode and fixed by several platinum wires, which led to localized pressure on the sample edge, while the center of the sample may have lost contact with the electrode.

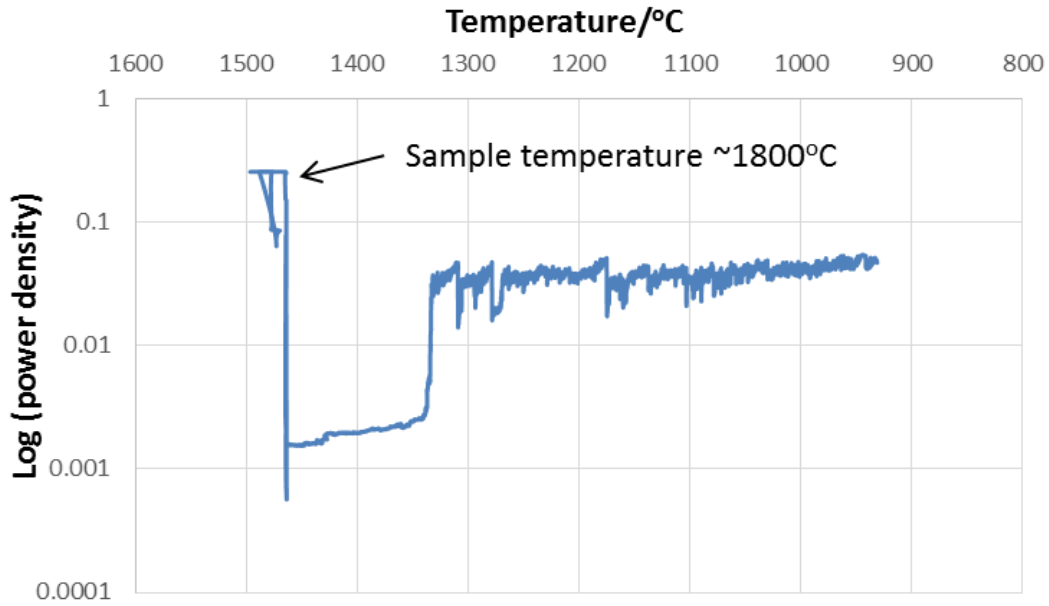

Figure 4.52 The relationship between power density and furnace temperature for the flash sintering of 10 wt% Ta-doped HfB_2

The occurrence of the 'flash' was also confirmed by the power density measured against the furnace temperature, as shown in Figure 4.52. At temperatures <1300°C, the change of power density was limited as the conductivity of the sample did not change significantly. The drop of powder density at ~1350°C was due to the partial loss of contact between the sample and electrodes as the platinum wire used to fix the sample will have softened and loosened at such a

temperature. Then the power density sharply increased at ~1450^{o}C, which was corresponding to the ‘flash’ occurring in the sample.

It is believed the ‘flash’ was related to the change in electric conductivity of the HfB_2-based sample, which had increased gradually with temperature until it reached a threshold value, then very significant heat was generated in the sample due to Joule heating, resulting in the sample temperature becoming 350^{o}C higher than the furnace temperature. However, 1800^{o}C was still insufficient for a HfB_2-based ceramic to be densified. It is possible that the electric and thermal conductivity values of the HfB_2-base ceramics were too high for flash sintering, as the heat generated by Joule heating could be readily dissipate by the sample. Sintering aids with low electric conductivities are probably required to modify the HfB_2-based ceramics to improve its viability for flash sintering.

4.3.2 Pressure assisted densification of HfB_2–based ceramics

4.3.2.1 Spark plasma sintering of HfB_2–based ceramics

The HfB_2–based powder obtained from the carbothermal and borothermal processes were densified at different temperatures using spark plasma sintering at Queen Mary University, London. The time-temperature and force profile of an SPS run at 2150^{o}C is given in Figure 4.53. A fast heating rate of 100^{o}C min^{-1} was employed to heat the sample to 1800^{o}C, followed by dwelling for 10 min to allow the volatiles, such as B_2O_3, to escape from the powder compact before the porosity closed during sintering. After that, a constant load of 19 kN was employed and the sample temperature was increased to 2150^{o}C and held for 30 min. The subsequent cooling rate was 100^{o}C min^{-1} and the pressure was gradually released to avoid cracking in the post-sintering samples. The time-temperature and force profile for the runs at 2100^{o}C and 2000^{o}C were similar to

that undertaken at 2150°C, with only the sintering temperature changed.

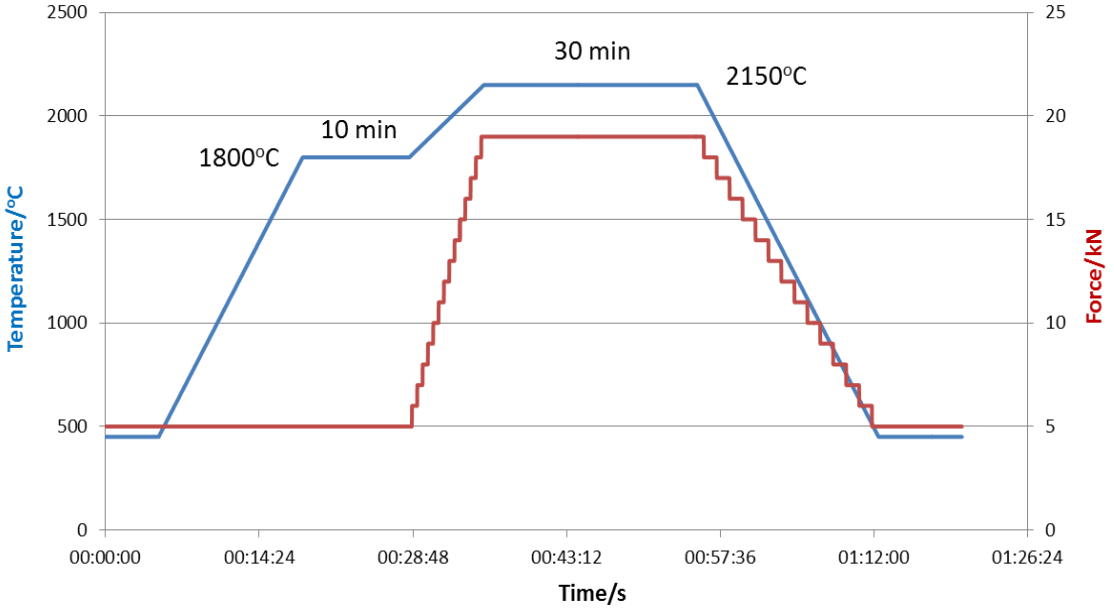

Figure 4.53 Force- and temperature-time profiles used for SPS of the HfB_2-based powders at 2150°C

The shrinkage rate and displacement profiles for the SPS runs were used to estimate whether the temperature was sufficient to achieve high density for HfB_2-based ceramics. Figure 4.54 (a)-(c) shows that the temperatures of 2000 and 2100°C were not high enough to fully densify the 15 wt% Ta-doped HfB_2 in 30 min as the displacements were still increasing after 30 min soaking time due to ongoing densification process, whilst the displacement measured in the SPS run at 2150°C, however, stabilized before the pressure was removed. The 15 wt% Ta-doped HfB_2 powder sintered at 2150°C also showed a higher shrinkage rate compared to the experiments at 2000 and 2100°C as expected. Figure 4.55 (a)-(c) confirms the sintering temperature of 2150°C led to the most dense HfB_2–based ceramic. Therefore, 2150°C, which was the maximum working temperature of the SPS equipment with the simultaneous employment of 50 MPa, was regarded as the 'optimized' SPS conditions for the densification of HfB_2-based ceramics. The shrinkage rate and displacement change of the pure HfB_2 was similar to that of 15 wt% Ta-doped HfB_2, as shown in Figure 4.54(d).

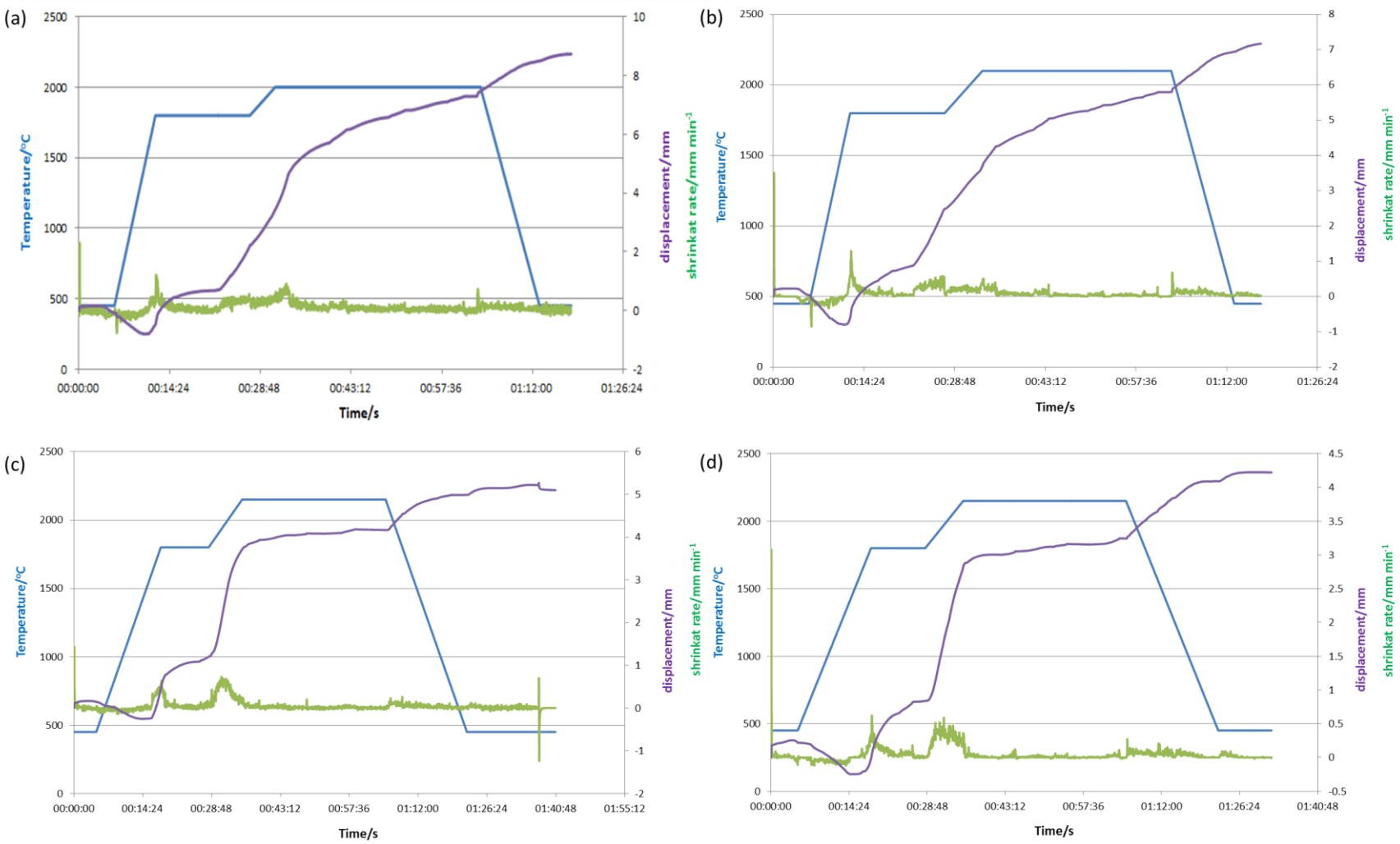

Figure 4.54 Temperature-, shrinkage- and displacement-time profiles measured during the SPS run of 15 wt% Ta-doped HfB_2 powders at (a) 2000°C, (b) 2100°C, (c) 2150°C and (d) pure HfB_2 powder at 2150°C

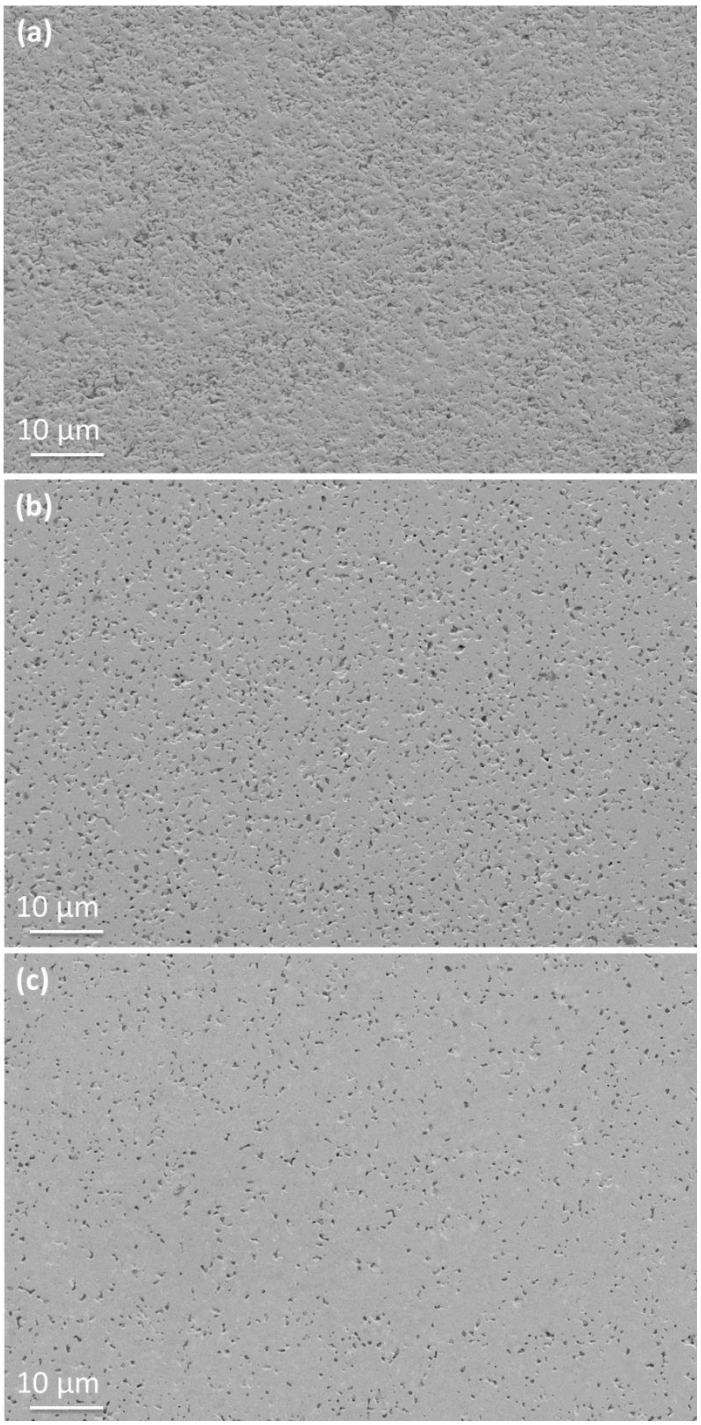

Figure 4.55 Polished surfaces of the 15 wt% Ta-doped HfB_2 samples sintered at (a) 2000, (b) 2100 and (c) 2150°C

4.3.2.2 Characterisation of sintered HfB_2–based ceramics

Table 4.10 shows the density and grain size of the post-SPS pure and Ta-doped

HfB_2 samples, which were prepared by various powder synthesis methods and sintered at various temperatures. It can be seen that the borothermal reduction derived powders led to higher density than these produced by carbothermal reduction and the highest density achieved was 97% of the 15 wt% Ta-doped HfB_2 from the borothermal reduction powders.

Table 4.10 Density and grain size of the sintered pure and Ta-doped HfB_2 ceramics, prepared by different synthesis methods

Powder source	Samples	Sintering temperature /°C	% of theoretical density*	Grain size / μm
Carbothermal reduction reaction	HfB_2	2150	~93	1-10
	5 wt% Ta-doped HfB_2	2150	~94	1-10
	10 wt% Ta-doped HfB_2	2150	~95	1-10
	15 wt% Ta-doped HfB_2	2150	~95	1-10
	15 wt% Ta-doped HfB_2	2100	~90	--
	15 wt% Ta-doped HfB_2	2000	~81	--
Borothermal reduction reaction	HfB_2	2150	~93	2-6
	5 wt% Ta-doped HfB_2	2150	~95	2-6
	10 wt% Ta-doped HfB_2	2150	~97	2-6
	15 wt% Ta-doped HfB_2	2150	~97	2-6
Treibacher powder	HfB_2	2150	~94	5-10

*Theoretical density of HfB_2 and TaB_2 used is 10.5 and 11.15 g cm^{-3}, respectively

The fracture surface of the HfB_2-based ceramic prepared from carbothermal reduction derived powders was shown in Figure 4.56. The addition of Ta-dopants significantly reduced the porosity in the sample, due to the formation of $(Hf,Ta)B_2$ solid solution, which had a lower melting point than pure HfB_2 and thus required less energy for the particles to rearrange. However, although very limited porosity was found in the sintered samples, based on subsequent EDX analysis, impurities, such as carbon, were detected in these samples prepared from carbothermal reduction-derived powders, as shown in Figure 4.57.

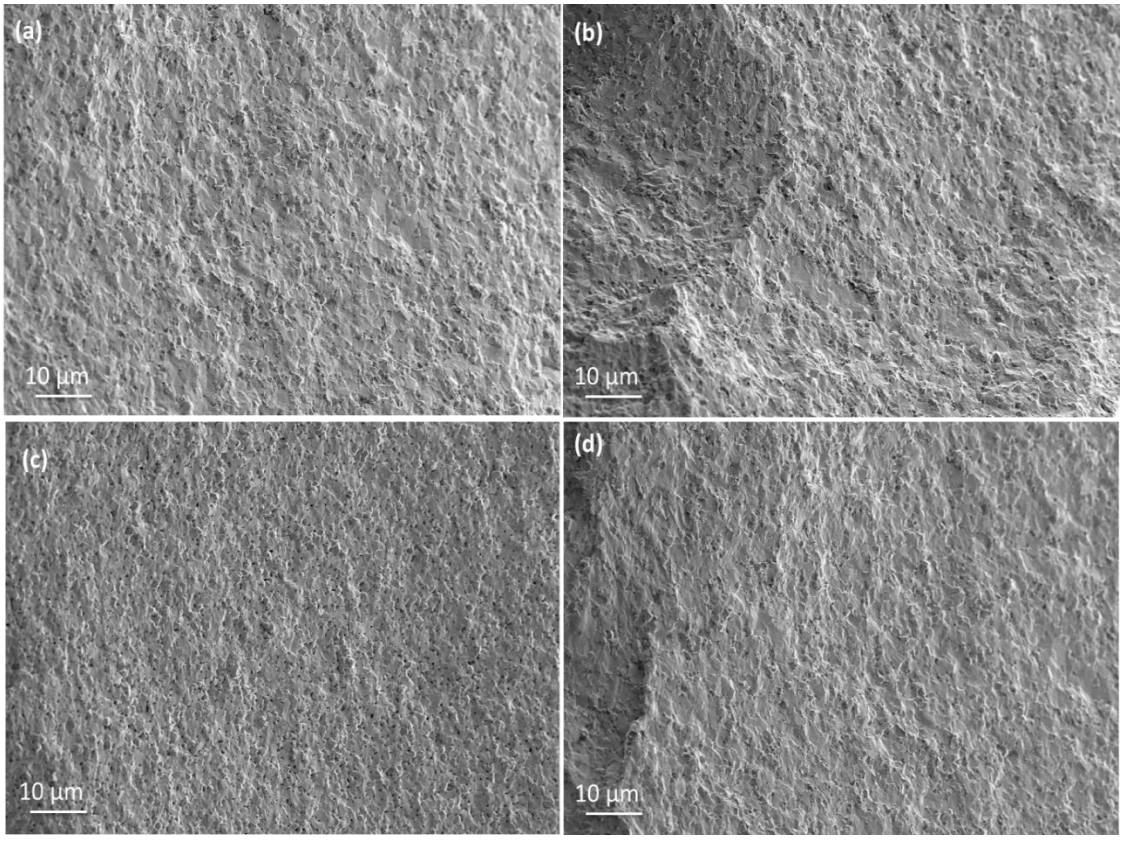

Figure 4.56 Fracture surfaces of (a) 0 wt%, (b) 5 wt%, (c) 10 wt% and (d) 15 wt% Ta-doped HfB_2 ceramics, sintered at 2150°C. The powders used for SPS were synthesized by carbothermal reduction reaction

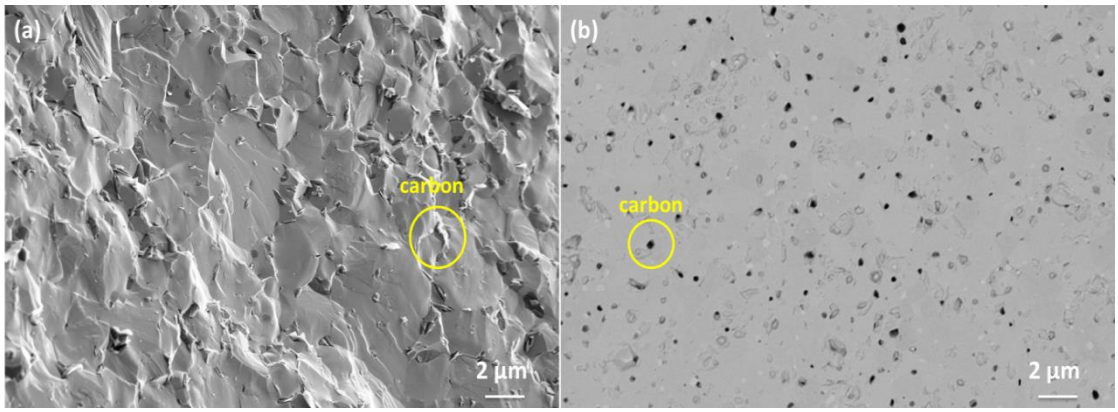

Figure 4.57 (a) Fracture surface and (b) polished surface of 15 wt% Ta-doped HfB_2 sintered at 2150°C at higher magnification. The powders used for SPS were synthesized by carbothermal reduction reaction

The polished surface of the HfB_2-based ceramics prepared by borothermal

reduction powders was shown in Figure 4.58. The use of Ta-dopants showed similar effect on the sinterability of HfB_2 as the density of the sintered samples increased with the increasing Ta-dopant percentage. Moreover, as the original powders were prepared by borothermal reduction method, no carbon was found in these samples.

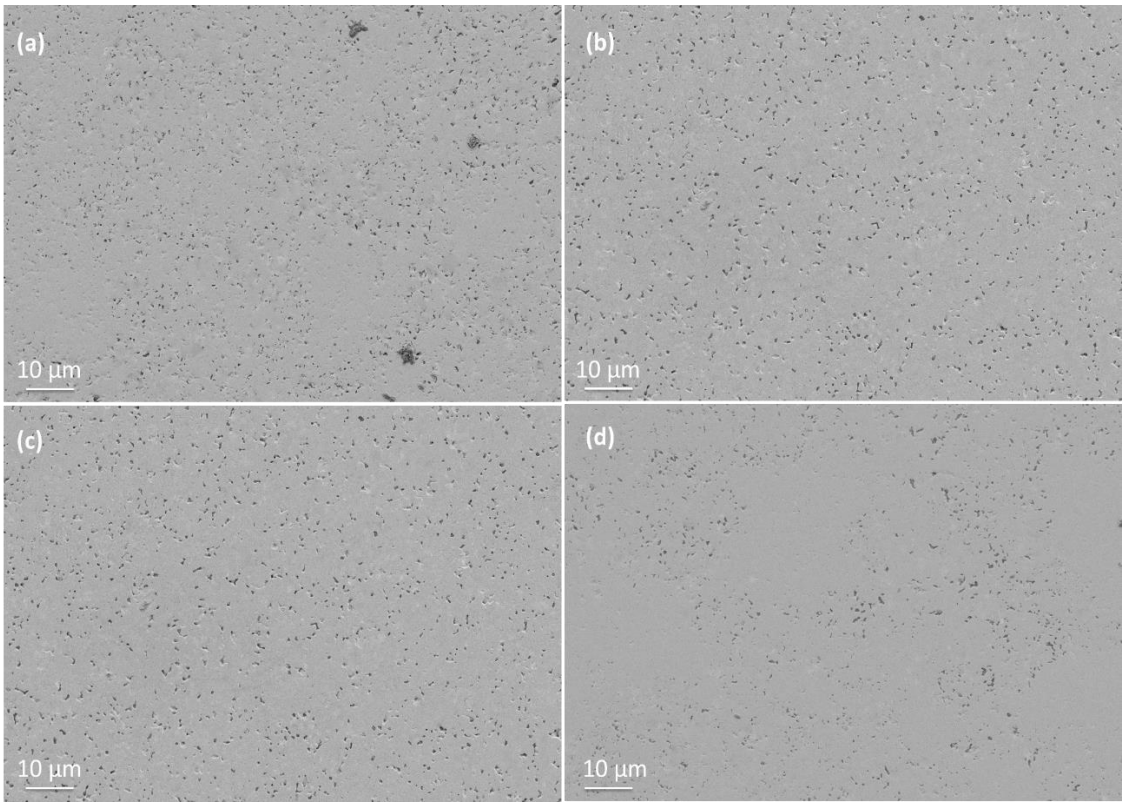

Figure 4.58 Polished surfaces of (a) 0, (b) 5, (c) 10 and (d) 15 wt% Ta-doped HfB_2 ceramics, sintered at 2150°C. The powders used were synthesized by borothermal reduction reaction

The grain sizes of the HfB_2-based ceramic prepared by the powders from different synthesis technique are compared in Figure 4.59 (a)-(b). Although the carbothermal reduction led to the formation of HfB_2-based powder with a particle size of ~200 nm, the resultant powder underwent significant grain growth and coarsening, which might be due to the presence of the large agglomerates. On the other hand, the particle size of the HfB_2-based powder from borothermal

reduction was ~600 nm, resulting in the grains ranging from 2 to 6 μm after SPS. Both these sythesized powders resulted in finer grains than that from the commercial HfB_2 powder.

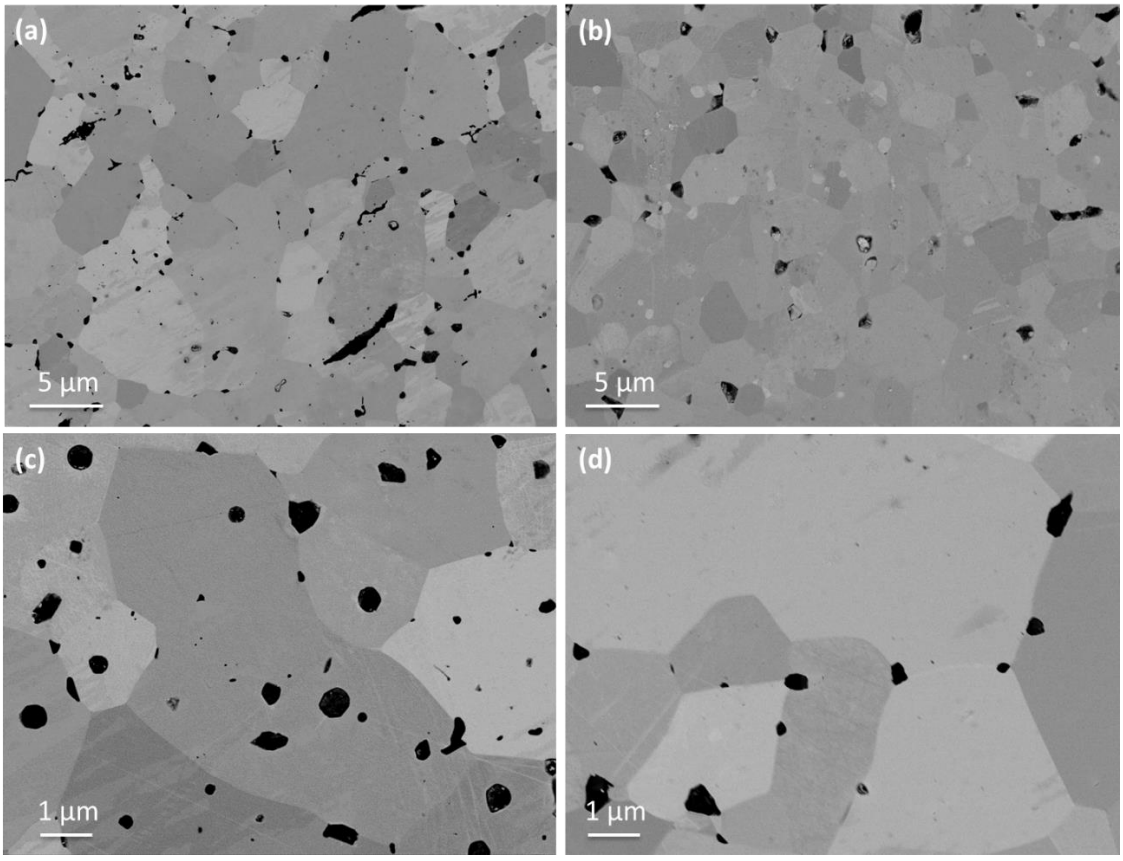

Figure 4.59 BSD images of the polished surface of 15 wt% Ta-doped HfB_2. (a) and (c) were prepared by the carbothermal reduction powders. (b) and (d) were prepared by the borothermal reduction powders. The colour difference of the HfB_2 grains in the BSD images is due to the orientation of the particles

Although >95% dense HfB_2-based ceramic suggested closed porosity inside the sintered bodies, it was still important to understand what hindered the densification process.In Figure 4.59 (c), based on supplemental EDX analysis, it was believed that the black spots inside the grain were due to carbon, which was trapped inside the agglomerates when the latter grew into large grains during densification. In Figure 4.59(d), the black spots which occurred along the

grain bounaries could be associated with pores. According to Figure 4.60, the EDX line scan confirmed the presence of pores as the signal from the copper mesh was picked up through the pore. Moreover, oxygen peaks observed on the wall of the pore suggested that the presence of HfO_2 and B_2O_3 may be the main reason for densification being inhibited.

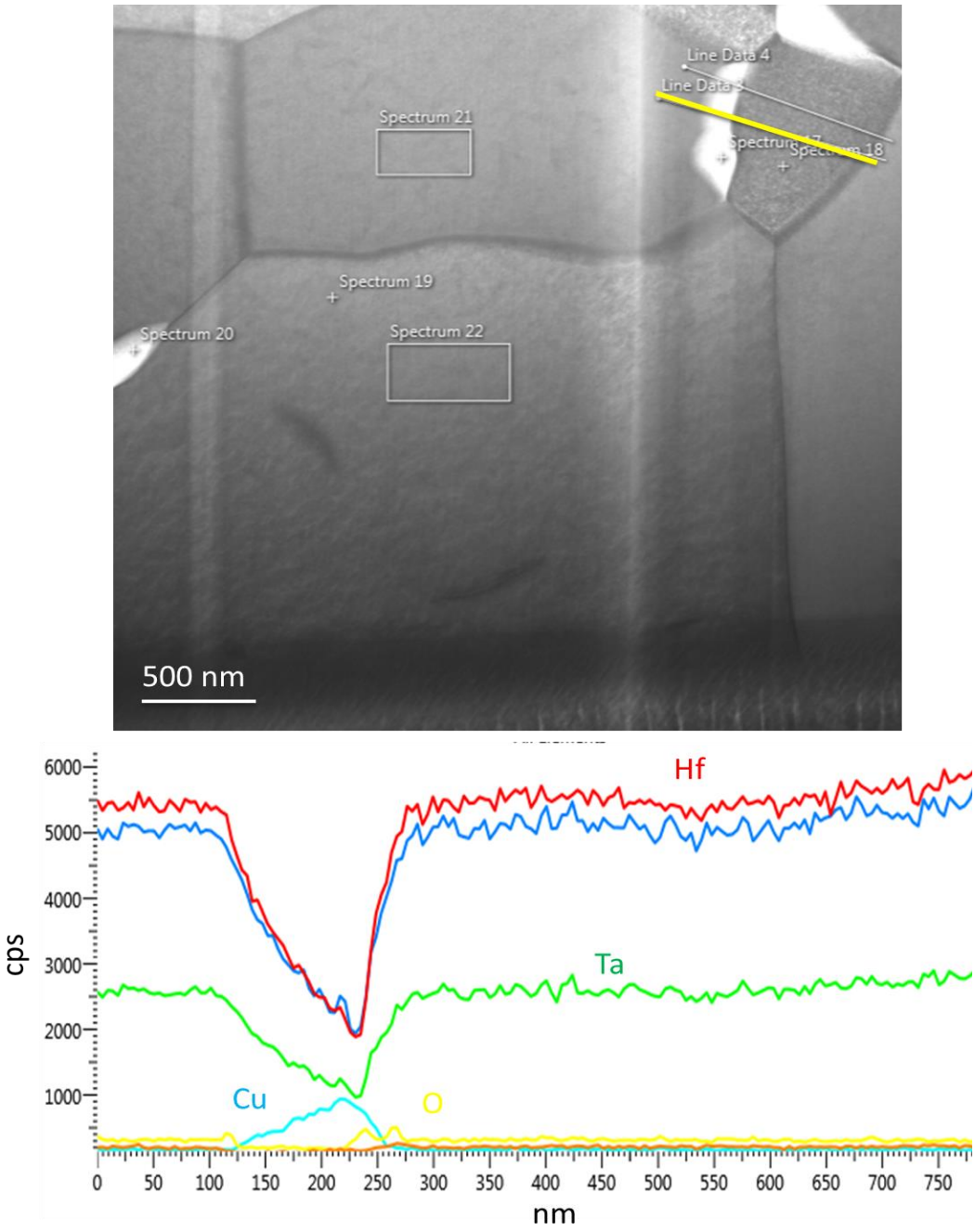

Figure 4.60 EDX elemental scan for 15 wt% Ta-doped HfB_2 grains preapared by FIB. The scan was performed along the solid yellow line across the pore

Oxygen impurities have been reported to limit the densification of diborides by the evaporation/condensation kinetics [277]. With increasing temperature, the boron oxide impurities started to melt and triggered densification of HfB_2 by causing localized particle rearrangement. However, the further densification would be inhibited due to the rapid collapse of the open pore structures during SPS, which led to that the B_2O_3 vapour generated was trapped within the closed pores. Regarding the grain sizes, it should be noted that finer powders have a much larger surface area, hence much greater surface energy, and so are susceptible to grain growth. Therefore, the HfB_2-based powders, which were synthesized by carbothermal reduction, with a starting particle size of ~200 nm could lead to the resultant grains up to 10 μm after sintering at 2150°C for 30 min. It was also reported that SPS could causing carbon contamination during the sintering of oxides [278], but for the sintering of HfB_2-based ceramics from the borothermal reduction synthesis, the carbon from the SPS die can react with any residual boron and reduce the HfO_2 impurities following Equation 4.3, hence improving the sinterability of these HfB_2-based materials.

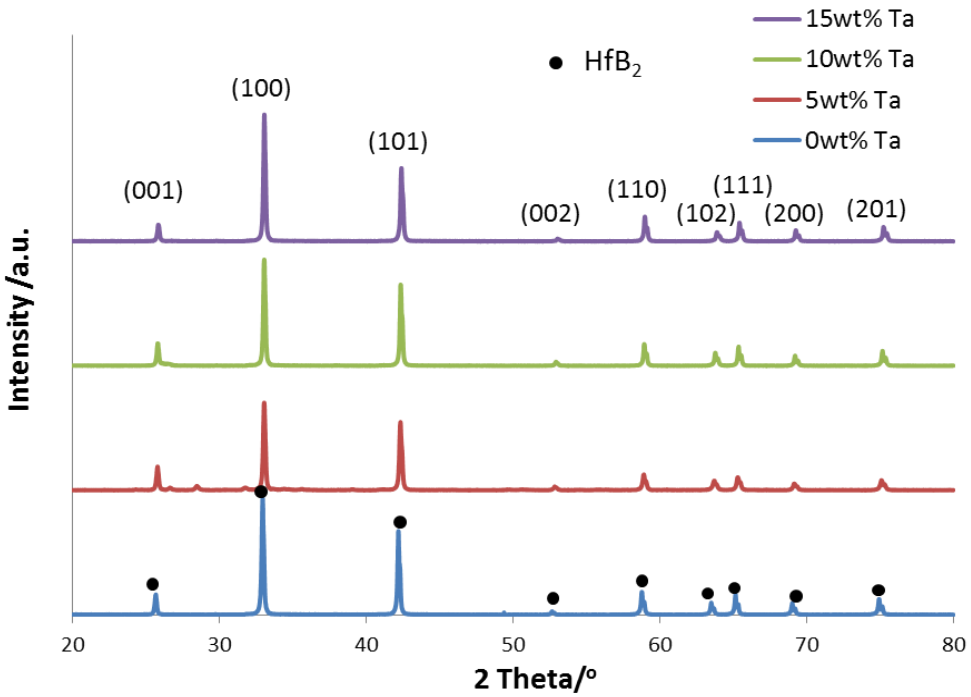

Figure 4.61 XRD pattern of the post-SPS pure and Ta-doped HfB_2 samples

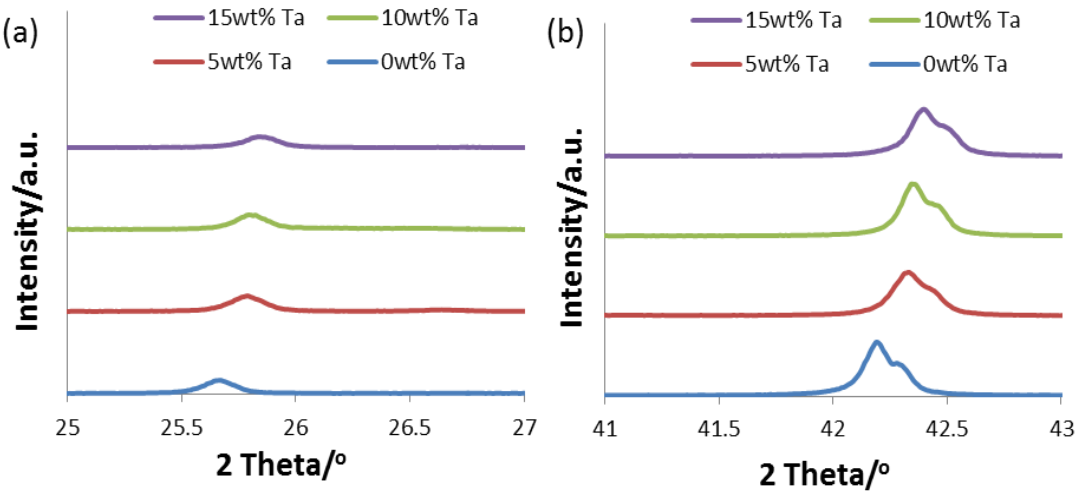

Figure 4.62 High resolution scan of (a) (001) and (b) (101) lattice plan of the post SPS pure and Ta-doped HfB_2

Based on the comparison between Figure 4.61 and 4.36, it can be seen that the $(Hf,Ta)B_2$ solid solution remains substantially the same after sintering at 2150°C. The extremely high temperature used probably allowed residual TaB_2 in the 15 wt% Ta-doped HfB_2 powder to further diffuse into the HfB_2 lattice to form single-phase $(Hf,Ta)B_2$ solid solution, as shown in Figure 4.62. Since the Ta-dopant did not form a precipitate during cooling down, it may be concluded that the solubility of TaB_2 in HfB_2 at 1600°C might >15 wt%. More work needs to be done to understand the Ta-Hf-B phase diagram at high temperatures, which hasn't been investigated yet.

4.4 Characterization of pure and Ta-doped HfB_2 sintered ceramics

4.4.1 Thermal and electrical conductivity measurements

The thermal conductivity, especially the high temperature thermal conductivity, is critical for hypersonic applications, as a higher thermal conductivity leads to lower surface temperature for UHTC components by conducting heat away.

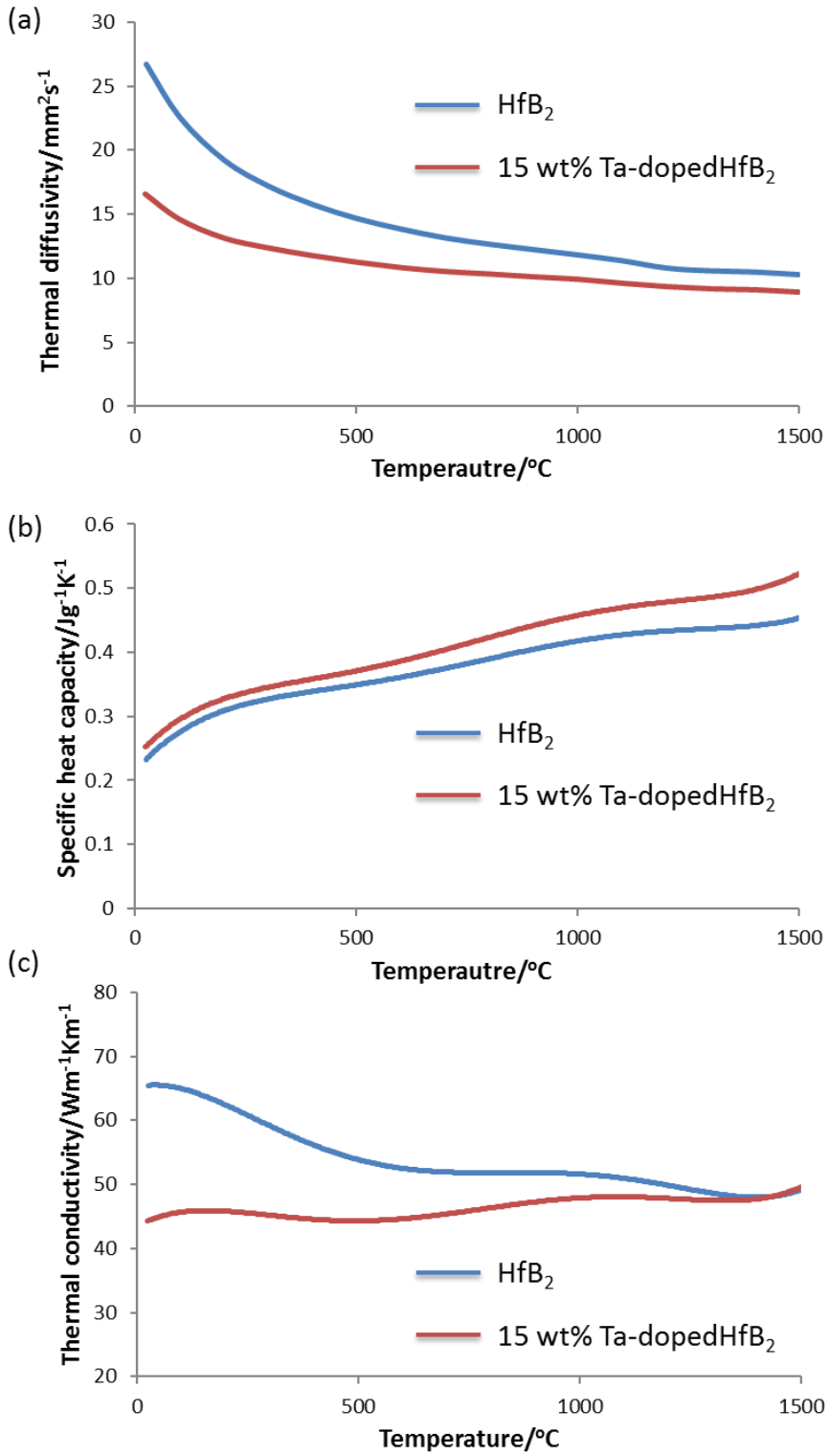

Figure 4.63 (a) Thermal diffusivity, (b) specific heat capacity and (c) thermal conductivity for pure and 15 wt% Ta-doped HfB_2, measured from room temperature to 1500°C. Thanks Dr. Zou from University of Birmingham for conducting the measurements

The thermal diffusivity and specific heat capacity of pure and 15 wt% Ta-doped HfB_2 were measured by laser flash method at University of Birmingham. The thermal conductivity values were calculated via Equation 4.13,

$$K=\alpha\rho C_p \quad (4\text{-}13)$$

where K is thermal conductivity, ρ is the density of pure and 15 wt% Ta-doped HfB_2 measured in Section 4.3.2 and C_p represents specific heat capacity. Figure 4.63 (a)-(c) shows the changes of thermal diffusivity, specific heat and thermal conductivity of pure and 15 wt% Ta-doped HfB_2 against temperature. The values of the thermal conductivity obtained for the investigated materials, are found to be slightly lower than those from the published literature [250], [252], as the density of the HfB_2-based ceramics used in this work is ~97%. The decrease in both thermal diffusivities and conductivities of the pure HfB_2 with increasing temperature, as shown in Figure 4.63 (a) and (c), can be attributed to lower mean free path for electronic transport and phonon scattering at higher temperatures, as has been pointed out by Zimmermann et.al. [254]. The thermal diffusivity of TaB_2 is lower than that of HfB_2, but the conductivity of 15 wt% Ta-doped HfB_2 increases slightly with the increase of temperature, probably due to the fact that there are more oxygen vacancies in $(Hf_{0.85}Ta_{0.15})B_2$ than that in HfB_2, which leads to longer mean free path for electronic transport and phonon scattering at higher temperatures.

The low electrical resistivity and the relatively high carrier density and Hall mobility of these HfB_2-based materials imply that electronic transport contributes substantially to heat transport. Figure 4.64 shows the change of electrical conductivity for pure and 15 wt% Ta-doped HfB_2 against temperature. The change of electrical conductivity was in a similar trend as that of thermal conductivity.

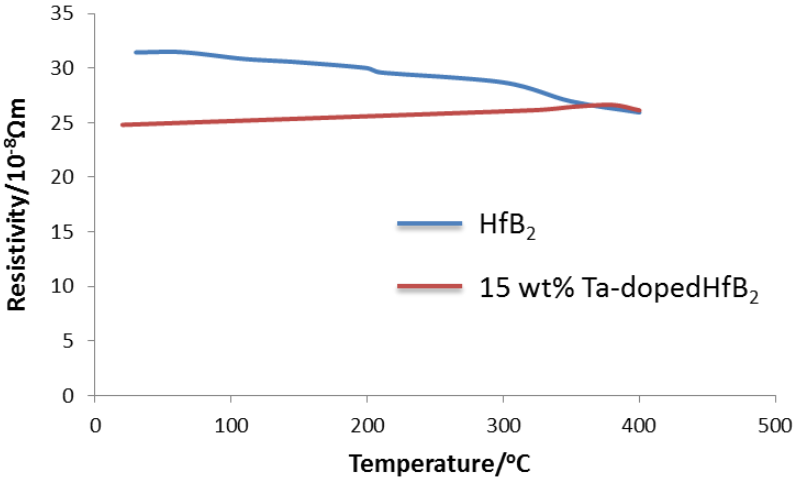

Figure 4.64 Electrical conductivity vs. temperature for pure and 15 wt% Ta-doped HfB_2

The ratio of the electronic component (λ_e) to total thermal conductivity (λ_t) at room temperature can be calculated via Wiedemann-Franz Law as below,

$$\frac{\lambda e}{\lambda t} = \frac{\delta TLo}{\lambda t} = \frac{TLo}{\rho \lambda t} \quad (4\text{-}14)$$

where σ is the electrical conductivity, ρ is the electrical resistivity and L_o is the Lorenz number, whose value has been taken as 2.45×10^{-8} W $\Omega^{-1}K^{-2}$. Based on the plots given in Figure 4.57 (c) and 4.58, at room temperature, the electronic contributions to thermal conductivity in the pure and 15 wt% Ta-doped HfB_2 were 90% and 87%, respectively. However, the electronic contributions decreased with the increasing temperature which enhanced photonic contributions [87].

4.4.2 Static oxidation testing

According to the XRD analysis of the pure and 15 wt% Ta-doped HfB_2 powders after heat treatment in air at different temperatures, Figure 4.65, it is seen that the oxidation of the HfB_2 powder started from 600°C. It should be noted that the

oxidation of pure HfB_2 resulted in the formation of monoclinic HfO_2, whilst the addition of 15wt% Ta-dopant led to the formation of tetragonal HfO_2, which was critical to understand the oxidation mechanism of Ta-doped HfB_2. It revealed the evidence that the use of Ta-dopant avoided the phase transformation of the oxidation product of HfB_2 at ultra-high temperature.

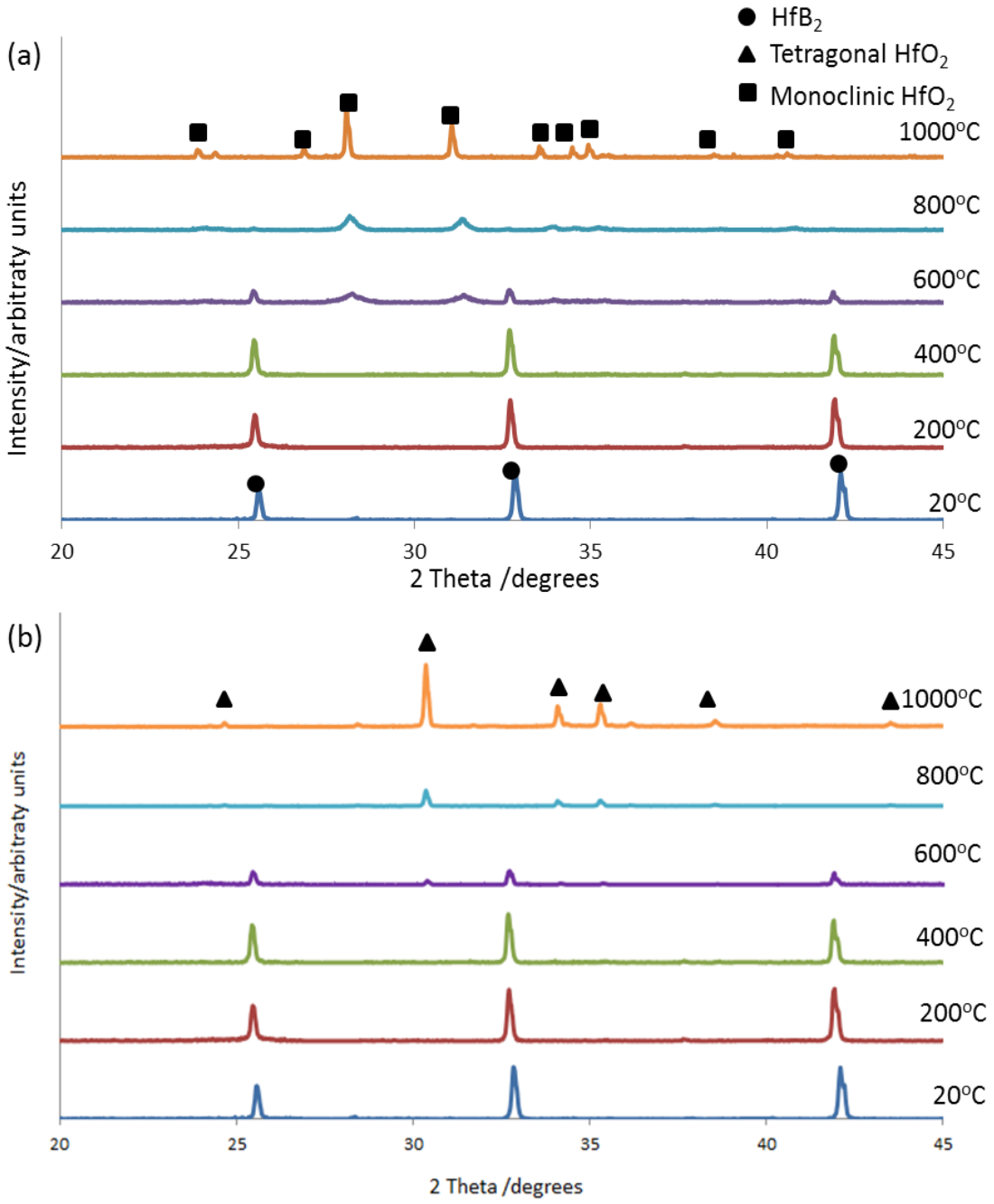

Figure 4.65 XRD patterns of the (a) pure HfB_2 and (b) 15 wt% Ta-doped HfB_2 powders oxidized in air at various temperatures

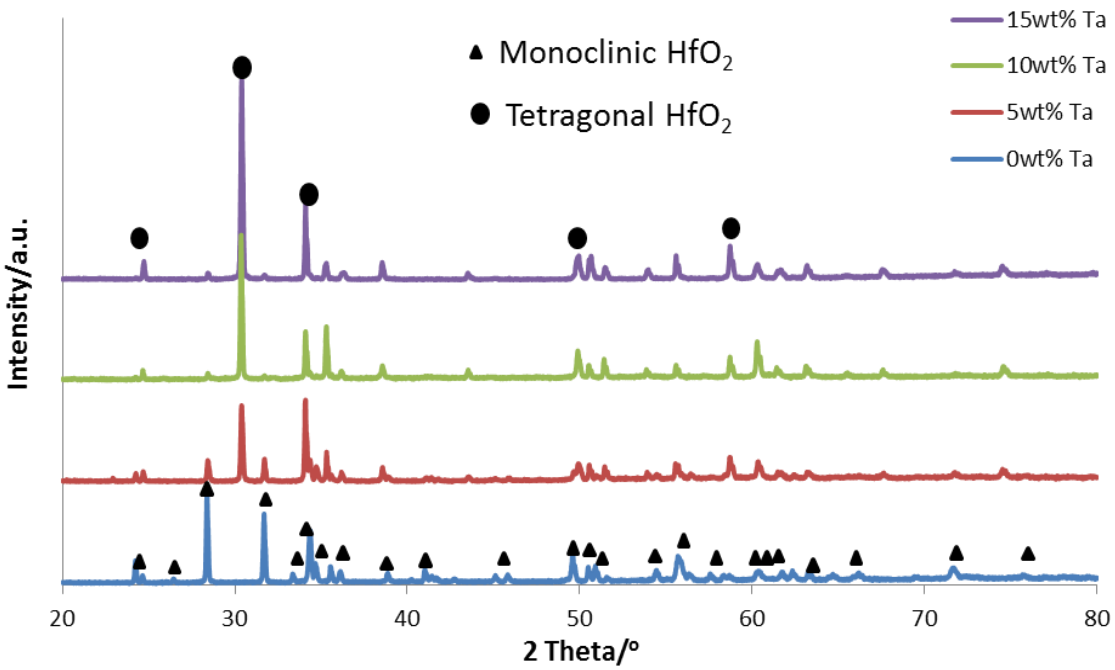

Figure 4.66 XRD patterns of the pure and Ta-doped HfB_2 powders left in oven at 1600°C for 30 min

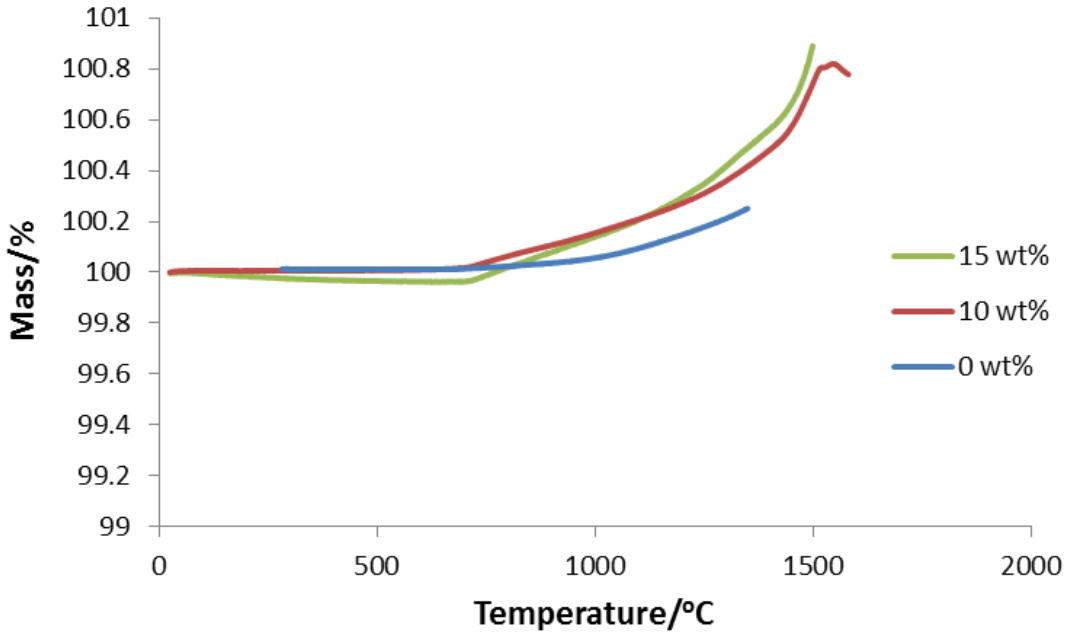

Figure 4.67 Mass change of the pure and Ta-doped HfB_2 powders at temperatures from room temperature to 1500°C with a heating rate of 5° min^{-1}

Furthermore, Figure 4.66 shows that the addition of 5 wt% Ta-dopant was insufficient to fully stabilize the oxidation product of HfB_2 in a tetragonal crystal structure, whilst 10 and 15 wt% Ta-dopant both resulted in the formation of almost fully stabilized tetragonal HfO_2.

According to Figure 4.67, the addition of Ta-dopant did not reduce the oxidation rate nor oxidation onset temperature of the HfB_2-based ceramics at temperatures <1600°C. The results were confirmed by measuring the thickness of the oxide scale of the HfB_2-based ceramics after oven oxidation, Figure 4.68. With the supplemental XRD and EDX analysis, the oxide scale of pure HfB_2 was ~15 µm in thickness and composed of monoclinic HfO_2 and B_2O_3, while the oxide scale of 15 wt% Ta-doped HfB_2 was ~25 µm in thickness and composed of tetragonal $(Hf,Ta)O_2$ and B_2O_3. At temperatures below 1600°C, the oxidation rate of the HfB_2-based ceramics was dominated by the rate of oxygen permeation through the protective B_2O_3 layer formed during HfB_2 oxidation. The addition of Ta dopant will have a very limited effect on the stability of the glassy B_2O_3 layer and hence did not improve the oxidation resistance of the HfB_2-based ceramics at temperatures <1600°C.

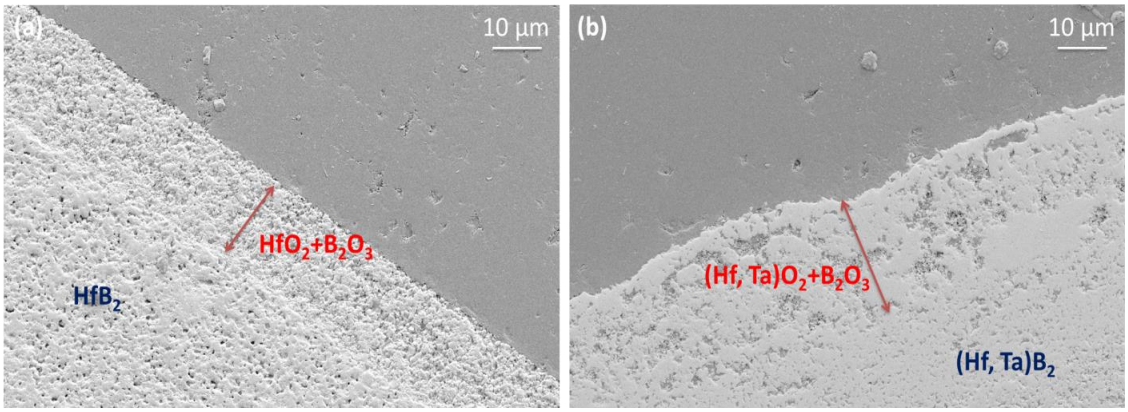

Figure 4.68 Cross-section of the pure and 15 wt% Ta-doped HfB_2 after exposing to air at 1600°C for 10 min

Table 4.11 Weight gain of the pure and Ta-doped HfB_2 after oven oxidation at 1000, 1300, 1600, 1700, 1800 and 1900°C for 10 min. Thanks Dr. Carney from AFRL for conducting the high-temperature oven oxidation tests.

Temperature /°C	Samples	Mass change / %	Thickness of oxide scale / μm
1000	HfB_2	0.1	<1
	5 wt% Ta-doped HfB_2	0.1	<1
	10 wt% Ta-doped HfB_2	0.1	<1
	15 wt% Ta-doped HfB_2	0.1	<1
1300	HfB_2	0.5	~4
	5 wt% Ta-doped HfB_2	0.5	~6
	10 wt% Ta-doped HfB_2	0.6	~5
	15 wt% Ta-doped HfB_2	0.7	~7
1600	HfB_2	1.2	~15
	5 wt% Ta-doped HfB_2	1.4	~18
	10 wt% Ta-doped HfB_2	1.4	~23
	15 wt% Ta-doped HfB_2	1.6	~25
1700	HfB_2	1.4	~55
	5 wt% Ta-doped HfB_2	3.6	~60
	10 wt% Ta-doped HfB_2	2.2	~53
	15 wt% Ta-doped HfB_2	2.9	~54
1800	HfB_2	1.8	~80
	5 wt% Ta-doped HfB_2	3.1	~80
	10 wt% Ta-doped HfB_2	2.5	~75
	15 wt% Ta-doped HfB_2	2.2	~75
1900	HfB_2	2.0	~110
	5 wt% Ta-doped HfB_2	3.1	~118
	10 wt% Ta-doped HfB_2	2.8	~108
	15 wt% Ta-doped HfB_2	0.4	~109

The scenario for the oxidation of HfB_2-based ceramics at temperatures >1600°C was quite different from that at temperatures <1600°C, since in the high temperature scenario, all B_2O_3 evaporates as soon as it was formed. The B_2O_3 volatiles did not only result in a porous HfO_2 layer, but also led to poor adherence of the oxides. It can be seen from Figure 4.69 that the oxide scale of the HfB_2 sample easily spalled off after the oven oxidation at 1700°C and 1800°C, whilst the oxides formed on the Ta-doped HfB_2 samples showed good adherence. At 1900°C, the oxide scale of both pure and Ta-doped HfB_2 showed a rough surface, which might be due to the rapid evaporation of B_2O_3. According

to the thickness measurements of the oxide scale in these samples, Table 4.10, it was believed that the use of Ta-dopants led to the formation of a similarly thick but more dense tetragonal $(Hf,Ta)O_2$ layer rather than the porous monoclinic HfO_2 layer with column-like structures, as shown in Figure 4.70. It should be noted that the mass change of the samples, which tested at temperatures >1600°C, Table 4.11, was not highly reliable since the oxide scale spalled off the sample could be missing during collection or transportation.

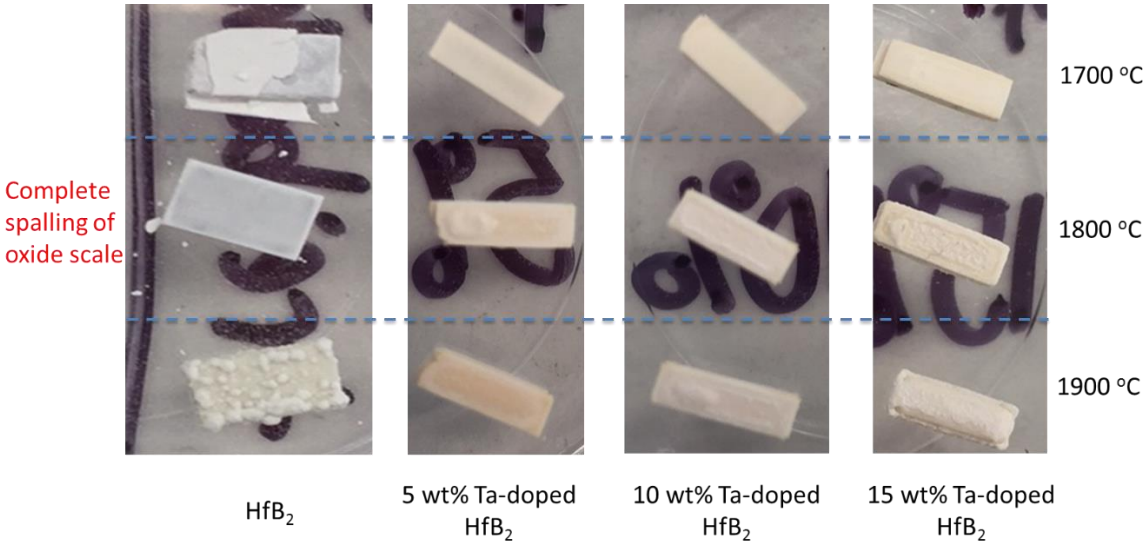

Figure 4.69 HfB_2-based ceramics after oxidation testing at 1700, 1800 and 1900°C in a zirconia oven

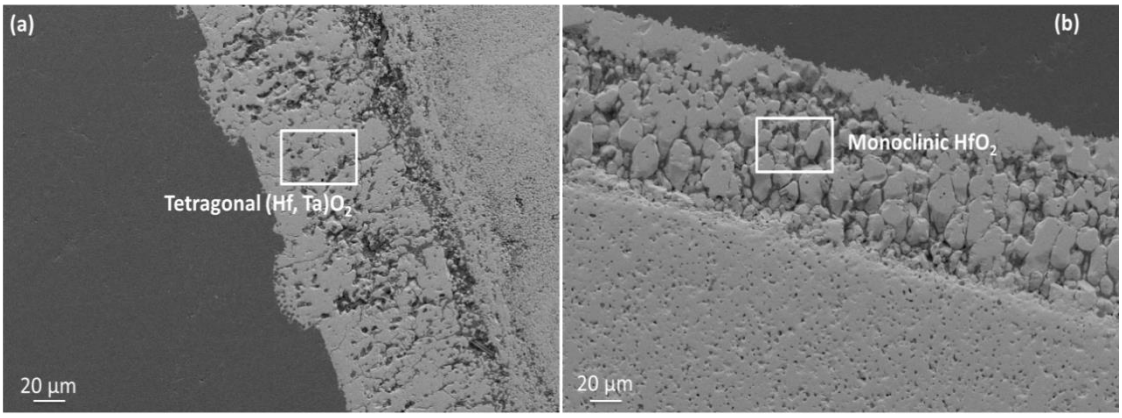

Figure 4.70 Cross section of the pure and 15 wt% Ta-doped HfB_2 after exposure to air at 1800°C for 10 min

4.4.3 Oxyacetylene torch testing

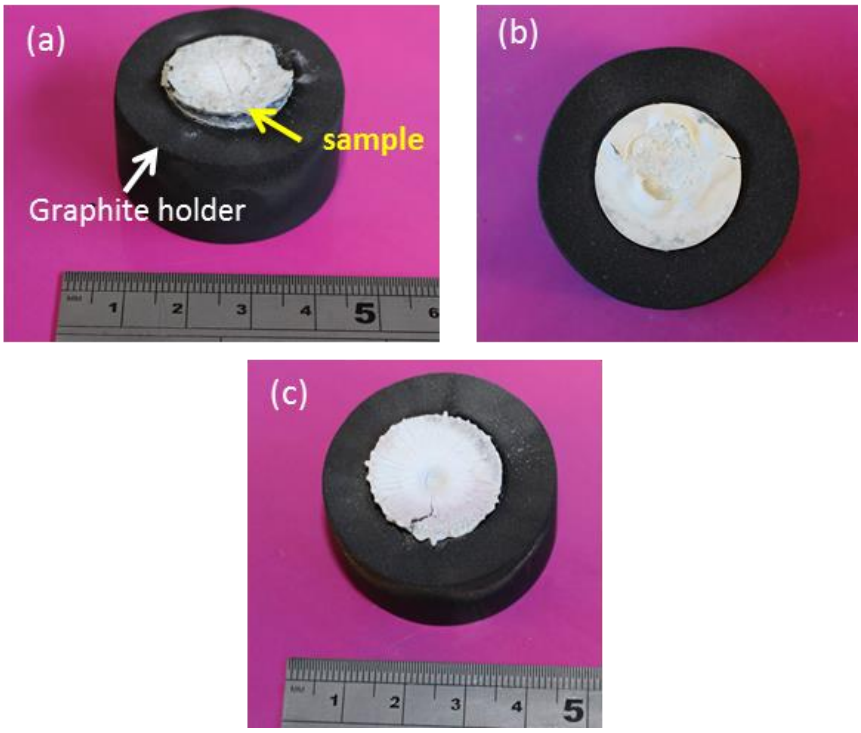

Figure 4.71 Sample photos of (a) HfB_2 and (b) 15 wt% Ta-doped HfB_2 tested at 2300^oC for 240 s and (c) 15 wt% Ta-doped HfB_2 tested at 2800^oC for 240s

Oxyacetylene torch tests were performed for the pure and 15 wt% Ta-doped HfB_2 samples with sample-nozzle distances of 10 and 20 mm and the same testing duration of 240 s. The time-temperature data after the test represented that the peak temperatures of both samples reached 2300 and 2800^oC for the sample-nozzle distances of 10 and 20 mm, respectively. Figure 4.71(a) shows that the pure HfB_2 sample had broken into several pieces after the test at 2300^oC, due to the thermal shock associated with rapid heating. The heating rate easily exceeded >100^oC s^{-1} during the test, as also reported by Paul et. al. for the oxyacetylene testing of TaC samples [263]. The 15 wt% Ta-doped HfB_2 samples, however, survived both the 2300^oC and 2800^oC tests without major structural fracture. Furthermore, Figure 4.71(b) shows that the 15 wt% Ta-doped

HfB_2 sample tested at 2300^oC resulted in a more continuous oxide scale with less major cracking compared to the post-test pure HfB_2 samples.

The oxide scales of these samples showed poor adherence, which could be due to the thermal expansion coefficient difference of the borides and their resultant oxides and the difference was enhanced by the very rapid heating that occurs during this particulate dynamic oxidation test. When the test temperature was increased to 2800^oC, it was clearly seen from Figure 4.71(c) that the oxide scale of the 15 wt% Ta-doped HfB_2 melted at such a high temperature. The melting point of HfO_2 is 2758^oC, but the melting point of the Ta-doped HfO_2 may be lower, though the exact value is unknown yet.

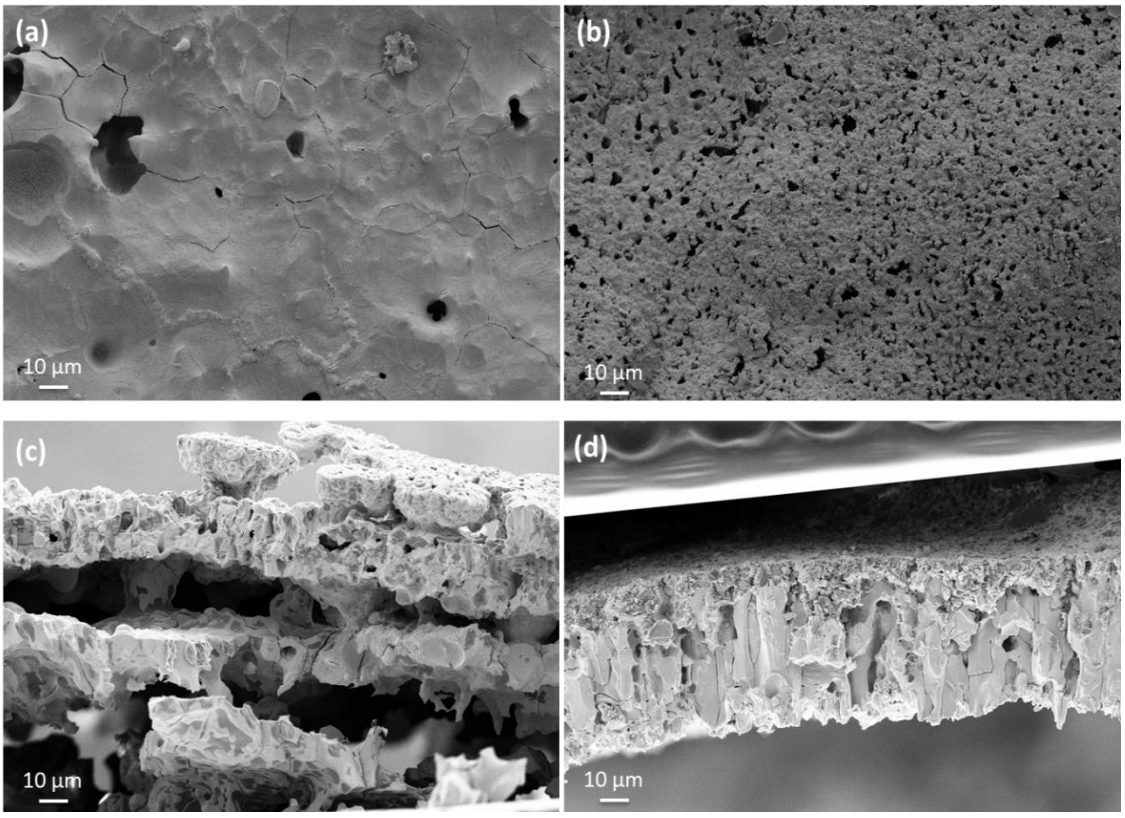

Figure 4.72 (a) Top surface and (c) fracture surface of 15 wt% Ta-doped HfB_2 tested at 2300^oC and (b) top surface and (d) fracture surface of pure HfB_2 tested at 2300^oC

The microstructure of the oxide scales for post-test pure and Ta-doped HfB_2 displayed in Figure 4.72 (a)-(c) also proved that a more dense oxide scale with tetragonal $(Hf,Ta)O_2$ was formed from the oxidation of 15 wt% Ta-doped HfB_2. Figure 4.72(d) shows that the monoclinic HfO_2, which was the oxidation product of pure HfB_2, had a column-like structure. Similar structure was observed from the oxide scale of the same material in static oven oxidation. The large gaps between the 'columns' was created after the evaporation of the volatiles such as B_2O_3. On the other hand, the more dense tetragonal $(Hf,Ta)O_2$ layer could temporarily trap the volatiles beneath the oxide scale, thus forming a multi-layered structure. However, the vapour pressure of the volatiles in the tetragonal $(Hf,Ta)O_2$ might eventually exceed a critical value, leading to spalling-off of the oxide scales.

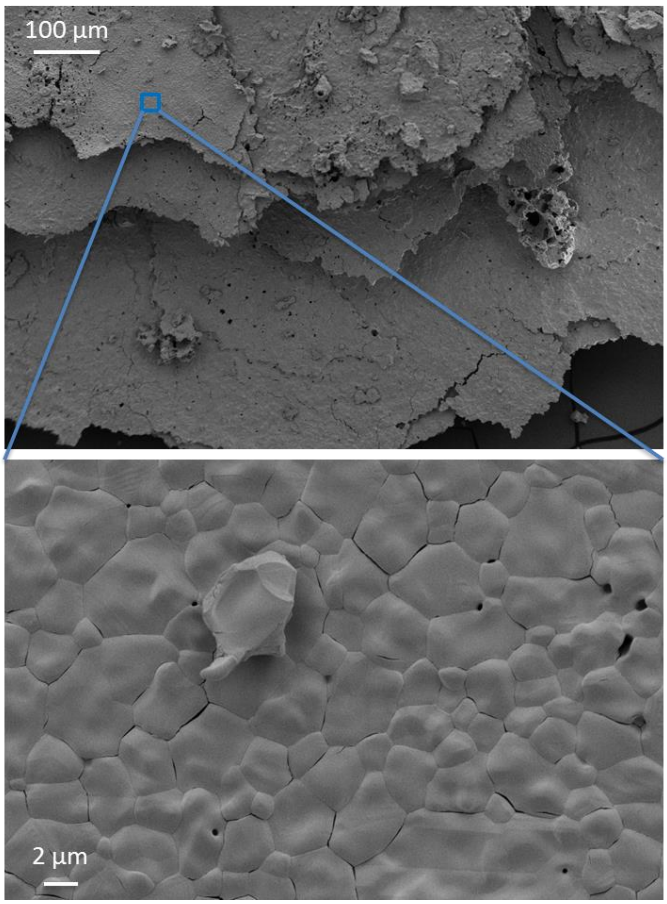

Figure 4.73 Top surface of 15 wt% Ta-doped HfB_2 tested at 2800°C

Figure 4.73 demonstrates the microstructure of the oxide scale of the 15 wt% Ta-doped HfB_2 after the test at 2800^{o}C. The oxide scale showed a multi-layer structure that was similar to the 2300^{o}C testing results. However, (Hf,Ta)O_2 was found to be melted at 2800^{o}C and then crystallised when cooling down. The (Hf,Ta)O_2 melt could be blown away by the ~Mach 0.65 gas flow which was employed in the oxyacetylene torch test. Therefore, it can be concluded that the Ta-doped HfB_2 components have the potential to be used for the hypersonic application with working temperatures in the range of 1700-2300^{o}C, which is above the phase transformation temperature of HfO_2 but below the melting point of Ta-doped HfO_2, and these components may be suitable for long-term use as the phase transformation of HfO_2 is hindered.

5. Conclusions

Doped HfB_2 powder was initially prepared by a low temperature sol-gel approach using $HfCl_4$, H_3BO_3 and phenolic resin as raw materials. From thermal degradation, the starting materials were found to be forming $HfOCl_2$, B_2O_3 and carbon as resultant precursors. Doped HfB_2 was formed via carbothermal reduction reaction of these precursors at temperatures as low as 1300°C, which is more than 200°C lower than the calculated on-set temperature of carbothermal reduction reaction. It is postulated that HfB_2 could form at 1300°C via the reaction between HfO_2 and highly reactive boron species, such as boron or boron ion, which was backed up by thermodynamic calculation on reaction sequence. In addition, the homogeneous mixing of the reactants achieved by sol-gel approach, the low B_2O_3 vapour pressure in the argon atmosphere and the lower reaction temperature also helped to improve the reaction rate. Though it was reported to require 25 h at 1300°C for the carbothermal reaction to complete, whilst that the completion of the carbothermal reaction only took 2 h at 1600°C.

The effect of changing the stoichiometry of the precursors on the purity of the final powders was also investigated. It was observed that twice amount of boron compared to the stoichiometric ratio was required to compensate for the boron loss during the synthesis to achieve pure as well as Ta-doped HfB_2 powders. The boron loss was attributed to the evaporation of B_2O_3 and the reaction of B_2O_3 with residual chlorine from $HfOCl_2$. The presence of chlorine not only raised the difficulties in controlling the purity of the HfB_2 powders obtained by carbothermal reduction, but also damaged the furnace set-up used for heat treatment through evaporation and condensation. Hence, the attempts to get rid of chlorine was calcining the precursors at 400°C (below the degradation temperature of carbon), were unable to completely resolve the issue. Then

NH_4OH was used to react with $HfOCl_2$ aqueous solution to remove chlorine by forming $Hf(OH)_4$ precipitates over a wide pH range from 4-10. It was found that the use of $Hf(OH)_4$ instead of $HfOCl_2$ significantly reduced boron loss and improved the control on the purity of HfB_2 powders. More importantly, the co-precipitation of $Hf(OH)_4$ and $Ta(OH)_5$ by adjusting pH value to 8.5 allowed homogeneous Ta distribution with Hf. HfB_2 rod formation was observed during the carbothermal reduction reactions under high concentrations of liquid B_2O_3. It was believed that the solid-liquid-gas grain growth mechanism was the main reason leading to the elongated particle growth. The mean particle size of the HfB_2 powder yielded from the carbothermal reduction reaction was ~200 nm. The sub-micron HfB_2 powder was probably resulted from the extremely fine HfO_2 nuclei derived by sol-gel approach and the presence of carbon from cross-linked phenolic resin which inhibited HfB_2 grain growth. However, agglomerates were observed in the powders yielded from carbothermal reduction reaction.

Two different dopants, Y- and Ta-containing compounds, which were added into HfB_2 by in-situ synthesis, were compared to understand their effect on the oxidation mechanism of HfB_2. The XRD results of the powders yielded by carbothermal reduction reaction revealed the formation of $(Hf,Ta)B_2$ solid solution while segregated Y_2O_3 was detected when Y was used as a dopant. As the aim of this work was to inhibit the volume change due to HfO_2 phase transformation during the HfB_2-based ceramic oxidation, it was deemed necessary to have a solid solution rather than segregated phases. The formation of $(Hf,Ta)B_2$ solid solution mainly depended on the diffusion of Ta into the HfB_2 lattice, which happened at temperatures >1400^oC. The excellent distribution of Ta from the co-precipitation approach lead to the formation of $(Hf,Ta)B_2$ solid solution at temperature as low as 1600^oC. The subsequent oxidation test performed on the powders showed that the oxidation product of 15 wt% Ta-doped HfB_2 was almost completely stabilized as tetragonal HfO_2.

Ta-doped HfB_2 was also synthesised by borothermal reduction reaction, which show better control on the purity of the powders yielded, as borothermal reduction only involved using boron as the reducing agent and the possible impurities, such as B_2O_3 can be easily removed by heat treatment at 1600^oC for longer time. Borothermal reduction reaction resulted in higher purity of Ta-doped HfB_2, but the particle size (~600 nm) of the resultant powders was larger than that from carbothermal reduction reaction, since there is no grain growth inhibition mechanism being operative.

Pure and Ta-doped HfB_2 powders were initially densified using pressure-less method such as flash and microwave sintering. Although the sample temperature reached 1800^oC in flash sintering trials, it was not enough to sinter the HfB_2-based ceramic without applying pressure. Pressure-assisted SPS sintering of the sub-micron Ta-doped HfB_2 powders obtained by borothermal reduction reaction at the maximum temperature of 2150^oC and 60MPa, resulted in 97% dense body. It was found the addition of Ta dopants slightly improved the densification, because less energy was required for the densification of $(Hf,Ta)B_2$. However, for the powders prepared by carbothermal reduction reaction, small amount of carbon was found in the sample and B_2O_3 was detected in the pores of the sintered ceramic. The density of the powder prepared by borothermal reduction reaction was similar as that prepared by carbothermal reduction reaction, which may be due to the compromise of higher purity of the powder and bigger particle size.

The thermal conductivity measurements showed that the 15 wt% Ta-doped HfB_2 had similar conductivity as pure HfB_2 at 1500^oC. The assessment of the oxidation behaviour of the sintered ceramics was carried out in static oven and by oxyacetylene torch testing. At temperatures <1600^oC, the oxidation rate was

controlled by the glassy B_2O_3 layer, therefore the addition of Ta dopant didn't improve the oxidation resistance of HfB_2 as $(Hf,Ta)B_2$ oxidized faster than pure HfB_2. But at temperatures >1600^oC, the addition Ta dopants lead to a denser and more adherent oxide scale, which was also found from the dynamic oxidation test at temperature up to 2300^oC. Therefore, the addition of Ta-dopant, which avoided the phase transformation of the oxide scale of HfB_2, was critical for the latter to be usable for hypersonic re-entry applications in extreme environments.

6. Future work

Although sol-gel synthesis of sub-micron pure and Ta-doped HfB_2 powders was successfully made in lab-scale batch, larger scale synthesis leads to problems of inhomogeneous mixing amongst the precursors and single phase HfB_2 could not be obtained all the times. In larger batch synthesis the flow of liquid B_2O_3 can also result in serious purity issues. In order to make sure the same level of mixing is obtained for larger batch synthesis, better high shear mixing equipment and heat treatment set-up with longer heating zone need to be used.

The powders prepared by carbothermal reduction or borothermal reduction need to be checked by the XPS, SEM and TEM to confirm the purity is consistent and reliable. More work need to be done to modify the ratio of the starting materials more precisely. For example, it may be necessary to use the Hf:B:C ratio between 1:3:5 and 1:4:5 for carbothermal reduction reaction to minimize the impurity phase. For the densification, even 1wt% carbon or B_2O_3 impurities can significantly reduce the resulting density of the final ceramic.

More work on flash and microwave sintering need to be performed to improve the possibility of the densification of these materials with pressure-less techniques, as it will be helpful to produce complex shaped UHTC components for hypersonic applications. In order to get high density from pressure-less sintering, sintering-aids such B_4C and $TaSi_2$ may also be used.

More work for developing an understanding of the mechanical properties of Ta-doped HfB_2 at elevated temperatures is needed.

The oxidation testing of the pure and Ta-doped HfB_2 should be repeated several times on the sample to investigate the effect of Ta-dopant addition for the long-

term use. If the multiple trials turned out to be successful, then it can be confirmed the stabilization of tetragonal HfO_2 could avoid the cracking due to the volume change from the cycles of fast heating and cooling during hypersonic flights.

7. References

[1] M. J. Neufeld, The Rocket and the Reich: Peenemünde and the Coming of the Ballistic Missile Era, Harvord University Press, pp. 11-16, 1995.

[2] J. W. Hicks, Flight Testing of Airbreathing Hypersonic Vehicles, NASA technical memorandum, no. 4524.

[3] http://naca.central.cranfield.ac.uk/reports/1957/naca-tn-4046.pdf.

[4] P. Watts and F. Fish,"The influence of passive, leading edge tubercles on wing performance," Proc. Twelfth Intl. Symp. Unmanned Untethered Submers. Technol., 2001.

[5] http://www.nasa.gov/missions/research/x43-main.html.

[6] http://www.cosmostv.org/2011/04/6-surprising-facts-about-nasas-space.html.

[7] G. Chapline, C. Snapp, M. Pessin, J. Butler, J. S. Sparks, P. Bauer and C. Stevenson, "Thermal protection systesms," Egineering Inovations, pp. 182–199, 2014

[8] P. Kolodziej,"Aerothermal performance constraints for hypervelocity small radius unswept leading edges and nosetips," Nasa Tech. Memo., July, 1997.

[9] S. Candane, C. Balaji and S. Venkateshan, "Ablation and aero-thermodynamic studies on thermal protection systems of sharp-nosed re-entry vehicles," Journal of Heat Transfer-Transactions of the Asme, vol. 129, no. 7, pp. 912-916, 2007.

[10] T. A. Parthasarathy, M. D. Petry, M. K. Cinibulk, T. Mathur and M. R. Gruber,"Thermal and oxidation response of UHTC leading edge samples exposed to simulated hypersonic flight conditions," J. Am. Ceram. Soc., vol. 96, no. 3, pp. 907-915, 2013.

[11] B. Berton, M. Bacos, D. Demange and J. Lahaye, "High-temperature oxidation of silicon carbide in simulated atmospheric re-entry conditions", J. Mater. Sci. vol. 27, pp. 3206-3210, 1992.

[12] H. Scott, "Phase relationships in the zirconia-yttria system," J. Mater. Sci. vol. 10, pp. 1527-1535, 1975.

[13] K. Upadhya, J. Yang and W. Hoffman, "Materials for ultra-high temperature structural applications", Am. Ceram. Soc. Bull. vol. 76, no. 12, pp. 51-56, 1997.

[14] A. Paul, S. Venugopal, J. Binner, B. Vaidhyanathan, A. Heaton and P. Brown,"UHTC–carbon fibre composites: preparation, oxyacetylene torch testing and characterisation," J. Eur. Ceram. Soc., vol. 33, no. 2, pp. 423–432, 2013.

[15] D. D. Jayaseelan, P. Brown and W. E. Lee, "Reactive infiltration processing (RIP) of ultra high temperature ceramics (UHTC) into porous C/C composite tubes," J. Eur. Ceram. Soc., vol. 31, no. 3, pp. 361–368, 2011.

[16] M. Zamharir, M. Asl, N. Vafa and M. Kakroudi, "Significance of hot pressing parameters and reinforcement size on densification behavior of ZrB_2-25 vol% SiC UHTCs," Ceram. Int., vol. 41, no. 5, pp. 6439–6447, 2015.

[17] F. Arianpour, F. Golestanifard, H. Rezaie, M. Mazaheri, A. Celik, F. Kara and G. Fantozzi, "Processing, phase evaluation and mechanical properties of $MoSi_2$ doped 4TaC–HfC based UHTCs consolidated by spark plasma sintering," Int. J. Refract. Met. Hard Mater., vol. 56, pp. 1–7, 2016.

[18] D. D. Jayaseelan, E. Zapata-Solvas, R. J. Chater and W. E. Lee, "Structural and compositional analyses of oxidised layers of ZrB_2-based UHTCs," J. Eur. Ceram. Soc., vol. 35, no. 15, pp. 4059–4071, 2015.

[19] F. Peng and R. F. Speyer, "Oxidation Resistance of Fully Dense ZrB_2 with SiC, TaB_2 , and $TaSi_2$ Additives," J. Am. Ceram. Soc., vol. 91, pp. 1489–1494, 2008.

[20] F. Monteverde, D. Alfano and R. Savino, "Effects of LaB_6 addition on arc-jet convectively heated SiC-containing ZrB_2-based ultra-high temperature ceramics in high enthalpy supersonic airflows," Corros. Sci., vol. 75, pp. 443–453, 2013.

[21] M. M. Opeka, I. G. Talmy, E. J. Wuchina, J. Zaykoski and S. J. Causey, "Mechanical, thermal, and oxidation properties of refractory hafnium and zirconium compounds," J. Eur. Ceram. Soc., vol. 19, no. 13–14, pp. 2405–2414, 1999.

[22] M. Mallik, K. K. Ray and R. Mitra, "Oxidation behavior of hot pressed ZrB_2-SiC and HfB_2-SiC composites," J. Eur. Ceram. Soc., vol. 31, pp. 199–215, 2011.

[23] J. F. Justin and A. Jankowiak, "Ultra high temperature ceramics: densification, properties and thermal stability," Aerosp. Lab J., vol. 8, no. 3, pp. 1–11, 2011.

[24] Z. Kováčová, Ľ. Bača, E. Neubauer and M. Kitzmantel, "Influence of sintering temperature, SiC particle size and Y_2O_3 addition on the densification, microstructure and oxidation resistance of ZrB_2–SiC ceramics," J. Eur. Ceram. Soc., vol. 36, no. 12, pp. 3041-3049, 2016.

[25] D. W. Ni, G. J. Zhang, F. F. Xu and W. M. Guo, "Initial stage of oxidation process and microstructure analysis of HfB_2-20 vol.% SiC composite at 1500^{o}C," Scr. Mater., vol. 64, no. 7, pp. 617–620, 2011.

[26] F. Monteverde and A. Bellosi, "The resistance to oxidation of an HfB_2-SiC composite," J. Eur. Ceram. Soc., vol. 25, no. 7, pp. 1025–1031, 2005.

[27] Z. Wang, Z. Wu and G. Shi, "The oxidation behaviors of a ZrB_2-SiC-ZrC ceramic," Solid State Sci., vol. 13, no. 3, pp. 534–538, 2011.

[28] Z. Zhang, C. Nan, J. Xu, Z. Gao, M. Li and J. Wang, "Oxidation behaviors of C-ZrB_2-SiC composite at 2100ºC in air and O_2," J. Mater. Sci. Technol., vol. 30, no. 12, pp. 1223–1229, 2014.

[29] V. Medri, F. Monteverde, A. Balbo and A. Bellosi, "Comparison of ZrB_2-ZrC-SiC composites fabricated by spark plasma sintering and hot-pressing," Adv. Eng. Mater., vol. 7, no. 3, pp. 159–163, 2005.

[30] D. Sciti, L. Silvestroni and A. Bellosi, "Fabrication and properties of HfB_2-$MoSi_2$ composites produced by hot pressing and spark plasma sintering," J. Mater. Res., vol. 21, no. 6, pp. 1460–1466, 2006.

[31] S. Venugopal, A. Paul, B. Vaidhyanathan, J. Binner, A. Heaton and P. Brown, "Synthesis and spark plasma sintering of sub-micron HfB_2: Effect of various carbon sources," J. Eur. Ceram. Soc., vol. 34, no. 6, pp. 1471–1479, 2014.

[32] F. Monteverde, C. Melandri and S. Guicciardi, "Microstructure and mechanical properties of an HfB_2 + 30 vol.% SiC composite consolidated by spark plasma sintering," Mater. Chem. Phys., vol. 100, pp. 513–519, 2006.

[33] R. Savino, M. Fumo, L. Silvestroni and D. Sciti, "Arc-jet testing on HfB_2 and HfC-based ultra-high temperature ceramic materials," J. Eur. Ceram. Soc., vol. 28, pp. 1899–1907, 2008.

[34] R. Savino, M. Fumo, D. Paterna, A. Maso and F. Monteverde, "Arc-jet testing of ultra-high-temperature-ceramics," Aerosp. Sci. Technol., vol. 14, no. 3, pp. 178–187, 2010.

[35] P. Ritt, P. Williams, S. Splinter and J. Perepezko, "Arc jet testing and evaluation of Mo–Si–B coated Mo and SiC–ZrB_2 ceramics," J. Eur. Ceram. Soc., vol. 34, pp. 3521–3533, 2014.

[36] F. Zuo, L. Cheng, L. Xiang, L. Zhang and L. Li, "Ablative property of laminated ZrB_2–SiC ceramics under oxyacetylene torch," Ceram. Int., vol. 39, no. 4, pp. 4627–4631, 2013.

[37] J. Han, P. Hu, X. Zhang, S. Meng and W. Han, "Oxidation-resistant ZrB_2–SiC composites at 2200°C," Compos. Sci. Technol., vol. 68, no. 3–4, pp. 799–806, 2008.

[38] L. Xiang, L. Cheng, X. Fan, L. Shi, X. Yin and L. Zhang, "Effect of interlayer on the ablation properties of laminated HfC – SiC ceramics under oxyacetylene torch," Corros. Sci., vol. 93, pp. 172–179, 2015.

[39] E. L. Courtright, H. C. Graham, A. P. Katz and R. J. Kerans, Ultrahigh Temperature Assessment Study-Ceramic Matrix Composites, WL-TR-91-4061, Wright-patterson Air Force Base, OH, 1991.

[40] M.J. Gasch, "Ultra high temperature ceramic composites," pp.197-225 in Handbook of Ceramic Composites, edited by N. Bansal, Boston: Kluwer Academic Publishers, 2005.

[41] S.A. Ghaffari, M.A. Faghihi-Sani, F. Golestani-Fard and H. Mandal, "Spark plasma sintering of TaC–HfC UHTC via disilicides sintering aids," J. Eur. Ceram. Soc., vol. 33, no. 8, pp. 1479-1484, 2013.

[42] A. L. Chamberlain, W. G. Fahrenholtz, G. E. Hilmas and D. T. Ellerby, "Characterization of zirconium diboride for thermal protection systems," Key Engineering Materials, vol. 264, pp. 493-496, 2004.

[43] M. A. Levinstein, in Proceedings of Metallurgical Society Conference on Refractory Metals and Alloys, Chicago, edited by M. Semchysen and I. Perlmutter (Interscience Publishers, New York, London, 1963) pp. 269, April 1962.

[44] K. J. Zeitsch and J. M. Criscione, Technical Report WADD TR 61-72, Vol. XXX, AFML WPAFB, April 1964.

[45] G. V. Samsonov, Refractory Transition Metal Compounds: High Temperature Cermets, Academic Press, New York, 1964.

[46] E. V. Clougherty, R. J. Hill, W. H. Rhodes and E. T. Peters, Research and Development of Refractory Oxidation-resistant Diborides, Part II,

vol. II, 'Processing and characterization', Cambridge, MA, ManLabs Inc, 1970.

[47] E. Wuchina, M. Opeka, S. Causey, K. Buesking, J. Spain, A. Cull, J. Routbort and F. Guitierrez-Mora, "Designing for ultrahigh-temperature applications - the mechanical and thermal properties of HfB_2, HfC_x, HfN_x and αHf(N)," J. Mater. Sci., vol. 39, pp. 5939–5949, 2004.

[48] E. Wuchina, E. Opila, M. Opeka, W. Fahrenholtz and I. Talmy, "UHTCs: ultra-High temperature ceramic materials for extreme environment applications," Electrochem. Soc. Interface, pp. 30–36, 2007.

[49] R.Borrelli, A. Riccio, D. Tescione, R. Gardi, and G. Marino, "Thermo-structural behaviour of an UHTC made nose cap of a reentry vehicle," Acta Astronautica, vol. 65, no. 3–4, pp. 442-456, 2009.

[50] S. M. Johnson, M. J. Gasch, T. H. Squire and J. W. Lawson, Ultra High Temperature Ceramics: Issues and Prospects, 'High Temperature Ceramic Materials and Composites', Edited by W. Krenkel and J. Lamon, 7th International Conference on High Temperature Ceramics, 2011.

[51] R. Savino, M. Fumo, D. Paterna and M. Serpico, "Aerothermodynamic study of UHTC-based thermal protection systems," Aerosp. Sci. Technol., vol. 9, no. 2, pp. 151–160, 2005.

[52] M. Gasch, S. Johnson and J. Marschall, "Thermal conductivity characterization of hafnium diboride-based ultra high temperature ceramics," J. Am. Ceram. Soc., vol. 91, no. 5, pp. 1423–1432, 2008.

[53] G. A. Galhano, L. F. Valandro, R. M. Melo, R. Scotti and M. A. Bottino, "Evaluation of the flexural strength of carbon fiber-, quartz fiber-, and glass fiber-based posts," J. Endod., vol. 31, no. 3, pp. 209-211, 2005.

[54] P. Schwarzkopf and R. Kieffer, Refractory Hard Metals, Chapter 26, Mac-Millan Co., New York, 1953.

[55] G. W. Goward, "Progress in coatings for gas turbine airfoils," Surf. Coatings Technol., vol. 108–109, no. 1–3, pp. 73–79, 1998.

[56] L. Kaufman, E. V. Clougherty and J. B. Berkowitz-Mattuck, "Oxidation characteristics of hafnium and zirconium diboride," Trans Met. Soc AIME, vol. 239, pp. 458–466, 1967.

[57] W. C. Tripp and H. C. Graham, "Thermogravimetric study of the oxidation of ZrB_2 in the temperature range of 800 to 1500^{o}C," J. Electrochem. Soc., vol. 118 no. 7, pp. 1195–1199, 1972.

[58] E. V. Clougherty and D. Kalish, Research and Development of Refractory Oxidaton Resistant Diborides, AFML-TR-68-190, ManLabs Inc., Cambridge, MA, 1968.

[59] L. Kaufman and E. V. Clougherty, Investigation of Boride Compounds for Very High Temperature Applications, RTD-TRD-N63-4096, Part III, ManLabs Inc., Cambridge, MA, 1966.

[60] W. G. Fahrenholtz, E. J. Wuchina, W. E. Lee and Y. Zhou, Ultra-High Temperature Ceramics: Materials for Extreme Environment Applications, 1st Edition, Wiley Inc., pp. 1-6, 2014.

[61] E. L. Courtright, H. C. Graham and A. P. Katz, Ultra High Temperature Assessment Study – Ceramic Matrix Composites, AFWAL-TR-91- 4061, Wright Patterson Air Force Base, Ohio, 1992.

[62] S. M. Johnson, M. Gasch, J. W. Lawson, M. I. Gusman and M. M. Stackpoole, Recent Developments in Ultra High Temperature Ceramics at NASA Ames, Baseline, pp. 1–52, 2003, http://ntrs.nasa.gov/archive/nasa/casi.ntrs.nasa.gov/20100023450.pdf

[63] 'High Temperature Ceramic Materials and Composites,' in Proceedings of 7th international conference on high temperature ceramic matrix composite (HT-CMC 7), edited by W. Krenkel, 2010.

[64] J. W. Zimmermann, G. E. Hilmas, W. G. Fahrenholtz, F. Monteverde and A. Bellosi, "Fabrication and properties of reactively hot pressed

ZrB_2–SiC ceramics," J. Eur. Ceram. Soc., vol. 27, no. 7, pp. 2729-2736, 2007.

[65] S. Q. Guo, Y. Kagawa, T. Nishimura and H. Tanaka, "Pressureless sintering and physical properties of ZrB_2-based composites with $ZrSi_2$ additive," Scr. Mater., vol. 58, no. 7, pp. 579–582, 2008.

[66] W. G. Fahrenholtz and G. E. Hilmas, "Oxidation of ultra-high temperature transition metal diboride ceramics," Int. Mater. Rev., vol. 57, no. 1, pp. 61–72, 2012.

[67] L. M. Doney, "Some properties of hafnium oxide, hafnium silicate, calcium hafnate, and hafnium carbide," J. Am. Ceram. Soc., vol. 37, no. 10, pp. 458–465, 1954.

[68] H. Scott, "Phase relationships in the zirconia-yttria system," J. Mater. Sci., vol. 10, no. 9, pp. 1527–1535, 1975.

[69] A. Murphy, "Transport coefficients of argon, nitrogen, oxygen, argon-nitrogen, and argon-oxygen plasmas," Plasma Chem. Plasma Process., vol. 14, no. 4, pp. 451–490, 1994.

[70] C. M. Carney, P. Mogilvesky and T. A. Parthasarathy, "Oxidation behavior of zirconium diboride silicon carbide produced by the spark plasma sintering method," J. Am. Ceram. Soc., vol. 92, no. 9, pp. 2046–2052, 2009.

[71] T. H. Squire and J. Marschall, "Material property requirements for analysis and design of UHTC components in hypersonic applications," J. Eur. Ceram. Soc., vol. 30, pp. 2239–2251, 2010.

[72] http://accuratus.com/silinit.html, http://accuratus.com/silicar.html, 12/1/2016.

[73] A. Bronson, Y. Ma and R. Musto, "Compatibility of refractory metal boride/oxide composites at ultrahigh temperatures," J. Electrochem. Soc., vol. 139, no. 11, pp. 3183-3196, 1992.

[74] J. Marschall, "Testing and modeling ultra-high temperature ceramic (UHTC) materials for hypersonic flight," SRI International. Menlo Park CA , Final technical rept., no. ADA553582, 2011.

[75] A. Paul, D. Jayaseelan, S. Venugopal, E. Zapata-Solvas, J. Binner, B. Vaidhyanathan, A. Heaton and P. Brown, "UHTC composites for hypersonic applications," Am. Ceram. Soc. Bull., vol. 91, no. 22–29, 2012.

[76] L. Weng, X. Zhang, J. Han, W. Han and C. Hong, "The effect of B_4C on the microstructure and thermo-mechanical properties of HfB_2-based ceramics," J. Alloys Compd., vol. 473, no. 1–2, pp. 314–318, 2009.

[77] S. Guo, K. Naito and Y. Kagawa, "Mechanical and physical behaviors of short pitch-based carbon fiber-reinforced HfB_2–SiC matrix composites," Ceram. Int., vol. 39, no. 2, pp. 1567–1574, 2013.

[78] G. Zhang, W. Guo, D. Ni and Y. Kan, "Ultrahigh temperature ceramics (UHTCs) based on ZrB_2 and HfB_2 systems: powder synthesis, densification and mechanical properties," J. Phys. Conf. Ser., vol. 176, no. 1, pp. 1–12, 2009.

[79] J. J. Meléndez-Martínez, A. Domínguez-Rodríguez, F. Monteverde, C. Melandri and G. Portu, "Characterisation and high temperature mechanical properties of zirconium boride-based materials," J. Eur. Ceram. Soc., vol. 22, pp. 2543–2549, 2002.

[80] L. Scatteia, R. Borrelli, G. Cosentino, E. Bêche, J. L. Sans and M. Balat-Pichelin, "Catalytic and radiative behaviors of ZrB_2/SiC ultrahigh temperature ceramic composites," J. Spacecraft and Rockets, vol. 43, no. 5, pp. 1004-1012, 2006.

[81] L. Scatteia, D. Alfano, F. Monteverde, J. L. Sans and M. Balat-Pichelin, "Effect of machining method on the catalytic and emissivity of ZrB_2 and ZrB_2/HfB_2-based ceramics," J. Am. Ceram. Soc., vol. 91, no. 5, pp. 1461-1468, 2008.

[82] D. Balat-Pichelin, E. Bêche, D. Sciti and D. Alfano, "Emissivity, catalycity and microstructural characterization of ZrB_2–SiC fiber based UHTC at high temperature in a non-equilibrium air plasma flow," Ceram. Int., vol. 40, no. 7, pp. 9731–9743, 2014.

[83] D. Alfano, L. Scatteia, F. Monteverde, E. Bêche and M. Balat-Pichelin, "Microstructural characterization of ZrB_2-SiC based UHTC tested in the MESOX plasma facility," J. Eur. Ceram. Soc., vol. 30, no. 11, pp. 2345-2355, 2010.

[84] R. Telle, L. S. Sigl and K. Takagi, Boride-Based Hard Materials, pp. 802-945 in Handbook of Ceramic Hard Materials, Edited by R. Riedel. Wiley-VCH, Weinheim, Germany, 2000.

[85] L. Chamberlain, W. G. Fahrenholtz, G. E. Hilmas and D. T. Ellerby, "High-strength zirconium diboride-based ceramics," J. Am. Ceram. Soc., vol. 87, no. 6, pp. 1170–1172, 2004.

[86] P. Vajeeston, P. Ravindran, C. Ravi and R. Asokamani, "Electronic structure, bonding, and ground-state properties of AlB_2-type transition-metal diborides," Phys. Rev. B, vol. 63, no. 4, pp. 045115, 2001.

[87] M. Mallik, A. J. Kailath, K. K. Ray and R. Mitra, "Electrical and thermophysical properties of ZrB_2 and HfB_2 based composites," J. Eur. Ceram. Soc., vol. 32, no. 10, pp. 2545–2555, 2012.

[88] JCPDS Card number 75-1050, Powder Diffraction File, International Centre for Diffraction Data.

[89] JCPDS Card number 89-3651, Powder Diffraction File, International Centre for Diffraction Data.

[90] F. Matt, K. Paul and F. Becher, "Effect of microstructure on the properties of TiB_2 ceramics," J. Am. Ceram. Soc., vol. 66, no. 1, pp. 90–98, 1983.

[91] J. W. Lawson, C. W. Bauschlicher and M. S. Daw, "Ab initio computations of electronic, mechanical, and thermal properties of ZrB_2 and HfB_2," J. Am. Ceram. Soc., vol. 94, no. 10, pp. 3494–3499, 2011.

[92] E. Deligoz, K. Colakoglu and Y. O. Ciftci, "Lattice dynamical and thermodynamical properties of HfB_2 and TaB_2 compounds," Comput. Mater. Sci., vol. 47, no. 4, pp. 875–880, 2010.

[93] B. Post, F. Glaser and D. Moskowitz, "Transition metal diborides," Acta Metall., vol. 2, no.1, pp. 20-25, 1954.

[94] F. G. Keihn and E. J. Keplin, "High-temperature thermal expansion of certain Group IV and Group V diborides," J. Am. Cer. Soc., vol. 50, no. 2, pp. 81-84, 1967.

[95] H. C. Graham, H. H. Davis, I. A. Kvernes and W. C. Tripp, Microstructural Features of Oxide Scales Formed on Zirconium Diboride Materials, pp. 35-48 in Ceramics in Severe Environments, Edited by W. W. Kriegel and H. Palmour III. Plenum Press, New York, 1970.

[96] A. K. Kuriakose and J. L. Margrave, "The oxidation kinetics of zirconium diboride and zirconium carbide at high temperatures," J. Electrochem. Soc., vol. 111, no. 7, pp. 827-831, 1964.

[97] C. B. Bargeron, R. C. Benson, R. W. Newman, A. N. Jette and T. E. Phillips, "Oxidation mechanisms of hafnium carbide and hafnium diboride in the temperature range 1400^{o}C and 2100^{o}C, J. Hopkins APL Tech. Digest, vol. 14, no. 1, pp. 29-36, 1993.

[98] F. Monteverde and A. Bellosi, "Oxidation of ZrB_2-based ceramics in dry air," J. Electrochem. Soc., vol. 150, no. 11, pp. 552-559, 2003.

[99] T. A. Parthasarathy, R. A. Rapp and M. Opeka, "Effects of phase change and oxygen permeability in oxide scale on oxidation kinetics of ZrB_2 and HfB_2," J. Am. Ceram. Soc., vol. 92, no.5, pp. 1079-1086, 2009.

[100] L. Kaufman, E. V. Clougherty and J. B. Berkowitz-Mattuck, "Oxidation Characteristics of Hafnium and Zirconium Diboride," Trans. Metall. Soc. AIME, vol. 239, no.4, pp.458–66, 1967.

[101] A. Rezaie, W. G. Fahrenholtz and G. Hilmas, "Oxidation of zirconium diboride–silicon carbide at 1500°C at a low partial pressure of oxygen," J. Am. Ceram. Soc., vol. 89, no. 10, pp.3240-3245, 2006

[102] A. Chamberlain, W. G. Fahrenholtz, G. Hilmas and D. Ellerby, "Oxidation of ZrB_2–SiC ceramics under atmospheric and reentry conditions," Refract. Appl. Trans., vol. 1, no. 2, pp. 1-8, 2005.

[103] J. Berkowitz-mattuck, "High-Temperature Oxidation Zirconium and Hafnium Diborides," J. Electr. Soc., vol. 113, pp. 908–914, 1966.

[104] X. Luo, W. Zhou, S. V. Ushakov, A. Navrotsky and A. A. Demkov, "Monoclinic to tetragonal transformations in hafnia and zirconia: a combined calorimetric and density functional study," Phys. Rev. B 80 vol. 80, no.13, pp. 134119, 2009.

[105] L. A. McClaine, Thermodynamic and Kinetic Studies for a Refractory Materials Program, Technical Documentary Report No. ASD-TDR-62-204, Part III, NASA, 1964.

[106] W. G. Fahrenholtz, "The ZrB_2 Volatility Diagram" J. Am. Ceram. Soc., vol. 88, no. 12, pp. 3509–3512, 2005.

[107] J. Marschall, D. A. Pejakovic, W. G. Fahrenholtz, G. E. Hilmas, S. Zhu and J. Ridge, "Oxidation of ZrB_2-SiC ultrahigh-temperature ceramic composites in dissociated air," Journal of Thermophysics and Heat Transfer, vol. 23, no. 2, pp. 267-278, 2009.

[108] T. Parthasarathy, R. Rapp, M. Opeka, and R. J. Kerans, "A model for the oxidation of ZrB_2, HfB_2 and TiB_2," Acta Mater., vol. 55, no. 17, pp. 5999–6010, 2007.

[109] J. R. Fenter, "Refractory diborides as engineering materials," SAMPE Quarterly, vol. 2, no. 3, pp. 1–15, 1971.

[110] R. Mitra, S. Upender, M. Mallik, S. Chakraborty and K. K. Ray, "Mechanical, thermal and oxidation behaviour of zirconium diboride based ultra-high temperature ceramic composites", Key Engineering Materials, vol. 395, pp. 55-68, 2009.

[111] T. Parthasarathy, R. Rapp, M. Opeka and R. J. Kerans, "A model for transitions in oxidation regimes of ZrB_2," Mater. Sci. Forum, vol. 595–598, pp. 823–832, 2008.

[112] Y. H. Koh, S. Y. Lee and H. E. Kim, "Oxidation behavior of titanium boride at elevated temperatures," J. Am. Ceram. Soc., vol. 54, no. 1, pp. 229–241, 2001.

[113] E. Rudy, S. Windisch and Y. Chang, Ternary Phase Equilibria in Transition Metal-Boron-Carbon-Silicon Systems, Part I. Related Binary Systems, Volume VIII. Zr-C System, 1965.

[114] E. Rudy and D.Harmon, Ternary Phase Equilibria in Transition Metal-Boron-Carbon-Silicon Systems, Part I. Related Binary Systems, Volume V. Ta-C System, 1965.

[115] G. A. Rao and V. Venugopal, Kinetics and mechanism of the oxidation of ZrC, Journal of Alloys and Compounds, vol. 206, pp. 237-242, 1994.

[116] E. Rudy and S. Windisch, Ternary Phase Equilibria in Transition Metal-Boron-Carbon-Silicon Systems, Part I. Related Binary Systems, Volume II. Hf-C System, 1965.

[117] S. Shimada, K. Nakajima and M. Inagaki, "Oxidation of single crystals hafnium carbide in a temperature range of 600 to 900^{o}C, J. Am. Ceram. Soc., vol. 80, no. 7, pp. 1749-1756, 1997.

[118] S. Shimada, "A thermoanalytical study on the oxidation of ZrC and HfC powders with formation of carbon," Solid State Ionics, vol. 149, pp. 319-326, 2002.

[119] E. J. Wuchina and M. M. Opeka, "The oxidation behavior of HfC, HfN, and HfB_2," pp. 136-143 in High Temperature Corrosion and Materials Chemistry III, The Electrochemical Society, Inc.: New Jersey, 2001.

[120] C. Bargeron, R. Benson, N. Jette and T. Phillips, "Oxidation of hafnium carbide in the temperature range 1400° to 2060°C," J. Am. Ceram. Soc., vol. 76, no. 4, pp. 1040–46, 1993.

[121] G. D. Li, X. Xiong, B. Y. Huang and Y. L. Zeng, "Oxidized characteristic and oxidized mechanism of TaC coating," The Chinese Journal of Nonferrous Metals, vol. 17, no. 3, pp. 360-367, 2007.

[122] K. Upadhya, J. M. Yang and W. Hoffman, Advanced Materials for Ultrahigh Temperature Structural Applications above 2000°C, AFRL report No.PR-ED-TP-1998-007, 1998.

[123] C. Tsai, Y. Lai and J. S. Chen, "Thermal stability of hafnium and hafnium nitride gates on HfO_2 gate dielectrics," Journal of Alloys and Compounds, vol. 487, pp. 687-692, 2009.

[124] H. Okamoto, Bullet Alloy Phase Diagrams, vol. 11, pp.146, 1990.

[125] E. Jung, J. Kim, S. Jung and S. Choi, "Synthesis of ZrB_2 powders by carbothermal and borothermal reduction," Journal of Alloys and Compounds, vol. 538, pp. 164-168, 2012.

[126] H. E. Çamurlu and F. Maglia, "Preparation of nano-size ZrB_2 powder by self-propagating high-temperature synthesis," J. Eur. Ceram. Soc., vol. 29, no. 8, pp. 1501–1506, 2009.

[127] A. L. Chamberlain, W. G. Fahrenholtz and G. E. Hilmas, "Reactive hot pressing of zirconium diboride," J. Eur. Ceram. Soc., vol. 29, no. 16, pp. 3401–3408, 2009.

[128] D. D. Radev and D. Klissurski, "Mechanochemical synthesis and SHS of diborides of titanium and zirconium," J. Mater. Synth. Process., vol. 9, no. 3, pp. 131–136, 2001.

[129] R. Licheri, R. Orrù, C.Musa and G. Cao, "Combination of SHS and SPS techniques for fabrication of fully dense ZrB_2-ZrC-SiC composites," Materials Letters, vol. 62, no. 3, pp. 432-435, 2008.

[130] S. K. Mishra, S. Das and L. C. Pathak, "Defect structures in zirconium diboride powder prepared by self-propagating high-tempeture synthesis," Mater. Sci. Eng. A, vol. 364, no. 1–2, pp. 249–255, 2004.

[131] Y. D. Blum, J. Marschall, D. Hui, B. Adair and M. Vestel, "Hafnium reactivity with boron and carbon sources under non-self- propagating high-temperature synthesis conditions," J. Am. Ceram. Soc.,vol. 91, no. 5, pp. 1481–1488, 2008.

[132] L. Chen, Y. Gu, Z. Yang, L. Shi, J. Ma and Y. Qian, "Preparation and some properties of nanocrystalline ZrB_2 powders," Scr. Mater., vol. 50, no. 7, pp. 959–961, 2004.

[133] L. Chen, Y. Gu, L. Shi, Z. Yang, J. Ma and Y. Qian, "Synthesis and oxidation of nanocrystalline HfB_2," Journal of Alloys and Compounds, vol. 368, no. 1-2, pp. 353-356, 2004.

[134] D. L. Segal, "Chemical routes for the preparation of powders," pp. 3–11 in The Physics and Chemistry of Carbides, Nitrides and Borides, edited by R. Freer, Springer Netherlands, 1990.

[135] Y. D. Blum and H. J. Kleebe, "Chemical reactivities of hafnium and its derived boride, carbide and nitride compounds at relatively mild temperature," J. Mater. Sci., vol. 39, pp. 6023–6042, 2004.

[136] N. Akçamlı, D. Ağaoğulları, Ö. Balcı, M. Lütfi Öveçoğlu and İ. Duman, "Synthesis of HfB_2 powders by mechanically activated borothermal reduction of $HfCl_4$," Ceram. Inter., vol. 42, no. 3, pp. 3797-3807, 2016

[137] S. Bégin-Colin, G. Caër, E. Barraud and O. Humbert, "Mechanically activated synthesis of ultrafine rods of HfB_2 and milling induced phase transformation of monocrystalline anatase particles," J. Mater. Sci., vol. 39, no. 16–17, pp. 5081–5089, 2004.

[138] J. K. Sonber and A. K. Suri, "Synthesis and consolidation of zirconium diboride: review," Advances in Applied Ceramics, vol. 110, no. 6, pp. 321-334, 2011.

[139] R. Thomson, "Production, fabrication, and uses of borides," pp.113-120 in The physics and Chemistry of Carbides, Nitrides and Borides, Edited by R. Freer, Kluwer Academic Publishers, Dordrecht, 1990.

[140] W. M. Guo, Z. G. Yang and G. J. Zhang, "Synthesis of submicrometer HfB_2 powder and its densification," Mater. Lett., vol. 83, pp. 52–55, 2012.

[141] S. Venugopal, A. Paul, B. Vaidhyanathan, J. Binner, A. Heaton and P. Brown, "Nano-crystalline ultra high temperature HfB_2 and HfC powders and coatings using a sol-gel approach," Conferenc Proceedings: Adv. Ceram. Coatings Mater. Extrem. Environ., pp. 151–159, 2011.

[142] L. J. Yang, S. Z. Zhu, Q. Xu, Z. Y. Yan and L. Liu, "Synthesis of ultrafine ZrB_2 powders by sol-gel process," Front. Mater. Sci. China, vol. 4, no. 3, pp. 285–290, 2010.

[143] Y. Yan, Z. Huang, S. Dong and D. Jiang, "New route to synthesize ultra-fine zirconium diboride powders using inorganic-organic hybrid precursors," J. Am. Ceram. Soc., vol. 89, pp. 3585–3588, 2006.

[144] Y. Yan, Z. Huang, S. Dong and D. Jiang, "Carbothermal preparation of ultra-fine TiB_2 powders using solution-derived precursors via sol-gel method," Key Eng. Mater., vol. 336–338, pp. 944–947, 2007.

[145] P. Peshev and G. Bliznakov, "On the borothermic preparation of titanium, zirconium and hafnium diborides," J. Less Common Met., vol. 14, no. 1, pp. 23–32, 1968.

[146] X. G. Wang, W. M. Guo and G. J. Zhang, "Pressureless sintering mechanism and microstructure of ZrB_2–SiC ceramics doped with boron," Scr. Mater., vol. 61, no. 2, pp. 177–180, 2009.

[147] D. W. Ni, G. J. Zhang, Y. M. Kan and P. L. Wang, "Synthesis of monodispersed fine hafnium diboride powders using carbo/borothermal reduction of hafnium dioxide," J. Am. Ceram. Soc., vol. 91, no. 8, pp. 2709–2712, 2008.

[148] G. Zhang, W. Guo, D. Ni and Y. Kan, "Ultrahigh temperature ceramics (UHTCs) based on ZrB_2 and HfB_2 systems: powder synthesis, densification and mechanical properties," Journal of Physics: Conference Series, vol. 176, no. 1, pp. 1-12, 2009.

[149] H. Y. Qiu, W. M. Guo, J. Zou, and G. J. Zhang, "ZrB_2 powders prepared by boro/carbothermal reduction of ZrO_2: the effects of carbon source and reaction atmosphere," Powder Technol., vol. 217, pp. 462–466, 2012.

[150] B. Soediono, "Preparation of zirconium diboride powders," J. Chem. Inf. Model., vol. 53, no. 1, p. 160, 1989.

[151] H. Wang, S. H. Lee and H. D. Kim, "Nano-hafnium diboride powders synthesized using a spark plasma sintering apparatus," J. Am. Ceram. Soc., vol. 95, no. 5, pp. 1493–1496, 2012.

[152] S. C. Zhang, G. E. Hilmas and W. G. Fahrenholtz, "Pressureless densification of zirconium diboride with boron carbide additions," J. Am. Ceram. Soc., vol. 89, no. 5, pp. 1544–1550, 2006.

[153] Y. Xie, T. H. Sanders and R. F. Speyer, "Solution-based synthesis of submicrometer ZrB_2 and ZrB_2-TaB_2," J. Am. Ceram. Soc., vol. 91, pp. 1469–1474, 2008.

[154] H. Ping, G. Wang and W. Zhi, "Oxidation mechanism and resistance of ZrB_2–SiC composites," Corrosion Science, vol. 51, no. 11, pp. 2724–2732, 2009.

[155] D. L. Hu, Q. Zheng, H. Gu, D. W. Ni and G. J. Zhang, "Role of WC additive on reaction, solid-solution and densification in HfB_2-SiC ceramics," J. Eur. Ceram. Soc., vol. 34, no. 3, pp. 611–619, 2014.

[156] X. H. Zhang, P. Hu, J. C. Han, L. Xu and S. H. Meng, "The addition of lanthanum hexaboride to zirconium diboride for improved oxidation resistance," Scr. Mater., vol. 57, no. 11, pp. 1036–1039, 2007.

[157] P. Hu, X. H. Zhang, J. C. Han, X. G. Luo and S. Y. Du, "Effect of various additives on the oxidation behavior of ZrB_2-based ultra-high-temperature ceramics at 1800 °C," J. Am. Ceram. Soc., vol. 93, no. 2, pp. 345–349, 2010.

[158] I. G. Talmy, J. Zaykoski and M. M. Opeka, "High-temperature chemistry and oxidation of ZrB_2 ceramics containing SiC, Si_3N_4, Ta_5Si_3, and $TaSi_2$," J. Am. Ceram. Soc., vol. 91, no. 7, pp. 2250–2257, 2008.

[159] Y. Cao, H. Zhang, F. Li, L. Lu and S. Zhang, "Preparation and characterization of ultrafine ZrB_2–SiC composite powders by a combined sol–gel and microwave boro/carbothermal reduction method," Ceram. Int., vol. 41, no. 6, pp. 7823–7829, 2015.

[160] F. Monteverde, "Ultra-high temperature HfB_2-SiC ceramics consolidated by hot-pressing and spark plasma sintering," J. Alloys Compd., vol. 428, pp. 197–205, 2007.

[161] F. Monteverde and A. Bellosi, "Microstructure and properties of an HfB_2-SiC composite for ultra high temperature applications," Adv. Eng. Mater., vol. 6, no. 5, pp. 331–336, 2004.

[162] Y. Wang, L. Luo, J. Sun and L. An, "ZrB_2–SiC(Al) ceramics with high resistance to oxidation at 1500°C," Corros. Sci., vol. 74, pp. 154–158, 2013.

[163] P. Williams, R. Sakidja, J. H. Perepezko and P. Ritt, "Oxidation of ZrB_2-SiC ultra-high temperature composites over a wide range of SiC content," J. Eur. Ceram. Soc., vol. 32, no. 14, pp. 3875–3883, 2012.

[164] B. Zhao, Y. Zhang, J. Li, B. Yang, T. Wang, Y. Hu, D. Sun, R. Li, S. Yin, Z. Feng and T. Sato, "Morphology and mechanism study for the

synthesis of ZrB_2 – SiC powders by different methods," J. Solid State Chem., vol. 207, pp. 1–5, 2013.

[165] M. Avilés, J. M. Córdoba, M. J. Sayagués, M. D. Alcalá and F. J. Gotor, "Mechanosynthesis of $Hf_{1-x}Zr_xB_2$ solid solution and $Hf_{1-x}Zr_xB_2$ /SiC composite powders," J. Am. Ceram. Soc., vol. 93, no. 3, pp. 696–702, 2010.

[166] D. L. McClane, W. G. Fahrenholtz and G. E. Hilmas, "Thermal properties of (Zr, TM)B_2 solid solutions with TM = Ta, Mo, Re, V, and Cr," J. Am. Ceram. Soc., vol. 98, no. 2, pp. 637-644, 2015.

[167] D. L. McClane, W. G. Fahrenholtz, and G. E. Hilmas, "Thermal properties of (Zr,TM)B_2 solid solutions with TM = Hf, Nb, W, Ti, and Y," J. Am. Ceram. Soc., vol. 97, no. 5, pp. 1552–1558, 2014.

[168] S. Otani, T. Aizawa and N. Kieda, "Solid solution ranges of zirconium diboride with other refractory diborides: HfB_2, TiB_2, TaB_2, NbB_2, VB_2 and CrB_2," J. Alloys Compd., vol. 475, no. 1–2, pp. 273–275, 2009.

[169] M. Dehdashti, W. G. Fahrenholtz and G. E. Hilmas, "Oxidation of zirconium diboride with niobium additions," J. Eur. Ceram. Soc., vol. 33, no. 10, pp. 1591–1598, 2013.

[170] S. Venugopal, E. E. Boakye, A. Paul, K. Keller, P. Mogilevsky, B. Vaidhyanathan, J. G. P. Binner, A. Katz and P. M. Brown, "Sol–gel synthesis and formation mechanism of ultrahigh temperature ceramic: HfB_2," J. Am. Ceram. Soc., vol. 99, no. 1, pp. 92–99, 2014.

[171] Y. Jiang, R. Li, Y. Zhang, B. Zhao, J. Li and Z. Feng, "Tungsten doped ZrB_2 powder synthesized synergistically by co-precipitation and solid-state reaction methods," 2011 Chinese Materials Conference, Procedia Eng., vol. 27, pp. 1679–1685, 2012.

[172] D. Sciti, V. Medri and L. Silvestroni, "Oxidation behaviour of HfB_2–15 vol.% $TaSi_2$ at low, intermediate and high temperatures," Scr. Mater., vol. 63, no. 6, pp. 601–604, 2010.

[173] S. C. Zhang, G. E. Hilmas and W. G. Fahrenholtz, "Improved oxidation resistance of zirconium diboride by tungsten carbide additions," J. Am. Ceram. Soc., vol. 91, pp. 3530–3535, 2008.

[174] S. C. Zhang and G. E. Hilmas, "Oxidation of zirconium diboride with tungsten carbide additions," J. Am. Ceram. Soc., vol. 94, no. 4, pp. 1198–1205, 2011.

[175] R. He, X. Zhang, W. Han, P. Hu and C. Hong, "Effects of solids loading on microstructure and mechanical properties of HfB_2-20 vol% $MoSi_2$ ultra high temperature ceramic composites through aqueous gel-casting route," Mater. Des., vol. 47, pp. 35–40, 2013.

[176] F. Monteverde and R. Savino, "Stability of ultra-high-temperature ZrB_2-SiC ceramics under simulated atmospheric re-entry conditions," J. Eur. Ceram. Soc., vol. 27, pp. 4797–4805, 2007.

[177] A. Sayir, "Carbon fiber reinforced hafnium carbide composite," J. Mater. Sci., vol. 39, no. 19, pp. 5995-6003, 2004.

[178] C. Sauder, J. Lamon and R. Pailler, "The tensile behavior of carbon fibers at high temperatures up to 2400^{o}C," Carbon, vol. 42, no. 4, pp. 715-725, 2004.

[179] S. R. Levine, E. J. Opila, M. C. Halbig, J. D. Kiser, M. Singh and J. a Salem, "Evaluation of ultra-high temperature ceramics for aeropropulsion use," J. Eur. Ceram. Soc., vol. 22, no. 14–15, pp. 2757–2767, 2002.

[180] S. Tang, J. Deng, S. Wang, W. Liu and K. Yang, "Ablation behaviors of ultra-high temperature ceramic composites," Mater. Sci. Eng. A, vol. 465, pp. 1–7, 2007.

[181] M. Pavese, P. Fino, C. Badini, A. Ortona and G. Marino, "HfB_2/SiC as a protective coating for 2D Cf/SiC composites: Effect of high temperature oxidation on mechanical properties," Surf. Coatings Technol., vol. 202, no. 10, pp. 2059–2067, 2008.

[182] W. Richerson, Modern Ceramic Engineering: Properties, Processing, and Use in Design, 3rd edition, CRC Press, 2006.

[183] D. W. Ni, G. J. Zhang, Y. M. Kan and P. L. Wang, "Hot pressed HfB_2 and HfB_2–20 vol% SiC ceramics based on HfB_2 powder synthesized by borothermal reduction of HfO_2," International Journal of Applied Ceramic Technology, vol. 7, no. 6, pp. 830-836, 2010.

[184] D. Kalish, E. V Clougherty and K. Kreder, "Strength, fracture mode, and thermal stress resistance of HfB_2 and ZrB_2," J. Am. Ceram. Soc., vol. 52, no. 1, pp. 30–36, 1969.

[185] D. Kalish and E. V. Clougherty, "Densification mechanisms in high-pressure hot-pressing of HfB_2," J. Am. Ceram. Soc., vol. 52, no. 1, pp. 26–30, 1969.

[186] S. Guo, "Densification of ZrB_2-based composites and their mechanical and physical properties: A review," J. Eur. Ceram. Soc., vol. 29, no. 6, pp. 995–1011, 2009.

[187] G. Zhang, Z. Deng, N. Kondo, J. Yang and T. Ohji, "Reactive hot pressing of ZrB_2 –SiC composites," J. Am. Ceram. Soc., vol. 83, no.9, pp. 2330–2332, 2000.

[188] F. Monteverde, "Beneficial effects of an ultra-fine α-SiC incorporation on the sinterability and mechanical properties of ZrB_2," Appl. Phys. A, vol. 82, no. 2, pp. 329–337, 2006.

[189] F. Monteverde and A. Bellosi, "Effect of the addition of silicon nitride on sintering behaviour and microstructure of zirconium diboride," Scr. Mater., vol. 46, no.3, pp. 223–228, 2002.

[190] F. Monteverde, A. Bellosi and S. Guicciardi, "Processing and properties of zirconium diboride-based composites," J. Eur. Ceram. Soc., vol. 22, pp. 279–288, 2002.

[191] I. G. Talmy, J. A. Zaykoski, M. M. Opeka and A. H. Smith, "Properties of ceramics in the System ZrB_2–Ta_5Si_3," J. Mater. Res., vol. 21, no. 10, pp. 2593–2599, 2006.

[192] J. K. Sonber, T. Murthy, C. Subramanian, N. Krishnamurthy, R. C. Hubli and A. K. Suri, "Effect of $CrSi_2$ and HfB_2 addition on densification and properties of ZrB_2," Int. J. Refract. Met. Hard Mater., vol. 31, pp. 125–131, 2012.

[193] J. K. Sonber, T. Murthy, C. Subramanian, S. Kumar, R. K. Fotedar and A. K. Suri, "Investigations on synthesis of ZrB_2 and development of new composites with HfB_2 and $TiSi_2$," Int. J. Refract. Met. Hard Mater., vol. 29, no. 1, pp. 21–30, 2011.

[194] F. Monteverde, "Progress in the fabrication of ultra-high-temperature ceramics: ‘In situ’ synthesis, microstructure and properties of a reactive hot-pressed HfB_2-SiC composite," Compos. Sci. Technol., vol. 65, no. 11–12, pp. 1869–1879, 2005.

[195] A. L. Chamberlain, W. G. Fahrenholtz and G. E. Hilmas, "Low-temperature densification of zirconium diboride ceramics by reactive hot pressing," J. Am. Ceram. Soc., vol. 89, no. 12, pp. 3638–3645, 2006.

[196] A. Bellosi, F. Monteverde and D. Sciti, "Fast densification of ultra-high-temperature ceramics by spark plasma sintering," Int. J. Appl. Ceram. Technol., vol. 3, no. 1, pp. 32–40, 2006.

[197] D. Sciti, L. Silvestroni and M. Nygren, "Spark plasma sintering of Zr- and Hf-borides with decreasing amounts of $MoSi_2$ as sintering aid," J. Eur. Ceram. Soc., vol. 28, no. 6, pp. 1287–1296, 2008.

[198] D. M. Hulbert, A. Anders, J. Andersson, E. J. Lavernia and A. K. Mukherjee, "A discussion on the absence of plasma in spark plasma sintering," Scr. Mater., vol. 60, no. 10, pp. 835–838, 2009.

[199] R. K. Enneti, C. Carney, S. Park and S. Atre, "Taguchi analysis on the effect of process parameters on densification during spark plasma

sintering of HfB_2 -20SiC," Int. J. Refract. Met. Hard Mater., vol. 31, pp. 293–296, 2012.

[200] A. Chang, B. Zhang, Y. Wu, Q. Zhao, H. Zhang, J. Yao and J. Xu, "Spark plasma sintering of negative temperature coefficient thermistor ceramics," pp. 25-36, Chapter 2 in Sintering Techniques of Materials, Edited by A. Lakshmanan, InTech Press, 2015.

[201] S. Grasso, J. Poetschke, V. Richter, G. Maizza, Y. Sakka and M. J. Reece, "Low-temperature spark plasma sintering of pure nano WC powder," J. Am. Ceram. Soc., vol. 96, no. 6, pp. 1702–1705, 2013.

[202] R. Licheri, R. Orrù, C. Musa, A. M. Locci and G. Cao, "Spark plasma sintering of ZrB_2- and HfB_2-based ultra high temperature ceramics prepared by SHS,", International Journal of Self-Propagating High-Temperature Synthesis, vol. 18, no. 1, pp 15–24, 2009.

[203] C. Ang, A. Seeber, T. Williams, and Y. B. Cheng, "SPS densification and microstructure of ZrB_2 composites derived from sol–gel ZrC coating," J. Eur. Ceram. Soc., vol. 34, no. 12, pp. 2875–2883, 2014.

[204] M. Cologna, B. Rashkova and R. Raj, "Flash sintering of nanograin zirconia in <5 s at 850°C," J. Am. Ceram. Soc., vol. 93, no. 11, pp. 3556–3559, 2010.

[205] R. Raj, "Joule heating during flash-sintering," J. Eur. Ceram. Soc., vol. 32, no. 10, pp. 2293–2301, 2012.

[206] X. Hao, Y. Liu, Z. Wang, J. Qiao and K. Sun, "A novel sintering method to obtain fully dense gadolinia doped ceria by applying a direct current," J. Power Sources, vol. 210, pp. 86–91, 2012.

[207] M. Cologna, J. Francis and R. Raj, "Field assisted and flash sintering of alumina and its relationship to conductivity and MgO-doping," J. Eur. Ceram. Soc., vol. 31, no. 15, pp. 2827–2837, Dec. 2011.

[208] M. Gasch and S. Johnson, "Physical characterization and arcjet oxidation of hafnium-based ultra high temperature ceramics fabricated

by hot pressing and field-assisted sintering," J. Eur. Ceram. Soc., vol. 30, no. 11, pp. 2337–2344, 2010.

[209] S. Grasso, T. Saunders, H. Porwal, O. Cedillos-Barraza, D. D. Jayaseelan, W. E. Lee and M. J. Reece, "Flash spark plasma sintering (FSPS) of pure ZrB_2," J. Am. Ceram. Soc., vol. 97, no. 8, pp. 2405–2408, 2014.

[210] V. M. Gropyanov, "Effect of dispersion on powder sintering," Refractories, no. 34, pp. 769–775, 1969.

[211] S. K. Mishra, K. Suman and C. P. Lokesh, "Self-propagating high-temperature synthesis (SHS) of advanced high-temperature ceramics." Key Engineering Materials, Trans Tech Publications, vol. 395, pp. 15-38, 2009.

[212] D. Sciti, S. Guicciardi, A. Bellosi and G. Pezzotti, "Properties of a pressureless-sintered ZrB_2-$MoSi_2$ ceramic composite," J. Am. Ceram. Soc., vol. 89, no. 7, pp. 2320-2322, 2006.

[213] D. Sciti, M. Brach and A. Bellosi, "Oxidation behaviour of a pressureless sintered ZrB_2–$MoSi_2$ ceramic composite," J. Mater. Res., vol. 20, no. 4, pp. 922–930, 2005.

[214] A. L. Chamberlain, W. G. Fahrenholtz and G. E. Hilmas, "Pressureless sintering of zirconium diboride," J. Am. Ceram. Soc., vol. 89, no. 2, pp. 450–456, 2006.

[215] G. Zhang and J. Zou, "Formation of tough interlocking microstructure in ZrB_2–SiC-based ultrahigh-temperature ceramics by pressureless sintering," Journal of Materials Research, vol. 24, no. 7, pp 2428-2434, 2009.

[216] D. Ni, J. Liu and G. Zhang, "Pressureless sintering of HfB_2–SiC ceramics doped with WC," J. Eur. Ceram. Soc., vol. 32, no. 13, pp. 3627–3635, 2012.

[217] J. Zou, G. J. Zhang and Y. M. Kan, "Pressureless densification and mechanical properties of hafnium diboride doped with B_4C: from solid state sintering to liquid phase sintering," J. Eur. Ceram. Soc., vol. 30, no. 12, pp. 2699–2705, 2010.

[218] J. Zou, G. J. Zhang, Y. M. Kan and T. Ohji, "Pressureless sintering mechanisms and mechanical properties of hafnium diboride ceramics with pre-sintering heat treatment," Scr. Mater., vol. 62, no. 3, pp. 159–162, 2010.

[219] W. G. Fahrenholtz, G. E. Hilmas, I. G. Talmy and J. A. Zaykoski, "Refractory diborides of zirconium and hafnium," J. Am. Ceram. Soc., vol. 90, no. 5, pp. 1347–1364, 2007.

[220] A. Rezaie, W. G. Fahrenholtz and G. E. Hilmas, "Evolution of structure during the oxidation of zirconium diboride-silicon carbide in air up to 1500°C," J. Eur. Ceram. Soc., vol. 27, no. 6, pp. 2495–2501, 2007.

[221] V. Medri, C. Capiani and A. Bellosi, "Properties of slip-cast and pressureless sintered ZrB_2–SiC composites," Int. J. Appl. Ceram. Technol., vol. 8, pp. 351–359, 2011.

[222] E. J. Opila and M. C. Halbig, "Oxidation of ZrB_2-SiC," Conference Proceedings: Elec. Chem. Soc. Proc., vol. 12, pp. 221–228, 2002.

[223] O. N. Grigoriev, B. Galanov, V. Lavrenko, A. D. Panasyuk, S. M. Ivanov, A. V. Koroteev and K. G. Nickel, "Oxidation of ZrB_2-SiC-$ZrSi_2$ ceramics in oxygen," J. Eur. Ceram. Soc., vol. 30, no. 11, pp. 2397–2405, 2010.

[224] H. Li, L. Zhang, Q. Zeng and L. Cheng, "Thermodynamic calculation of HfB_2 volatility diagram," J. Phase Equilibria Diffus., vol. 32, no. 5, pp. 422–427, 2011.

[225] W. G. Fahrenholtz, "Thermodynamic analysis of ZrB_2-SiC oxidation: Formation of a SiC-depleted region," J. Am. Ceram. Soc., vol. 90, no. 1, pp. 143–148, 2007.

[226] C. M. Carney, T. A. Parthasarathy and M. K. Cinibulk, "Separating test artifacts from material behavior in the oxidation studies of HfB_2-SiC at 2000°C and above," Int. J. Appl. Ceram. Technol., vol. 10, no. 2, pp. 293–300, 2013.

[227] C. M. Carney, T. A. Parthasarathy and M. K. Cinibulk, "Oxidation resistance of hafnium diboride ceramics with additions of silicon carbide and tungsten boride or tungsten carbide," J. Am. Ceram. Soc., vol. 94, no. 8, pp. 2600–2607, 2011.

[228] S. R. Levine, E. J. Opila and R. C. Robinson, "Characterization of an ultra-high temperature ceramic composite (UHTCC) by ultrasonic testing," NASA report No. TM-2004-213085, pp. 1–26, 2004.

[229] S. Gangireddy, S. N. Karlsdottir, S. J. Norton, J. C. Tucker and J. W. Halloran, "In situ microscopy observation of liquid flow, zirconia growth, and CO bubble formation during high temperature oxidation of zirconium diboride-silicon carbide," J. Eur. Ceram. Soc., vol. 30, no. 11, pp. 2365–2374, 2010.

[230] F. Peng, Y. Berta and R. F. Speyer, "Effect of SiC, TaB_2 and $TaSi_2$ additives on the isothermal oxidation resistance of fully dense zirconium diboride," J. Mater. Res., vol. 24, no. 5, pp. 1855–1867, 2011.

[231] D. Sciti, A. Balbo and A. Bellosi, "Oxidation behaviour of a pressureless sintered HfB_2-$MoSi_2$ composite," J. Eur. Ceram. Soc., vol. 29, no. 9, pp. 1809–1815, 2009.

[232] E. J. Opila, S. R. Levine and J. Lorincz, "Oxidation of ZrB_2- and HfB_2-based ultra-high temperature ceramics: effect of Ta additions," J. Mater. Sci., vol. 39, no. 19, pp. 5969 – 5977, 2004.

[233] S. R. Levine and E. J. Opila, "Tantalum addition to zirconium diboride for improved oxidation resistance," Nasa report No. Tm-2003-212483, pp. 1–13, 2003.

[234] X. Zhang, G. E. Hilmas and W. G. Fahrenholtz, "Densification, mechanical properties, and oxidation resistance of TaC-TaB_2 ceramics,", J. Am. Ceram. Soc., vol. 91, no. 12, pp. 4129–4132, 2008.

[235] R. Licheri, C. Musa and G. Cao, "Synthesis, densification and characterization of TaB_2-SiC composites," Ceram. Int., vol. 36, no. 3, pp. 937–941, 2010.

[236] M. M. Opeka, I.Talmy and J. Zaykoski, "Oxidation-based materials selection for 2000^oC+ hypersonic aerosurfaces: theoretical considerations and historical experience," J. Mater. Sci., vol. 39, no. 19, pp. 5887–5904, 2004.

[237] X. Zhang, P. Hu, J. Han and S. Meng, "Ablation behavior of ZrB_2-SiC ultra high temperature ceramics under simulated atmospheric re-entry conditions," Compos. Sci. Technol., vol. 68, no. 7–8, pp. 1718–1726, 2008.

[238] F. Monteverde and R. Savino, "ZrB_2 -SiC sharp leading edges in high enthalpy supersonic flows," J. Am. Ceram. Soc., vol. 95, no. 7, pp. 2282–2289, 2012.

[239] J. Marschall and D. G. Fletcher, "High-enthalpy test environments, flow modeling and in situ diagnostics for characterizing ultra-high temperature ceramics," J. Eur. Ceram. Soc., vol. 30, no. 11, pp. 2323–2336, 2010.

[240] A. Cecere, R. Savino, C. Allouis and F. Monteverde, "Heat transfer in ultra-high temperature advanced ceramics under high enthalpy arc-jet conditions," Int. J. Heat Mass Transf., vol. 91, pp. 747–755, 2015.

[241] F. Marra, G. Pulci, J. Tirillo, C. Bartuli and T. Valente, "Numerical simulation of oxy-acetylene testing procedure of ablative materials for re-entry space vehicles," J. Mater. Des. Appl., vol. 225, no. 1, pp. 32–40, 2011.

[242] X. Zhang, Z. Chen, X. Xiong, R. Liu and Y. Zhu, "Morphology and microstructure of ZrB_2–SiC ceramics after ablation at 3000^oC by oxy-acetylene torch," Ceram. Int., vol. 42, no. 2, pp. 2798–2805, 2016.

[243] D. D. Jayaseelan, H. Jackson, E. Eakins, P. Brown and W. E. Lee, "Laser modified microstructures in ZrB_2, ZrB_2/SiC and ZrC," J. Eur. Ceram. Soc., vol. 30, no. 11, pp. 2279–2288, 2010.

[244] H. F. Jackson, D. D. Jayaseelan, D. Manara, C. P. Casoni and W. E. Lee, "Laser melting of zirconium carbide: determination of phase transitions in refractory ceramic systems," J. Am. Ceram. Soc., vol. 94, no. 10, pp. 3561–3569, 2011.

[245] D. Manara, M. Sheindlin, W. Heinz and C. Ronchi, "New techniques for high-temperature melting measurements in volatile refractory materials via laser surface heating," Rev. Sci. Instrum., vol. 79, no. 11, pp. 113901, 2008.

[246] E. Beche, M. Balat-Pichelin, V. Flaud, J. Esvan, T. Duguet, D. Sciti and D. Alfano, "XPS and AES studies of UHTC ZrB_2 -SiC-Si_3N_4 treated with solar energy," Surf. Interface Anal., vol. 46, no. 10-11, pp. 817-822,

[247] M. Ikegami, K. Matsumura, S. Q. Guo, Y. Kagawa and J. M. Yang, "Effect of SiC particle dispersion on thermal properties of SiC particle-dispersed ZrB_2 matrix composites," J. Mater. Sci., vol. 45, no. 19, pp. 5420–5423, 2010.

[248] S. Guo, Y. Kagawa, T. Nishimura and H. Tanaka, "Thermal and electric properties in hot-pressed ZrB_2-$MoSi_2$-SiC composites," J. Am. Ceram. Soc., vol. 90, no. 7, pp. 2255–2258, 2007.

[249] S. Q. Guo, Y. Kagawa, T. Nishimura, D. Chung and J. M. Yang, "Mechanical and physical behavior of spark plasma sintered ZrC-ZrB_2-SiC composites," J. Eur. Ceram. Soc., vol. 28, no. 6, pp. 1279–1285, 2008.

[250] E. Zapata-Solvas, D. D. Jayaseelan, P. M. Brown and W. E. Lee, "Thermal properties of La_2O_3-doped ZrB_2- and HfB_2-based ultra-high temperature ceramics," J. Eur. Ceram. Soc., vol. 33, no. 15–16, pp. 3467–3472, 2013.

[251] J. M. Lonergan, W. G. Fahrenholtz and G. E. Hilmas, "Zirconium diboride with high thermal conductivity," J. Am. Ceram. Soc., vol. 97, no. 6, pp. 1689-1691, 2014

[252] L. Zhang, D. a. Pejaković, J. Marschall and M. Gasch, "Thermal and electrical transport properties of spark plasma-sintered HfB_2 and ZrB_2 ceramics," J. Am. Ceram. Soc., vol. 94, no. 8, pp. 2562–2570, 2011.

[253] C. N. Sun, M. C. Gupta and W. D. Porter, "Thermophysical properties of laser-sintered Zr-ZrB_2 cermets," J. Am. Ceram. Soc., vol. 94, no. 8, pp. 2592–2599, 2011.

[254] J. W. Zimmermann, G. E. Hilmas, W. G. Fahrenholtz, R. B. Dinwiddie, W. D. Porter and H. Wang, "Thermophysical properties of ZrB_2 and ZrB_2 –SiC ceramics," J. Am. Ceram. Soc., vol. 91, pp. 1405–1411, 2008.

[255] F. Nakamori, Y. Ohishi, H. Muta, K. Kurosaki, K. Fukumoto and S. Yamanaka, "Mechanical and thermal properties of bulk ZrB_2," J. Nucl. Mater., vol. 467, part II, pp. 612–617, 2015.

[256] D. E. Wiley, W. R. Manning and O. Hunter, "Elastic properties of polycrystalline TiB_2, ZrB_2 and HfB_2 from room temperature to 1300°C," J. Less Common Met., vol. 18, no. 2, pp. 149–157, 1969.

[257] J. Maloy, A. H. Heuer and J. Lewandowski, "Carbon additions to molybdenum disilicide: improved high temperature mechanical properties," J. Am. Ceram. Soc., vol. 74, no. 10, pp. 2704–2706, 1991.

[258] H. Kodama and T. Miyoshi, "Study of fracture behavior of very fine-grained silicon carbide ceramics," J. Am. Ceram. Soc, vol. 73, no. 10, pp. 3081–3086, 1990.

[259] Z. Zhou, X. Peng and Z. Wei, "A thermo-chemo-mechanical model for the oxidation of zirconium diboride," J. Am. Ceram. Soc., vol. 98, no. 2, pp. 629–636, 2015.

[260] E. Zapata-Solvas, D. D. Jayaseelan, H. T. Lin, P. Brown and W. E. Lee, "Mechanical properties of ZrB_2- and HfB_2-based ultra-high temperature ceramics fabricated by spark plasma sintering," J. Eur. Ceram. Soc., vol. 33, no. 7, pp. 1373–1386, 2013.

[261] E. Barraud, F. Villieras and O. Barres, "Thermal decomposition of $HfCl_4$ as a function of its hydration state," J. Solid State Chem., vol. 179, no. 6, pp. 1842–1851, 2006.

[262] S. Venugopal, A. Paul, J. G. P. Binner, B. Vaidhyanathan and P. Brown, "Sol-gel synthesis and characterization of HfB_2 powders", Engineering Conferences International ECI Digital Archives, pp. 1, 2012. http://dc.engconfintl.org/cgi/viewcontent.cgi?article=1026&context=uhtc

[263] A. Paul, J. G. P. Binner, B. Vaidhyanathan, C. J. Heaton and P. Brown, "Oxyacetylene torch testing and microstructural characterization of tantalum carbide," J. Microsc., vol. 250, no. 2, pp. 122–129, 2013.

[264] http://webbook.nist.gov/chemistry/

[265] S. Venugopal, "Synthesis and processing of sub-micron hafnium diboride powders and carbon fibre-hafnium diboride composites," PhD thesis, Loughbrgh. University, April, 2013.

[266] I. Poljanšek and M. Krajnc, "Characterization of phenol-formaldehyde prepolymer resins by in line FT-IR spectroscopy," Acta Chim. Slov., vol. 52, no. 3, pp. 238–244, 2005.

[267] M. André, M. E. Malmström and I. Neretnieks, "Specific surface area measurements on intact drillcores and evaluation of extrapolation methods for rock matrix surfaces," J. Contam. Hydrol., vol. 110, no. 1, pp. 1–8, 2009.

[268] S. Venugopal, D. D. Jayaseelan, A. Paul, B. Vaidhyanathan, J. G. P. Binner and P. Brown, "Screw dislocation assisted spontaneous growth of HfB_2 tubes and rods," J. Am. Ceram. Soc., vol. 98, no. 7, pp. 2060–2064, 2015.

[269] D. Cunningham, "A first-principles examination of dopants in HfO_2," Honors Scholar Thesis, Paper No. 359, University of Connecticut, 2014

[270] E. V. Chulkov, P. M. Echenique and V. M. Silkin, "First-principles calculations of dielectric and optical properties of MB_2," Phys. Rev. B, vol. 78, no. 22, p. 2245-2502, 2008.

[271] P. Deblonde, A. Chagnes, S. Bélair and G. Cote, "Solubility of niobium(V) and tantalum(V) under mild alkaline conditions," Hydrometallurgy, vol. 156, pp. 99–106, 2015.

[272] S. Ran, O. Biest and J. Vleugels, "ZrB_2 powders synthesis by borothermal reduction," J. Am. Ceram. Soc., vol. 1590, pp. 1586–1590, 2010.

[273] M. Oghbaei and O. Mirzaee, "Microwave versus conventional sintering: a review of fundamentals, advantages and applications," Journal of Alloys and Compounds, vol. 494, no. 1–2. pp. 175–189, 2010.

[274] S. Zhu, W. G. Fahrenholtz, G. E. Hilmas, S. C. Zhang, E. J. Yadlowsky and M. D. Keitz, "Microwave sintering of a ZrB_2-B_4C particulate ceramic composite," Compos. Part A: Appl. Sci. Manuf., vol. 39, no. 3, pp. 449–453, 2008.

[275] L. Presenda, M. D. Salvador, F. L. Pearanda-Foix, R. Moreno and A. Borrell, "Effect of microwave sintering on microstructure and mechanical properties in Y-TZP materials used for dental applications," Ceram. Int., vol. 41, no. 5, pp. 7125–7132, 2015.

[276] D. Johnson, V. Kramb and D. Lynch, "Plasma Sintering of Ceramics," pp. 207-211, Conference Proceedings: Emergent Process Methods for

High-Technology Ceramics, Volume 17 of the series Materials Science Research, 1982.

[277] L. Rangaraj and C. Divakar, "Processing of refractory metal borides, carbides and nitrides," Key Eng. Mater., vol. 395, pp. 69–88, 2009.

[278] P. Ramanujam, "Synthesis and processing of nanocrystalline YAG (yttrium aluminium garnet) ceramics," PhD thesis, Loughborough University, 2015.